Long-term Analysis of Toronto-Area Atmospheric Composition

by

Shoma Yamanouchi

A thesis submitted in conformity with the requirements
for the degree of Doctor of Philosophy

Department of Physics
University of Toronto

Long-term Analysis of Toronto-Area Atmospheric Composition

Shoma Yamanouchi
Doctor of Philosophy

Graduate Department of Physics
University of Toronto
2021

Abstract

This thesis examines total columns of C_2H_2, C_2H_6, CH_4, CH_3OH, CO, H_2CO, HCl, HCN, HCOOH, HF, HNO_3, N_2O, NH_3, and O_3 measured using Fourier transform infrared (FTIR) spectroscopy to study Toronto-area atmospheric composition. The thesis has three scientific objectives: to quantify trends in the time series of trace gas concentrations, to determine how emissions from biomass burning events affect air quality over Toronto and whether observations in Toronto can be used to quantify wildfire emissions, and to examine the spatial representativeness and temporal variability of the FTIR NH_3 columns over Toronto.

Trends and enhancement events were determined by fitting trended Fourier series to the total columns, and bootstrapping was used to identify the statistical significance. Trends from 2002 to 2019 were examined, and the GEOS-Chem chemical transport model was used to identify major sources of CO and CH_4 over Toronto, which were CH_4 oxidation and wetland emissions, respectively.

Transport of wildfire plumes over the site results in enhanced columns of biomass burning species. Several simultaneous enhancements of CO, HCN, and C_2H_6 were observed, and the measured columns were used to derive emission ratios and emission factors for HCN and C_2H_6 for fire events in 2012, 2015, and 2017. For the 2015 and 2017 events, simultaneous enhancements of HCOOH and CH_3OH were observed, and their emission ratios and emission factors were also examined.

Atmospheric NH_3 is a pollutant, and a major source of fine particulate matter. In this study, three NH_3 datasets were used: TAO FTIR total columns, three years of surface in situ measurements, and ten years of total column measurements from the Infrared Atmospheric Sounding Interferometer (IASI). The datasets were used to quantify NH_3 temporal variability over Toronto, Canada. All three time series showed positive trends in NH_3 over Toronto: 3.56 ± 0.85 %/year from 2002 to 2019 in the FTIR columns, 8.88 ± 5.08 %/year from 2013 to 2017 in the surface in situ data, and 8.38 ± 1.54 %/year from 2008 to 2018 in the IASI columns. The multiscale datasets were also compared to assess the representativeness of the FTIR measurements.

Acknowledgments

I would first like to thank my advisor, Professor Kimberly Strong, who has guided and supervised the research presented in this thesis, for her continued support, guidance, and mentoring throughout my doctoral program. Her encouragement has been instrumental in making my graduate studies some of the most enjoyable, exciting, and rewarding experiences that I have yet to encounter.

I would also like to express my gratitude to my advisory committee members, Professor Dylan Jones and Professor Jennifer Murphy. I am grateful for Professor Jones for being my co-supervisor, providing guidance with the GEOS-Chem model, and valuable feedback for my research. I would also like to thank Professor Murphy for the insightful and helpful discussions that I have had with her.

I would also like to thank the students, post-docs, and interns who have taken measurements with the TAO FTIR, and provided help and feedback on my research, particularly Dr. Stephanie Conway and Sébastien Roche. I would like to express my gratitude to Dr. Erik Lutsch, who has provided me with many helpful insights and discussions, as well as guidance on both TAO retrievals and GEOS-Chem analysis, as well as Research Officer Orfeo Colebatch for his continued support in making TAO measurements. I would also like to express my gratitude to Drs. Camille Viatte, Cathy Clerbaux, Martin Van Damme, Lieven Clarisse, and Pierre-Francois Coheur for their valuable input for one of my research projects.

Contents

List of Tables

List of Figures

List of Abbreviations

ACE Atmospheric Chemistry Experiment

AIRS Atmospheric InfraRed Sounder

AmmonAQ Ammonia Air Quality

AUST Australia, New Zealand (source region defined in GEOS-Chem)

BOAS Boreal Asia (source region defined in GEOS-Chem)

BONA Boreal North America (source region defined in GEOS-Chem)

CAC Criteria Air Contaminants

CAMS Copernicus Atmospheric Monitoring System

CARE Centre for Atmospheric Research Experiments

CEAM Central America (source region defined in GEOS-Chem)

CEAS Central East Asia (source region defined in GEOS-Chem)

CFC chlorofluorocarbon

COVID-19 Coronavirus disease 2019

CrIS Cross-track Infrared Sounder

CTM chemical transport model

DOFS degrees of freedom for signal

ECCC Environment and Climate Change Canada

EDGAR Emission Database for Global Atmospheric Research

EF emission factor

EnhR enhancement ratio

EPA Environmental Protection Agency

EQAS Equatorial Asia (source region defined in GEOS-Chem)

ER emission ratio

EURO Europe (source region defined in GEOS-Chem)

FLEXPART Flexible Particle model

FTIR Fourier transform infrared

FTS Fourier transform spectrometer

FWHM full width half maximum

GEOS Goddard Earth Observing System

GFAS Global Fire Assimilation System

GFED Global Fire Emission Database

GHG greenhouse gas

GWP global warming potential

HITRAN High-resolution Transmission Molecular Absorption Database

HWHM half width half maximum

HYSPLIT Hybrid Single Particle Lagrangian Integrated Trajectory

IASI Infrared Atmospheric Sounding Interferometer

ILS instrument line shape

IPCC Intergovernmental Panel on Climate Change

ITCZ intertropical convergence zone

LATMOS Laboratoire atmosphères, milieux, observations spatiales

MERRA Modern-Era Retrospective analysis for Research and Applications

ME modulation efficiency

MIDE Middle East (source region defined in GEOS-Chem)

MODIS Moderate Resolution Imaging Spectroradiometer

NAPS National Air Pollution Surveillance Program

NAS National Academy of Sciences

NCAR National Center for Atmospheric Research

NCEP National Centers for Environmental Prediction

NDACC Network for the Detection of Atmospheric Change

NEI National Emissions Inventory

NHAF Northern Hemisphere Africa (source region defined in GEOS-Chem)

NPRI National Pollutant Release Inventory

OEM optimal estimation method

OPD optical path difference

PBL planetary boundary layer

PE phase error

QFED Quick Fire Emission Database

RD rapid delivery

RF radiative forcing

SEAS Southeast Asia (source region defined in GEOS-Chem)

SHAF Southern Hemisphere Africa (source region defined in GEOS-Chem)

SHSA Southern Hemisphere South America (source region defined in GEOS-Chem)

SNR signal-to-noise ratio

TAO University of Toronto Atmospheric Observatory

TCCON Total Carbon Column Observing Network

TENA Temperate North America (source region defined in GEOS-Chem)

ULB Université Libre de Bruxelles

UV ultraviolet

VMR volume mixing ratio

VOC volatile organic compound

WHO World Health Organization

WMO World Meteorological Organization

ZPD zero path difference

Chapter 1

Introduction

1.1 Motivation

Measuring the concentrations of the constituents of Earth's atmosphere is an important, yet challenging endeavor. The atmosphere is a complex cocktail of molecules that not only provides the air we breathe, but is also responsible for the hospitable climate that we enjoy; changes to the atmosphere and its composition may therefore have profound effects on the planet and its inhabitants, including human beings. Ensuring that the atmosphere and its composition stay favorable to human beings, and the biosphere as a whole, has become increasingly urgent, as modern anthropogenic activities have proved to be capable of altering the atmosphere. For example, outdoor air quality became a major problem in the industrial age, largely due to emissions of chemicals that have detrimental effects on human health. These pollutants are known to cause severe respiratory illness, including death (Bell et al., 2005; Ministry of the Environment and Climate Change, 2016; Vohra et al., 2021). Additionally, anthropogenic emissions have been linked to negative effects on the biosphere as a whole, due to processes such as ocean acidification (NAS, 2016), climate change (IPCC, 2014; NAS, 2016), and ozone layer depletion (NAS, 2016; WMO, 2018).

Pollutants that have been deemed hazardous to human health are monitored regularly in many parts of the world, including Canada. These pollutants include carbon monoxide (CO), ozone (O_3), particulate matter that is smaller than 2.5 microns ($PM_{2.5}$), nitrogen oxides (NO_x), and in some cases, ammonia (NH_3). In Ontario, the most populous province in Canada, air quality has overall been improving; provincial standards set for CO, nitrogen oxides, and sulfur dioxide (SO_2) are rarely exceeded (Wentworth et al., 2015; Ministry of the Environment and Climate Change, 2016). However, O_3 continues to exhibit exceedances, particular in summer months (Ministry of the Environment and Climate Change, 2016) due to meteorological conditions that allow for O_3 formation (Whaley et al., 2015).

O_3 remains a difficult pollutant to control. This is largely because O_3 is not directly emitted, but rather created by photochemical reactions in the atmosphere (Jacob, 1999). Furthermore, the production scheme is nonlinear, meaning that reduced emissions of precursors may not lead to decreased O_3, and in some cases, can even lead to increases. While local emission regulations (e.g., application of catalytic converters on vehicles) may impact the formation of O_3, there is evidence that long-range transport can also lead to surface O_3 enhancement. A recent study (Connecticut Department of Energy and Environmental Protection, 2017) has indicated that surface O_3 in Connecticut, United States, may have been enhanced due to long-range transport of biomass burning plumes from severe wildfires in Alberta, Canada, which is more than 3000 km upwind.

Biomass burning plumes have caused enhancements in total column measurements of several gases in Toronto as well (e.g., Lutsch et al., 2016, 2020). While several analyses using data from Toronto to estimate upwind emissions have been performed (e.g., Lutsch et al., 2016), further analysis is needed to obtain estimates for species emitted during fires, and to better constrain emissions.

Another pollutant that has received recent attention is NH_3. NH_3 concentrations have been steadily increasing in many parts of the world (e.g., Warner et al., 2016; Lachatre et al., 2019), raising concerns due to the role NH_3 plays in particulate matter formation (e.g., Lachatre et al., 2019; Viatte et al., 2020). While advancements in our understanding of, and our ability to measure and model, atmospheric NH_3 have been made in recent years, further study is needed to better understand its spatial and temporal variability, assess model performance, and validate satellite measurements of NH_3 (Van Damme et al., 2015a; Viatte et al., 2020; Tournadre et al., 2020).

In addition to monitoring pollutants with detrimental health effects, careful monitoring of gases with radiative effects is crucial for understanding their impact on climate change (e.g., Sheese et al., 2016; Innocenti et al., 2017), and improving the accuracy and predictive capacities of atmospheric models (e.g., Jose et al., 2016). To understand the atmosphere and how it is changing, long-term observations are needed. In this thesis, long-term atmospheric composition measurements made in Toronto, the largest city in Canada, will be examined.

1.2 Scientific Objectives

Three scientific objectives will be explored in this thesis. These studies will make use of the 18-year time series of trace gases measurements made with a Fourier Transform InfraRed (FTIR) spectrometer situated in downtown Toronto at the University of Toronto Atmospheric Observatory (TAO), combined with model simulations and observations on the ground and from space. The scientific objectives of this thesis are:

(1) To quantify trends in the time series of trace gas concentrations over Toronto, and for CO, to examine if it is possible to identify what drives the trend.

(2) To determine how emissions from biomass burning events affect air quality over Toronto, and whether observations in Toronto can be used to quantify wildfire emissions.

(3) To examine the spatial representativeness and temporal variability of the FTIR NH_3 columns in Toronto.

1.3 Thesis Outline

This thesis is organized as follows: in this chapter, the following Section (Section 1.4) will discuss the background and current understanding of basic atmospheric physics and chemistry (Section 1.4.1), atmospheric NH_3 (Section 1.4.2), emissions from biomass burning (Section 1.4.3), and greenhouse gases and their role in climate change (Section 1.4.4). The rest of the thesis is as follows:

Chapter 2: Methods

This chapter introduces relevant spectroscopic theory, and details the workings of the FTIR spectrometer, followed by an overview of retrieval theory used to obtain column profiles of trace gases from infrared solar absorption spectra. This chapter also discusses the specifics of the experimental set-up used to obtain the data used in the thesis, the algorithm used for retrieval, and the models used to interpret observational data.

Chapter 3: Trends of Trace Gases at TAO

This chapter describes the methodologies used to obtain trends in the TAO time series, and presents the resulting trends of all trace gases that are currently being retrieved. It also includes an analysis using the GEOS-Chem model to aid in understanding what drives the trends in CO seen with the FTIR, and a discussion of results.

Chapter 4: Biomass Burning Enhancements at TAO

This chapter discusses estimates of emissions from wildfires using three enhancement events of biomass burning species observed at TAO. It includes the analysis methodologies, a discussion on attributing sources using models, as well as a discussion on the results, including the limitations of the approach employed.

Chapter 5: NH_3 Observations Over Toronto

This chapter includes comparisons of TAO NH_3 total columns with space-borne observations and in-situ (surface) observations, as well as a comparison with the GEOS-Chem model simulation, in an attempt to discern the spatial representativeness the FTIR NH_3 columns, as well as the temporal variability of NH_3 in Toronto. Trends seen in NH_3 using space-borne and in-situ observation are also discussed, using the same methodology used to obtain trends in the TAO time series.

Chapter 6: Conclusions and Future Work

This chapter summarizes the analyses done in order to address the scientific objectives posed in Section 1.2, and offers the conclusions from this thesis. It also includes suggestions for future work.

1.4 Background

1.4.1 Brief Overview of Atmospheric Physics and Chemistry

The vertical structure of the atmosphere has several layers, with the troposphere at the bottom, followed by the stratosphere, mesosphere, and thermosphere. The boundary between the troposphere and stratosphere is called the tropopause, and is generally located about 8-18 km from the surface, varying depending on latitude and season (Jacob, 1999). These layers, however, are not defined by altitude, but rather by temperature; in the troposphere, temperature decreases with altitude (at a rate known as the lapse rate), and the stratosphere is said to begin when this *inverts* (temperature inversion). This results in the stratosphere being highly stratified (as the name suggests), with strong stability in the vertical direction. This is in contrast to the troposphere, where the temperature profile allows for vertical mixing. There are several important atmospheric transport mechanisms that combine vertical, longitudinal and latitudinal motion.

Long-range transport in the atmosphere is largely dictated by trade winds, westerlies, and jet streams. These winds are driven by a combination of global meridional circulation and the Coriolis force. The Hadley cell is characterized by an upwelling in the intertropical convergence zone (ITCZ) near the equator, flowing poleward at altitudes from 10-15 km, then down towards the surface (subsidence) in the sub-trropics (around 30°) (Held and Hou, 1980; Jacob, 1999; Hartmann, 2016). The meridional circulation, coupled with the Coriolis force, drives winds such as the low-altitude easterlies and high-altitude westerlies that are seen in between the ITCZ and mid-latitudes (Jacob, 1999; Hay, 2013). Zonal transport is much faster than meridional transport; typical wind speeds may be on the order of 10 m/s in the zonal direction, compared to around 1 m/s in the meridional direction. Zonal winds can circumnavigate the globe in a few weeks, while air parcels from the mid-latitudes may take 1 to 2 months to reach the poles or tropics (see Figure 1.1). Another zonal air current is the jet stream. Jet streams are fast-flowing, narrow eastward air currents that occur near the tropopause. They form at the transition points between the Hadley, Ferrel and Polar circulation cells. These jet streams meander, and the periodicity of the meandering wave is given by the Rossby wave, which arises due to conservation of angular momentum. Polar jets form at lower altitudes than the subtropical jet stream (which occurs between the Hadley and Ferrel cells), and are known to affect weather (Riehl, 1954).

Another important transport mechanism is the Brewer-Dobson circulation, which involves meridional motion that transports air from the tropics to the extratropics. The process initiates with a rising motion in the tropics driven by wave forcing at higher latitudes (Ueyama et al., 2013; Butchart, 2014; Cohen et al., 2014) that takes air from the troposphere into the stratosphere. This air is advected poleward in the stratosphere, which then descends in the mid to high/polar latitudes. This flow explains the high concentrations of O_3 in the polar regions despite much of the O_3 being

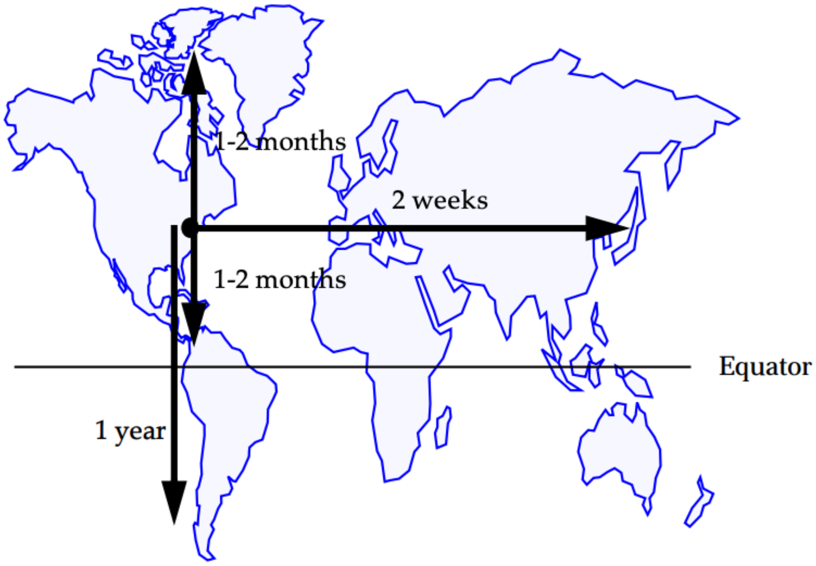

Figure 1.1: Typical time scales of global tropospheric transport. Figure taken from Jacob (1999).

produced in the tropics (Brewer, 1949; Dobson, 1956). The Brewer-Dobson circulation also affects atmospheric composition in the mid-latitudes, particularly during polar vortex (large low-pressure system that forms over the winter poles) intrusion events, where columns of species like O_3 are increased, while longer-lived tropospheric species (e.g., nitrous oxide) are decreased (Schoeberl et al., 1992). Several polar vortex intrusion events have been observed over Toronto (Whaley et al., 2013).

Multiple chemical, physical, and radiative factors determine the chemical composition of the atmosphere, and understanding them is imperative for understanding and interpreting observational data, as well as for building and utilizing robust and accurate models of the atmosphere (NAS, 2016). In general, four processes must be accounted for. Emissions of chemical species into the atmosphere, which can be anthropogenic, biogenic or other (e.g. volcanic emissions), and the deposition of atmospheric gases back to the Earth's surface, can increase or decrease concentrations of gases in the air, respectively. Chemical reactions in the atmosphere can also lead to the formation or destruction of species, and lastly, transport of air parcels must be considered (Jacob, 1999).

While these four factors determine atmospheric composition, the atmosphere is also a part of the larger Earth system. From this perspective, atmospheric composition is controlled by biogeochemical cycles, which exchange elements between several reservoirs of the Earth system (Jacob, 1999) (see Figure 1.2). The latter two of the aforementioned processes (chemical reactions and transport of species in the atmosphere) are contained in the atmosphere box in the diagram, while processes like gas-water exchange, decay and photosynthesis (which is sometimes collectively called deposition and emission) link the biosphere and hydrosphere to the atmosphere. The diagram does not include anthropogenic activities. Some of these geochemical cycles can take hundreds of thousands of years if not more, but can be accelerated by anthropogenic means (Jacob, 1999). The increase in atmospheric carbon dioxide (CO_2) due to anthropogenic activities is well documented, and this can be seen as an example of carbon stored in the lithospheric reservoir (inside the Earth) making its way into the atmosphere (in a relatively short period of time) due to anthropogenic influences (i.e., positive net outflow from the reservoir into the atmosphere). This is also discussed in Sections 1.4.3 and 1.4.4. While organic compounds have large effects on the atmosphere, nitrogen (in the form of N_2) is by far the most abundant chemical constituent in the atmosphere, making up 78% of the air by mole fraction. Nitrogen is closely tied to the biosphere by a process known as fixation (in which nitrogen in the air is converted to NH_3). Nitrogen can be deposited onto the surface, usually in

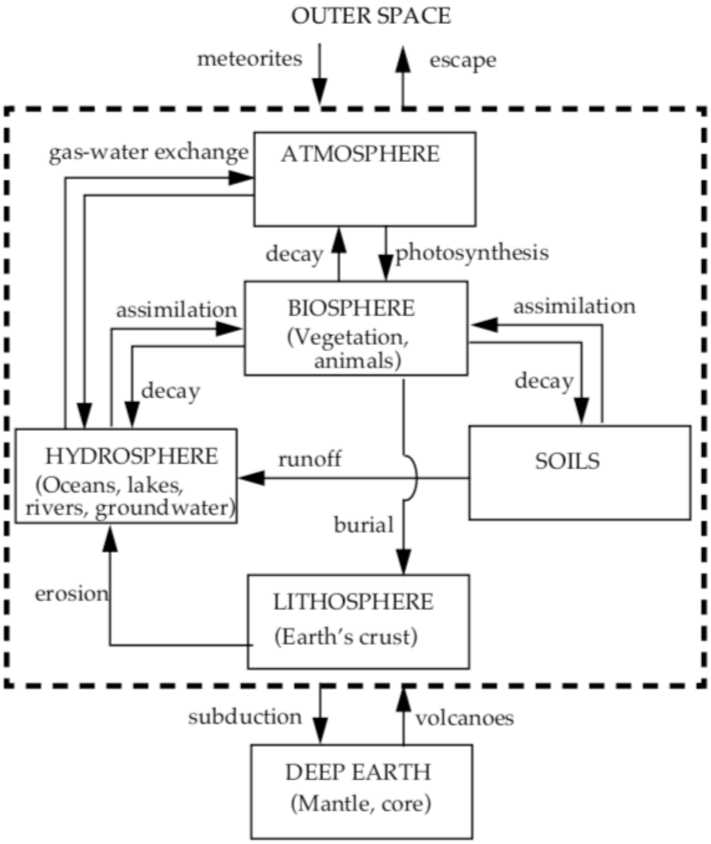

Figure 1.2: The atmosphere is connected to the biosphere as well as the oceans and other surface water systems. Note that anthropogenic emissions are not explicitly listed here. Figure taken from Jacob (1999).

the form of nitric acid (HNO_3) dissolved in rain. N_2 in the atmosphere can also be converted to NO via lightning strikes, which results in HNO_3 via oxidation, which will be discussed in more detail in the coming paragraphs.

Although many chemical species are present in the atmosphere at any given time, a large number are short-lived and will quickly be oxidized. While the most ubiquitous oxidants in the atmosphere are O_2 and O_3, reactions with these species are relatively slow, and the hydroxyl (OH) radical is the most active oxidant. OH is produced via the reaction:

$$O(^1D) + H_2O \longrightarrow 2\ OH \tag{1.1}$$

where the $O(^1D)$ is produced via photolysis of O_3:

$$O_3 + h\nu \longrightarrow O_2 + O(^1D). \tag{1.2}$$

In the stratosphere, Equation 1.2 can occur freely due to the abundant incoming solar UV radiation. However, in the troposphere, where the bulk of the atmosphere is located (85% by mass), much of the UV radiation has already been absorbed by stratospheric O_3. OH production, however, can still take place due to a much higher concentration of water vapor present in the troposphere.

The OH radical is known as the "detergent" of the atmosphere due to its ability to oxidize most of the chemicals in the air (Nicely et al., 2018) (exceptions include anthropogenic species like chlorofluorocarbons (CFCs)). The main sinks of OH are CO and CH_4, and thus gaining knowledge about the concentrations of these species can provide insight on OH concentrations, and the oxidation chemistry happening in the troposphere. OH chemistry in the troposphere is also driven by NO_x (NO + NO_2). NO_x, together with HO_x (H + OH + HO_2), can catalyze O_3 formation in the troposphere (it is interesting to remark that NO_x can catalytically destroy O_3 in the stratosphere), allowing for more tropospheric OH production (see Figure 1.3).

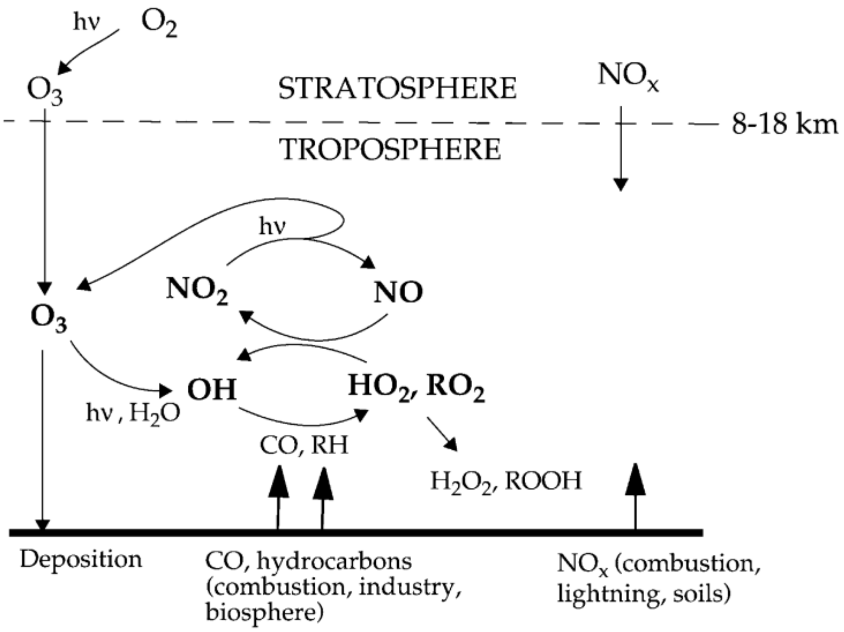

Figure 1.3: O_3 production chemistry in the troposphere. Figure taken from Jacob (2000).

1.4.2 NH_3 in the Atmosphere

Ammonia (NH_3) in the atmosphere plays an important role in the formation of ammonium salts (e.g., ammonium nitrate and ammonium sulfate), is a major pollutant, and is known to be involved in numerous biochemical exchanges affecting all ecosystems (Erisman et al., 2008; Hu et al., 2014). As one of the main sources of reactive nitrogen in the atmosphere, NH_3 is also associated with acidification and eutrophication of soils and surface waters, which can negatively affect biodiversity (Vitousek et al., 1997; Krupa, 2003; Bobbink et al., 2010). Furthermore, NH_3 reacts with nitric acid and sulfuric acid to form ammonium salts, which are known to account for a large fraction of inorganic particulate matter (Kleeman et al., 1999; Schaap et al., 2004; Schiferl et al., 2014; Pozzer et al., 2017; Viatte et al., 2021), and are thought to contribute to smog and haze (Wu et al., 2016; Liu et al., 2019;

Wielgosiński and Czerwińska, 2020). Understanding how particulate matter forms is helpful in addressing air quality concerns (Schiferl et al., 2014), as particulate matter, especially that smaller than 2.5 microns ($PM_{2.5}$), poses serious health hazards affecting life expectancy in the United States (Pope et al., 2009) and globally (Giannadaki et al., 2014). Studies have shown that NH_3 in urban areas with active photochemistry can lead to ammonium nitrate aerosol formation, which can degrade air quality (e.g., Kleeman et al., 1999). Furthermore, high concentrations of NH_3 can shift the thermodynamic equilibrium to favor condensation of ammonium nitrate onto particles, leading to the formation of particulate matter (Nowak et al., 2010).

Due to the negative impacts NH_3 can have on public health and the environment, NH_3 emissions are regulated in some parts of the world (e.g., the 1999 Gothenburg Protocol to Abate Acidification, Eutrophication and Ground-level Ozone). However, global NH_3 emissions are increasing (Warner et al., 2016; Lachatre et al., 2019), and this has been attributed to increases in agricultural livestock numbers and increased nitrogen fertilizer usage (Warner et al., 2016) (see Figure 1.4). In addition, as the world population continues to grow, and the demand for food rises, NH_3 emissions are expected to further increase (van Vuuren et al., 2011). Models and surface observation show increasing abundance of atmospheric NH_3. For example, trends as high as 12% annually were seen in the Eastern United States by Yu et al. (2018), who used a combination of model (GEOS-Chem) and surface observations. Yu et al. (2018) concluded that the increase in NH_3 abundance was in part due to decreasing SO_2 and nitrogen oxides NO_x ($NO + NO_2$), owing to more stringent emissions regulations. SO_2 and NO_x are precursors to acidic species (sulfuric and nitric acid, respectively)

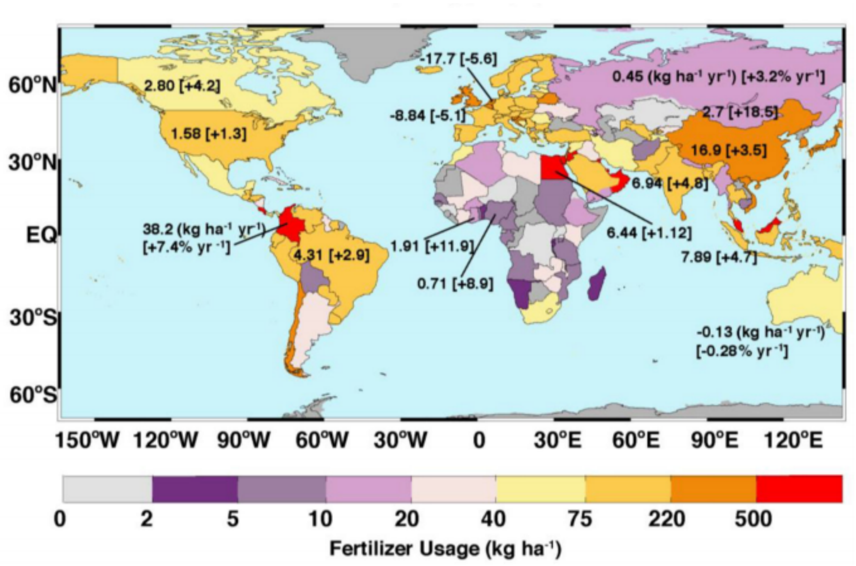

Figure 1.4: Annual fertilizer usage by region (in kg/ha), from 2002 to 2013. The numbers inside the square brackets indicate annual percentage change. Figure taken from Warner et al. (2017). Fertilizer usage has been linked to increasing atmospheric NH_3 (Warner et al., 2017).

that react with NH_3, and thus their abundances in the atmosphere determine the amount of NH_3 that stays in the gaseous phase.

Atmospheric NH_3 is rapidly removed by wet and dry deposition as well as by heterogeneous reactions with acids in the atmosphere, and thus has a relatively short lifetime ranging from a few hours to a few days (Galloway et al., 2003; Dammers et al., 2019). NH_3 lifetime may be longer for certain cases, such as biomass burning emissions that inject NH_3 into the free troposphere (Höpfner et al., 2016), attenuating depositional and chemical losses, although physical and chemical mechanisms that lead to transport of NH_3 in biomass burning plumes over long distances remain uncertain (Lutsch et al., 2016, 2019).

NH_3 simulations by atmospheric chemical transport models can be used to interpret observations (Liu et al., 2017). However, ground-level NH_3 abundances are poorly modeled, due to coarse model resolution, uncertain emissions inventories, and simplification of chemistry schemes (Liu et al., 2017). Dependence of $PM_{2.5}$ formation on NH_3 over urban areas also remains uncertain, and models have difficulty simulating NH_3 and $PM_{2.5}$ (e.g., Van Damme et al., 2014a; Fortems-Cheiney et al., 2016; Schiferl et al., 2016; Viatte et al., 2020). Additionally, long-term trend analyses using models have been sparse (Yu et al., 2018). Representative measurements of NH_3 on both local and regional scales, as well as their spatiotemporal variabilities, are needed to better understand and model NH_3 and $PM_{2.5}$ formation (Viatte et al., 2020).

1.4.3 Emissions from Biomass Burning

Biomass burning events are a common occurrence in North American summers, with substantial ecological, atmospheric and economic impacts (Colarco et al., 2004; Jacobson, 2014; Schoennagel et al., 2017). Estimates of annual global total carbon combustion distribution are shown in Figure 1.5. In recent years, the expansion of residential areas into areas at high risk for fires has made the effects of wildfires increasingly costly (Schoennagel et al., 2017). Furthermore, there is evidence of climate affecting the severity and frequency of wildfires in North America and elsewhere (Flannigan and Cantin, 2012).

Kirchmeier-Young et al. (2019) have shown that climate change can make wildfire extremes more likely and increase the area burned. This is noteworthy, as the gross effect of wildfires on the boreal carbon reservoir flux is determined by wildfire intensity as well as its frequency. Based on simulations and data collected from 31 fire events in Alaska, Turetsky et al. (2010) estimated that the annual burned area over boreal regions will increase 2 to 3 fold in the next 50 to 100 years. Furthermore,

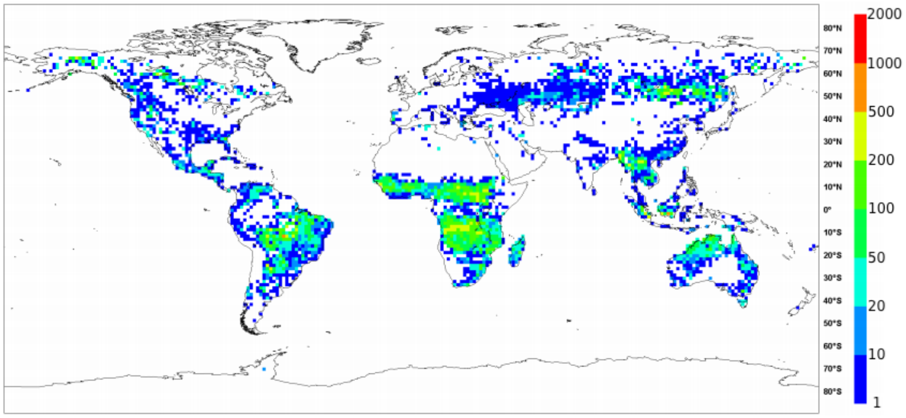

Figure 1.5: Estimated biomass burning carbon combustion distribution, annual average during 2003-2008 (g/m^2/year). Figure taken from Kaiser et al. (2012).

fire severity in those regions is also predicted to increase. These increases in burning in northern boreal regions can trigger a positive feedback between fire severity and permafrost melting, and hence the potential for the release of greenhouse gases (Turetsky et al., 2010).

Wildfires are a considerable source of atmospheric carbon, injecting up to 2 Pg of carbon into the air globally every year (van der Werf et al., 2010; Worden et al., 2017). The radiative forcing (RF) due to biomass burning is difficult to quantify, especially as there are competing cooling and warming effects. It has been estimated that black carbon and organic aerosols from biomass burning have RF values of 0.2 and -0.2 W/m^2 respectively, meaning that the net effect of these aspects of biomass burning emissions is zero (IPCC, 2014). However, another study by Jacobson (2014) estimates a $\sim$0.4 K global warming over the course of a 20-year model run. This study was the first to include brown carbon absorption (also known as tar balls), anthropogenic heat and moisture fluxes, and cloud absorption effects I and II in its model simulations. Cloud absorption effects I and II are the absorption *inside* water vapor particles, and absorption by aerosols between water vapor in clouds, respectively (Jacobson, 2014).

Additionally, there is evidence to suggest that there is a feedback loop that amplifies the effects of fire events in the Arctic; this is because emissions from wildfires can lower surface albedo in the Arctic, which can lead to warming of the region, which then can lead to more frequent and severe wildfire events (Kim et al., 2005; Ramanathan and Carmichael, 2008; Coogan et al., 2019). A recent study by Lisok et al. (2018) investigated the impact of aerosols emitted from biomass burning at high latitudes by examining plumes transported from Alaska to Ny-Ålesund in early July 2015, and using a radiative transfer model, determined an RF value of 31.9 W/m^2. Recent findings by Peterson et al. (2018) have shown that wildfires can also perturb the radiative and chemical properties of the lower stratosphere, and that the magnitude of these perturbations is comparable to that of volcanic intrusions.

In addition to carbon aerosols, biomass burning emits several chemical species that are of importance not only for climate and the carbon cycle, but also for public health. These emissions, even after long-range transport, can have adverse effects on air quality when the plume is entrained within the planetary boundary layer (PBL) and is subsequently transported to the surface. In a study conducted by Colarco et al. (2004), emissions from a Canadian forest fire were seen to have affected air quality in Washington, DC after the traveling plume descended to near the surface, transported with a turbulent PBL flow. In fact, degraded air quality due to biomass burning emissions is thought to have caused anywhere from 73,000 to 435,000 premature deaths/year globally, over 90% of which have been attributed to particulate matter, and the rest to photochemical production of O_3 resulting from emissions of precursor gases like NO_x (Goode et al., 2000; Turetsky et al., 2010; Jacobson, 2014).

Given the human, ecological, and environmental impacts of biomass burning, accurate atmospheric models are needed to understand wildfire episodes, emissions, and their effects downwind. These models rely on emission estimates (inventories) from wildfires. Wildfire emissions are quantified by calculating the emission factor (EF) (e.g., Akagi et al., 2011), which is the amount of a trace gas emitted for every kilogram of fuel (wood, bark, etc.) consumed. The EF can vary significantly depending on factors such as the phase of combustion (e.g., smoldering versus flaming), the vegetation type being burned, and the atmospheric conditions during the fire (e.g., Akagi et al., 2011; Viatte et al., 2013; Jen et al., 2019). EF can be multiplied by the amount of fuel consumed, which is estimated by the area of the burnt land (e.g., using satellite observations) to obtain emissions estimates (e.g., Zhou et al., 2017). CO, hydrogen cyanide (HCN) and ethane (C_2H_6) are often utilized as tracers for biomass burning events due to their long lifetimes (Urbanski, 2014; Viatte et al., 2014), but estimates of their emission factors vary widely, possibly due to the natural variability in the emissions (due to the reasons listed above), and/or the differences between measurement methodologies, which can range from laboratory observations to estimates made from ground-based instruments (which may be nearby, or downwind of the fire) and satellite measurements (e.g., Andreae and Merlet, 2001; Akagi et al., 2011; Viatte et al., 2013; Andreae, 2019).

Methanol (CH_3OH) is also emitted from biomass burning. CH_3OH is the second most abundant organic compound in the atmosphere (after methane), and is a major source of CO and formaldehyde (Jacob et al., 2005). Another trace gas emitted from biomass burning is formic acid (HCOOH), a species which is also noted for being one of the most abundant atmospheric volatile organic compounds (VOCs), and for its potential for increasing rain acidity in remote areas (Chameides and Davis, 1983; Jacob, 1986). Despite its important role in the atmosphere, HCOOH emissions are underestimated by models, and much about its chemistry remains uncertain (Paulot et al., 2011; Stavrakou et al., 2012; Millet et al., 2015).

1.4.4 Greenhouse Gases

Greenhouse gases (GHGs) in the atmosphere play an important role in controlling the temperature of the Earth. The main source of energy on the surface of the Earth is the radiation from the Sun, which acts to increase the temperature of the surface and atmosphere of Earth. Without GHGs, the temperature on the surface of the Earth would be so cold as to not allow for the existence of liquid water, something crucial to maintaining life (Manabe and Strickler, 1964). The following will briefly explain the mechanisms of the greenhouse effect, which GHGs are important to monitor, and the current understanding of the abundance and trends of GHGs.

The incoming radiation from the Sun heats up the surface of the Earth, and continues to do so until the outgoing energy due to the blackbody radiation of Earth equals the incoming solar energy. The incoming and outgoing energy can be calculated by first considering the Stefan-Boltzmann law:

$$\Phi = \sigma T^4, \tag{1.3}$$

where Φ is the outgoing energy per area per time (i.e., with units Wm^{-2}), and σ is the Stefan-Boltzmann constant (about 5.67×10^{-8} $\mathrm{Wm}^{-2}\mathrm{K}^{-4}$). Since the temperature of the Sun (T_s) is about 5800 K, the total energy output of the Sun can then be calculated by multiplying the σT_s^4 by the surface area of the Sun. The solar radiation arriving at Earth can then be estimated by the multiplying the flux of the solar radiation at distance $d = 1$ Au (Earth–Sun distance) and the cross-sectional area of Earth. A fraction of that may be reflected (e.g., by clouds and snow); this fraction is estimated to be around 0.29 (Stephens et al., 2015; Hartmann, 2016). Assuming no greenhouse effect takes place, equating the energy from the incoming radiation and the outgoing radiation (also calculated with Equation 1.3) results in a temperature of 255 K, well below the freezing point of water.

Clearly, much of the surface of the Earth is above freezing, as evidenced by the existence of lakes and oceans, and the greenhouse effect provides an explanation. The incoming radiation is high frequency (high energy), and the gases present in the atmosphere are mainly invisible to this radiation. However, as the solar radiation heats the Earth's surface, Earth radiates blackbody radiation, mainly in the infrared spectral range. The outgoing infrared radiation can then be absorbed by molecules in the atmosphere (see Section 2.1), increasing their vibrational energy. The gases are warmed by the terrestrial radiation, and they in turn, emit blackbody radiation, some of which radiates back down to the surface of Earth. This process results in the warming of the surface of Earth.

Several gases contribute significantly to this process. These include water (H_2O), CO_2, methane (CH_4), nitrous oxide (N_2O) and CFCs. H_2O is a powerful GHG and is abundant; and while H_2O has significant radiative forcing effects, it also condenses out of the atmosphere as precipitation. Other gases, such as CO_2 and CH_4, do not condense, meaning they stay in the atmosphere for a long time. CO_2 and CH_4 are the two most influential anthropogenic greenhouse gases (Jacob, 1999; IPCC, 2007), and their increasing atmospheric concentrations greatly contribute to climate change (IPCC, 2014; Matthews et al., 2004). The amount of heat a greenhouse gas traps in the atmosphere can be understood by the global warming potential (GWP). The GWP depends on several key attributes of the gas, namely: its absorption of infrared radiation, and its atmospheric lifetime. CO_2 is defined to have a GWP of 1, while CH_4 has a GWP value of 84 when looking over a 20-year time span (IPCC, 2014) and 28 when calculated over 100 years. This difference is due to CH_4 having a relatively short lifetime of 12.4 years compared to 30-95 years for CO_2 (IPCC, 2014). N_2O is another major greenhouse gas, with a GWP of 264 and 265 calculated over 20 and 100 year time spans, respectively (IPCC, 2014). The N_2O GWP is slightly larger over 100 years because the lifetime of N_2O is longer than that of CO_2, at about 121 years.

Another metric used to quantify greenhouse gas capacity for causing warming is radiative forcing (RF). RF is defined to be the net radiative flux density at the tropopause after the stratosphere had sufficient time to come to radiative equilibrium (this is known fully as stratospherically adjusted RF, and is the primary metric used in Intergovernmental Panel on Climate Change (IPCC) documents). As an energy flux density, RF has units W/m^2, and a change in RF can be multiplied by a climate sensitivity parameter to obtain a temperature change at the surface (IPCC, 1995). For CO_2, the change in RF (compared to 1750, the pre-industrial baseline) was estimated

Table 1.1: Table of lifetimes, GWP and RF values of major anthropogenic greenhouse gases (IPCC, 2014).

Gas	Lifetime (years)	GWP_{20yr}	GWP_{100yr}	GWP_{500yr}	RF (W/m^2)
CO_2	30-95	1	1	1	1.82 ± 0.19
CH_4	12.4	84	28	7.6	0.48 ± 0.05
N_2O	121	265	265	153	0.17 ± 0.03
CFC-12	100	10800	10200	5200	0.17 ± 0.17
HCFC-22	12	5280	1760	549	0.0477 ± 0.0355

to be around 1.82 W/m^2 (IPCC, 2014) (for a list of GWP and RF values of major greenhouse gases see Table 1.1).

While anthropogenic emissions have led to increased carbon in the atmosphere (Canadell et al., 2010), some emissions are natural. A major natural CH_4 source is wetlands (Jacob, 1999). The emissions from biomass burning are thought to have a significant impact on climate (see Section 1.4.3). The breakdown of atmospheric CH_4 sources is illustrated in Figure 1.6.

While atmospheric CO_2 levels are undoubtedly rising, it should be noted that

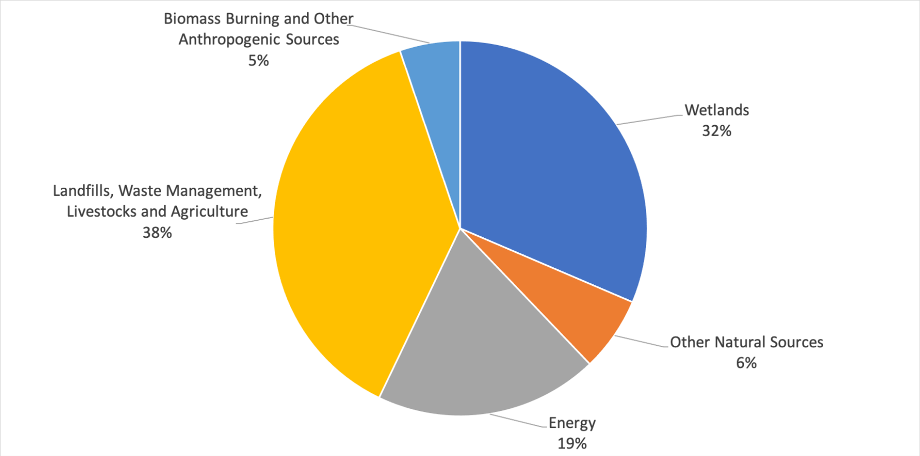

Figure 1.6: CH_4 global inventory. Data from Saunois et al. (2020).

they are not rising as rapidly as emissions suggest. This is mainly due to the ocean and the biosphere acting as reservoirs by absorbing gaseous CO_2. However, the ocean uptake of CO_2 leads to the acidification of the ocean, as CO_2 dissolving in water forms carbonic acid, which dissociates to HCO_3^- (bicarbonate) and CO_3^{2-} (carbonate). As the acidity of the ocean increases, its ability to absorb CO_2 decreases. Due to the logarithmic nature of acidity, the amount of CO_2 the ocean can absorb is extremely sensitive to pH. Currently, the ocean has pH of about 8.2, and for this value, only about 0.03 mole fraction of CO_2 is in the atmosphere. It should be noted, however, that the dissolved CO_2 is not well mixed; the time scales for which water in the ocean mixes can vary from 18 years in the top (near-surface) layer, to 40 years in the intermediate layer, to 120 years for the deep ocean. It is estimated that it takes several hundred years for the entire ocean to come to equilibrium when atmospheric CO_2 is perturbed (Maier-Reimer and Hasselmann, 1987; Enting et al., 1994; Archer et al., 1997).

After CO_2, CH_4 and N_2O are two of the most powerful anthropogenic greenhouse gases in the atmosphere, and accurate concentration estimates are needed to model their climate change effects (IPCC, 2014; NAS, 2016). N_2O, which primarily comes from microbial activity, has been increasing steadily, at about 0.26 %/year (IPCC, 2007) (estimated using surface measurements). A study by Angelbratt et al. (2011a) using FTIR spectrometers in Europe gave similar trends in N_2O columns. N_2O is also an important stratospheric O_3-depleting gas (Ravishankara et al., 2009), and a recent study suggests that agricultural emissions of N_2O have led to an increase in emissions faster than previously estimated by IPCC (Thompson et al., 2019).

CH_4 concentration has also been increasing and it was suggested by Franco et al. (2016a) that increasing oil and gas production in North America is the source of this upward trend; they estimated that CH_4 from oil and gas production increased by 15 Tg/year over the period from 2008 to 2014. Similarly, Turner et al. (2016) estimated that overall North American CH_4 emissions have risen by more than 30% over the period from 2002 to 2014. However, Bruhwiler et al. (2017) have argued that such claims that increasing CH_4 is largely due to oil and gas production are not consistent with observations, and uncertainties regarding CH_4 trends still remain. Because C_2H_6 is co-emitted with CH_4 during oil and gas production, examining both species provides a tool for investigating sources, and there is evidence that C_2H_6 columns are also increasing (Franco et al., 2016a; Helmig et al., 2016).

1.5 Contributions

This thesis will build on our existing understanding of the atmosphere, some of which was discussed above, by utilizing observations made with an FTIR spectrometer situated in downtown Toronto. The TAO FTIR spectrometer and trace gas retrievals were set up by Kimberly Strong and former PhD candidates, Aldona Wiacek and Jeffrey Taylor. Numerous other students, interns, and postdoctoral fellows have since been involved in making measurements, including Cyndi Whaley, Stephanie Conway, Orfeo Colebatch, Sébastien Roche, Erik Lutsch, and myself. Orfeo Colebatch has also provided maintenance, training, troubleshooting, and performed the LINEFIT v14.5 analysis shown in Section 2.4.3. Since 2018, I have been retrieving and submitting data (CH_4, CO, and O_3) approximately biweekly to the Copernicus Atmospheric

Monitoring Service (CAMS) Rapid Delivery (RD) system. I have also retrieved and performed quality control on the data that is archived annually to Network for the Detection of Atmospheric Composition Change (NDACC) (see Section 2.4), building on work done by Stephanie Conway. This includes the entire time series of CH_4, CO, and O_3, as well as the data since 2018 for the other species.

GEOS-Chem, the primary model used in the studies presented here, is a community model developed by its users, primarily by the Atmospheric Chemistry Modeling Group at Harvard University. It was implemented in the Physics Department at the University of Toronto by Dylan Jones. The runs presented in this thesis were performed by Erik Lutsch (tagged CO run used in Chapters 3 and 4) and myself (tagged CH_4 run used in Chapter 3 and full chemistry run used in Chapter 5), with guidance from Dylan Jones.

The work in Chapter 3 was carried out by myself, Kimberly Strong, Orfeo Colebatch, Stephanie Conway, Dylan Jones, Erik Lutsch, and Sébastien Roche. I performed the analyses with guidance from Kimberly Strong and Dylan Jones, and wrote the manuscript on this work. Some of the analysis tools used in the study were built on previous work done by Rodrigue Sandrin and Natalie Gervasi. The study in Chapter 4 was carried out by myself, Kimberly Strong, Erik Lutsch, and Dylan Jones. I performed the analysis with guidance from Kimberly Strong, and help from Erik Lutsch, wrote the paper, and responded to reviewer comments. The work in Chapter 5 was done in collaboration with the Laboratoire atmosphères, milieux, observations spatiales (LATMOS) as part of the AmmonAQ project. The study was carried out by myself, Camille Viatte, Kimberly Strong, Erik Lutsch, Dylan Jones, Cathy Clerbaux, Martin Van Damme, Lieven Clarisse, and Pierre-Francois Coheur. This project was conceived by Camille Viatte, Kimberly Strong, and myself. The satellite (IASI) data used in this study were retrieved by Martin Van Damme and his team at Université Libre de Bruxelles (ULB). I wrote the paper and responded to reviewer comments.

Chapter 2

Methods

2.1 Spectroscopy

2.1.1 Molecular Spectroscopy

Many molecules have distinct absorption and emission features, due to their structures, and these features are governed by quantum mechanics. Molecules with electric dipole moments, in particular, can exhibit rovibrational transitions, which will be the primary focus in this discussion.

Photons with a specific energy are absorbed or emitted when molecules transition from one internal energy state to another. Because energy is directly proportional to frequency and inversely proportional to wavelength, the emission features can be used to identify these molecules. The internal energy transitions can be rotational, vibrational (or a combination of the two), or electronic. The molecular energies are often treated as separate terms, i.e., $E_{\mathrm{Total}} = E_{\mathrm{Electronic}} + E_{\mathrm{Vibrational}} + E_{\mathrm{Rotational}}$. This follows from the assumption that the motion of electrons and the motion of the nucleus in molecules can be separated; this assumption is referred to as the Born-Oppenheimer approximation (there is a fourth energy associated with nuclear spin, but is often omitted as it is much smaller than the other terms) (McNab, 2017). The energies associated with these transitions differ by orders of magnitude; rotational transitions are characterized by emission and absorption in the microwave region of the electromagnetic wave spectrum, while the vibrational transitions occur in the infrared. As mentioned above, these spectral signatures can be used to identify molecules and quantify their abundance, and this can be applied to gain insight into the constituents of the atmosphere.

The simplest example of an absorption feature is the hydrogen atom transitioning from the ground state ($n = 1$) to the next level ($n = 2$). In this case, a photon of wavelength 121.6 nm (equivalent to energy of 10.2 eV) is absorbed, and the electron in the hydrogen atom transitions from energy state $n = 1$ to 2. The hydrogen atom will eventually emit a photon of the same wavelength, as the electron transitions back to the ground state. For molecules, this process is more complex, as the transitions are not confined to electronic energy states, but also rotational and vibrational states. Quantum theory dictates what these energy states may be (Bernath, 2005).

The energy associated with the vibrational motion of a simple diatomic molecule (ignoring anharmonicity) is given by (McQuarrie et al., 1997):

$$E_{\text{Vibrational}}(v) = h\nu_e \left(v + \frac{1}{2}\right), \tag{2.1}$$

where h is the Planck constant, ν_e is the vibrational constant for the molecule, and v is the vibrational quantum number ($v \in \mathbb{N}$). The energy associated with the rotational motion of a diatomic molecule is given by (McQuarrie et al., 1997):

$$\begin{aligned} E_{\text{Rotational}}(J) &= \frac{h^2}{8\pi^2 I} J(J+1) \\ &= BJ(J+1), \end{aligned} \tag{2.2}$$

where I is the moment of inertia of the molecule, J is the rotational quantum number ($J \in \mathbb{N}$), and B is the rotational constant. Vibrational and rotational transitions are particularly important for infrared spectroscopy, as vibrational and rovibrational transitions occur in the infrared region of the electromagnetic spectrum. Rovibrational transitions refer to transitions between a low vibration state and a higher vibrational state while also going down in rotational state (known as the P branch of transition), or up in rotational state (R branch of transition). Transitions where only vibrational levels change are known as the Q branch (McQuarrie et al., 1997). Q branch transitions are not present in molecules with no angular momentum (e.g., O_2 and other homonuclear diatomic molecules). These transition schemes are visualized in Figure 2.1.

In practice, these spectral lines are broadened and have a certain width, depth and a unique shape. The shape of the spectral line is dependent on several factors of the absorbing gas, notably the temperature, the pressure, and the concentration of the molecules in the gas (Bernath, 2005).

2.1.2 Line Shape

Collisional broadening

Collisional broadening occurs when molecules in a gas collide with one another.

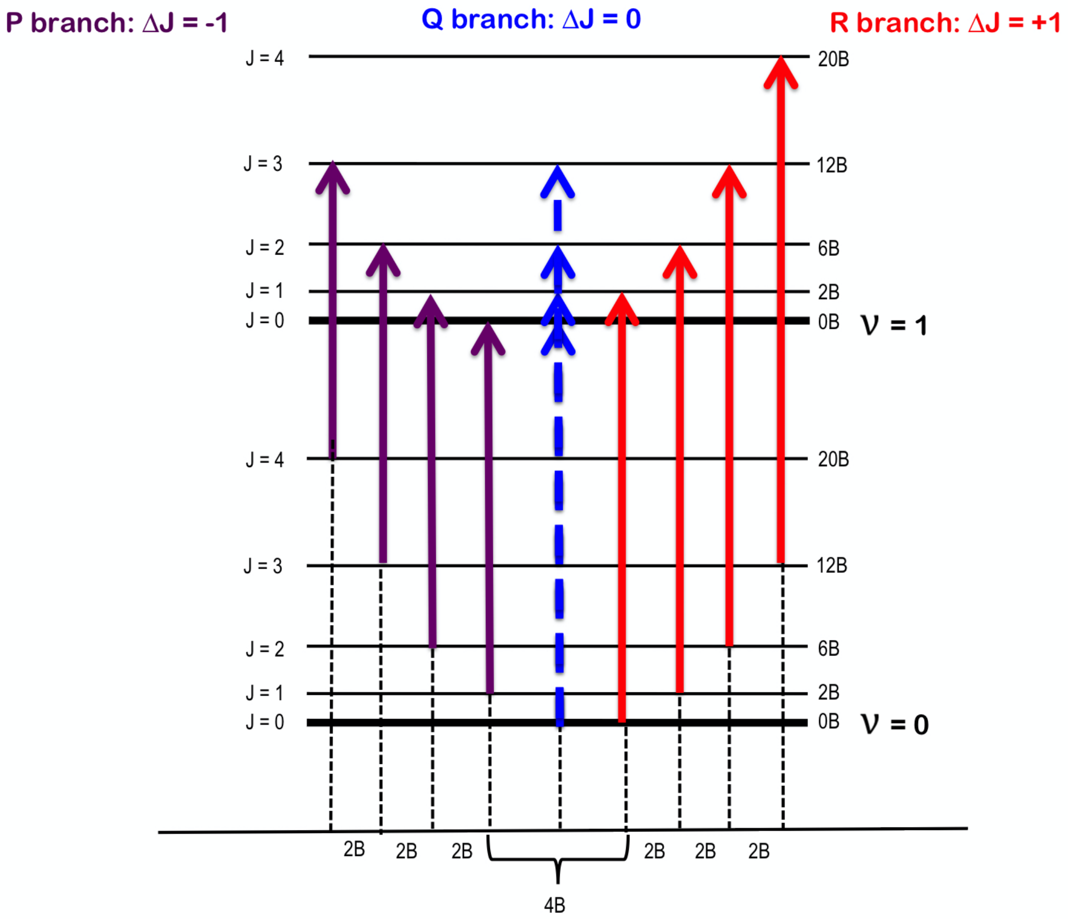

Figure 2.1: Rovibrational Transitions. P, Q, and R branches are depicted with purple, blue, and red arrows, respectively. The $E_{\mathrm{Rotational}}$ for the R branch, for example, is given by $2B(J+1)$, where B is defined by Equation 2.2. Figure taken from `https://chem.libretexts.org/` (last accessed: February, 2021) using material from McQuarrie et al. (1997).

This is notable when the pressure of the gas is high, such as in the troposphere. The line shape function, f_L, of the spectral line is described by a Lorentzian profile (Liou, 2002):

$$f_L(\widetilde{\nu}-\widetilde{\nu_0}) = \frac{1}{\pi}\frac{\alpha_L}{\alpha_L^2+(\widetilde{\nu}-\widetilde{\nu_0})^2}, \tag{2.3}$$

where $\widetilde{\nu_0}$ is the central wavenumber, α_L is the half width at half maximum (HWHM) of the collision-broadened line, which is proportional to pressure, and is given by:

$$\alpha_L = \alpha_0 \frac{P}{P_0} \sqrt{\frac{T_0}{T}}, \tag{2.4}$$

where α_0 is the HWHM at standard pressure P_0 and temperature, T_0 (STP values are typically used). Typical values of α_0 are around 0.1 cm^{-1}.

Doppler broadening

In cases where pressure is smaller, such as in the stratosphere and above, the line shape is dominated by the Doppler effect. The Doppler effect occurs due to the relative motion of the molecule as it travels along the line of sight. The resulting line shape function, f_D, is given by (Liou, 2002):

$$f_D(\widetilde{\nu} - \widetilde{\nu_0}) = \frac{1}{\alpha_D \sqrt{\pi}} \exp\left[-\frac{(\widetilde{\nu} - \widetilde{\nu_0})^2}{\alpha_D^2} \right], \tag{2.5}$$

where α_D is the HWHM of the spectral line divided by the square root of the natural log of 2, and is given by:

$$\begin{aligned} \alpha_D &= \widetilde{\nu_0} \sqrt{\frac{2k_bT}{mc^2}} \\ &= \frac{HWHM}{\sqrt{\ln 2}}, \end{aligned} \tag{2.6}$$

where k_b is the Boltzmann constant, c is the speed of light, and m is the mass of the molecule. It is notable that the broadened line is described by a Gaussian function, as shown in Equation 2.5. Doppler effects dominate in the stratosphere and higher, where molecular collisions occur with less frequency (Griffiths et al., 2007).

Voigt line shape

In reality, both collisional and Doppler effects occur, and thus the line shape can be modeled by convolving the Lorentz and Doppler line shape functions (Liou, 2002). This results in the Voigt line shape function, f_V, and is given by (Griffiths et al., 2007):

$$\begin{aligned} f_V(\widetilde{\nu}-\widetilde{\nu_0}) &= f_L(\widetilde{\nu}'-\widetilde{\nu_0}) * f_D(\widetilde{\nu}'-\widetilde{\nu_0}) \\ &= \int_{-\infty}^{\infty} \frac{\alpha_L}{\alpha_L^2+(\widetilde{\nu}'-\widetilde{\nu_0})^2} \frac{1}{\alpha_D\sqrt{\pi}} \exp\left[-\frac{(\widetilde{\nu}'-\widetilde{\nu_0})^2}{\alpha_D^2}\right] \mathrm{d}\widetilde{\nu}'. \end{aligned} \tag{2.7}$$

This function has a HWHM of (Griffiths et al., 2007):

$$\alpha_V = \frac{\alpha_L}{2} + \sqrt{\frac{\alpha_L^2}{4} + (\alpha_D + \ln 2)^2}. \tag{2.8}$$

Because the Voigt profile accounts for both collisional and Doppler effects (Liou, 2002), the Voigt profile is appropriate for analyses that measure absorption features from the entire atmosphere (i.e., total column measurements). Voigt line shapes omit line mixing effects (i.e., assumes that spectral lines are isolated).

2.1.3 Line Strength

When light passes through some medium, like the atmosphere, its intensity will be attenuated. Beer's law (sometimes referred to as the Beer-Lambert-Bouguer law) (Perrin, 1948) describes this attenuation; the law states that, given light of intensity $I(\widetilde{\nu})$, and atmosphere of some thickness dL, the intensity of light will be described by (Liou, 2002; Griffiths et al., 2007):

$$\mathrm{d}I(\widetilde{\nu}) = -\rho S f_V I(\widetilde{\nu})\mathrm{d}L, \tag{2.9}$$

where S is the line strength, and ρ is the density of the gas of interest. If we assume that ρ, S and f_V are constant over $\mathrm{d}L$, then Equation 2.9 simplifies to an ordinary differential equation, and can be integrated to give:

$$I(\widetilde{\nu}) = I_0(\widetilde{\nu}) \exp\left(-\rho S f_V L\right), \tag{2.10}$$

where $I_0(\widetilde{\nu})$ is the intensity at the top of the layer.

Line strength S is related to the absorption coefficient k, via the following equation:

$$k(\widetilde{\nu}) = S f_V \tag{2.11}$$

where $k(\widetilde{\nu})$ is the absorption coefficient at wavenumber $\widetilde{\nu}$. With this, Equation 2.10 becomes:

$$I(\widetilde{\nu}) = I_0(\widetilde{\nu}) \exp\left(-\rho k(\widetilde{\nu}) L\right). \tag{2.12}$$

Because transmittance, τ, is given by I/I_0, the following equation for atmospheric transmission follows:

$$\tau(\widetilde{\nu}) = \exp\left(-\rho k(\widetilde{\nu}) L\right). \tag{2.13}$$

Here, $\rho k(\widetilde{\nu})L$ may be interpreted as optical depth, or total column amount$\times k$. Combining the equations above allows us, in theory, to obtain information about the abundances of certain molecules in the atmosphere from spectral observations. In practice, this is done by splitting the atmosphere into several layers to account for variations in parameters (e.g., ρ, f_V) with altitude (see Section 2.5).

Beer's law can also be used to find the emissivity (by using Kirchhoff's law, which states that the emissivity of air is the same as its absorptivity) and the change in intensity of radiation along its path in the atmosphere. Schwarzschild's Equation (Equation 2.14) describes absorption and emission of infrared radiation in the absence of scattering, which is justified by the fact that the wavelength of infrared radiation is much larger than the size of air molecules, and is given by

$$\mathrm{d}I(\widetilde{\nu}) = \rho S f_V [I_B(\widetilde{\nu}, T) - I(\widetilde{\nu})]\mathrm{d}L, \tag{2.14}$$

where I_B is the blackbody intensity at some temperature T (Wallace and Hobbs, 2006).

2.2 Theory of Fourier Transform Spectroscopy

The spectroscopic theory outlined in Section 2.1 can be used to obtain information about gases in the atmosphere. A Fourier transform spectrometer is an instrument that uses optical path differences to obtain an interference pattern from an input wave, and it can be used to determine spectral signatures from trace gases by examining sunlight that has passed through the atmosphere. The Fourier transform spectrometer (FTS, also known as FTIR if the instrument is designed for infrared spectra) is one such instrument. The FTS at TAO (see Section 2.4) is an ABB Bomem DA8, a solar-pointing instrument that operates in the infrared spectral region. It is coupled to a solar tracker; the tracker directs sunlight into the laboratory, where it is directed and focused through a series of mirrors, and through an optical filter into the instrument (see Figure 2.2). The light passes through a beamsplitter, which reflects half of the light, while transmitting the other half. Both beams of light then travel to their respective mirrors, and recombine at the beamsplitter. The beam is then sent to a detector, which measures the incoming signal. The key element of an interferometer is that one of the mirrors (called the scan mirror) can move towards or away from the beamsplitter, changing the optical path. This creates, and changes, the optical path difference (OPD), and because the beams have traveled different paths, they may be out of phase. The scan mirror is constantly moving as the detector makes measurements, and so the phase of one of the beams will be changing continuously, leading to interference patterns. The detector measures this, and creates what is known as an interferogram.

The interferogram, which is a function in the space domain, can be put into the wavenumber domain via the Fourier transform, creating a spectrum. The detector measures the intensity of the incoming light as a function of the OPD, x, given by (Perkins, 1986; Griffiths et al., 2007):

$$I(x) = \frac{1}{2}\int_0^\infty B(\widetilde{\nu})\cos(2\pi\widetilde{\nu}x)\mathrm{d}\widetilde{\nu}. \tag{2.15}$$

Then, the spectrum, $B(\widetilde{\nu})$, obtained from a Fourier transform, can be expressed as the following:

$$B(\widetilde{\nu}) = 2\int_0^\infty I(x)\cos(2\pi\widetilde{\nu}x)\mathrm{d}x. \tag{2.16}$$

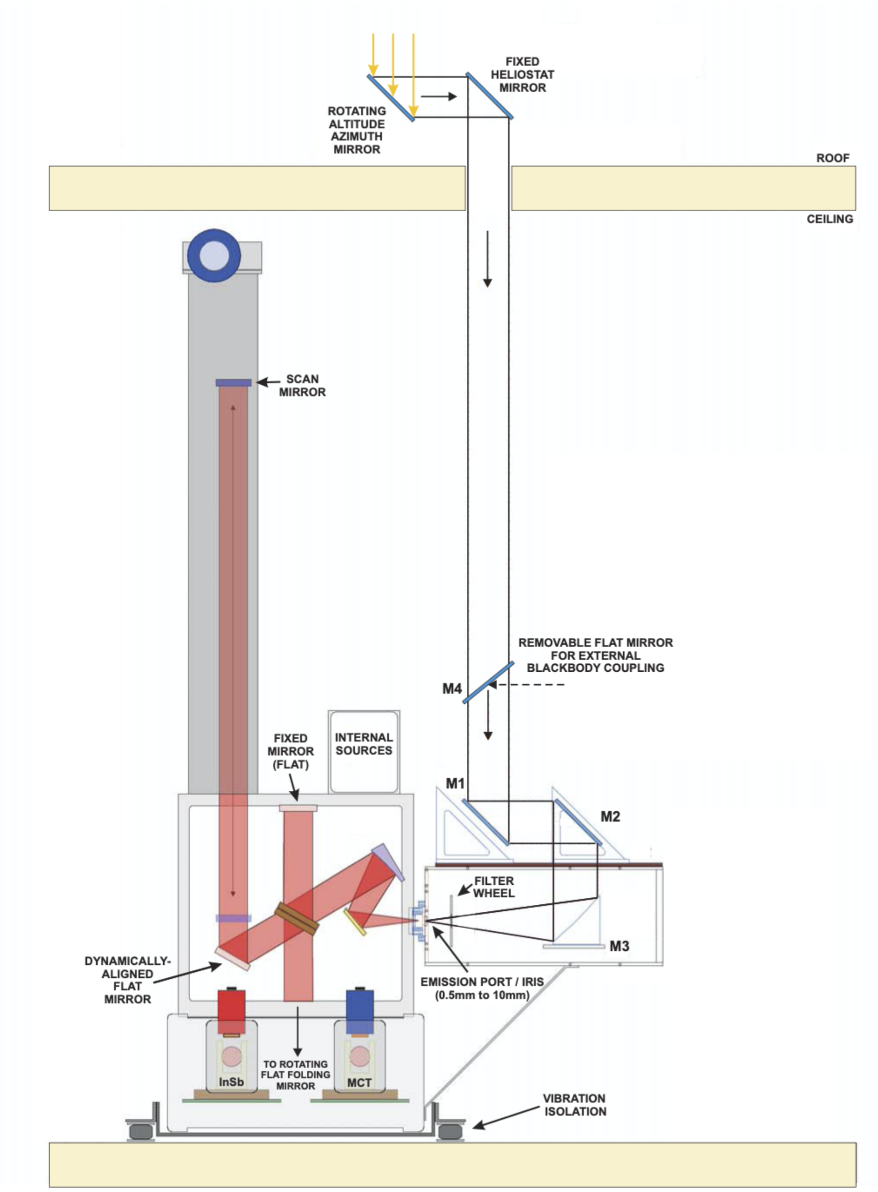

Figure 2.2: Optical components of the TAO DA8 solar-pointing FTIR spectrometer. Figure taken from Wiacek (2006).

The resulting spectrum, in combination with the theory outlined in Section 2.1, can be used to obtain information about trace gas concentrations in the atmosphere.

It should be noted that the integral in Equation 2.16 is evaluated from 0 to infinity, because OPD is assumed to range from 0 to infinity. In practice, this is not the case; there is a finite maximum OPD, x_{max}, and this necessitates an apodization function to be applied to Equation 2.15. The DA8 at TAO has a maximum OPD of 250 cm, and a boxcar apodization function, $D(x)$, described by Equation 2.17 is typically used.

$$D(x) = \begin{cases} 0 & \text{if } |x| > x_{\max} \\ 1 & \text{if } |x| \leq x_{\max} \end{cases} . \tag{2.17}$$

When Equation 2.16 is multiplied by $D(x)$ and fed through the Fourier transform, the resulting function is a sinc function with a dependence on $x_{\max}$. The spectral resolution of the spectrometer can be derived using the OPD and apodization function; using the full-width at half maximum of the sinc function for the boxcar apodization, the resolution is $0.6/x_{\max}$ (Bell, 1972). As the resolution varies by the apodization function used (e.g., the resolution is $0.9/x_{\max}$ when using a triangular function), $1/x_{\max}$ is typically chosen as the nominal resolution; the resolution of the DA8 is hence 0.004 cm^{-1}.

2.3 Advantages of Fourier Transform Spectroscopy

FTIR spectroscopy offers several advantages over other spectroscopic methods, such as scanning grating or scanning dispersive. These were described by Jacquinot et al. (1948), Fellget (1951), and Connes and Connes (1966). The Jacquinot advantage refers to the high optical throughput that an FTIR spectrometer offers. This is possible because a circular aperture, which controls the amount of light entering the spectrometer, is used in an FTIR spectrometer, allowing for minimal loss of signal within the instrument (compared to, e.g., a spectrometer with an entrance slit), leading to a higher signal-to-noise (SNR) ratio. This is also known as the throughput advantage (Stuart, 2005).

In addition, the FTIR is capable of measuring all wavelengths simultaneously. This is known as the Fellget advantage, and results in shorter sampling times over a given spectral range compared to dispersive spectrometers. This is also known as the multiplex advantage (Stuart, 2005).

Furthermore, an FTIR spectrometer is wavelength calibrated using a laser beam of known wavelength, and the position of the scanning mirror is defined by the zero path difference (ZPD) of the laser (as opposed to e.g., spatial position of a grating in a dispersive spectrometer). Because wavenumber precision is determined by the precision with which the position of the scanning mirror is known, this results in high wavenumber precision (Stuart, 2005). This is known as the Connes advantage.

2.4 The University of Toronto Atmospheric Observatory

The University of Toronto Atmospheric Observatory is located in downtown Toronto, Ontario, Canada (43.66°N, 79.40°W), 174 masl, on the top floor of the Burton Tower of the McLennan Physics Building on the St. George Campus of the University of Toronto. The primary instrument at TAO is the ABB Bomem DA8, an FTIR spectrometer, which has been operational since mid-2002. TAO is a member of the Network for the Detection of Atmospheric Composition Change (NDACC; `https://www.ndaccdemo.org/`, last accessed, March, 2021), an international network of observing stations with similar instruments. Retrievals at TAO conform to standards set by NDACC, and datasets are archived annually to the NDACC server and are publicly available. Select species retrieved at TAO (currently CH_4, CO, H_2CO, and O_3) are also contributed to the CAMS RD system (`https://atmosphere.copernicus.eu/`, last accessed: April, 2021).

2.4.1 Experimental Setup

The DA8 is configured as shown in Figure 2.2. In front of the entrance aperture is a filter wheel, with six optical filters that narrow the spectral range of the incoming solar radiation (labeled "Filter Wheel" in Figure 2.2). The filters act to reduce shot noise, the noise due to fluctuations in the number of detected photons, which is proportional to the square root of the average intensity (Bell, 1972). The spectral windows of the six filters used at TAO are listed in Table 2.1. The filtered solar radiation then passes through an external aperture (labeled "Emission Port / Iris" in Figure 2.2), and into the interferometer. The external aperture is typically set to 0.5 mm for filters 1, 2, 3, 4, and 5, and 1.0 mm for filter 6. The TAO DA8 is fitted with a KBr beamsplitter, which has a spectral range of 500-4500 cm^{-1}. The DA8 has a vertically moving scanning mirror, and the interferogram is recorded with two detectors with different spectral ranges; an InSb detector covers 1500-5000 cm^{-1}, and an MCT detector (HgCdTe) covers 700-4500 cm^{-1}. The MCT detector is used for filter 6. The setup includes an internal aperture for filter 6; this is due to the severe nonlinear response of MCT detectors when they operate at high light levels (Johnson et al., 2002).

The TAO DA8 is controlled by the PCDA data acquisition software and BGRAMS software, which run on a Windows 98 computer (ABB is no longer updating the software). This computer can be accessed remotely to facilitate easier measurement-acquisition. The DA8 scanning mirror is set to move at a speed of 1.0 cm/s, and is configured to complete four scans for each measurement. After the four scans, the computer records the raw interferogram with a boxcar apodization function (.IGN file), the phase-corrected interferogram (.IGM file), and the spectrum obtained via Fourier transform (.SPC file). Each measurement takes about 15 minutes. This allows up to ∼6 measurements for each filter in a given day. As the DA8 relies on solar radiation, it requires sunny conditions with clear skies; this means that measurements cannot be made during night, nor on days with cloudy or inclement weather, and transient clouds can lead to poor spectra that are rejected. Given this, and given that the system is not fully automated, TAO measurements are usually made from 9 AM to 5 PM on weekdays with clear skies, with 100-150 measurement days per year, which is typical of other NDACC FTIR instruments. Historical measurement days per year can be seen in Figure 2.3. The sparsity of the measurements, and the irregular intervals in which they are made, pose some of the biggest challenges when working with the dataset (e.g., Whaley, 2014).

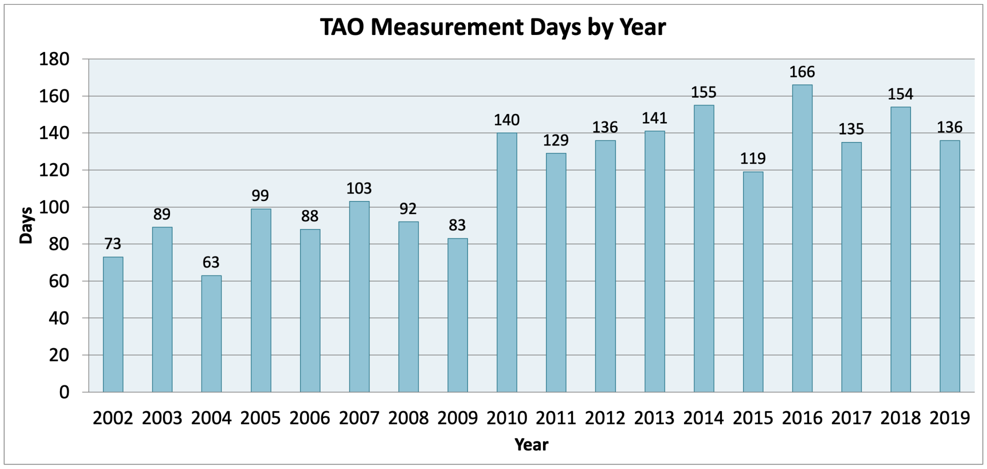

Figure 2.3: Number of measurement days with the TAO DA8 FTIR, from 2002 to 2019.

Table 2.1: Spectral coverage of the six filters used with the TAO DA8 FTIR, and the window used for calculating the SNR used in the retrieval (see Section 2.5.3).

Filter	Wavenumber range (cm^{-1})	Species measured	Window for SNR calculation
1	4000 - 4300	HF	4007.50 - 4007.64, 4038.727 - 4038.871
2	2900 3500	C_2H_2, H_2CO, HCN	3381.275 - 3381.536, 3485.65 - 3485.77
3	2400 - 3100	C_2H_6, CH_4, HCl, N_2O, O_3	2402.20 - 2402.30, 2924.866 - 2925.100
4	2000 - 2700	CO	2300.00 - 2300.50, 2526.228 - 2526.618
5	1500 - 2200	CO	1985.260 - 1985.510
6	750 - 1350	CH_3OH, HCOOH, HNO_3, NH_3, O_3	700.00 - 700.50, 1139.075 - 1139.168

2.4.2 Solar Tracking

The DA8 is coupled to a sun-tracker that actively tracks the sun during the day. The active tracking was provided by four photo-diodes from 2002-2014, and was updated to a camera and solar-disk-fitting system on 2 September 2014. The tracker is controlled by a Linux computer, which can be remotely accessed. The tracker was manufactured by Aim Controls and is driven by two stepper motors on elevation and azimuth axes. Further details of the solar-disk-fitting system can be found in Franklin (2015).

The upgraded tracker has a pointing accuracy of around 30 arcseconds; annual averages of pointing accuracy from all tracking points considered to be a "good fit" by the solar-fitting algorithm were 23.8, 25.0, and 30.8 arcseconds for 2017, 2018, and 2019, respectively (data from 2019 are shown in Figure 2.4). While a direct comparison with the previous photodiode system is not possible due to differences in modes of operation, the standard deviation (1σ) in solar line shifts (calculated from CO retrievals) decreased from 3.99×10^{-3} cm^{-1} (2002-2014) to 1.96×10^{-3} cm^{-1} (2014-2019) after switching to the camera solar-disk-fitting system (see Figure 2.5). Solar line shifts are caused by the the tracker failing to point at the center of the sun, resulting in Doppler shifting of the incoming solar radiation.

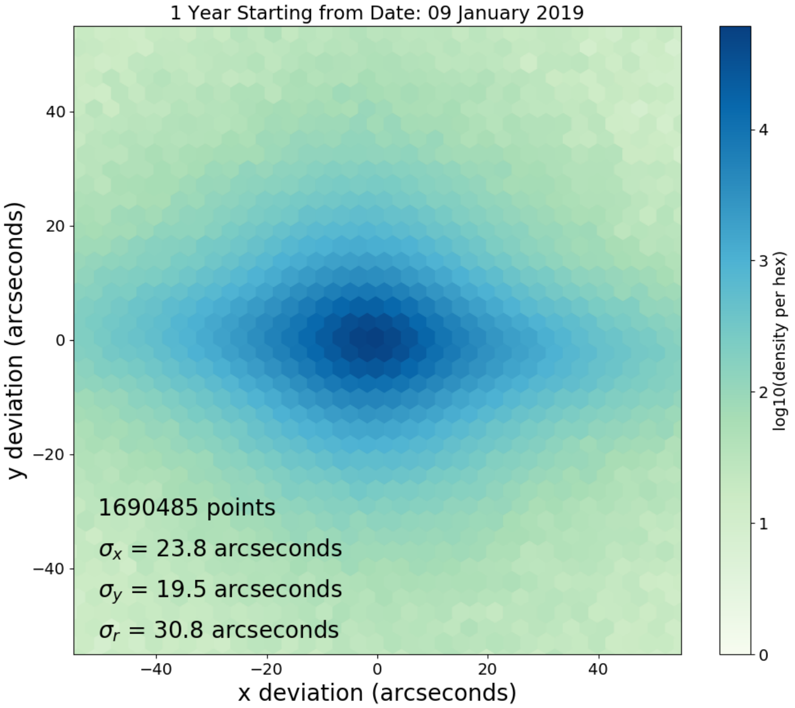

Figure 2.4: Average pointing accuracy from tracking data in 2019. Deviations in x and y reflect pointing accuracy seen by the camera, where the origin is defined as the ideal location of the solar disk fit.

2.4.3 Monitoring FTIR Performance

The DA8, as with other spectrometers, requires alignment to function properly. The instrument may become misaligned over time due to changes in pressure and temperature, and the alignment must be monitored to ensure that proper measure-

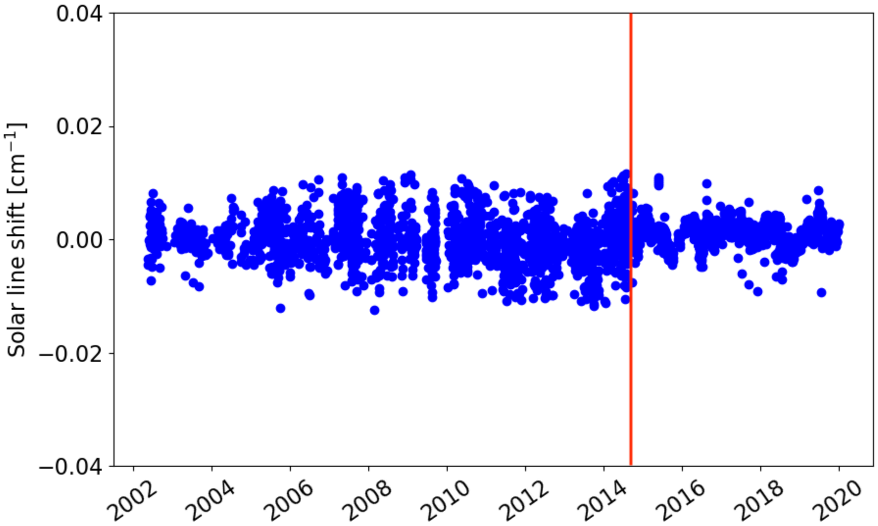

Figure 2.5: Time series of solar line shift (in cm^{-1}) from CO retrievals. The red line indicates 2 September 2014, when the solar tracker system was modified.

ments are being made. One way to check for alignment, and assess the performance of an FTIR is to do an instrument lineshape measurement (Hase, 2012) using a cell with a known spectroscopic feature. At TAO, a cell (#48) with a known quantity of HBr gas is used for this purpose. The instrument line shape is determined by the apodization function; for example, boxcar apodization will result in a sinc function (see Section 2.2).

The line shape is analyzed using a software called LINEFIT v14.5 (Hase, 2012). An instrument line shape measured on 13 May, 2020, is shown in Figure 2.6 (left), along with the corresponding modulation efficiencies (top, right) and phase error (bottom, right). The modulation efficiency indicates how the signal intensity varies as a function of OPD, and large variations in the modulation efficiency means a re-alignment of the instrument is needed. Ideally, the modulation efficiency should be close to 1 over the entire path. NDACC does not have a standard for modulation efficiencies, but the Total Carbon Column Observing Network (TCCON), a similar international network of atmospheric observing stations, specifies a range from 0.95 to 1.05. At TAO, values as low as 0.3 have been seen in the past (Wiacek, 2006), so the instrument is currently in a relatively good alignment state. In the August of 2019, the TAO FTIR underwent a realignment. The line shape should ideally be symmetric; if not, this is seen in the phase error (which is a measure of asymmetry of the line shape), and means that the interferometer mirrors are not aligned properly (phase error should be close to 0). The retrieved column of the HBr cell is shown in Figure 2.7. This should be stable over time.

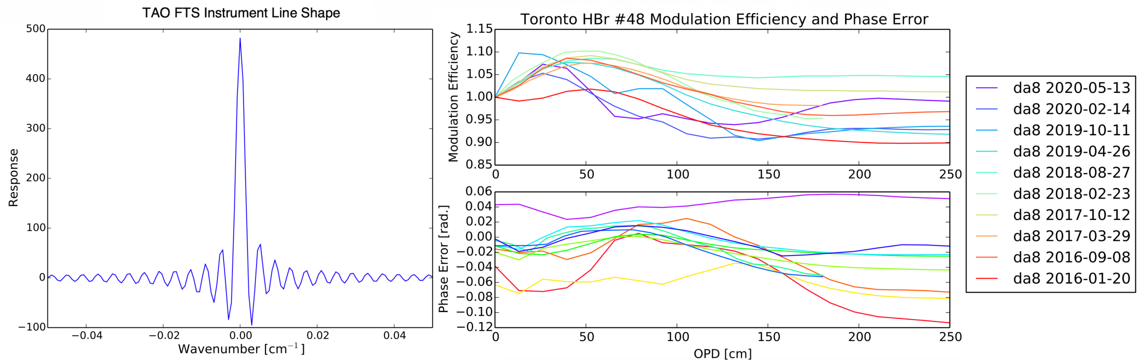

Figure 2.6: TAO DA8 solar instrument line shape (left) (taken on 13 May 2020), modulation efficiency (top, right) and phase error (bottom, right) (various measurements from 2016 to 2020 shown), with HBr (#48) cell at 0.004 cm^{-1} resolution, obtained using LINEFIT v14.5. Older modulation efficiency and phase error data can be found in Wiacek (2006) and Whaley (2014).

2.5 Trace Gas Retrieval

The spectra recorded by the DA8 are used to retrieve vertical profiles and partial and total columns of trace gases, using inverse methods such as the optimal estimation method (OEM) (Rodgers, 1990, 2000) and Tikhonov regularization (Sussmann et al.,

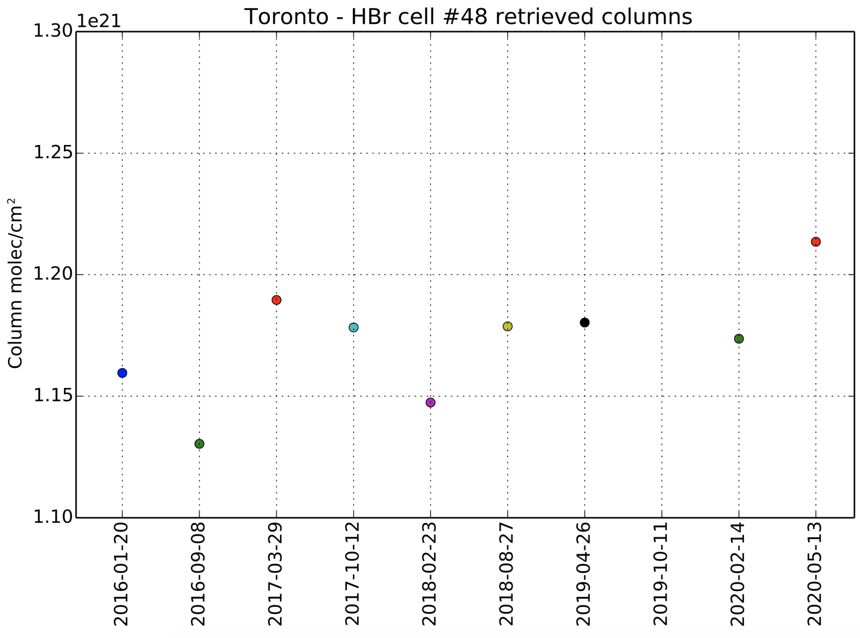

Figure 2.7: Retrieved column of the HBr (#48) cell (in molecules/cm^2) obtained from LINEFIT v14.5 while calculating line shapes since 2016.

2011). The following sections will briefly outline the theory behind the retrieval methods (Sections 2.5.1 and 2.5.2) as well as their implementation for TAO retrievals using the SFIT4 software (Section 2.5.3). Further details can be found in e.g., Rodgers (1990, 2000), Wiacek et al. (2007), and Sussmann et al. (2011).

2.5.1 Optimal Estimation Method

OEM is an inverse method that uses a forward model and iteratively works backwards to estimate, or retrieve, the true state. Given some spectrum, a small window, called a microwindow (MW), is selected, isolating the spectral line (or lines) of interest. The forward model, $\mathbf{F}$, which contains an initial estimate, $\mathbf{x}_a$, (often called the a priori) of the atmosphere (which includes an a priori vertical profile of the trace gas of interest) as well as a database of atmospheric absorption features, is then used to relate the true atmospheric state, $\mathbf{x}$ (vertical profiles of gases and water vapor) to an absorption spectrum, $\mathbf{y}$, which is in the measurement space, as follows:

$$\mathbf{y} = \mathbf{F}(\mathbf{x},\ \mathbf{b}) + \boldsymbol{\epsilon}, \tag{2.18}$$

where $\mathbf{b}$ is a vector of the additional model parameters, and $\boldsymbol{\epsilon}$ is the error. The goal is to estimate the atmospheric state, $\hat{\mathbf{x}}$, given $\mathbf{y}$. If we assume that the forward model, $\mathbf{F}$, is invertible, then the inverted function, $\mathbf{R}$, is given by:

$$\begin{aligned}\hat{\mathbf{x}} &= \mathbf{R}(\mathbf{y},\ \mathbf{b},\ \mathbf{x},\ \mathbf{c}) \\ &= \mathbf{R}(\mathbf{F}(\mathbf{x},\ \mathbf{b}) + \boldsymbol{\epsilon},\ \mathbf{b},\ \mathbf{x},\ \mathbf{c}),\end{aligned} \tag{2.19}$$

where the vector $\mathbf{c}$ denotes the parameters needed for the inverse model. If we assume that $\mathbf{F}$ and $\mathbf{R}$ are linear over the range of the a priori and the true state space, then Equation 2.19 can be Taylor expanded about $\mathbf{x} - \mathbf{x}_a$ to yield:

$$\hat{\mathbf{x}} = \mathbf{R}(\mathbf{F}(\mathbf{x}_a,\ \hat{\mathbf{b}}) + \mathbf{K}(\mathbf{x} - \mathbf{x}_a) + \mathbf{K}_b(\mathbf{b} - \hat{\mathbf{b}}) + \boldsymbol{\epsilon},\ \hat{\mathbf{b}},\ \hat{\mathbf{x}},\ \mathbf{c}), \tag{2.20}$$

where $\hat{\mathbf{b}}$ denotes the best estimate of the forward model parameters, $\mathbf{K}$ denotes the weighting function matrix, and $\mathbf{K}_b$ is the parameter space weighting function matrix. $\mathbf{K}$ and $\mathbf{K}_b$ represent the sensitivity of the forward model to the state vector and ancillary parameters, respectively, and are defined as:

$$\begin{aligned}\mathbf{K} &= \frac{\partial \mathbf{F}}{\partial \mathbf{x}} \\ \mathbf{K}_b &= \frac{\partial \mathbf{F}}{\partial \mathbf{b}}.\end{aligned} \tag{2.21}$$

Taylor expanding Equation 2.20 then gives:

$$\begin{aligned}\hat{\mathbf{x}} &= \mathbf{x}_a + \mathbf{GK}(\mathbf{x} - \mathbf{x}_a) + \mathbf{GK}_b(\mathbf{b} - \mathbf{b}_a) + \mathbf{G}\boldsymbol{\epsilon} \\ &= \mathbf{x}_a + \mathbf{A}(\mathbf{x} - \mathbf{x}_a) + \boldsymbol{\epsilon}_{\mathbf{x}},\end{aligned} \tag{2.22}$$

where $\boldsymbol{\epsilon}_{\mathbf{x}}$ denotes the combined error term, **G** is the gain matrix, and **A** is the averaging kernel. The gain matrix **G** represents the sensitivity of the retrieved state to the measurements, defined as:

$$\mathbf{G} = \frac{\partial \mathbf{R}}{\partial \mathbf{y}}, \tag{2.23}$$

and the averaging kernel matrix **A** is equal to **GK**, i.e.,

$$\begin{aligned}\mathbf{A} &= \mathbf{GK} \\ &= \frac{\partial \mathbf{R}}{\partial \mathbf{y}} \cdot \frac{\partial \mathbf{F}}{\partial \mathbf{x}} \\ &= \frac{\partial \hat{\mathbf{x}}}{\partial \mathbf{x}},\end{aligned} \tag{2.24}$$

and represents the sensitivity of the retrieved state to the true atmospheric state $\hat{\mathbf{x}}$. From this, the sensitivity of the retrieval can be defined as the sum of the terms in the rows of the averaging kernel, representing the amount of information the retrieval gained from the measurement (as opposed to the a priori) (Rodgers, 2000; Vigouroux et al., 2009). In addition, the Degrees of Freedom for Signal (DOFS) is defined as the trace of the averaging kernel, and can be used to quantify the vertical information content of the retrieval. For example, DOFS of 1 indicates that there is one piece of vertical information that can be discerned from the retrieval, while higher values indicate that more vertical information is available in the retrieval.

The problem now is to find the best estimate of $\hat{\mathbf{x}}$, and from Equation 2.22, we see that we first need to find $\mathbf{G}$. Recall that $\mathbf{F}$ maps the true state of the atmosphere $\mathbf{x}$ to measurement space. However, the error term, $\boldsymbol{\epsilon}_{\mathbf{x}}$, is only known statistically, and thus the image of it under a mapping is described by a probability distribution function (PDF). To account for this, we use Bayes' Theorem, which states that the probability of some event x, given some condition y (known as conditional probability), is equal to the probability of y given x, multiplied by the probability of x, divided by probability of y:

$$P(x|y) = \frac{P(y|x)P(x)}{P(y)}. \tag{2.25}$$

Now, assuming that the PDFs describing observations ($\mathbf{y}$) are normally distributed (Gaussian), we see that (Rodgers, 2000):

$$\begin{aligned} P(\mathbf{y}) &= \frac{1}{(2\pi)^{n/2}|\mathbf{S}_y|^{1/2}} \exp\left[-\frac{1}{2}(\mathbf{y}-\bar{\mathbf{y}})^{\mathrm{t}}\mathbf{S}_y^{-1}(\mathbf{y}-\bar{\mathbf{y}})\right] \\ \ln[P(\mathbf{y})] &= -\frac{1}{2}(\mathbf{y}-\bar{\mathbf{y}})^{\mathrm{T}}\mathbf{S}_y^{-1}(\mathbf{y}-\bar{\mathbf{y}}) - \ln[(2\pi)^{n/2}|\mathbf{S}_y|^{1/2}] \\ &= -\frac{1}{2}(\mathbf{y}-\bar{\mathbf{y}})^{\mathrm{T}}\mathbf{S}_y^{-1}(\mathbf{y}-\bar{\mathbf{y}}) + C_{\mathrm{y}}, \end{aligned} \tag{2.26}$$

where $\mathbf{S}_y$ is the measurement error covariance matrix, n is the dimensionality of the $\mathbf{y}$, $\bar{\mathbf{y}}$ is the observation mean, and C_{y} is some constant term. Assuming $\mathbf{x}$ is also normally distributed, the same analysis can be done for $P(\mathbf{x})$, which gives:

$$\ln[P(\mathbf{x})] = -\frac{1}{2}(\mathbf{x}-\mathbf{x}_a)^{\mathrm{T}}\mathbf{S}_a^{-1}(\mathbf{x}-\mathbf{x}_a) + C_{\mathrm{x}}, \tag{2.27}$$

where $\mathbf{S}_a$ is the a priori covariance matrix, and $P(\mathbf{y}|\mathbf{x})$:

$$\ln[P(\mathbf{y}|\mathbf{x})] = -\frac{1}{2}[\mathbf{y} - \mathbf{F}(\mathbf{x},\ \mathbf{b})]^{\mathrm{T}}\mathbf{S}_{\boldsymbol{\epsilon}}^{-1}[\mathbf{y} - \mathbf{F}(\mathbf{x},\ \mathbf{b})] + C_{\mathrm{yx}}, \tag{2.28}$$

where $\mathbf{S}_{\boldsymbol{\epsilon}}$ is the error covariance matrix. Combining Equations 2.27 and 2.28 with Bayes' Theorem (Equation 2.25), and recalling that $\ln\left[\frac{x}{y}\right] = \ln(x) - \ln(y)$ gives:

$$\begin{aligned}\ln[P(\mathbf{x}|\mathbf{y})] &= \ln[P(\mathbf{y}|\mathbf{x})] + \ln[P(\mathbf{x})]\\ &= -\frac{1}{2}\{[\mathbf{y} - \mathbf{F}(\mathbf{x},\ \mathbf{b})]^{\mathrm{T}}\mathbf{S}_{\boldsymbol{\epsilon}}^{-1}[\mathbf{y} - \mathbf{F}(\mathbf{x},\ \mathbf{b})] + (\mathbf{x} - \mathbf{x}_a)^{\mathrm{T}}\mathbf{S}_a^{-1}(\mathbf{x} - \mathbf{x}_a)\} + C_{\mathrm{comb}}\\ &= -\frac{1}{2}\mathbf{J}_{\mathrm{cost}}(\mathbf{x}),\end{aligned} \tag{2.29}$$

where the constants have been combined into C_{comb}, and $\mathbf{J}_{\mathrm{cost}}(\mathbf{x})$ is the cost function. Note that the $P(\mathbf{y})$ term was omitted (absorbed into C_{comb}), as in practice, this is only a normalizing factor (Rodgers, 2000). By taking the derivative of Equation 2.29 and setting it to zero, we see that $P(\mathbf{x}|\mathbf{y})$ is maximized when the cost function is at its minimum. This optimization problem can be iteratively solved (assuming that the system can be linearized). The optimal solution after i iterations is given by:

$$\begin{aligned}\hat{\mathbf{x}}_i &= \hat{\mathbf{x}}_{i-1} - [\nabla_{\hat{\mathbf{x}}_{i-1}}\nabla_{\hat{\mathbf{x}}_{i-1}}\mathbf{J}_{\mathrm{cost}}(\hat{\mathbf{x}}_{i-1})]^{-1}\nabla_{\hat{\mathbf{x}}_{i-1}}\mathbf{J}_{\mathrm{cost}}(\hat{\mathbf{x}}_{i-1})\\ &= \mathbf{x}_a + (\mathbf{S}_a^{-1} + \mathbf{K}_{i-1}^{\mathrm{T}}\mathbf{S}_{\boldsymbol{\epsilon}}^{-1}\mathbf{K}_{i-1})^{-1}\mathbf{K}_{i-1}^{\mathrm{T}}\mathbf{S}_{\boldsymbol{\epsilon}}^{-1}[\mathbf{y} - \mathbf{F}(\hat{\mathbf{x}}_{i-1}) - \mathbf{K}_{i-1}(\mathbf{x}_a - \hat{\mathbf{x}}_{i-1})],\end{aligned} \tag{2.30}$$

where $i-1$ denotes the previous iteration. Note that the second step was obtained using $\mathbf{K} = \frac{\partial\mathbf{F}}{\partial\mathbf{x}}$ (Equation 2.21).

Several factors can lead to errors (i.e., $\hat{\mathbf{x}} - \mathbf{x}$) during retrieval. Because the retrieval can be considered to be an estimate of a state smoothed by the averaging kernel, smoothing error can arise. This is described by $(\mathbf{A} - \mathbf{I})(\mathbf{x} - \mathbf{x}_a)$, where $\mathbf{I}$ is the identity matrix of appropriate size (Rodgers, 2000). Errors in the forward model parameters can also contribute to errors. This is given by $\mathbf{G}\mathbf{K}_b(\mathbf{b} - \hat{\mathbf{b}})$. In practice, the forward model $\mathbf{F}$ is often a linearized model of a complex function $\mathbf{f}$, i.e., $\mathbf{F}(\mathbf{x},\ \mathbf{b}) \approx \mathbf{f}(\mathbf{x},\ \mathbf{b},\ \mathbf{b'})$, where $\mathbf{b'}$ represents the forward function parameters that are ignored during the construction of the model. This gives rise to modeling error, which is given by $\mathbf{G}\Delta\mathbf{f} = \mathbf{G}[\mathbf{f}(\mathbf{x},\ \mathbf{b},\ \mathbf{b'}) - \mathbf{F}(\mathbf{x},\ \mathbf{b})]$ (Rodgers, 2000). Retrieval noise can also contribute to errors, and is described by $\mathbf{G}\boldsymbol{\epsilon}$ (Rodgers, 2000).

2.5.2 Tikhonov Regularization

In cases where the a priori profile of the trace gas of interest is not well known, Tikhonov regularization (Tikhonov, 1963; Tikhonov and Glasko, 1965; Sussmann et al., 2011) may be used instead of OEM. Assuming a linear model $\mathbf{F}$ that maps the true state $\mathbf{x}$ to measurement $\mathbf{y}$, i.e.:

$$\mathbf{y} = \mathbf{F}\mathbf{x}, \tag{2.31}$$

an estimate of the true state can then be made by minimizing the distance (Euclidean norm) of $\mathbf{F}\mathbf{x} - \mathbf{y}$. Tikhonov method attempts to do this, but the norm is minimized with an additional regularization term:

$$\|\mathbf{F}\mathbf{x} - \mathbf{y}\|^2 + \|\boldsymbol{\Gamma}\mathbf{x}\|^2, \tag{2.32}$$

where the second term is the regularization term, characterized by a Tikhonov regularization matrix $\mathbf{\Gamma}$, which is defined as:

$$\mathbf{\Gamma} = \alpha \mathbf{L}_1^{\mathrm{T}} \mathbf{T} \mathbf{L}_1. \tag{2.33}$$

Here, $\mathbf{L}_1$ is constructed so that the retrieval favors the difference $\mathbf{x} - \mathbf{x}_a$ to be a constant profile, and is called the discrete first derivative operator (Sussmann et al., 2011). $\mathbf{L}_1$ is given by:

$$\mathbf{L}_1 = \begin{pmatrix} -1 & 1 & 0 & \cdots & 1 \\ 0 & -1 & 1 & \ddots & \vdots \\ \vdots & \ddots & \ddots & \ddots & 0 \\ 0 & \cdots & 0 & -1 & 1 \end{pmatrix} \in \mathbb{R}^{(n-1)\times n}. \tag{2.34}$$

$\mathbf{T}$ is a diagonal matrix, with the elements defined by:

$$\mathbf{T}_{ii} = \Delta z_i^{-2}, \tag{2.35}$$

where Δz_i is the thickness of the ith retrieval layer; this is required as the retrieval grid used varies with altitude (Sussmann et al., 2011). The $\mathbf{\Gamma}$ regularization term is an additional constraint on the solution to the inverse problem, and reduces oscillating profiles (Sussmann et al., 2011). Lastly, the α term is adjusted to "tune" the retrieval to obtain an appropriate DOFS; since Tikhonov regularization is used when the a priori profile is highly uncertain, the α parameter may be used to account for the lack of a priori knowledge.

2.5.3 Retrievals Using SFIT4

SFIT4 is the algorithm package used to retrieve trace gas profiles at TAO. Specifically, SFIT4 version 0.9.4.4 is currently used at TAO, and uses the OEM discussed in Section 2.5.1. SFIT4 is the standard retrieval algorithm used by most NDACC Infrared Working Group (IRWG) stations (`https://wiki.ucar.edu/display/sfit4/`, last accessed: February, 2021). Originally released in 2014, SFIT4 is based on the previous retrieval algorithm called SFIT2. Both algorithms perform retrievals by iteratively adjusting the target species volume mixing ratio (VMR) profile until the difference between the calculated spectrum and the measured spectrum, and the difference between the retrieved state vector and the a priori profile are minimized (Rinsland et al., 2009). SFIT4 is written in Fortran, but is "wrapped" with a python script called Layer1.

Spectroscopic information is required to run the forward model in SFIT4, and at TAO, the HIgh-resolution TRANsmission molecular absorption database (HITRAN) 2008 spectral line list (Rothman et al., 2009) is used as currently recommended by the NDACC IRWG. Other parameters needed for the model include meteorological data (temperature and pressure profiles), which are provided by the US National Centers for Environmental Prediction (NCEP). The retrievals also require a priori profiles of the trace gases of interest; these are obtained from a 40-year mean (1980-2020) for Toronto from the Whole Atmosphere Community Climate Model (WACCM v4; Eyring et al., 2007; Marsh et al., 2013) as generated for the NDACC IRWG. The exception to this is NH_3; the a priori profile for NH_3 was based on the a priori used at the NDACC site in Bremen (Dammers et al., 2015), which was obtained from balloon-based measurements (Toon et al., 1999). The NH_3 retrieval methodology used at TAO is described in detail in Lutsch et al. (2016).

With the relevant input information, the forward model can be run. The SFIT4 retrieval starts with the creation of a model atmosphere using the forward model and meteorological information, and the a priori spectra for the selected microwindows (see Table 2.2) are calculated using a priori profiles of the target species, and interfering species, if any. Then, the profile of the trace gas of interest is iteratively adjusted; at each step, the profile to be retrieved is adjusted, and the spectrum is calculated and compared to the measured spectrum. This iterative process is repeated until the calculated and measured spectra converge. Convergence criteria are determined by examining the chi-squared (χ^2) value of the root mean square (RMS) of the difference between the calculated and measured spectra. When the change in χ^2 value between successive iterations is less than a specified amount (this value is denoted as "`rt.convergence`" in SFIT4, and is usually set to ∼0.1), the retrieval is said to have converged. SFIT4 will attempt 17 iterations, and if the criterion is not met, the retrieval is said to have no convergence. Spectra with low signal (and therefore low signal-to-noise ratio) can lead to retrievals not converging, and thus spectra should be examined (preferably on a daily basis) to filter out those with poor quality. Retrieved profiles are also filtered by RMS/DOFS ratio (see Table 2.3), and for the RD species, further quality control is done to meet the standards set by CAMS (submitted files must pass an automated quality assurance filter).

The error covariance matrix ($\mathbf{S}_{\boldsymbol{\epsilon}}$) in SFIT4 is defined as a diagonal matrix with the diagonal elements set to $1/\mathrm{SNR}^2$, where the SNR (signal-to-noise ratio) values are

Table 2.2: Microwindows for the TAO FTIR total column retrievals, mean retrieval errors, and mean DOFS. Mean values are for the 2002-2019 time series.

Species	Microwindows (cm^{-1})	Mean random error (%)	Mean systematic error (%)	Mean total error (%)	Mean DOFS
C_2H_2	3250.4−3250.8, 3268.25−3268.75, 3304.7−3305.4	25.1	8.8	26.9	1.5
C_2H_6	2976.77−2976.95, 2983.2−2983.55, 2986.5−2986.95	2.1	4.3	4.9	1.9
CH_4	2613.7−2615.4, 2835.5−2835.8, 2921.0−2921.6	2.0	3.9	4.4	2.1
CH_3OH	992.0−998.7, 1029.0−1037.0	3.7	15.3	15.8	1.5
CO	2057.7−2058.0, 2069.56−2069.76, 2157.5−2159.15	1.7	2.4	3.0	2.2
H_2CO	2763.425−2763.60, 2765.725−2765.975, 2778.15−2779.1, 2780.65−2782.0	8.4	12.7	16.5	1.2
HCl	2727.73−2727.83, 2775.7−2775.8, 2925.8−2926.0	1.6	2.0	2.7	1.8
HCN	3268.05−3268.4, 3287.1−3287.35, 3299.3−3299.6, 3331.4−3331.8	5.1	3.9	6.5	2.2
HCOOH	1102.0−1109.0, 1178.4−1178.8	9.4	10.7	16.2	1.1
HF	4038.86−4039.05	1.9	2.3	3.3	1.9
HNO_3	867.6−870.0	3.4	0.4	3.4	1.3
N_2O	2481.2−2482.6, 2526.4−2528.2, 2537.85−2538.8, 2540.1−2540.7	1.5	3.6	4.0	3.0
NH_3	930.32−931.32, 966.97−967.675	13.1	11.8	19.0	1.1
O_3	782.56−782.86, 788.85−789.37, 993.3−993.8, 1000.0−1004.5	1.5	5.3	5.5	4.4

obtained directly from the spectral data. SFIT4 also allows the user to add weighting to the SNR, although this approach is not usually taken at TAO. The SNR values are obtained by taking the ratio of the maximum signal and the RMS residuals from predefined spectral windows for each of the filters. The wavenumber ranges used for SNR calculations are listed in Table 2.1. The a priori covariance matrix ($\mathbf{S}_a$) can be directly specified in the input files for running SFIT4. This matrix should capture the natural variability in the profile of the retrieved species, and can be used as a tuning parameter of the retrieval. In general, $\mathbf{S}_a$ is a diagonal matrix, with the diagonal elements defined as the expected spread in the trace gas profile for that particular region of the atmosphere. It is usually expressed as a percentage value.

Uncertainties in the retrievals include forward model errors, measurement noise, and smoothing errors that arise due to the discretized vertical resolution. Forward model errors include temperature, pressure, line width, line strength, and solar zenith angle uncertainties, while measurement noise error include errors due to uncertainties in instrument line shape, interfering species, and wavelength shifts. Error analyses were done following Rodgers (2000). Spectral line parameter errors were taken from HITRAN 2008 (if they are not available, an uncertainty of 20 % was used), and the solar zenith angle (SZA) error was taken to be 0.43°, which is the average change in SZA during a 10-minute period (total scan time for each filter) throughout the year in Toronto. Temperature errors (divided into random and systematic errors) were derived by comparing NCEP daily temperature profiles at Toronto and radiosonde data from Buffalo Niagara International airport (42.56°N, 78.44°W, 215 masl), 145 km away and across Lake Ontario, and are listed in Table 2.4. The comparison was done

Table 2.3: Table of the RMS/DOFS ratio used to filter out poor quality retrievals before archiving to NDACC. Species labeled CAMS use the standards set for the Rapid Delivery submission and not the RMS/DOFS ratio.

Species	RMS/DOFS ratio
C_2H_2	7.5
C_2H_6	4.75
CH_4	CAMS
CH_3OH	5.5
CO	CAMS
H_2CO	3.5
HCl	2.95
HCN	2.4
HCOOH	9.6
HF	4.5
HNO_3	4.0
N_2O	0.3
NH_3	5.4
O_3	CAMS

Table 2.4: Systematic and random forward model temperature uncertainties (in K) used for retrieval error analysis at TAO. These were derived from comparison of NCEP daily temperature profiles at Toronto and radiosonde data from Buffalo Niagara International airport for 2010.

Height (km)	Systematic error (K)	Random error (K)
0.3507	1.91	2.56
0.7516	2.62	3.32
1.1848	2.57	3.22
1.6591	2.34	2.89
2.1697	1.72	2.16
2.7165	1.16	1.52
3.3044	1.11	1.44
3.9286	1.50	1.88
4.5890	1.63	2.02
5.2856	1.62	2.02
6.0183	1.52	1.92
6.7923	1.21	1.59
7.6025	1.29	1.78
8.4489	1.56	2.05
9.3315	1.49	2.06
10.25	1.50	1.85
11.21	2.13	2.80
12.205	2.45	3.21
13.235	1.53	2.02
14.30	1.66	1.83
15.40	2.31	2.53
16.54	2.50	2.79
17.715	1.88	1.87
18.925	1.54	1.77
20.17	1.45	1.82
21.45	1.58	1.95
22.77	1.37	1.71
24.125	1.47	1.72
25.515	1.57	1.98
26.94	1.96	2.40
28.40	2.17	2.72
29.915	2.75	3.72
31.53	2.00	5.00
33.30	2.00	5.00
35.285	2.00	6.00
37.555	2.00	6.00
40.17	2.00	7.00
43.19	2.00	7.00
46.68	2.00	7.00
50.70	2.00	9.00
55.315	2.00	9.00
60.59	2.00	9.00
66.585	2.00	9.00
73.385	2.00	9.00
81.10	2.00	9.00
89.85	2.00	9.00
100.25	2.00	9.00
113.00	2.00	9.00

for the year 2010. Radiosonde temperature measurements decrease in accuracy above 30 km (Luers and Eskridge, 1994); therefore, the mean value for the systematic error from 0.55 to 29.14 km for the systematic error and the NCEP error for the random error were used above this height. Furthermore, the calculated values at the lowest level were replaced with mean uncertainties from 0.55-29.14 km in an attempt to mitigate the effect of the difference in location between the radiosonde measurement and the NCEP profile. Error analysis was performed on all retrievals, grouped into random and systematic uncertainties, and added in quadrature. The resulting mean uncertainties on the total columns of the retrieved species, averaged over the entire time series, are listed in Table 2.2. The DOFS (see Section 2.5.1) for each species averaged over the time series are also listed in Table 2.2.

2.6 GEOS-Chem

The GEOS-Chem (`geos-chem.org`, last accessed: April, 2021) global 3D chemical transport model (CTM) was used to interpret observational data in the studies presented in this thesis. The simulations used in this work were run at 2° × 2.5° resolution (latitude × longitude), and were driven by MERRA-2 (Modern-Era Retrospective analysis for Research and Applications, Version 2) meteorological fields (Molod et al., 2015).

The model can be run in several modes. The standard model is a full chemistry run, and was used in the study presented in Chapter 5. In this study, GEOS-Chem (v11-01) was used to interpret and compare against observational data, and used the EDGAR v4.2 emissions database (Janssens-Maenhout et al., 2019) for anthropogenic emissions. For NH_3, EDGAR v4.2 in combination with GEIA were used as global inventories, with GEIA providing the natural source of NH_3 (Bouwman et al., 1997; Olivier et al., 1998; Croft et al., 2016). The global inventories were replaced with the US Environmental Protection Agency (EPA) National Emission Inventory for 2011 (NEI11; `https://www.epa.gov/air-emissions-inventories/2011-national-emissions-inventory-nei-data`, last accessed: November, 2020) in the United States, and by the Criteria Air Contaminants (CAC) from the National Pollutant Release Inventory in Canada (`https://www.ec.gc.ca/inrp-npri/`, last accessed: November, 2020). The NEI11 emissions were scaled between the years 2006–2013, whereas the CAC NH_3 emissions used 2008 as the base year, with no scaling applied. The NEI11 emissions were hourly, whereas the CAC emissions were monthly. For SO_2 and NO, which can lead to formation of sulfates and nitrates that influence NH_3 uptake to aerosols, EDGAR and CAC inventories were used for anthropogenic emissions. Additionally, GEOS-Chem extensions were used for SO_2 emissions from volcanos and NO_x from soil, and GFED inventory (Randerson et al., 2017) was used for emissions from biomass burning. The GEOS-Chem model includes a detailed tropospheric oxidant chemistry, as well as aerosol simulation (e.g., H_2SO_4-HNO_3-NH_3 simulation) (Park et al., 2004). NH_3 gas-aerosol partitioning is calculated using the ISORROPIA II model (Fountoukis and Nenes, 2007). Chemistry and transport are calculated with 20 and 10 minute timesteps, respectively. The model was spun up for one year, and output was saved every hour from 2002 to 2018.

GEOS-Chem can also be run in a “tagged” simulation mode, which linearizes the chemistry to enable “tagging” of select species, including CO and CH_4, by various sources. The GEOS-Chem tagged CO simulation was used in the studies presented in Chapters 3 and 4, and tagged CH_4 was used in the study presented in Chapter 3. In Chapter 3, the GEOS-Chem (v.12.1.1) tagged CO simulation was used to identify major sources of CO over Toronto. The model was run using MERRA-2 meteorological fields and GFAS (Global Fire Assimilation System) biomass burning emissions database (Kaiser et al., 2012). The tagged run uses prescribed monthly mean OH fields to account for the chemical loss of CO, and allows CO to be traced back to sources, including biomass burning emissions from specific regions, CO produced from CH_4 oxidation (Fisher et al., 2017) and anthropogenic emissions (e.g., Whaley et al., 2015). CO production rates from CH_4 (and NMVOC) oxidation were obtained from an archived full chemistry run by Fisher et al. (2017). The model was run from 2002 to 2018, and model output from 2003 and onwards was used for analysis (one year for spin-up). Further details of the GEOS-Chem tagged CO simulation can be found in Lutsch et al. (2020). This model was also used in Chapter 4 to interpret FTIR observations to examine biomass burning enhancement events. The model was used to interpret the FTIR data (which has gaps in its time series), and to analyze emission sources.

In Chapter 3, the GEOS-Chem (v.12.3.2) tagged CH_4 simulation was used to estimate sources of CH_4 over Toronto. In this study, the model was run at 2° × 2.5° resolution using MERRA-2 meteorological fields. This model is able to trace back CH_4 emitted from sources, including oil, gas and coal mining operations, wetlands, livestock, and other anthropogenic sources. The EDGAR v4.3.2 (Janssens-Maenhout et al., 2019) and EPA (Maasakkers et al., 2016) emissions databases were used, and the oil, gas and coal mining emission inventories of CH_4 over Canada and Mexico were taken from Sheng et al. (2017). The QFEDv2.4r8 inventory (`https://gmao.gsfc.nasa.gov/pubs/docs/Darmenov796.pdf`, last accessed: November, 2020) was used for biomass burning emissions. The model was spun-up for 25 years, then subsequently spun-up again from 1992, resulting in an "effective" spin-up period of over 35 years. The longer spin-up period is required for CH_4 (compared to CO) due to the much longer lifetime of CH_4 (Bader et al., 2017).

Chapter 3

Trends of Trace Gases at TAO

This chapter examines trends in a suite of trace gases using 18 years of TAO FTIR columns. This work has been submitted for publication in Environmental Research Communications (Yamanouchi et al., 2021a). In this study, all of the trace gases retrieved at TAO and archived to NDACC were analyzed. The data span from mid-2002 to the end of 2019 and have been submitted to the NDACC data archive. The measurements at TAO are valuable for assessing trends of long-lived species like N_2O, CH_4 and C_2H_6 (e.g., Franco et al., 2016a; Bader et al., 2017; Tzompa-Sosa et al., 2017, 2019). As discussed in Section 1.4.4, CH_4 and N_2O are two of the most powerful greenhouse gases in the atmosphere, and accurate concentration estimates are needed to model their climate change effects (IPCC, 2014; NAS, 2016). Trends of N_2O and CH_4, as well as C_2H_6, a gas that is co-emitted with CH_4 during oil and gas production, are estimated in this study.

Furthermore, tropospheric pollutants such as O_3 and CO (see Section 1.1), as well as NH_3 (see Section 1.4.2) are also examined. TAO measurements also include C_2H_2, which is primarily emitted from biofuel and fossil fuel combustion as well as biomass burning (Duflot et al., 2015); CH_3OH, which is known to be a major source of CO and H_2CO (Jacob et al., 2005); as well as H_2CO itself, which is an important air pollutant (Luecken et al., 2018). Other gases retrieved at TAO and analyzed for trends include HCl, a stratospheric gas and the largest chlorine reservoir (Mahieu et al., 2014); HCN, a key tracer species for identifying biomass burning enhancements (e.g., Viatte et al., 2013); HCOOH, a gas known for its potential for increasing rain acidity as well as being one of the most abundant VOCs in the atmosphere (Millet et al., 2015); HF, which is a reservoir for stratospheric halogens (Cheng, 2018), and HNO_3, an acidic pollutant that is a reservoir of NO_x (Hanke et al., 2003). All analyses were done using total columns, with the only exception being O_3. Because O_3 had a mean DOFS of 4.4 (see Table 2.2), tropospheric (0-12 km) and stratospheric (12-50 km) columns were analyzed separately (following Vigouroux et al., 2015). For C_2H_6 and CH_4, two disjointed trends, for 2002-2008 and 2009-2019, were fitted following the analysis done by Franco et al. (2016a). They observed a sharp increase in C_2H_6 starting 2009, attributed this to North American oil and gas production, and estimated that CH_4 emissions also grew in association with the rise in C_2H_6.

3.1 Datasets

All of the trace gas datasets examined in this study were retrieved from the TAO FTIR spectra using SFIT4 V0.9.4.4, as discussed in Section 2.5.3. The averaging kernels from the retrievals are shown in Figures 3.1 (C_2H_2), 3.2 (C_2H_6), 3.3 (CH_4), 3.4 (CH_3OH), 3.5 (CO), 3.6 (H_2CO), 3.7 (HCl), 3.8 (HCN), 3.9 (HCOOH), 3.10

(HF), 3.11 (HNO_3), 3.12 (N_2O), 3.13 (NH_3), and 3.14 (O_3). Sensitivities of the retrieval (sum of the rows of the averaging kernels) are also plotted (see Section 2.5 for discussion on retrievals). For some species, such as C_2H_2, C_2H_6, and NH_3, the retrieval sensitivity is primarily in the lower part of the atmosphere, while for others (e.g., O_3), the sensitivity may extend much further up in the atmosphere. Similar results were found for retrievals at Eureka (80.1°N, 86.4°W) (Lutsch, 2019). The total column time series are discussed in the following sections along with their trends. The intra-annual variabilities (seasonalities) of the trace gases can be seen in the annual cycle plots, where the columns are color coded and plotted by year (Figures 3.15 to 3.29). Some species, such as CH_4 and N_2O, have less pronounced seasonal cycles than others. Enhancement events can also be seen in these plots (e.g., a spike in CO in August 2014).

TAO datasets have been used in a number of recent studies. In addition to the publications associated with this thesis, over the past five years, TAO data have been used to study tropospheric O_3 (Whaley et al., 2015), oil and gas emissions (Franco et al., 2016a; Tzompa-Sosa et al., 2017, 2019), CH_4 (Bader et al., 2017), harmonized H_2CO retrievals (Vigouroux et al., 2018), HCOOH (Franco et al., 2020), HCN (Sun et al., 2020), and biomass burning (Lutsch et al., 2016, 2020). TAO data have also contributed to the validation of satellite date products, including IASI NH_3 (Dammers et al., 2016), CrIS NH_3 (Dammers et al., 2019), MOPITT CO (Gaubert et al., 2016; Buchholz et al., 2017), GOSAT CH_4 (Olsen et al., 2017), and TROPOMI H_2CO (Vigouroux et al., 2020). TAO data was also included in a study examining reductions in tropospheric O_3 in 2020 due to the lockdown caused by the global

COVID-19 pandemic (Steinbrecht et al., 2021). A complete list of TAO publications can be found at `https://www.atmosp.physics.utoronto.ca/TAO/Publications.html` (last accessed: January, 2021).

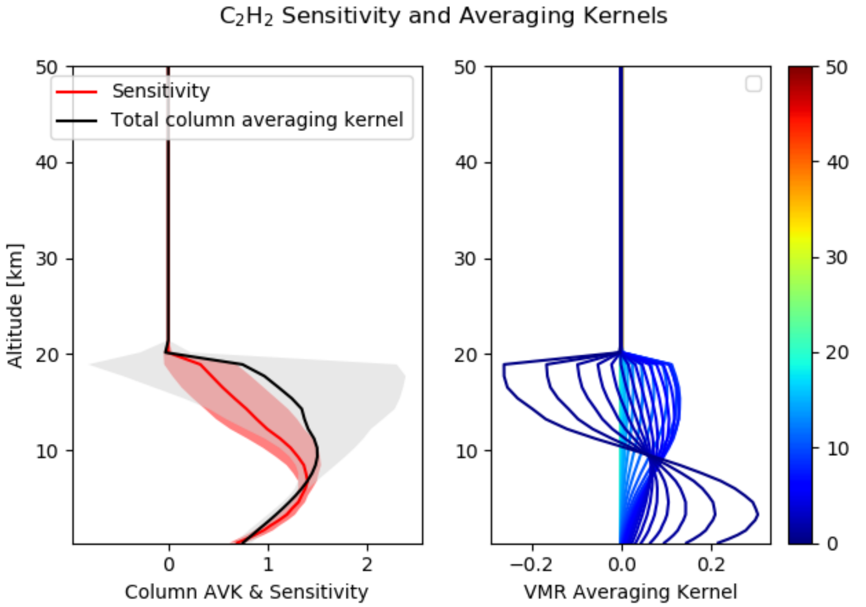

Figure 3.1: Total column averaging kernel and sensitivity (left) and VMR averaging kernel (right) averaged from 2002 to 2019 for C_2H_2. In the total column averaging kernel and sensitivity plots, the shading indicates $\pm 1\sigma$ standard deviation. In the VMR averaging kernel plot, the color bar indicates the retrieval altitude (km).

3.2 Trend Analysis Methodology

While a trend analysis using monthly averages is possible (e.g., Angelbratt et al., 2011a), this study fitted Fourier series of several orders (Weatherhead et al., 1998). Bootstrap resampling was utilized to derive the confidence interval of the trends, and a Q value (the number of bootstrap resampling ensemble members generated for statistical analysis) of 5000 was used (Gardiner et al., 2008). All of these techniques were combined to assess the intra- and inter-annual trends of the trace gases measured at TAO. Trends were calculated using the mean over the time series as the base value.

The Fourier fit was also used to identify enhancement events, following Zellweger et al. (2009). This analysis is done by taking the negative residuals of the fit (i.e., when measurements are smaller than the fitted values), mirroring them, and calculating the standard deviation (σ) of the mirrored residuals. Any measurements that are 2σ above the fit are considered enhancement events. This analysis eliminates biases in the spread due to enhancement events by using only the mirrored negative residuals to derive the spread. In this study, Fourier series of order 3 were utilized for all analyses. An analysis was done by comparing Fourier series fits of order 1 to 7, and checking for overfitting by running the residuals of the fit through a Kolmogorov-Smirnov normality test (Ghasemi and Zahediasl, 2012). While overfitting was not observed at higher orders, they did not give more statistically-significant trends, so order 3 was chosen.

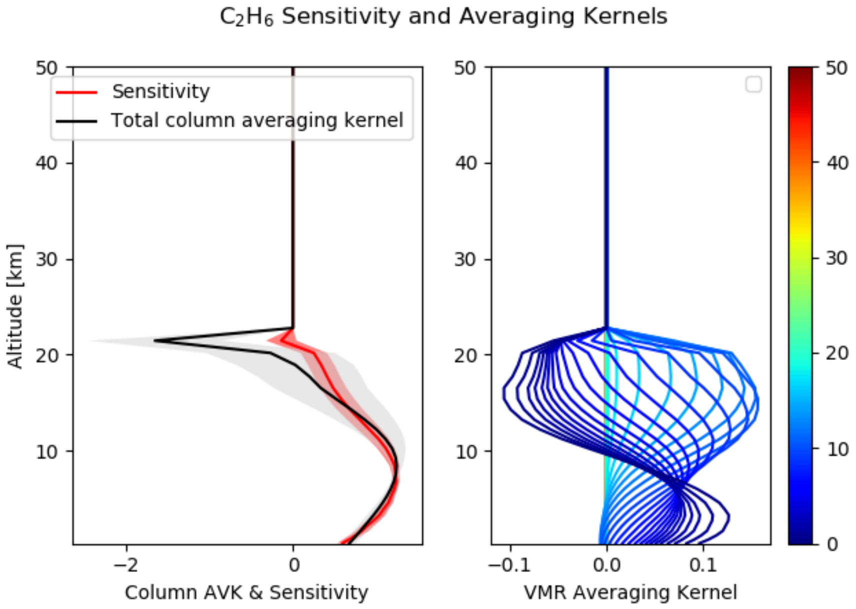

Figure 3.2: Total column averaging kernel and sensitivity (left) and VMR averaging kernel (right) averaged from 2002 to 2019 for C_2H_6. In the total column averaging kernel and sensitivity plots, the shading indicates ± 1σ standard deviation. In the VMR averaging kernel plot, the color bar indicates the retrieval altitude (km).

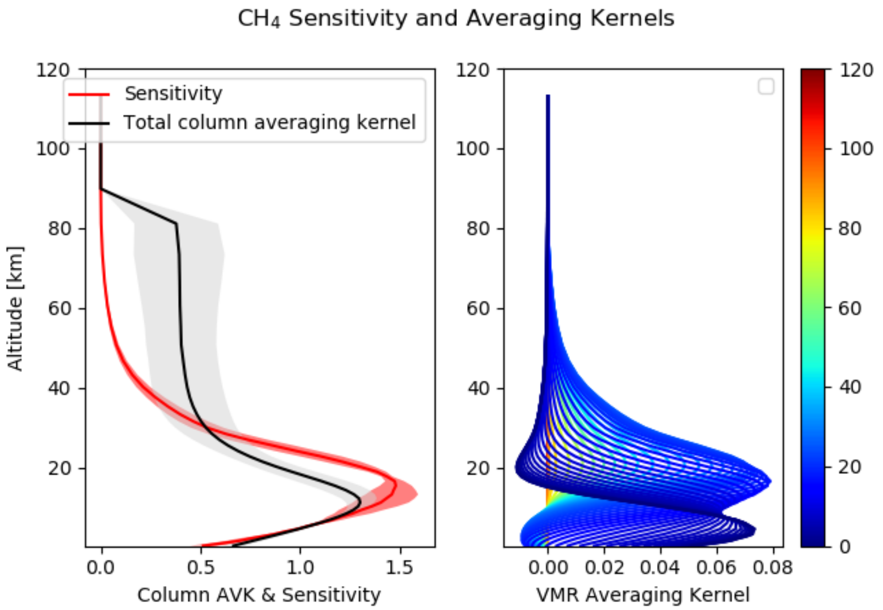

Figure 3.3: Total column averaging kernel and sensitivity (left) and VMR averaging kernel (right) averaged from 2002 to 2019 for CH_4. In the total column averaging kernel and sensitivity plots, the shading indicates ± 1σ standard deviation. In the VMR averaging kernel plot, the color bar indicates the retrieval altitude (km).

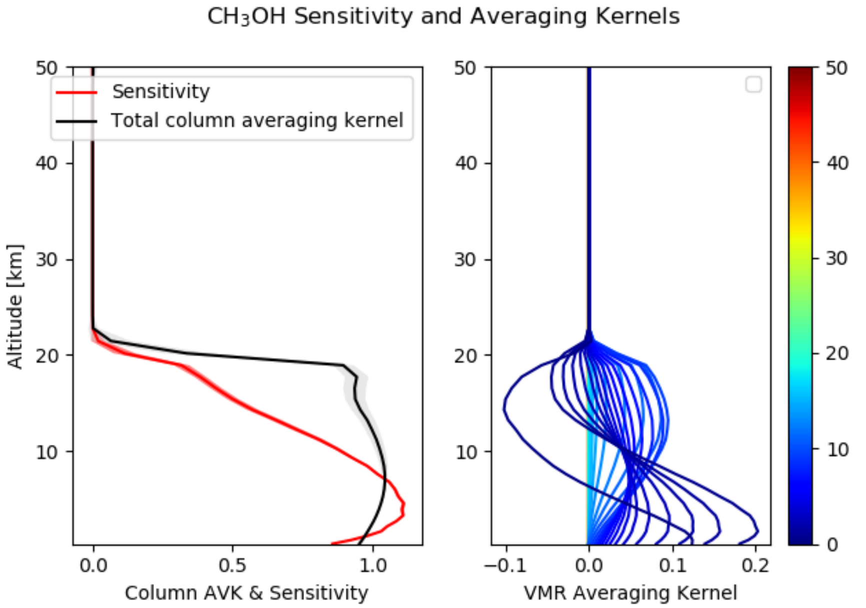

Figure 3.4: Total column averaging kernel and sensitivity (left) and VMR averaging kernel (right) averaged from 2002 to 2019 for CH_3OH. In the total column averaging kernel and sensitivity plots, the shading indicates ± 1σ standard deviation. In the VMR averaging kernel plot, the color bar indicates the retrieval altitude (km).

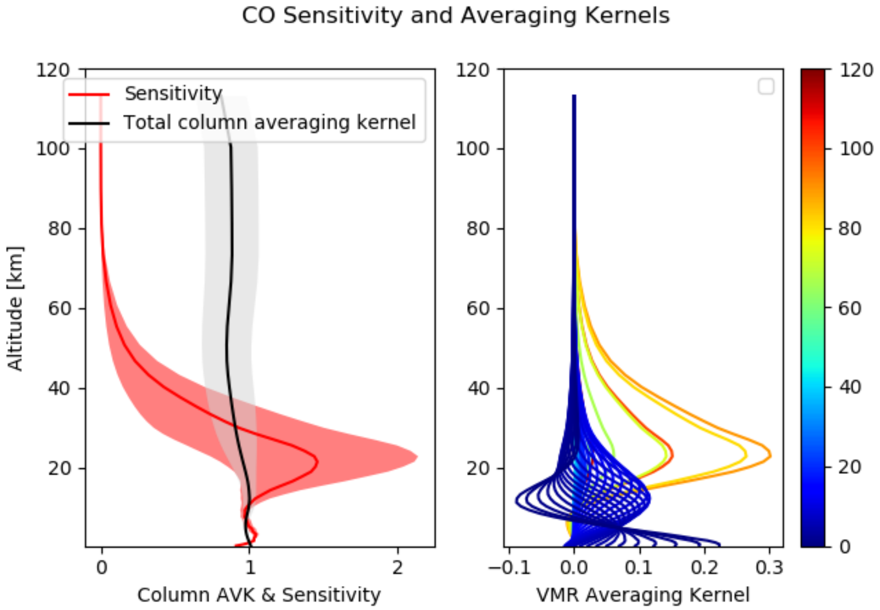

Figure 3.5: Total column averaging kernel and sensitivity (left) and VMR averaging kernel (right) averaged from 2002 to 2019 for CO. In the total column averaging kernel and sensitivity plots, the shading indicates ± 1σ standard deviation. In the VMR averaging kernel plot, the color bar indicates the retrieval altitude (km).

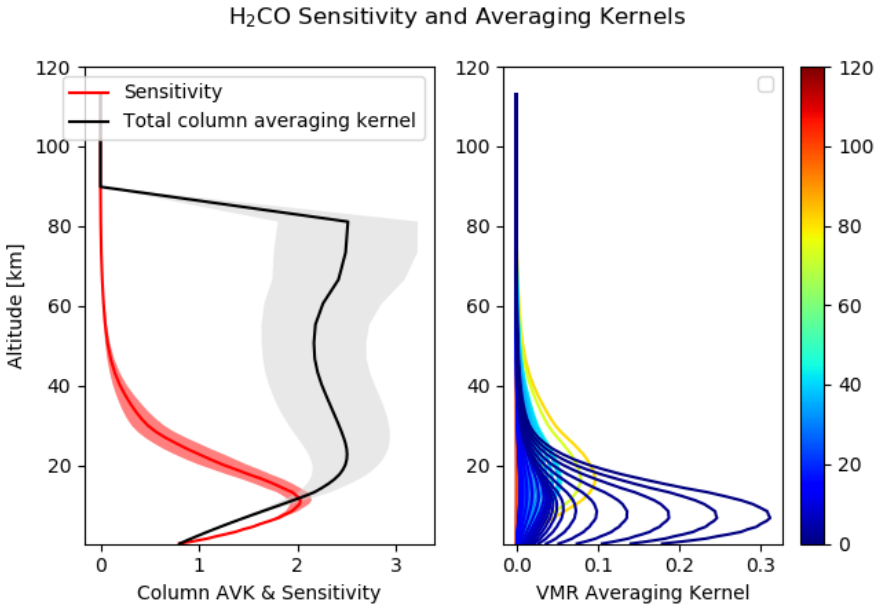

Figure 3.6: Total column averaging kernel and sensitivity (left) and VMR averaging kernel (right) averaged from 2002 to 2019 for H_2CO. In the total column averaging kernel and sensitivity plots, the shading indicates ± 1σ standard deviation. In the VMR averaging kernel plot, the color bar indicates the retrieval altitude (km).

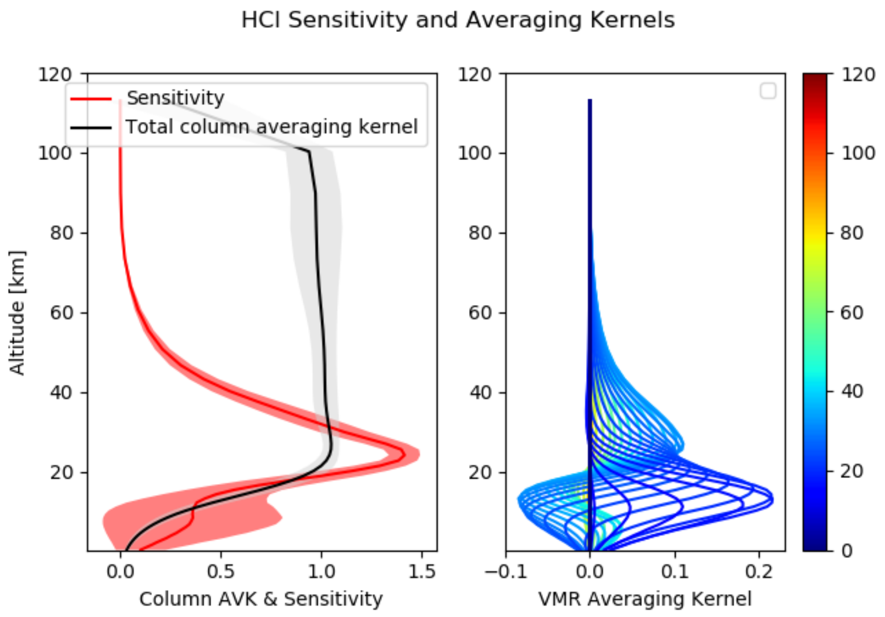

Figure 3.7: Total column averaging kernel and sensitivity (left) and VMR averaging kernel (right) averaged from 2002 to 2019 for HCl. In the total column averaging kernel and sensitivity plots, the shading indicates ± 1σ standard deviation. In the VMR averaging kernel plot, the color bar indicates the retrieval altitude (km).

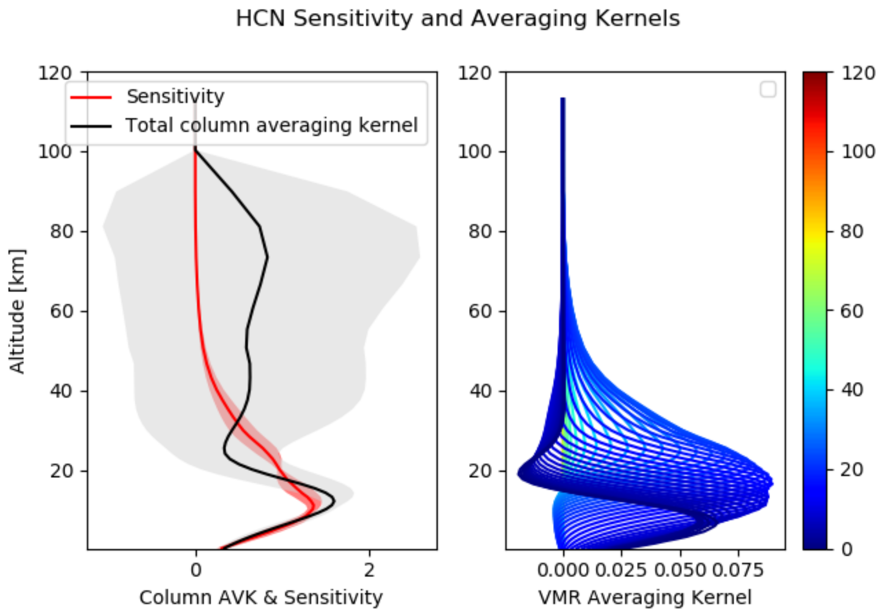

Figure 3.8: Total column averaging kernel and sensitivity (left) and VMR averaging kernel (right) averaged from 2002 to 2019 for HCN. In the total column averaging kernel and sensitivity plots, the shading indicates ± 1σ standard deviation. In the VMR averaging kernel plot, the color bar indicates the retrieval altitude (km).

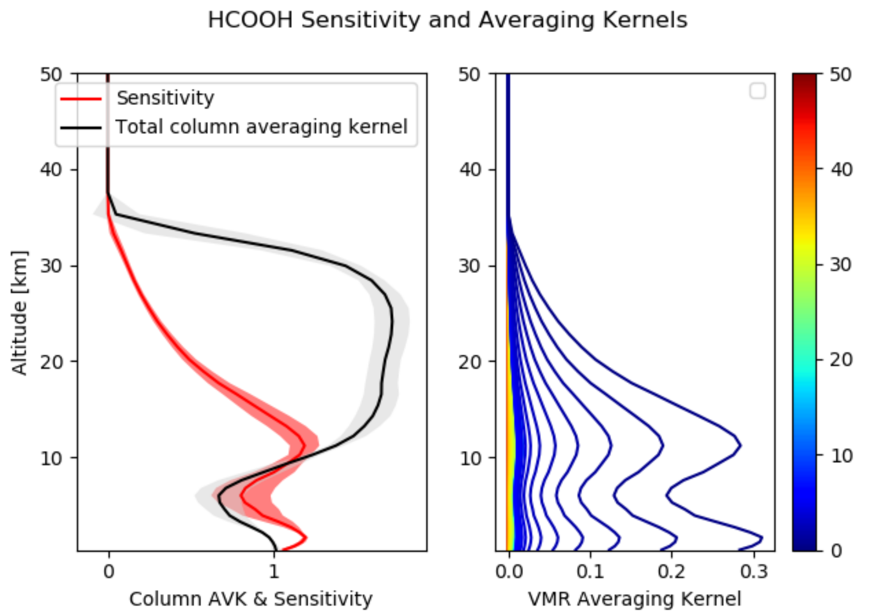

Figure 3.9: Total column averaging kernel and sensitivity (left) and VMR averaging kernel (right) averaged from 2002 to 2019 for HCOOH. In the total column averaging kernel and sensitivity plots, the shading indicates ± 1σ standard deviation. In the VMR averaging kernel plot, the color bar indicates the retrieval altitude (km).

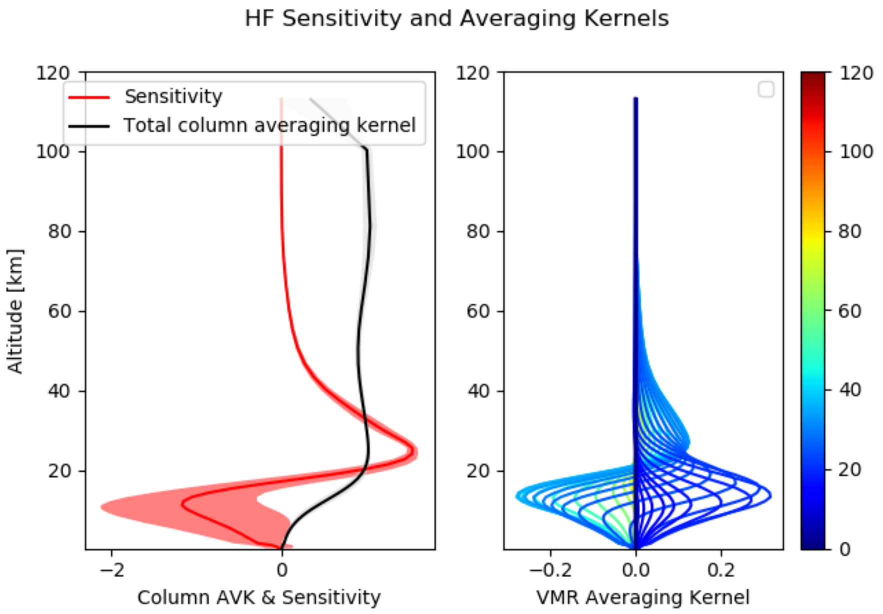

Figure 3.10: Total column averaging kernel and sensitivity (left) and VMR averaging kernel (right) averaged from 2002 to 2019 for HF. In the total column averaging kernel and sensitivity plots, the shading indicates ± 1σ standard deviation. In the VMR averaging kernel plot, the color bar indicates the retrieval altitude (km).

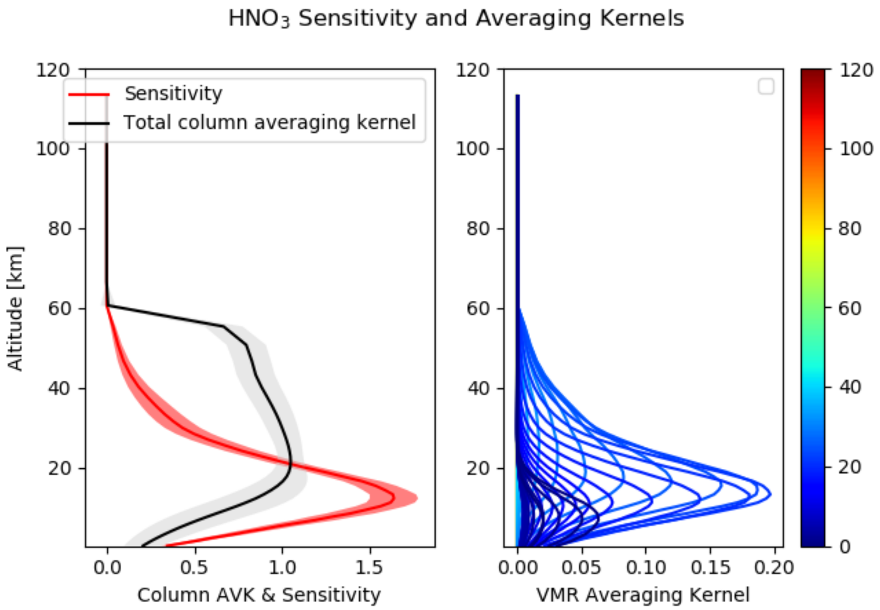

Figure 3.11: Total column averaging kernel and sensitivity (left) and VMR averaging kernel (right) averaged from 2002 to 2019 for HNO_3. In the total column averaging kernel and sensitivity plots, the shading indicates ± 1σ standard deviation. In the VMR averaging kernel plot, the color bar indicates the retrieval altitude (km).

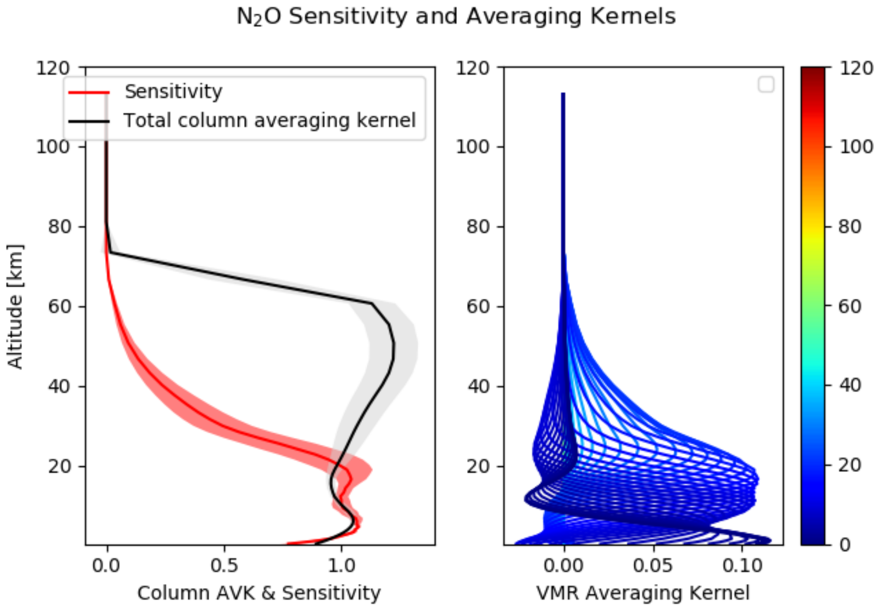

Figure 3.12: Total column averaging kernel and sensitivity (left) and VMR averaging kernel (right) averaged from 2002 to 2019 for N_2O. In the total column averaging kernel and sensitivity plots, the shading indicates ± 1σ standard deviation. In the VMR averaging kernel plot, the color bar indicates the retrieval altitude (km).

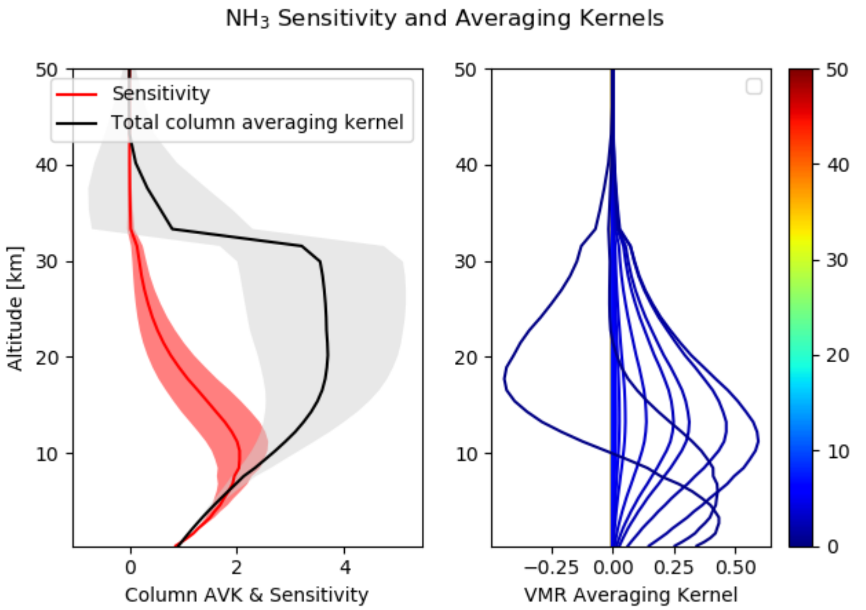

Figure 3.13: Total column averaging kernel and sensitivity (left) and VMR averaging kernel (right) averaged from 2002 to 2019 for NH_3. In the total column averaging kernel and sensitivity plots, the shading indicates ± 1σ standard deviation. In the VMR averaging kernel plot, the color bar indicates the retrieval altitude (km).

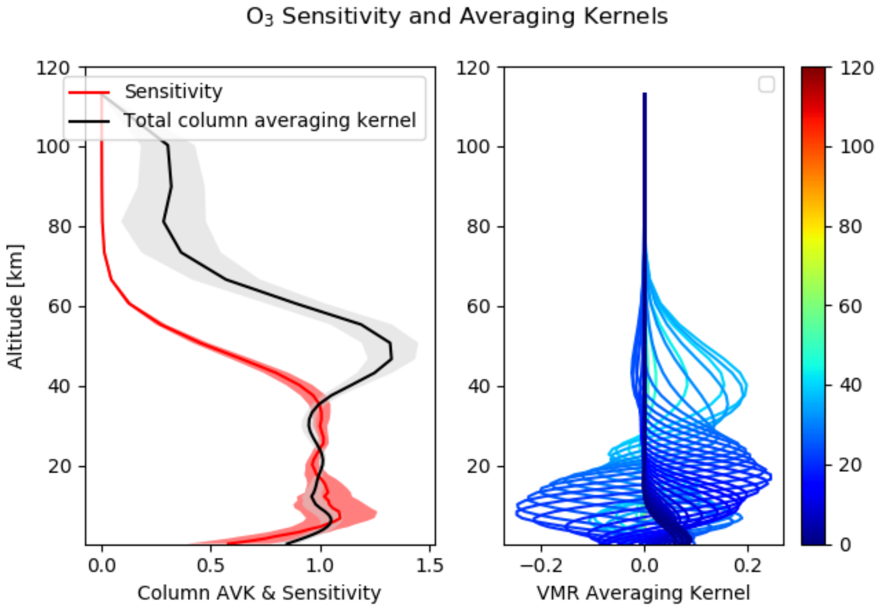

Figure 3.14: Total column averaging kernel and sensitivity (left) and VMR averaging kernel (right) averaged from 2002 to 2019 for O_3. In the total column averaging kernel and sensitivity plots, the shading indicates ± 1σ standard deviation. In the VMR averaging kernel plot, the color bar indicates the retrieval altitude (km).

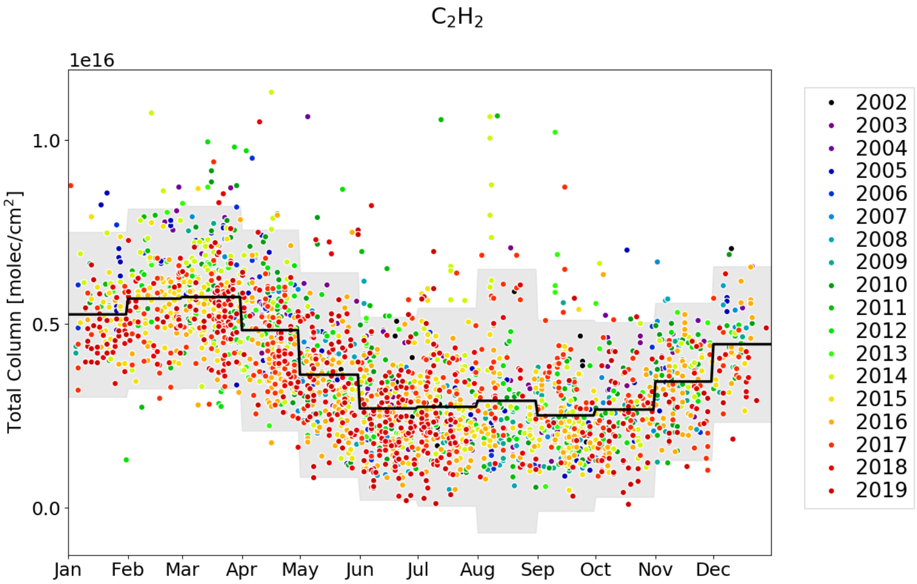

Figure 3.15: TAO total columns from 2002 to 2019 plotted from January to December for C_2H_2. Monthly averages and ± 2σ (standard deviation) are indicated by the black line and shading, respectively.

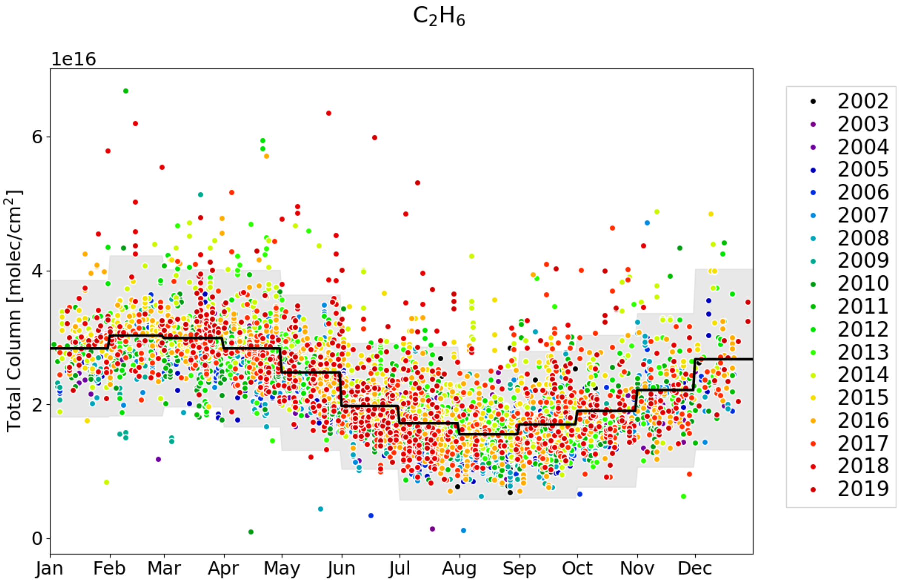

Figure 3.16: TAO total columns from 2002 to 2019 plotted from January to December for C_2H_6. Monthly averages and ± 2σ (standard deviation) are indicated by the black line and shading, respectively.

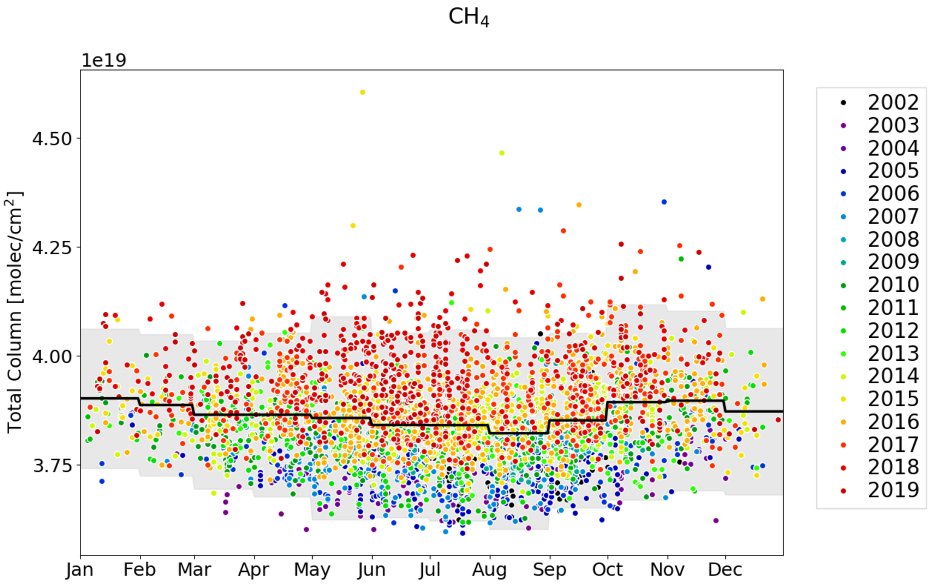

Figure 3.17: TAO total columns from 2002 to 2019 plotted from January to December for CH_4. Monthly averages and ± 2σ (standard deviation) are indicated by the black line and shading, respectively.

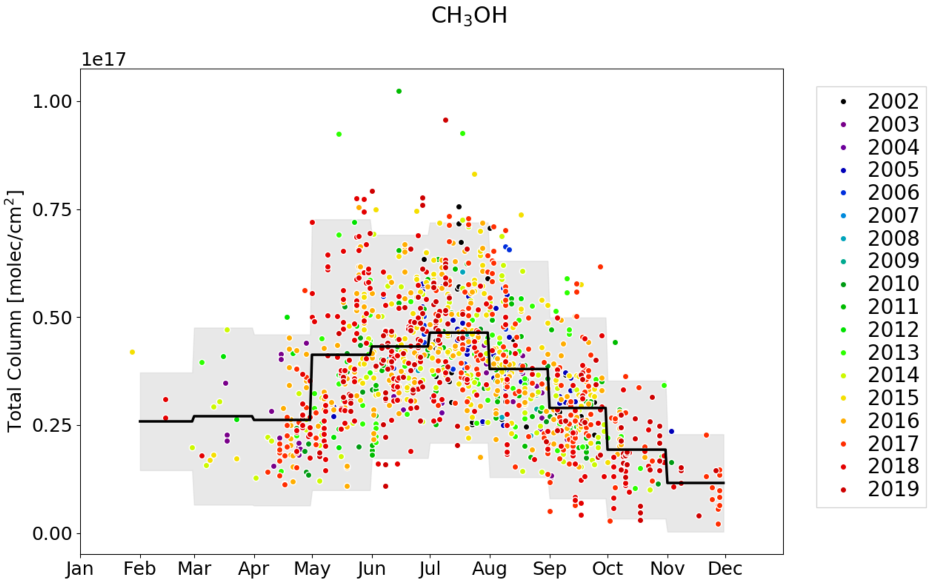

Figure 3.18: TAO total columns from 2002 to 2019 plotted from January to December for CH_3OH. Monthly averages and ± 2σ (standard deviation) are indicated by the black line and shading, respectively. Note that for CH_3OH, only one measurement was made in January, and none in December throughout the TAO time series, and therefore, the monthly mean and the standard deviation for these two months are not plotted.

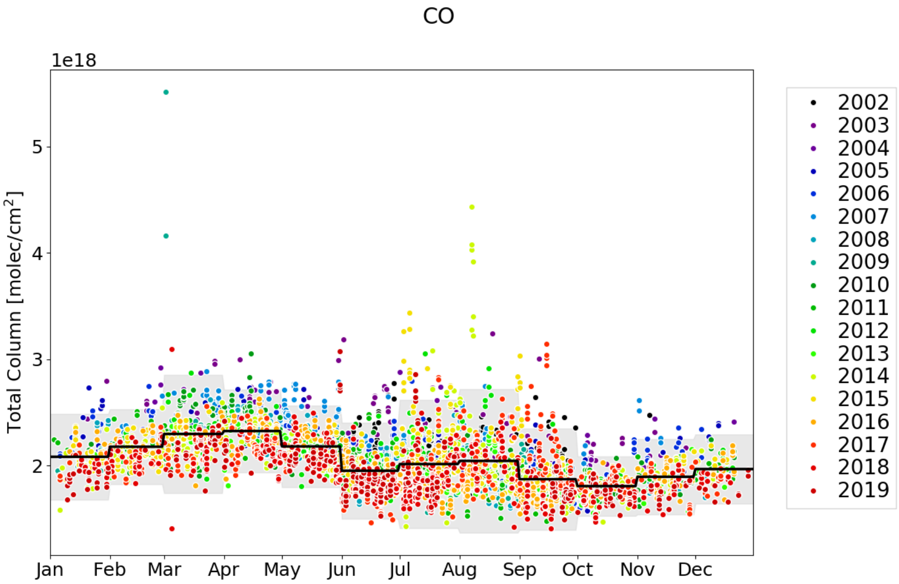

Figure 3.19: TAO total columns from 2002 to 2019 plotted from January to December for CO. Monthly averages and ± 2σ (standard deviation) are indicated by the black line and shading, respectively.

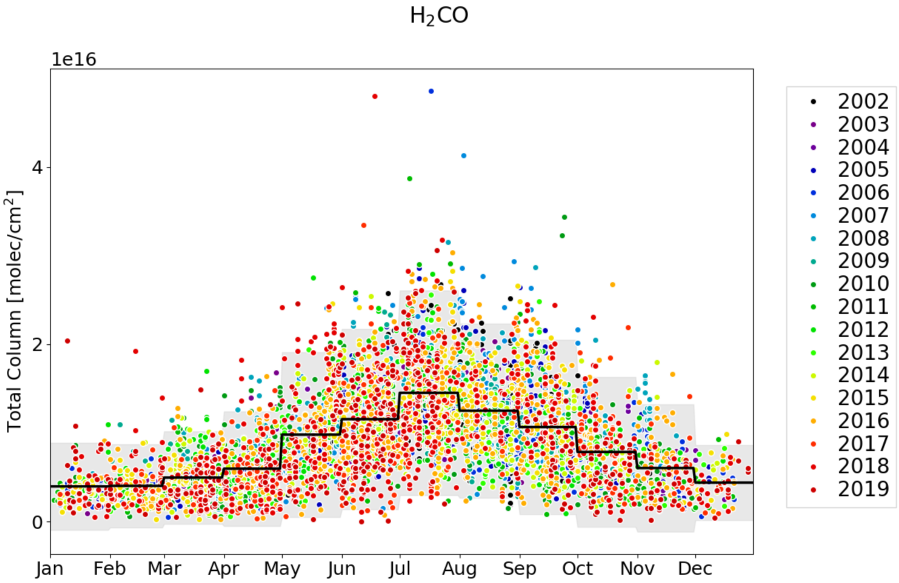

Figure 3.20: TAO total columns from 2002 to 2019 plotted from January to December for H_2CO. Monthly averages and ± 2σ (standard deviation) are indicated by the black line and shading, respectively.

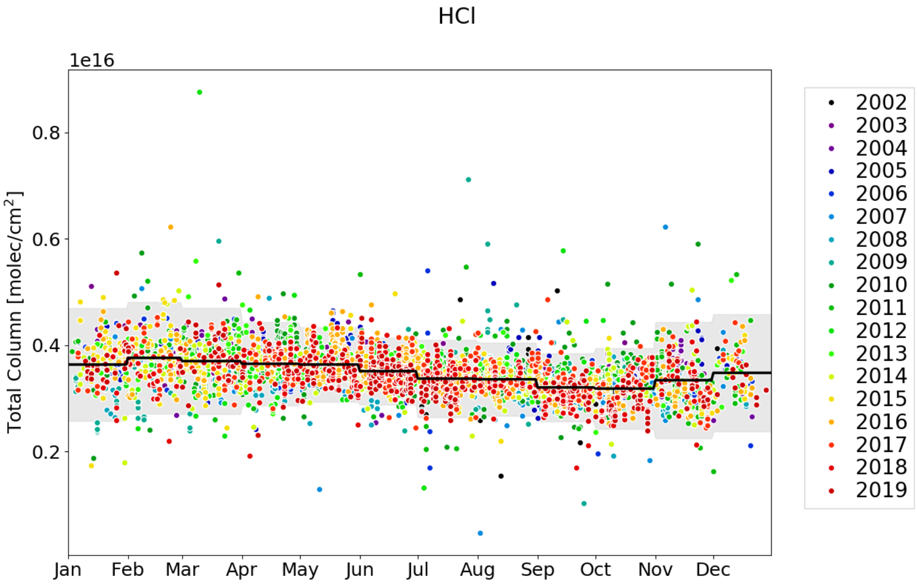

Figure 3.21: TAO total columns from 2002 to 2019 plotted from January to December for HCl Monthly averages and ± 2σ (standard deviation) are indicated by the black line and shading, respectively.

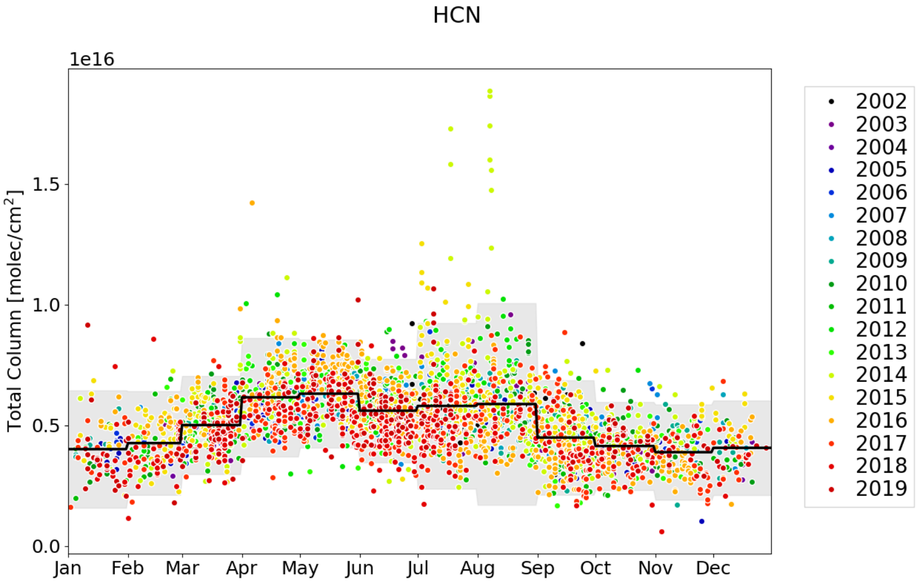

Figure 3.22: TAO total columns from 2002 to 2019 plotted from January to December for HCN. Monthly averages and ± 2σ (standard deviation) are indicated by the black line and shading, respectively.

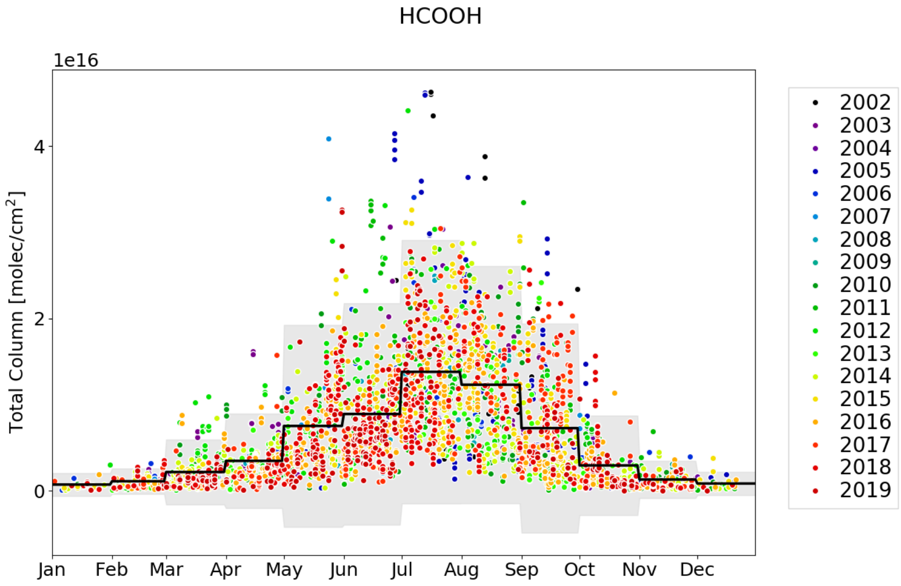

Figure 3.23: TAO total columns from 2002 to 2019 plotted from January to December for HCOOH. Monthly averages and ± 2σ (standard deviation) are indicated by the black line and shading, respectively.

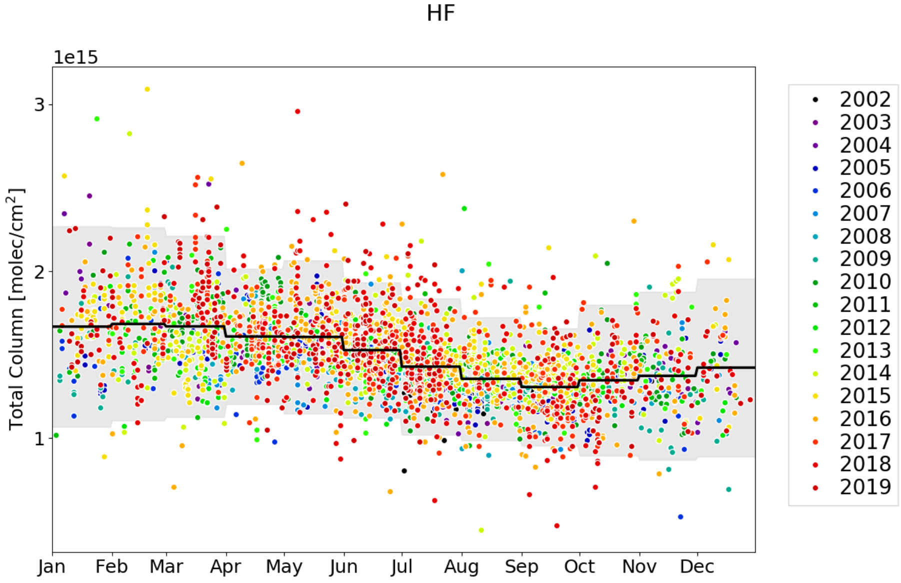

Figure 3.24: TAO total columns from 2002 to 2019 plotted from January to December for HF. Monthly averages and ± 2σ (standard deviation) are indicated by the black line and shading, respectively.

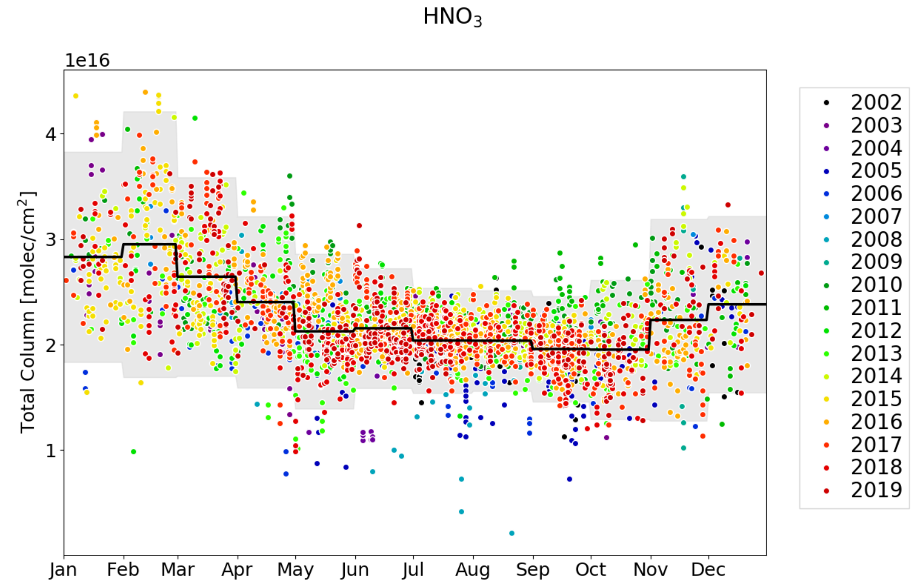

Figure 3.25: TAO total columns from 2002 to 2019 plotted from January to December for HNO_3. Monthly averages and ± 2σ (standard deviation) are indicated by the black line and shading, respectively.

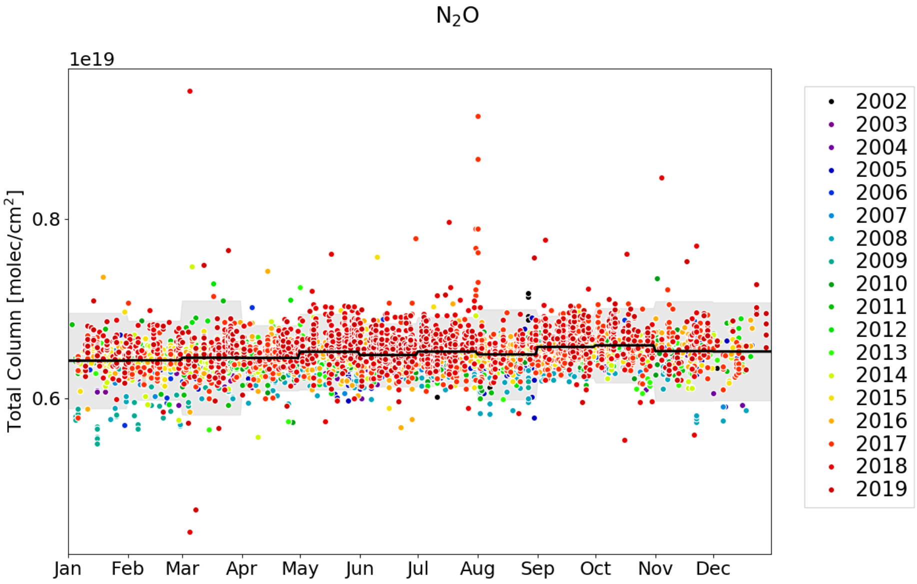

Figure 3.26: TAO total columns from 2002 to 2019 plotted from January to December for N_2O. Monthly averages and ± 2σ (standard deviation) are indicated by the black line and shading, respectively.

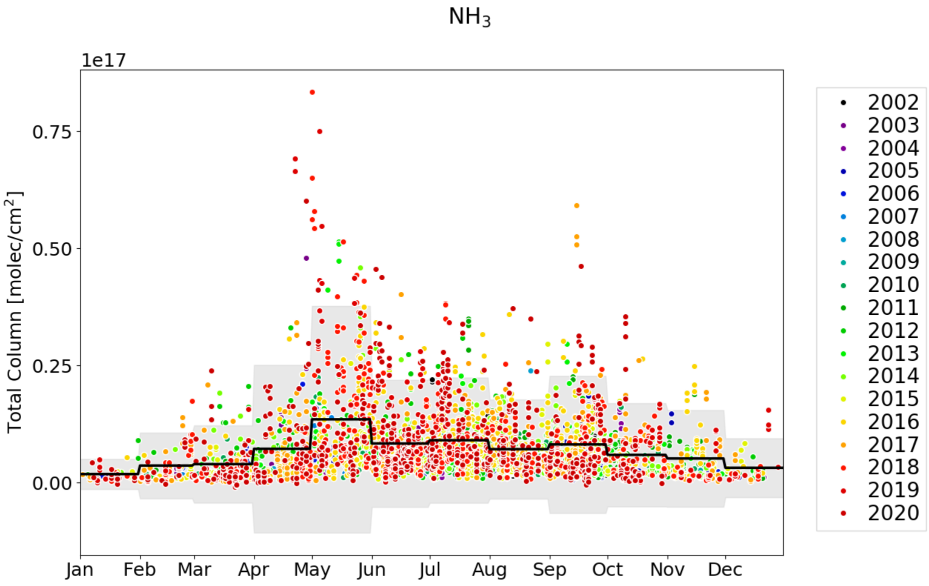

Figure 3.27: TAO total columns from 2002 to 2019 plotted from January to December for NH$_3$. Monthly averages and ± 2σ (standard deviation) are indicated by the black line and shading, respectively.

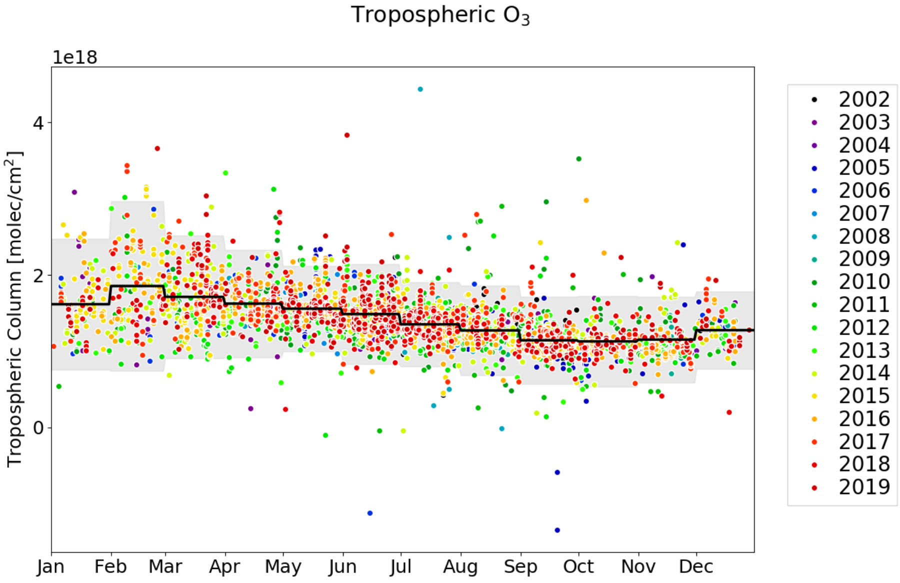

Figure 3.28: TAO tropospheric columns from 2002 to 2019 plotted from January to December for O$_3$. Monthly averages and ± 2σ (standard deviation) are indicated by the black line and shading, respectively.

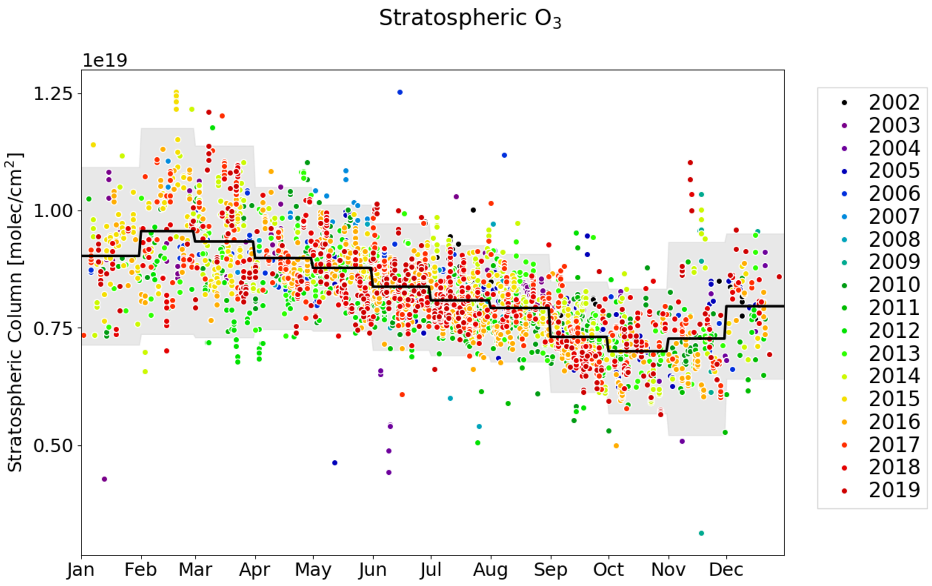

Figure 3.29: TAO stratospheric columns from 2002 to 2019 plotted from January to December for O_3. Monthly averages and ± 2σ (standard deviation) are indicated by the black line and shading, respectively.

3.2.1 Models Used to Interpret Observations

The GEOS-Chem (v.12.1.1) chemical transport model (CTM) tagged CO simulation was used to identify major sources contributing to CO over Toronto. Additionally, the GEOS-Chem (v.12.3.2) tagged CH_4 simulation was used to quantify the sources contributing to CH_4 over Toronto. The tagged CH_4 simulation was previously used by Bader et al. (2017) to assess contributions to increased CH_4 over NDACC FTIR stations. Recent studies (e.g., Baray et al., 2018) have shown that Canadian oil-sands CH_4 emissions may be higher than expected, and thus may result in the model underestimating the oil and gas contributions to CH_4 over Toronto. In fact, Baray et al. (2018) have shown, through aircraft measurements taken in summer 2013, that CH_4 emissions from the Athabasca Oil Sands Region were 48 ± 8 % higher than the values in the 2013 Canadian Greenhouse Gas Reporting Program inventory. Due to these issues, the tagged CH_4 model was not used in this study to attribute drivers of trends seen in the FTIR data, only to estimate sources of CH_4 over Toronto. Model data from 2002 to 2018 were used for this study. Details of the models and their configurations can be found in Section 2.6. GEOS-Chem tagged runs of CH_4 and CO are discussed in Sections 3.3 and 3.5, respectively.

3.3 CH_4 Trends

CH_4 total columns over TAO from 2002 to 2008 were found to have a positive trend of 0.26 ± 0.10 and 0.24 ± 0.07 %/year, with and without enhancement events, respectively (see Figure 3.30). The gap in the time series around 2007-2009 is due to issues with the DA8 FTIR, which affected CH_4 in particular. Observed trends and their significances are summarized in Table 3.1. These values are consistent with findings from Angelbratt et al. (2011a), where analysis of European (Jungfraujoch (46.6°N, 8.0°E), Kiruna (67.8°N, 20.4°E) and Zugspitze (47.4°N, 11.0°E)) FTIR data from 1996 to 2007 yielded linear trends ranging from 0.13 ± 0.01 to 0.25 ± 0.02 %/year. In the subsequent years (2009 to 2019), the TAO trend increased to 0.41 ± 0.03 %/year and 0.38 ± 0.02 %/year, with and without enhancement events, respectively. The slightly smaller trend after the removal of enhancement events suggests that enhancement events are becoming more frequent.

The tagged GEOS-Chem run shows the largest contributor to CH_4 over TAO to be wetland emissions, which contributed 31.7 ± 0.5 % of the CH_4 column, averaged from 2002 to 2018. Oil, gas and coal mining emissions accounted for 20.4 ± 0.3 % of CH_4. Oil and gas alone accounted for 14.9 ± 0.2 %, and coal, 5.5 ± 0.1 %.

Table 3.1: Trends of trace gas columns measured with the TAO FTIR spectrometer (2002 to 2019), along with their respective uncertainties (± 2σ). Positive and negative trends are highlighted green and red, respectively (if the 2σ error bars do not overlap 0 %).

Species	Annual trend (%/year)	Annual trend with enhancement events removed (%/year)
C_2H_2	−1.12 ± 0.30	−1.21 ± 0.26
C_2H_6[a]	−0.74 ± 0.73	−1.31 ± 0.61
C_2H_6[b]	1.19 ± 0.27	0.94 ± 0.20
CH_4[a]	0.26 ± 0.10	0.24 ± 0.07
CH_4[b]	0.41 ± 0.03	0.38 ± 0.02
CH_3OH	0.26 ± 0.47	0.00 ± 0.40
CO	−0.90 ± 0.07	−0.87 ± 0.05
H_2CO	−0.20 ± 0.28	−0.43 ± 0.25
HCl	−0.11 ± 0.07	−0.07 ± 0.06
HCN	−0.51 ± 0.21	−0.61 ± 0.16
HCOOH	−2.15 ± 0.64	−0.72 ± 0.53
HF	0.59 ± 0.11	0.47 ± 0.09
HNO_3	0.36 ± 0.13	0.43 ± 0.12
N_2O	0.28 ± 0.02	0.26 ± 0.02
NH_3	3.56 ± 0.85	2.36 ± 0.57
O_3[c]	0.28 ± 0.19	0.41 ± 0.15
O_3[d]	−0.05 ± 0.07	−0.05 ± 0.07

[a] Analysis of data from 2002 to 2008.

[b] Analysis of data from 2009 to 2019.

[c] Analysis of tropospheric column (0 to 12 km).

[d] Analysis of stratospheric column (12 to 50 km).

Livestock emissions also accounted for a significant portion of CH_4, at 20.1 ± 0.2 %. Contributions from other anthropogenic sources were smaller, at 4.0 ± 0.1 % (see Figure 3.31a). This may be due to the coarse resolution of the model (at 2° × 2.5°, the grid box is roughly 220 km by 200 km). The grid box containing TAO (and by extension downtown Toronto) also contains areas west of the city that have high livestock emissions, as estimated by the EDGAR emissions database. Additionally, as noted in Section 3.2.1, recent studies have shown CH_4 emissions from the Canadian oil sands region to be underestimated. Updated emissions databases are needed for reliable estimates of emissions contribution to CH_4 over TAO and elsewhere (e.g., Mostafavi Pak et al., 2019).

3.4 C_2H_6 Trends

C_2H_6 was found to be decreasing from 2002 to 2008, at rates of -0.74 ± 0.73 and -1.31 ± 0.61 %/year, with and without enhancement events, respectively (see Figure 3.32). This is in agreement with trends observed in Harestua (60.2°N, 10.8°E) and Kiruna from 1996 to 2006, at -1.09 ± 0.25 and -1.14 ± 0.18 %/year, respectively (Angelbratt et al., 2011b). The trends for the subsequent years (2009 to 2019) were reversed, with positive trends of 1.19 ± 0.27 and 0.94 ± 0.20 %/year, with and without enhancement events respectively. Bootstrap resampling error analysis shows these trends to be significant (i.e., the 2σ error bars do not overlap 0 %). The recent C_2H_6 trend retrieved in this analysis is lower than estimates given by Franco et al. (2016a), where growth rates of 3-5 %/year were seen when analyzing FTIR datasets from 2009 to 2014 from Eureka (80.1°N, 86.4°W), Thule (76.5°N, 68.8°W),

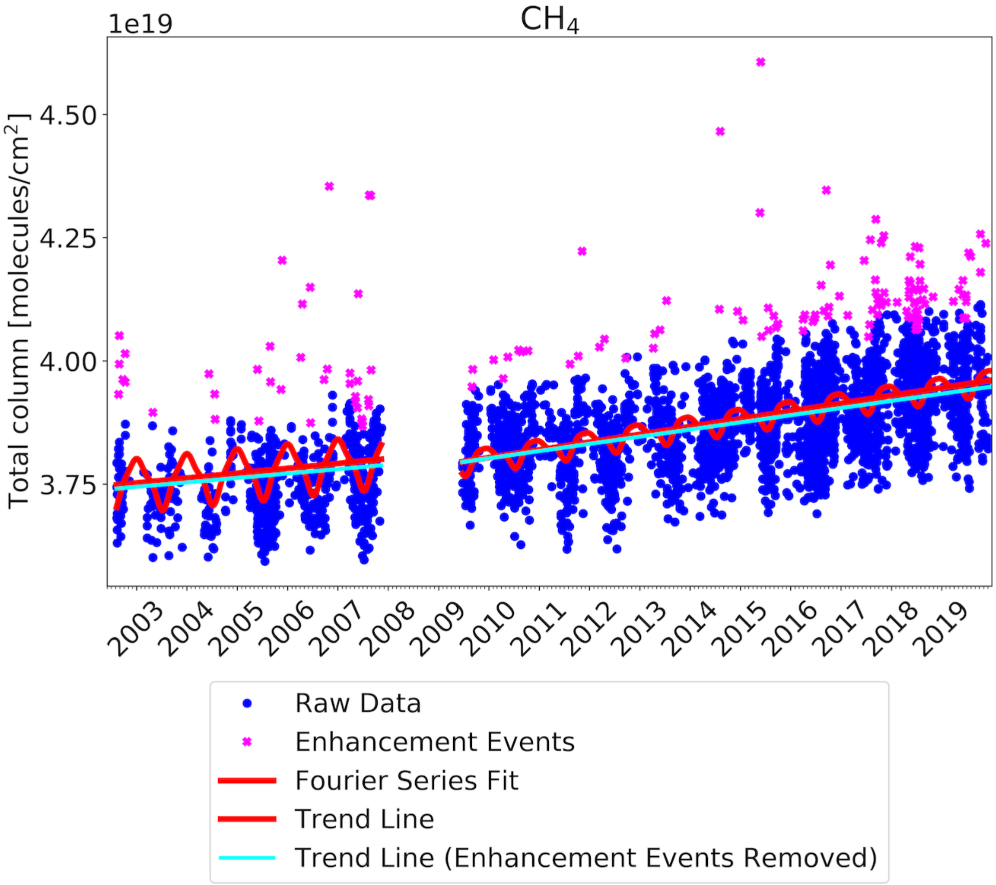

Figure 3.30: Time series and fitted trends of TAO total columns of CH$_4$. Separate fits were done for data before and after 2009. The gap in 2007-2009 is due to issues with the DA8 FTIR that affected the CH$_4$ retrievals.

TAO, Boulder (40.4°N, 102.5°W), and Mauna Loa (19.5°N, 155.6°W). For reference, the methodology used in this study yielded a trend of 5.17 ± 0.68 %/year using 2009-2014 data, and 0.30 ± 0.79 %/year for 2015-2019.

3.5 CO Trends

CO over TAO exhibited a negative trend (see Figure 3.33), at an annual rate of −0.90 ± 0.07 % (−0.87 ± 0.05 % after removal of enhancement events). This is in agreement with the CO trend seen in Zugspitze (1996 to 2006), which was

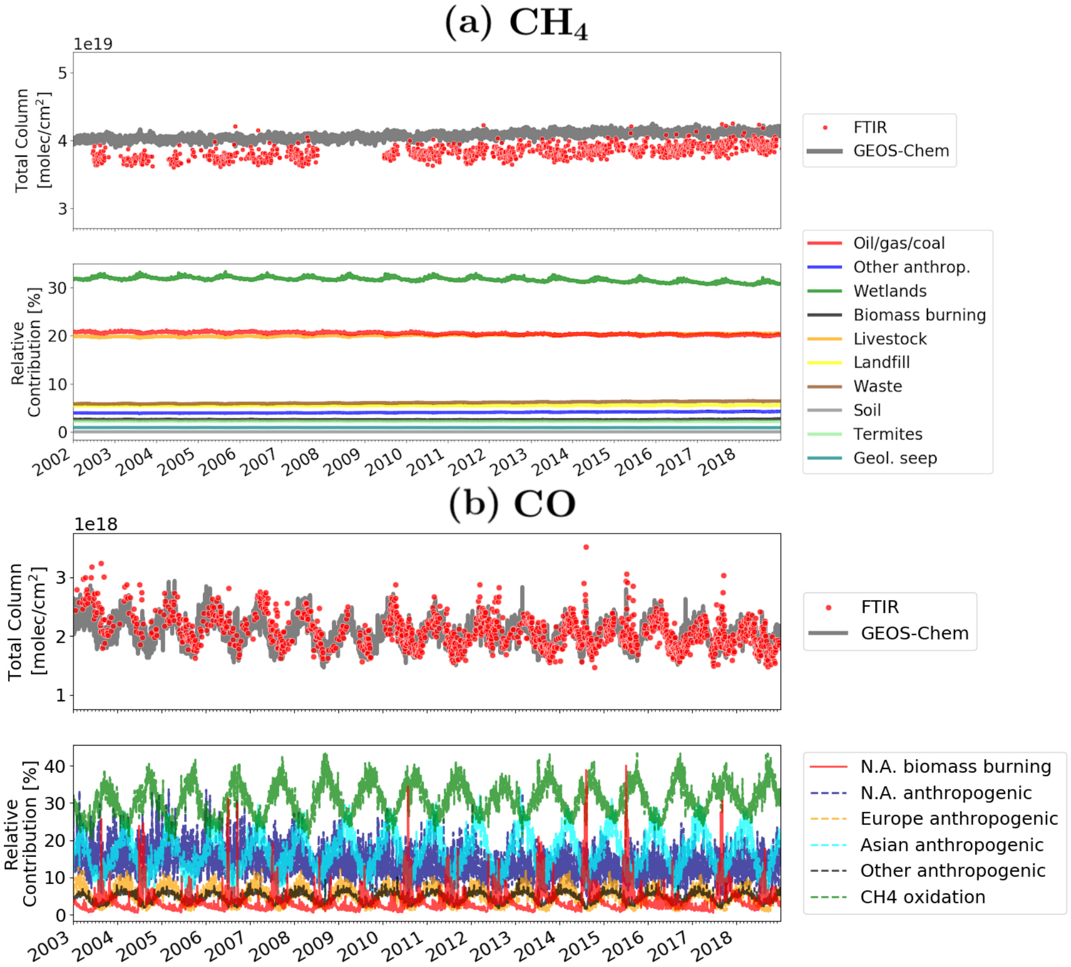

Figure 3.31: Time series of GEOS-Chem (a) tagged CH_4 output, and (b) tagged CO output over Toronto. For each subplot, the top panel shows FTIR total column measurements and GEOS-Chem total column output, and the lower panel shows the relative contributions (to CH_4 or CO) over Toronto from various sources.

observed to be -1.00 ± 0.24 %/year (Angelbratt et al., 2011b). This result is also comparable to values seen at Lauder, New Zealand (45°S, 170°E), and at Arrival Heights, Antarctica (78°S, 167°E), both from 1997 to 2009, where annual trends of -0.94 ± 0.47 and -0.92 ± 0.46 %/year were observed, respectively (Zeng et al., 2012). A study by Worden et al. (2013) showed that CO trend in the Northern and Southern Hemisphere are similar; from 2000 to 2011, MOPITT data showed that

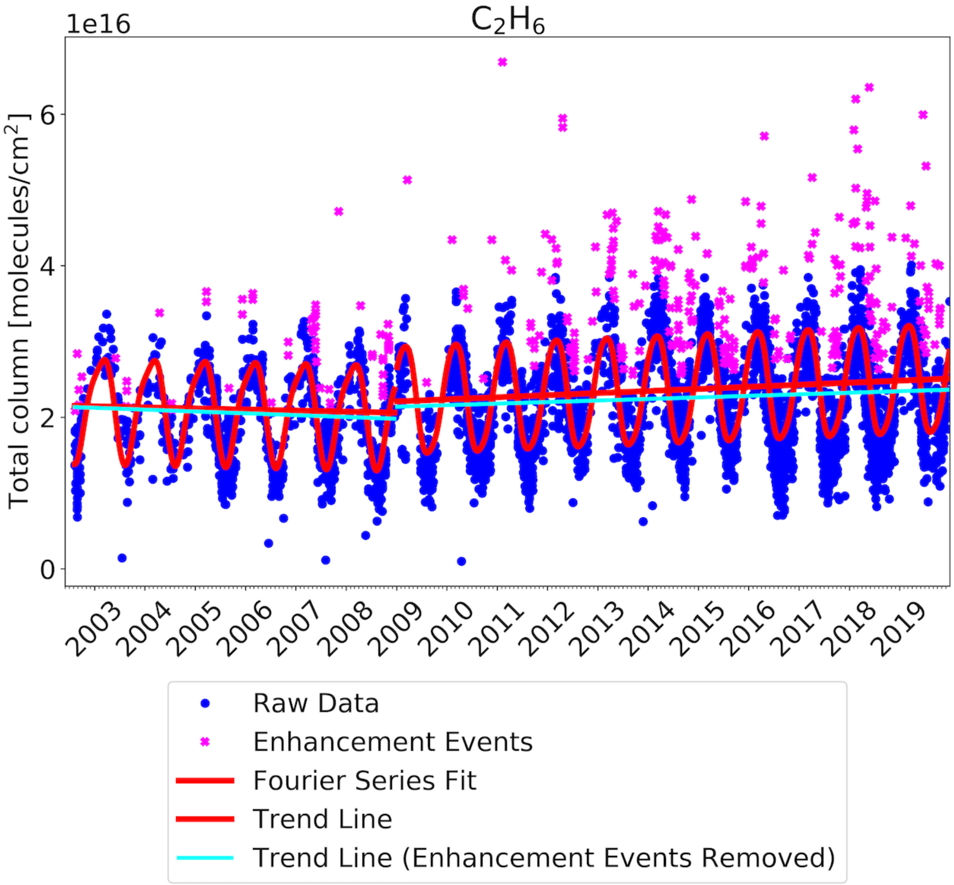

Figure 3.32: Time series and fitted trends of TAO total columns of C_2H_6. Separate fits were done for data before and after 2009.

the Northern Hemisphere trend was 0.92 ± 0.51 %/year, while in the Southern Hemisphere, it was 0.88 ± 0.52 %/year.

The GEOS-Chem tagged CO simulation shows CH_4 oxidation to be a major source of CO over Toronto, accounting for 30.9 ± 4.4 % of CO in the grid containing TAO, averaged over 2003 to 2018. North American fossil fuel emissions accounted for 13.9 ± 4.0 %, while Asian fossil fuel sources accounted for 16.8 ± 5.3 %. Fossil fuel contributions exhibit seasonality, peaking in the winter months. All other anthropogenic sources contributed 4.7 ± 1.3 % (see Figure 3.31b). North American biomass burning contributed 3.6 ± 3.4 %, although values as high as 39.8 % were seen in 2015, during a biomass enhancement event (see Chapter 4).

GEOS-Chem trends and their errors were obtained using the same methodology as the FTIR data. The modeled CO time series over Toronto showed a negative trend of −0.47 ± 0.04 %/year, and CO over Toronto from North American and European fossil fuel sources exhibited a negative trend of −2.64 ± 0.18 and −1.63 ± 0.14 %/year, respectively, while Asian fossil fuel sources showed a positive trend of 0.37 ± 0.08 %/year. North American biomass burning sources also showed an upward trend, at a rate of 1.56 ± 0.47 %/year.

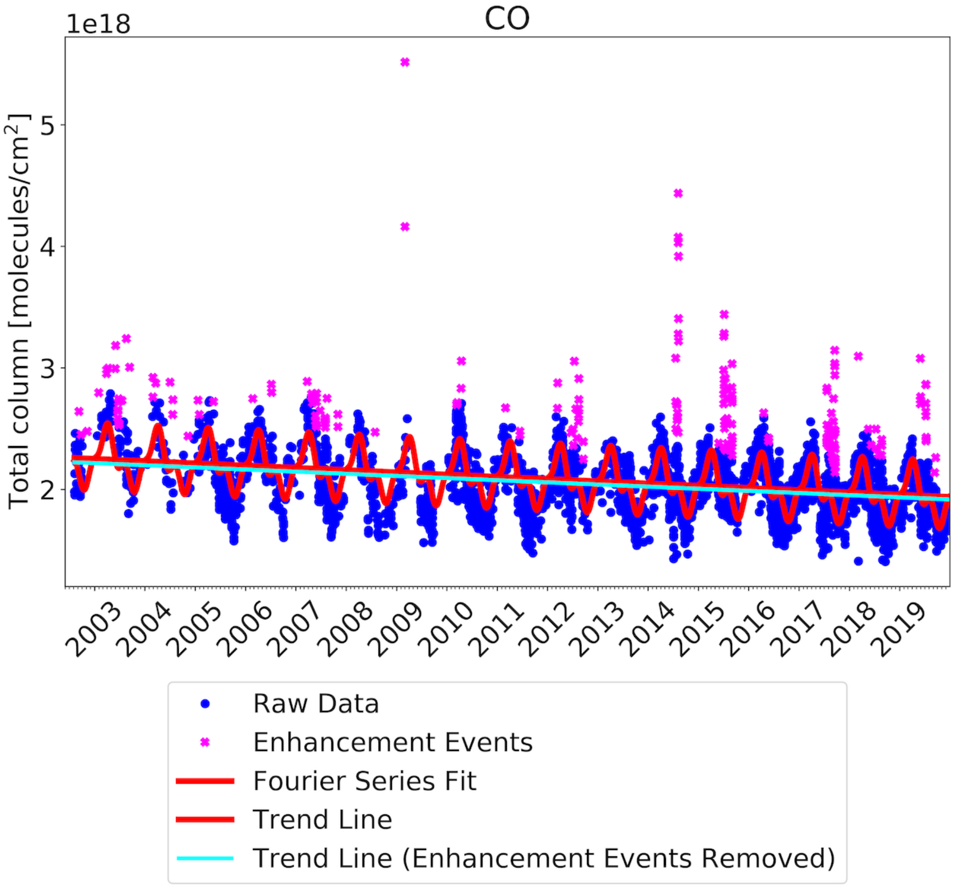

Figure 3.33: Time series and fitted trends of TAO total columns of CO.

3.6 N_2O Trends

The time series of TAO N_2O (see Figure 3.34) shows a steady and statistically robust trend, increasing at a rate of 0.28 ± 0.02 %/year (0.26 ± 0.02 %/year without enhancement events). This is similar to findings from other FTIRs, such as 0.21 ± 0.01, 0.19 ± 0.01, 0.40 ± 0.02, and 0.29 ± 0.02 %/year at Jungfraujoch, Zugspitze, Harestua, and Kiruna, respectively from 1996 to 2007 (Angelbratt et al., 2011a), as well as an estimate from surface observations given by IPCC (2007) of 0.26 %/year. This is also comparable to the global trend estimates obtained from satellite-borne instruments, such as 0.22 %/year from the Atmospheric InfraRed Sounder (AIRS) (trend estimated using data from 2003-2013, at 200-750 hPa) (Xiong et al., 2014), as well as 0.2559 ± 0.0080 %/year from the Atmospheric Chemistry Experiment (ACE) FTS (using data from 2004-2020, at 60°S to 60°N, 5.5 to 10.5 km in altitude) (Bernath et al., 2020).

3.7 O_3 Trends

Tropospheric and stratospheric time series of O_3 can be seen in Figures 3.35 and 3.36, respectively. TAO O_3 exhibits a seasonal cycle with a peak in February for both regions of the atmosphere. This can be contrasted with lower troposphere (0-5 km) and surface O_3 in Toronto, which peak in April-June and July, respectively (Whaley et al., 2015).

TAO tropospheric O_3 showed a positive trend of 0.28 ± 0.19 %/year (0.41 ± 0.15 %/year without enhancement events). Stratospheric O_3 did not exhibit a significant trend. The upward tropospheric O_3 trend seen in Toronto can be contrasted

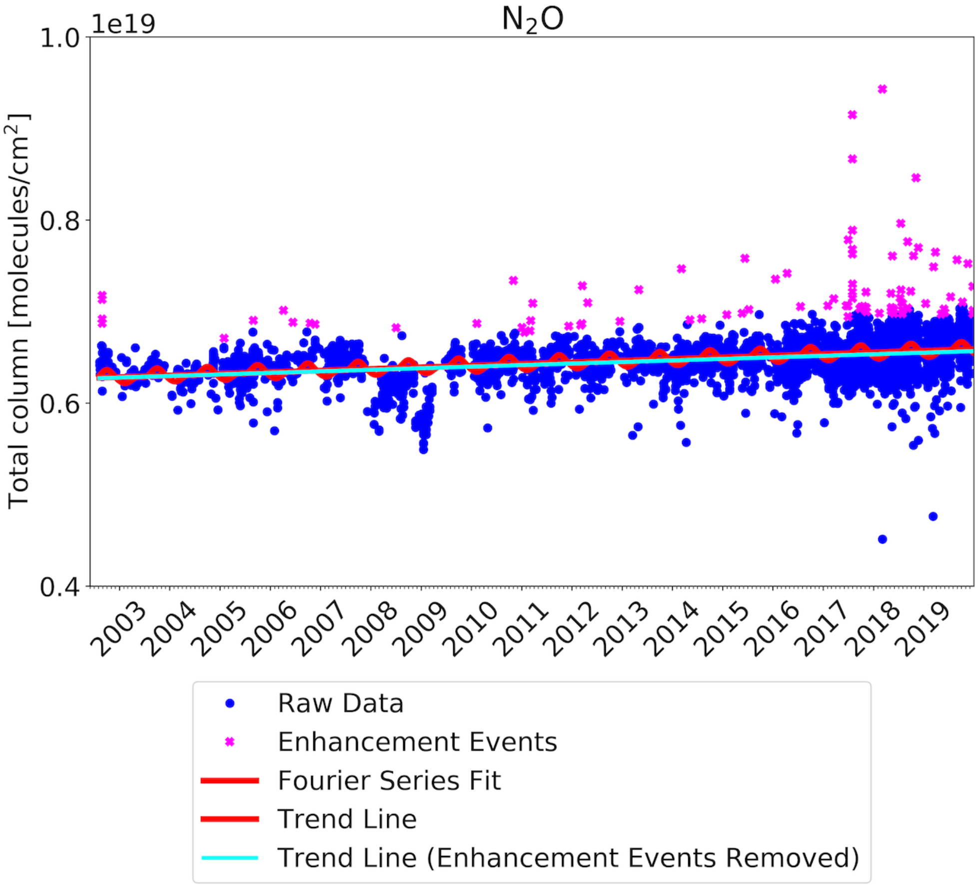

Figure 3.34: Time series and fitted trends of TAO total columns of N_2O.

to findings by Vigouroux et al. (2015), where tropospheric O_3 trends at Harestua, Ny-Ålesund (78.9°N, 11.9°E) and Thule were observed to be -3.1 ± 2.0 %/decade, -5.8 ± 3.2 %/decade and -5.3 ± 4.4 %/decade, respectively. These trends were observed with FTIR measurements from 1995 to 2012 (Harestua and Ny-Ålesund), and 1999 to 2012 (Thule). This may be due to differences in sources, given the urban location of TAO compared to these remote Arctic sites. Gaudel et al. (2018) found no consistent trend in tropospheric column ozone anomalies derived from time series at eight FTIR stations (Jungfraujoch, Izaña, Lauder, Wollongong (34.41°S, 150.88°E), Ny-Ålesund, Thule, Kiruna, and Arrival Heights (77.83°S, 166.67°E)). Whaley et al.

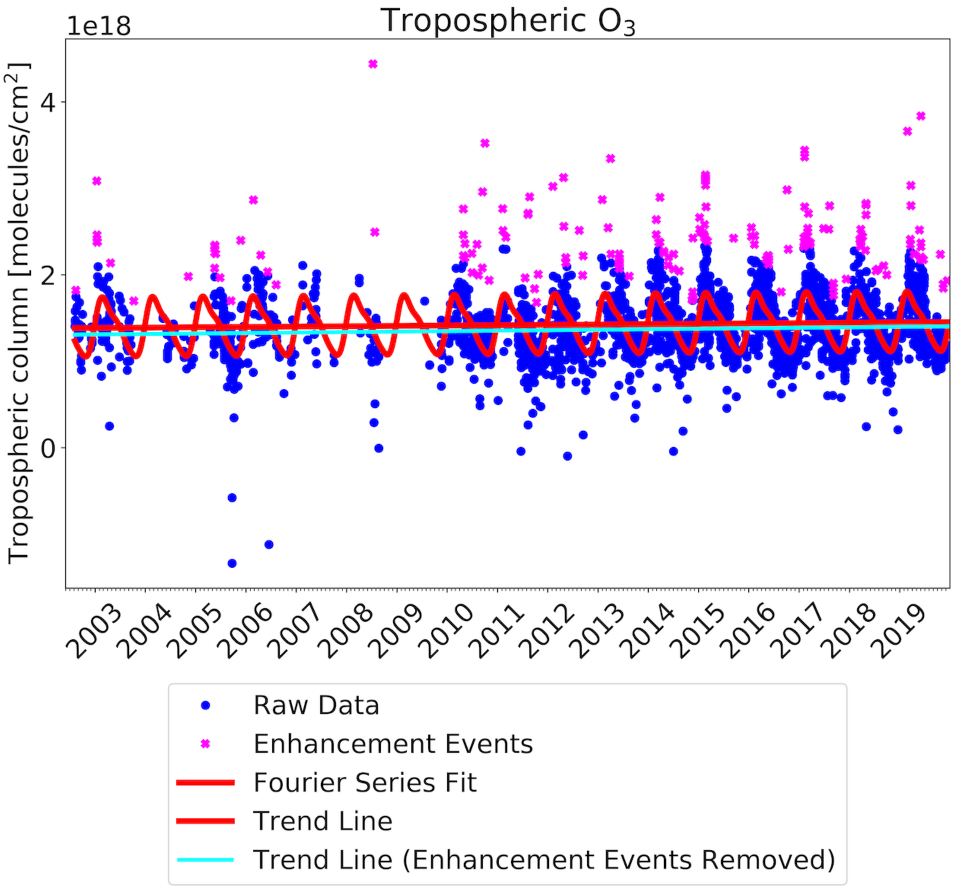

Figure 3.35: Time series and fitted trends of TAO tropospheric (0 to 12 km) column of O_3.

(2015) have shown that TAO lower tropospheric O_3 is highly sensitive to fossil fuel emissions of NO_x.

3.8 Trends of Other Tropospheric Species

Total columns of other gases measured at TAO exhibited statistically robust trends. The exception was CH_3OH, which showed no significant trends, with or without enhancements (see Figure 3.37). This is in agreement with findings by Bernath et al. (2020), who found no significant trends in CH_3OH using global ACE-FTS data. C_2H_2 exhibited (see Figure 3.38) a negative trend at a rate of -1.12 ±

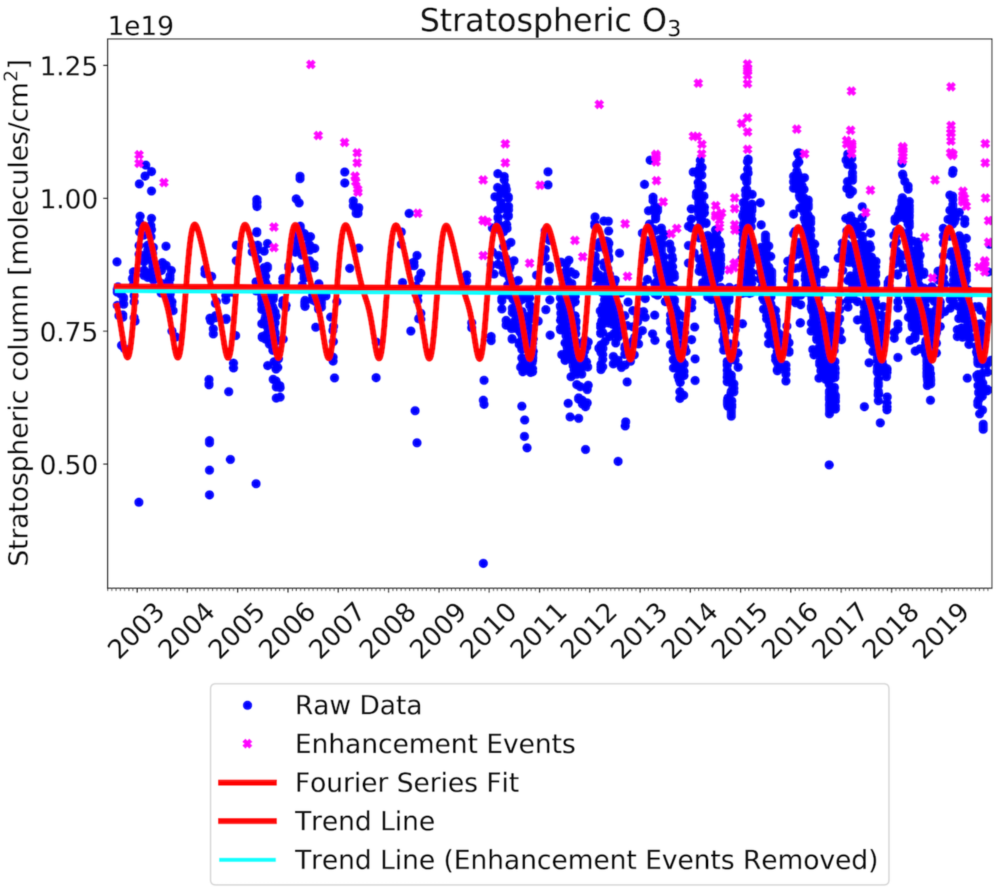

Figure 3.36: Time series and fitted trends of TAO stratospheric (12 to 50 km) column of O_3.

0.30 %/year (−1.21 ± 0.26 %/year without enhancement events), also comparable to −1.29 ± 0.38 %/year given by Bernath et al. (2020) (also with ACE-FTS). HCOOH showed a negative trend of −2.15 ± 0.64 %/year, but after removing enhancement events, the trend was found to be −0.73 ± 0.53 %/year (see Figure 3.39). This is a greater rate of decrease in HCOOH than the global trend estimate of −0.51 ± 0.28 %/year obtained from ACE-FTS (Bernath et al., 2020). HCN also showed a negative trend of −0.51 ± 0.21 %/year (see Figure 3.40), which can be compared with −0.93 ± 0.47 %/year seen at Lauder (Zeng et al., 2012). It should be noted that Lauder is in the Southern Hemisphere, and HCN is too short-lived in the atmosphere to be well-mixed globally. H_2CO showed a statistically significant trend (see Figure 3.41) only after removing enhancements (-0.43 ± 0.25 %/year). Another FTIR study by Lieschke et al. (2019) also observed a negative H_2CO trend using an FTIR at Wollongong, but with a larger magnitude, at -1.9 %/year (2σ confidence interval at -2.2 to -1.7) using data from 1996 to 2015. These can be contrasted with the value calculated by Franco et al. (2016b) of 0.81 ± 0.62 %/year, which was obtained by analyzing FTIR data from 2003 to 2015 at Jungfraujoch, a high-altitude location. NH_3 was found to be increasing at 3.56 ± 0.85 %/year (2.36 ± 0.57 %/year without enhancement events), comparable to 2.61 %/year obtained from AIRS satellite measurements over the USA from 2002 to 2016 (Warner et al., 2017) (see Figure 3.42). TAO NH_3 observations are discussed in more detail in Chapter 5.

3.9 Trends of Other Stratospheric Species

Several stratospheric species exhibited statistically significant trends. For HF, the trend was 0.59 ± 0.11 %/year (and 0.47 ± 0.09 %/year after removing enhancement events) (see Figure 3.43). A previous analysis of FTIR HF columns by Kohlhepp et al. (2012) obtained annual trends of 0.61 ± 0.70 %, -0.04 ± 0.61 %, 1.07 ± 0.28 % and 0.68 ± 0.58 %, over Ny-Ålesund, TAO, Lauder and Arrival Heights, respectively, using data from 2000 to 2009 (2002 to 2009 for TAO; using our methodology yields -0.19 ± 0.41 %/year for this period). The HF trend over Toronto can also be contrasted with ACE-FTS observations, which saw a trend of 0.864 ± 0.047 %/year (from 2004 to 2020) averaged over the globe (Bernath et al.,

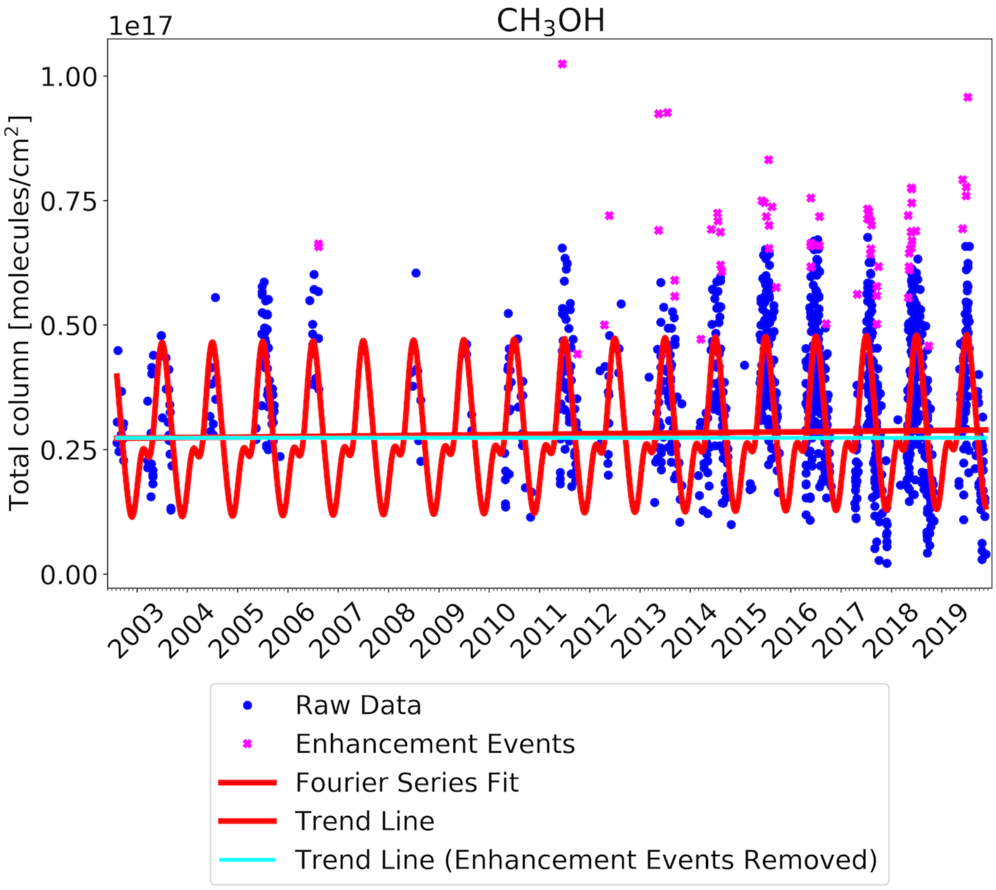

Figure 3.37: Time series and fitted trends of TAO total columns of CH_3OH.

2020). Kohlhepp et al. (2012) suggested that, because fluorine emission is not explicitly restricted, HF total columns are expected to keep increasing.

HCl showed a negative trend of −0.11 ± 0.04 %/year (and −0.07 ± 0.06 %/year after removing enhancement events, see Figure 3.44). This is a smaller magnitude negative trend compared to a previous analysis of TAO HCl by (Kohlhepp et al., 2012), who observed −1.22 ± 0.37 %/year when examining data from 2002 to 2009 (our methodology yields −1.36 ± 0.33 %/year for this period). HNO_3 was found to be increasing at 0.36 ± 0.13 %/year, or 0.43 ± 0.12 %/year after removing enhancement events (see Figure 3.45). This is lower than (although within combined errors of) the global trend from ACE-FTS of 0.60 ± 0.17 %/year (Bernath et al., 2020), and can be contrasted with older FTIR studies, which found no significant trends of HNO_3 (e.g., Rinsland et al., 1991).

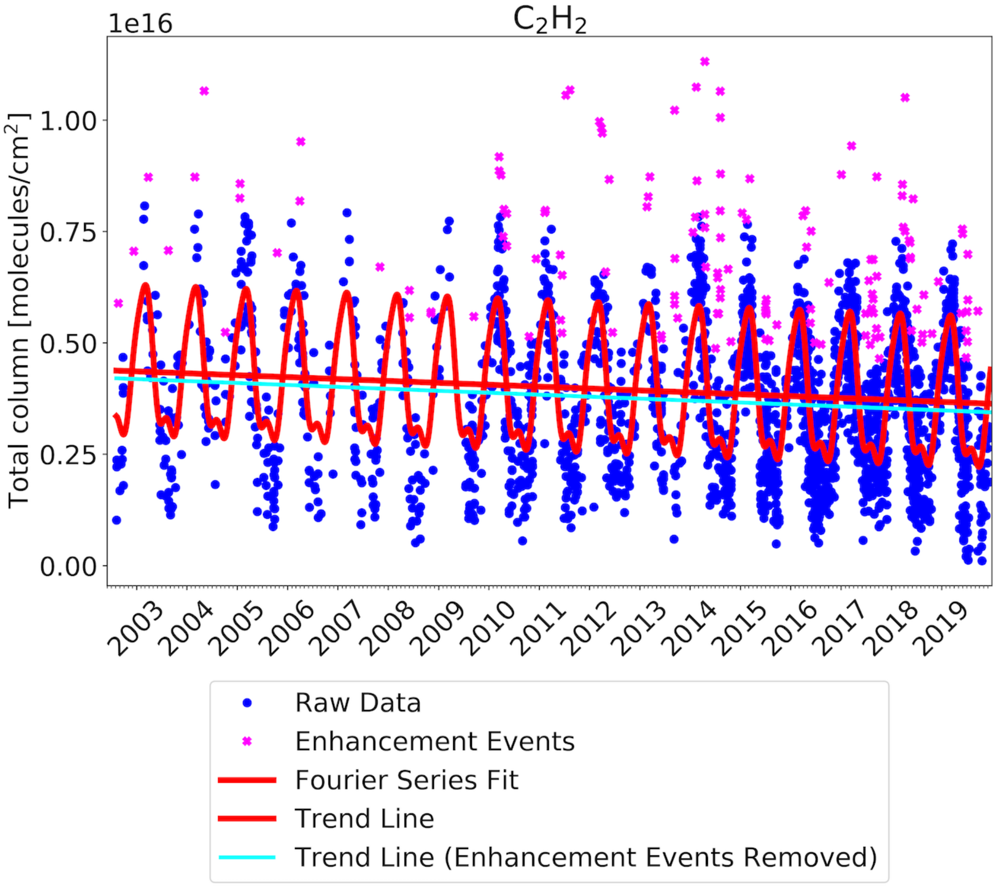

Figure 3.38: Time series and fitted trends of TAO total columns of C_2H_2.

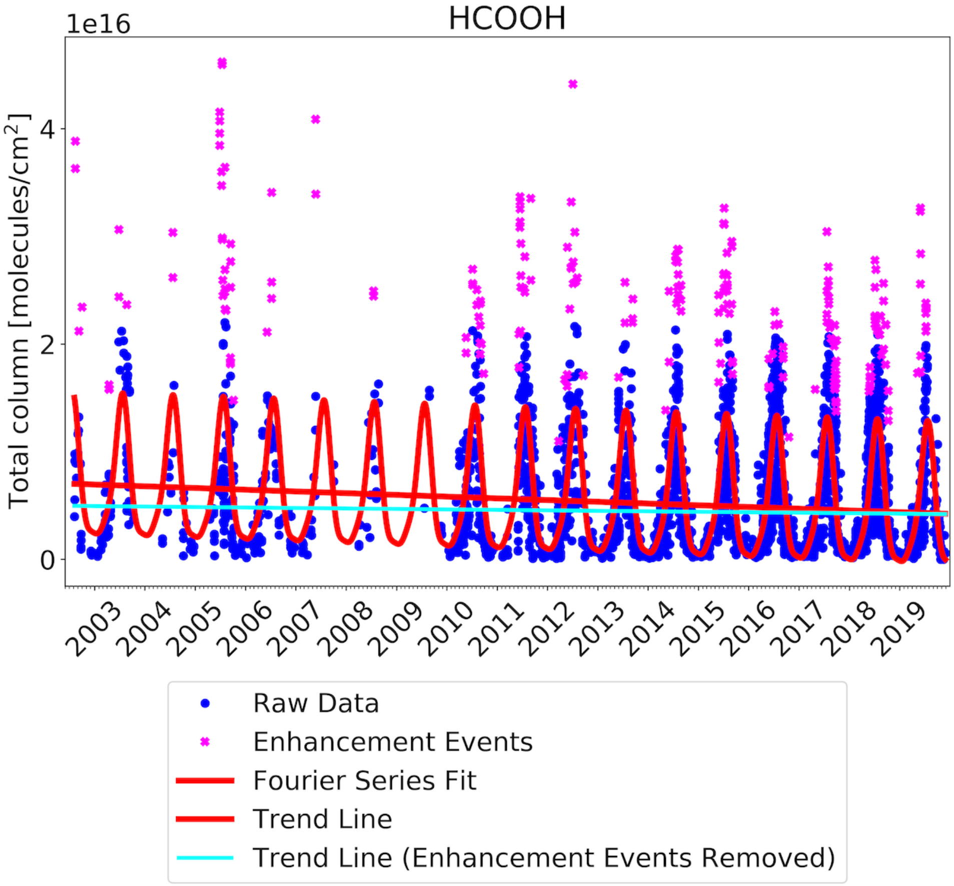

Figure 3.39: Time series and fitted trends of TAO total columns of HCOOH.

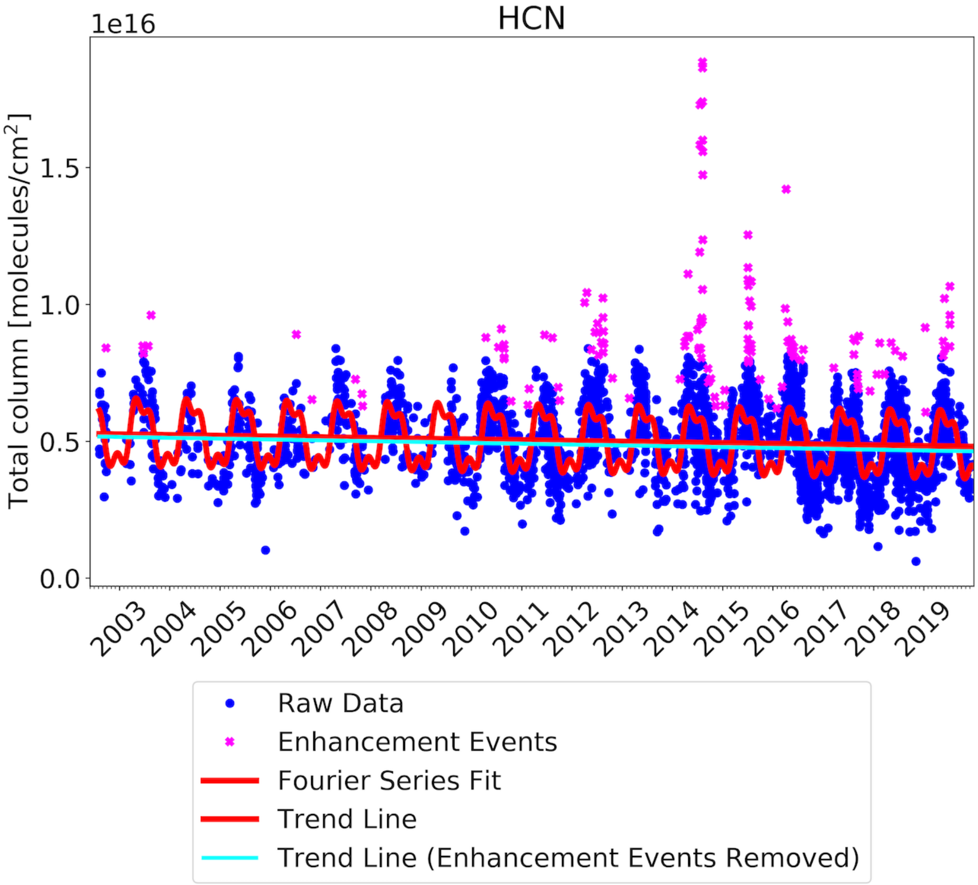

Figure 3.40: Time series and fitted trends of TAO total columns of HCN.

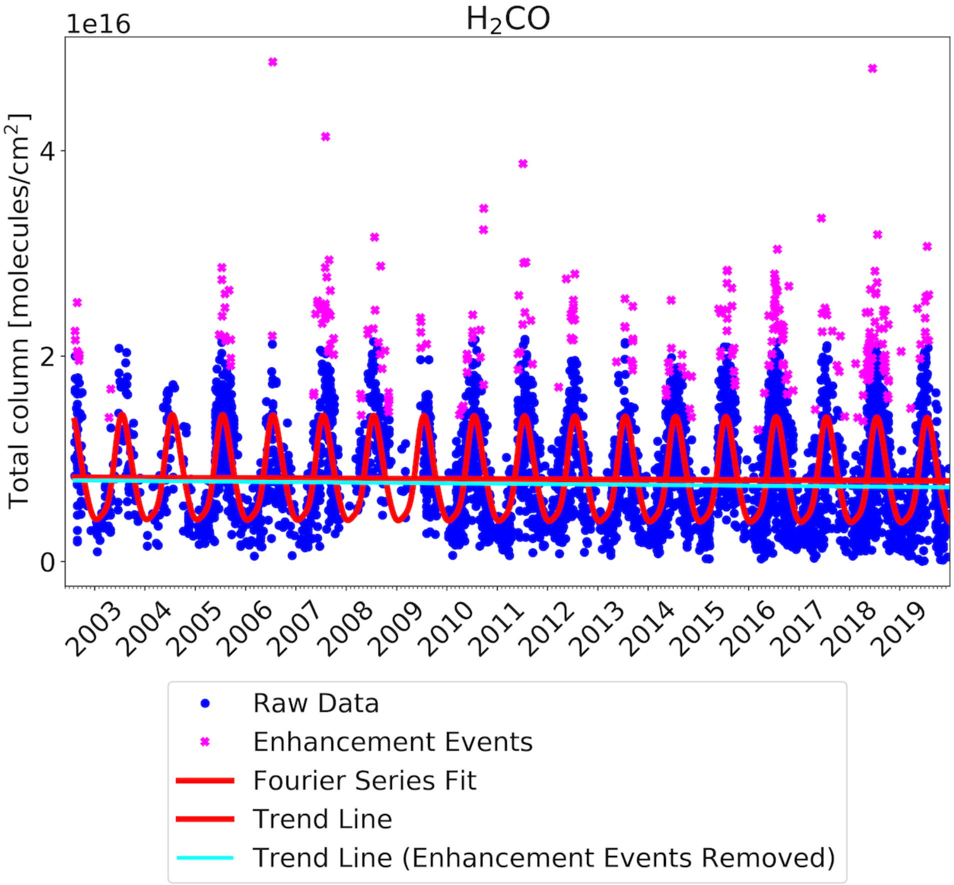

Figure 3.41: Time series and fitted trends of TAO total columns of H_2CO.

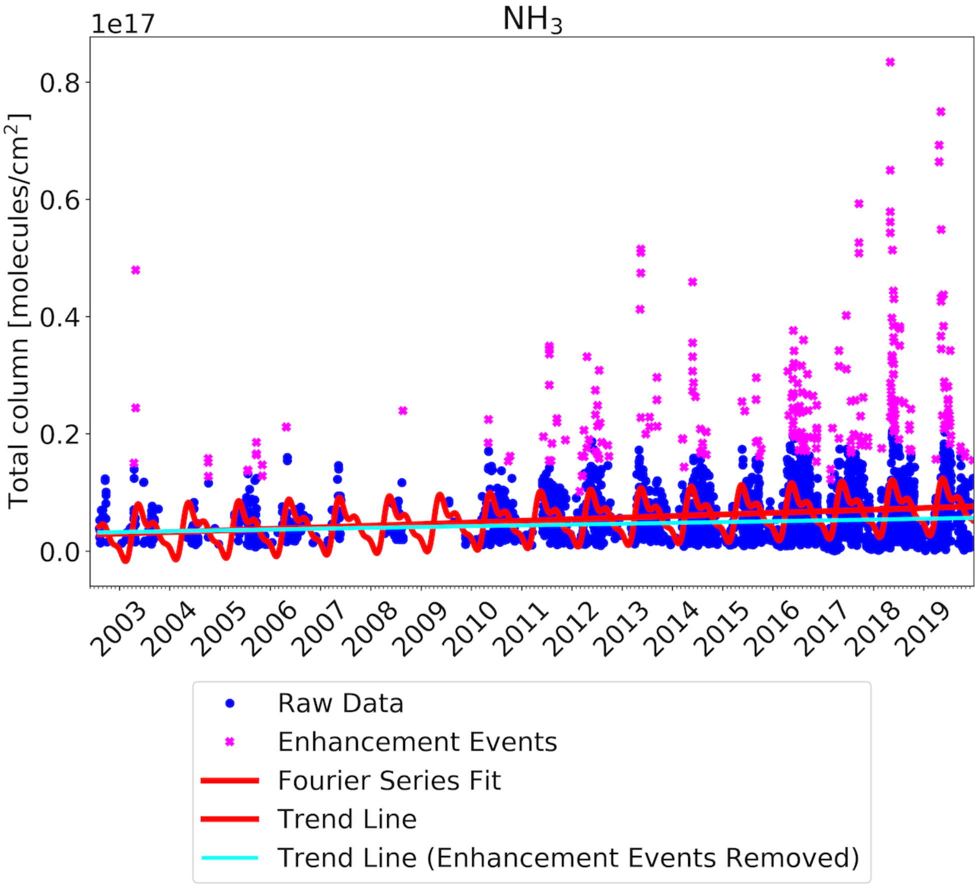

Figure 3.42: Time series and fitted trends of TAO total columns of NH_3.

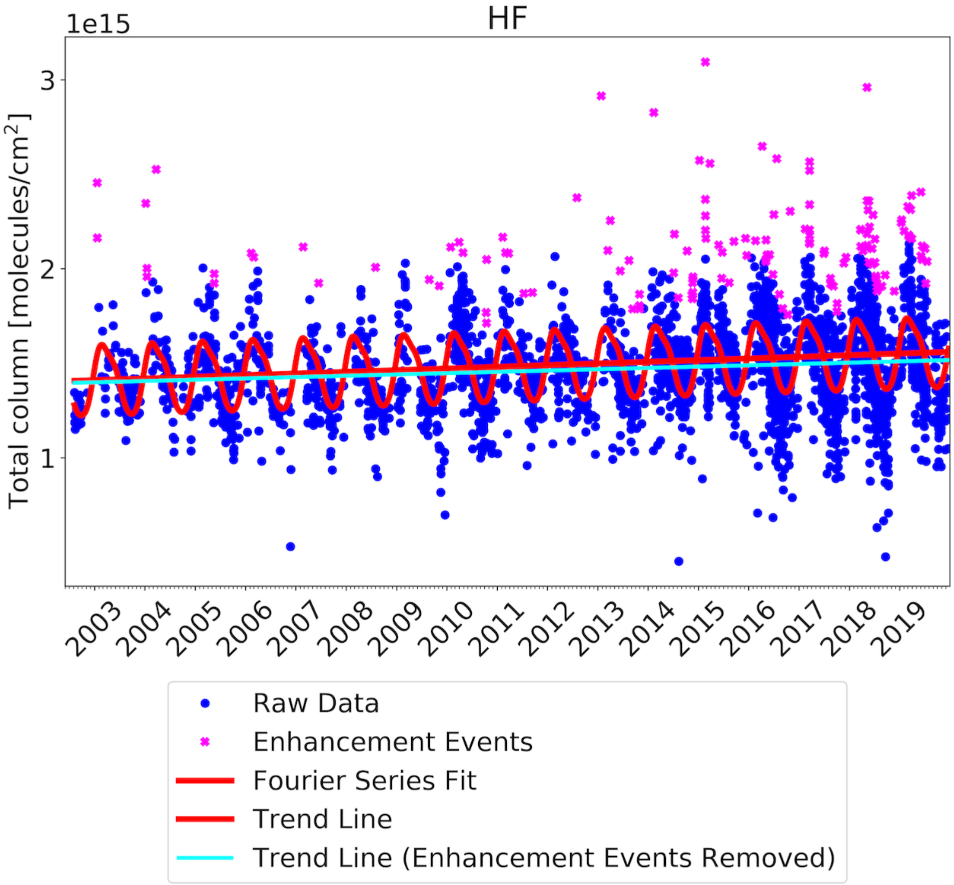

Figure 3.43: Time series and fitted trends of TAO total columns of HF.

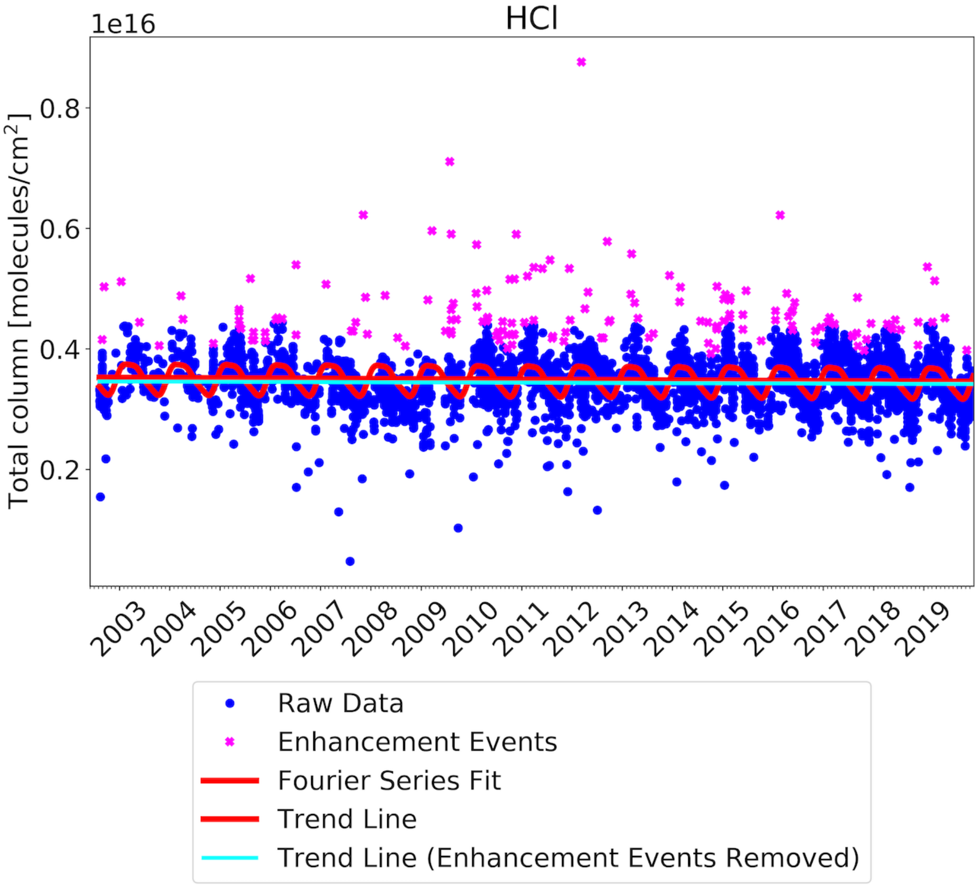

Figure 3.44: Time series and fitted trends of TAO total columns of HCl.

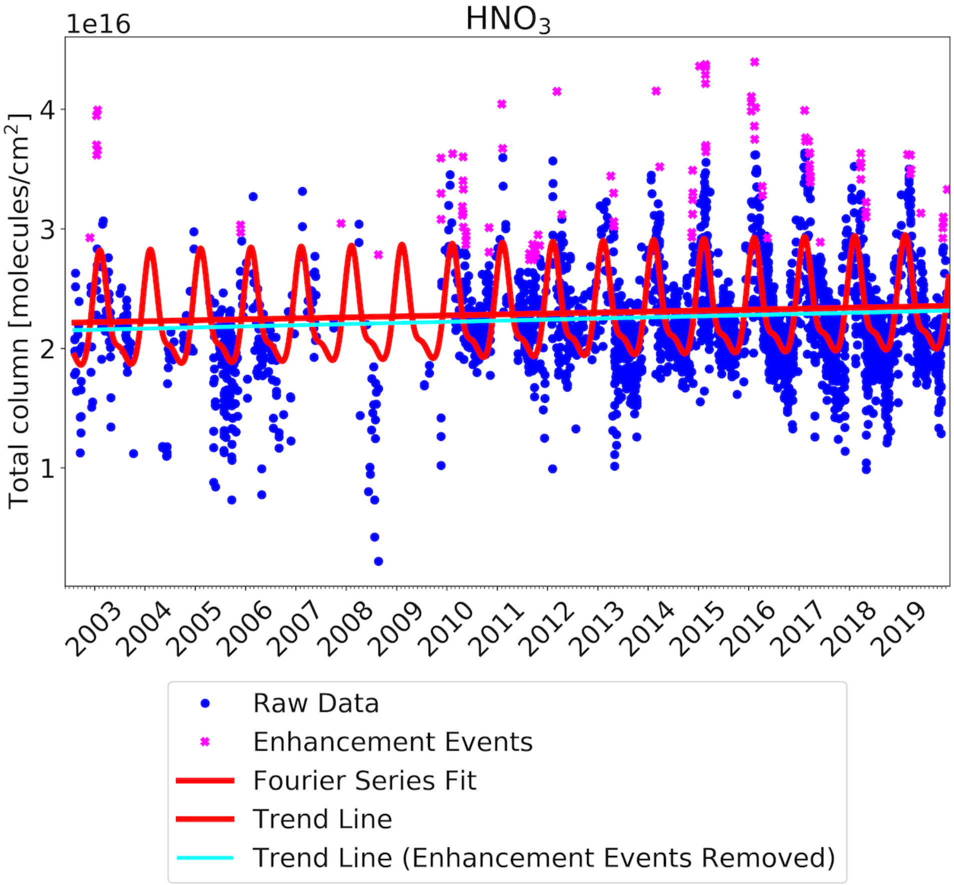

Figure 3.45: Time series and fitted trends of TAO total columns of HNO$_3$.

3.10 Effects of COVID-19 Lockdown on Total Column CO

In late 2019, several cases of respiratory illness were reported in China. The culprit was soon identified to be a strain of coronavirus, with some similarities to the virus responsible for the SARS epidemic in 2002-2004. The virus was named Severe Acute Respiratory Syndrome CoronaVirus 2 (SARS-CoV-2) (van Doremalen et al., 2020), and the disease it brings about, COVID-19. The virus quickly spread and was deemed to be an outbreak by the World Health Organization (WHO) in January 2020 and a pandemic in March 2020 (`https://www.who.int/emergencies/diseases/novel-coronavirus-2019/situation-reports/`, last accessed: April, 2021). The pandemic caused a global social and economic disruption, including a global recession comparable to the Great Depression, according to the International Monetary Fund (`https://blogs.imf.org/2020/04/14/`, last accessed: April, 2021). Over 1 million deaths have been attributed to the virus worldwide, including over 20,000 in Canada (as of February, 2021) (latest updates can be found on a COVID-19 tracking website hosted by Johns Hopkins University: `https://systems.jhu.edu/`, last accessed: April, 2021).

The virus first landed in Canada in 22 January, 2020, and has since had profound social and economic effects. On 16 March, 2020, Prime Minister Justin Trudeau recommended closure of all non-essential services (i.e., all recreation programs, libraries, private schools, daycares, and churches and other faith settings, as well as bars and restaurants, except those that offer takeout or delivery), and in Ontario, a state of emergency was declared a day later, resulting in closures of daycares, bars and restaurants, theaters and private schools (`https://www.canada.ca/coronavirus`, last accessed: April, 2021).

Ontario Premier Doug Ford released a "Framework for Reopening our Province" in late April, which described the gradual lifting of economic restrictions, divided into three "Stages." Stage 1 would allow the reopening of outdoor spaces, and select businesses. Stage 2 would allow for more businesses to reopen, and the limit on the participants would be increased. Stage 3 would further relax the restrictions, aside from restrictions on large public gatherings. The reopening processes began in mid-May. On 24 July, several parts of Ontario (see Figure 3.46 for a map of the regions around Toronto), including Hamilton, the regions of York, Durham, Halton and Niagara as well as the counties of Haldimand, Horfolk and Lambton were permitted to enter Stage 3 of the reopening plan set forth by the province, and a week later on 31 July, Toronto and Peel Region were also permitted to enter Stage 3 (`https://www.ontario.ca/page/reopening-ontario-stages`, last accessed: April, 2021). The pandemic is still ongoing as of April 2021, however, and Premier Ford declared the province to officially be in the "second wave" of the coronavirus pandemic on 28 September, 2020, and by 7 April, 2021, the province was experiencing a "third wave" of the pandemic. The Ontario government implemented additional public health measures ("modified" Stage 2) in Ottawa, Peel, and Toronto on 10 October, 2020, and a province-wide shutdown on 26 December, 2020 (`https://www.ontario.ca/page/covid-19-provincewide-shutdown`, last accessed: April, 2021), followed by a similar Stay-at-Home order on 7 April, 2021 (`https://news.ontario.ca/en/release/61029/ontario-enacts-provincial-emergency-and-stay-at-home-order`, last accessed: April, 2021). Similar preventative measures, often called lockdowns, were

Figure 3.46: Map of the regions around Toronto. Figure taken from Kesik (2015).

taken in many parts of the world.

These lockdowns have had significant effects on air quality. Emissions of NO_x in China were estimated to be down by 36 % from early January to mid-February, with more than 80 % of reductions occurring after their respective lockdown in most provinces (Miyazaki et al., 2020), and average NO_2 columns, measured by space-borne instruments (TROPOMI) decreased by 40% in all Chinese cities (Bauwens et al., 2020). Reduction in surface $PM_{2.5}$, NO_2, CO, and SO_2 concentrations were also observed in northern China, although the reduction in O_3 precursor (NO_x) emissions increased surface O_3 in northern China (Shi and Brasseur, 2020).

Here, we present preliminary findings indicating reduced total columns of CO from the FTIR at TAO during the lockdown. Figure 3.47 shows total column CO observations from 2020 in comparison to 2002-2019. Table 3.2 compares the monthly mean values of CO from 2002-2019 and 2020, as well as the 2020 monthly means extrapolated from 2002-2019 data, using the fit discussed in Section 3.2, which accounts for trends and seasonalities in the data. The lockdown in Ontario (and other parts of Canada) began in March, with some restrictions in Ontario being lifted towards the end of May and July. 2020 monthly averages of CO total columns in April, May and June are more than 1σ lower than the 2002-2019 counterparts (with respect to the 2020 standard deviation). When comparing with the extrapolated 2020 values, the observed mean value for April is more than 1σ lower. It should be noted here that the lifetime of CO is about 1 to 2 months, so reduced emissions may not be immediately evident.

Another point worthy of discussion is the spike in CO in 2020 September. This is likely due to a biomass burning plume traveling over Toronto (see Chapter 4 for discussion on biomass burning enhancement events). An analysis using the FLEXPART Lagrangian dispersion model (v8.2) (Pisso et al., 2019) in its back-trajectory mode, coupled with satellite-based Burned Area Data Product (Giglio et al., 2015) shows that TAO measurements made between 13 and 17 September (peak of the enhancement event) are sensitive to regions with fires, particularrly the large fires in the

Western USA (see Figure 3.48). Details of the source attribution methodology can be found in Section 4.1.1. This enhancement likely led to the high monthly average in CO for September 2020.

Similar analyses were done for NH_3 and tropospheric O_3 (see Figures 3.49, 3.50, and Tables 3.3, 3.4, respectively). NH_3 monthly mean variability is too large for meaningful comparison. The tropospheric O_3 in March and July, 2020 showed a reduction by more than 1σ (with respect to the 2020 standard deviation). Comparisons of the 2020 observations with extrapolated values also show $>1\sigma$ reductions in March and July. This is consistent with findings by Steinbrecht et al. (2021), who observed a 7 % reduction in northern extratropical free tropospheric (1 to 8 km) O_3 in late spring to summer of 2020, using multiple sites and instruments, including TAO FTIR. The analysis of TAO O_3 presented in this thesis was done with the tropospheric (0 to 12 km) column, and resulted in 10.8 % reduction when comparing the mean columns for January to October of 2002-2019 and 2020 data.

The effects of COVID-19 lockdowns are still under investigation in many parts of the world, and the data from TAO provide an urban dataset. The preliminary results shown here can be expanded upon to shed insight into the effects of the lockdown on urban air quality.

Table 3.2: Comparison of 2002-2019 and 2020 monthly mean (1σ in parenthesis) TAO FTIR CO total columns, and 2020 monthly mean extrapolated from 2002-2019 data (using the fit discussed in Section 3.2). Note the enhancement in September, 2020, which was likely due to a biomass burning plume.

Month	2002-2019 Mean Columns ($\times 10^{18}$ molecules/cm^2)	2020 Mean Columns ($\times 10^{18}$ molecules/cm^2)	2020 Extrapolated Mean Columns ($\times 10^{18}$ molecules/cm^2)
January	2.08 (0.20)	1.94 (0.12)	1.96
February	2.18 (0.18)	2.10 (0.24)	2.04
March	2.30 (0.28)	2.15 (0.10)	2.18
April	2.32 (0.19)	2.07 (0.10)	2.20
May	2.18 (0.19)	2.05 (0.12)	2.03
June	1.95 (0.23)	1.81 (0.14)	1.88
July	2.01 (0.30)	1.80 (0.12)	1.89
August	2.04 (0.34)	1.80 (0.16)	1.89
September	1.87 (0.24)	2.17 (0.45)	1.76
October	1.81 (0.14)	1.95 (0.17)	1.67

Table 3.3: Comparison of 2002-2019 and 2020 monthly mean (1σ in parenthesis) TAO FTIR NH_3 total columns, and 2020 monthly mean extrapolated from 2002-2019 data (using the fit discussed in Section 3.2).

Month	2002-2019 Mean Columns ($\times 10^{15}$ molecules/cm^2)	2020 Mean Columns ($\times 10^{15}$ molecules/cm^2)	2020 Extrapolated Mean Columns ($\times 10^{15}$ molecules/cm^2)
January	1.99 (1.73)	1.43 (1.14)	4.13
February	3.74 (3.61)	3.28 (2.98)	3.08
March	3.98 (3.95)	3.94 (4.92)	5.31
April	6.86 (8.65)	8.59 (9.85)	10.06
May	13.74 (12.34)	12.03 (10.17)	12.48
June	7.63 (5.80)	11.87 (9.48)	10.98
July	8.58 (6.30)	11.40 (7.92)	9.20
August	6.89 (4.89)	8.42 (6.71)	9.31
September	7.86 (6.82)	9.66 (9.25)	9.15
October	5.74 (4.36)	7.15 (9.86)	7.51

Table 3.4: Comparison of 2002-2019 and 2020 monthly mean (1σ in parenthesis) TAO FTIR O_3 tropospheric columns, and 2020 monthly mean extrapolated from 2002-2019 data (using the fit discussed in Section 3.2).

Month	2002-2019 Mean Columns ($\times 10^{18}$ molecules/cm^2)	2020 Mean Columns ($\times 10^{18}$ molecules/cm^2)	2020 Extrapolated Mean Columns ($\times 10^{18}$ molecules/cm^2)
January	1.62 (0.43)	1.47 (0.37)	1.64
February	1.85 (0.56)	1.41 (0.37)	1.80
March	1.71 (0.40)	1.37 (0.22)	1.76
April	1.62 (0.35)	1.61 (0.23)	1.66
May	1.56 (0.28)	1.42 (0.20)	1.58
June	1.49 (0.33)	1.37 (0.22)	1.51
July	1.35 (0.28)	1.20 (0.12)	1.39
August	1.27 (0.29)	1.13 (0.23)	1.28
September	1.14 (0.29)	1.06 (0.22)	1.19
October	1.13 (0.30)	1.04 (0.12)	1.13

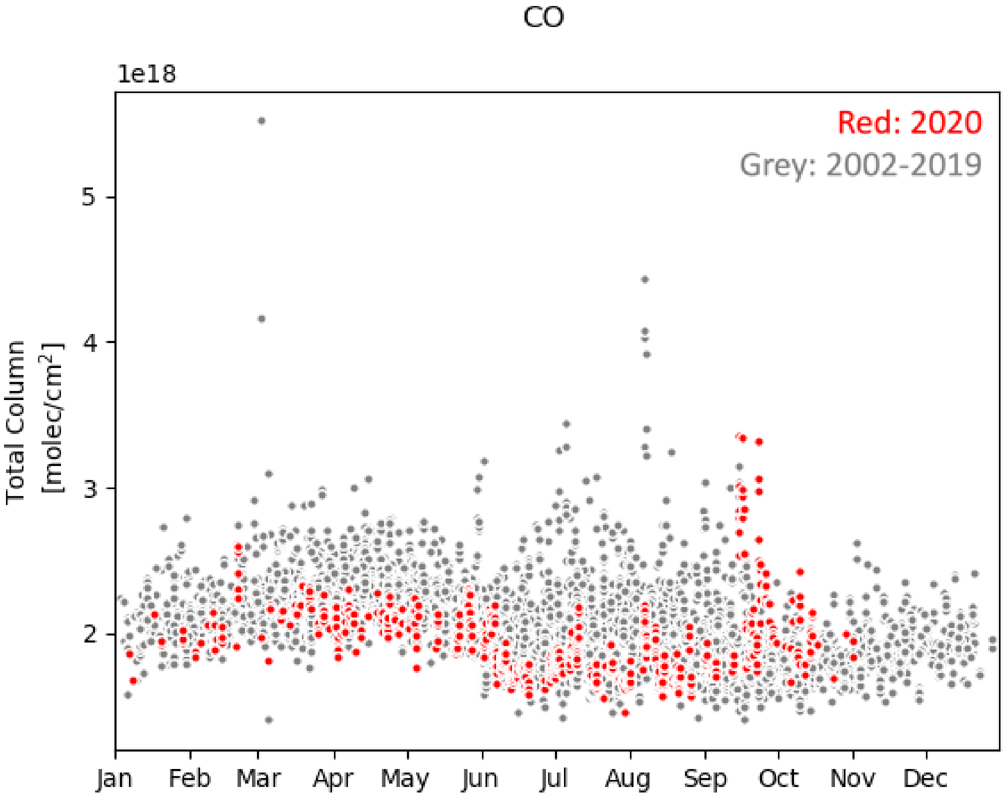

Figure 3.47: TAO CO total columns from 2002 to 2020 October. Data from 2002 to 2019 are shown as grey points and 2020 are shown by red points. Note the spike in CO in September, 2020; this may be a biomass burning enhancement event.

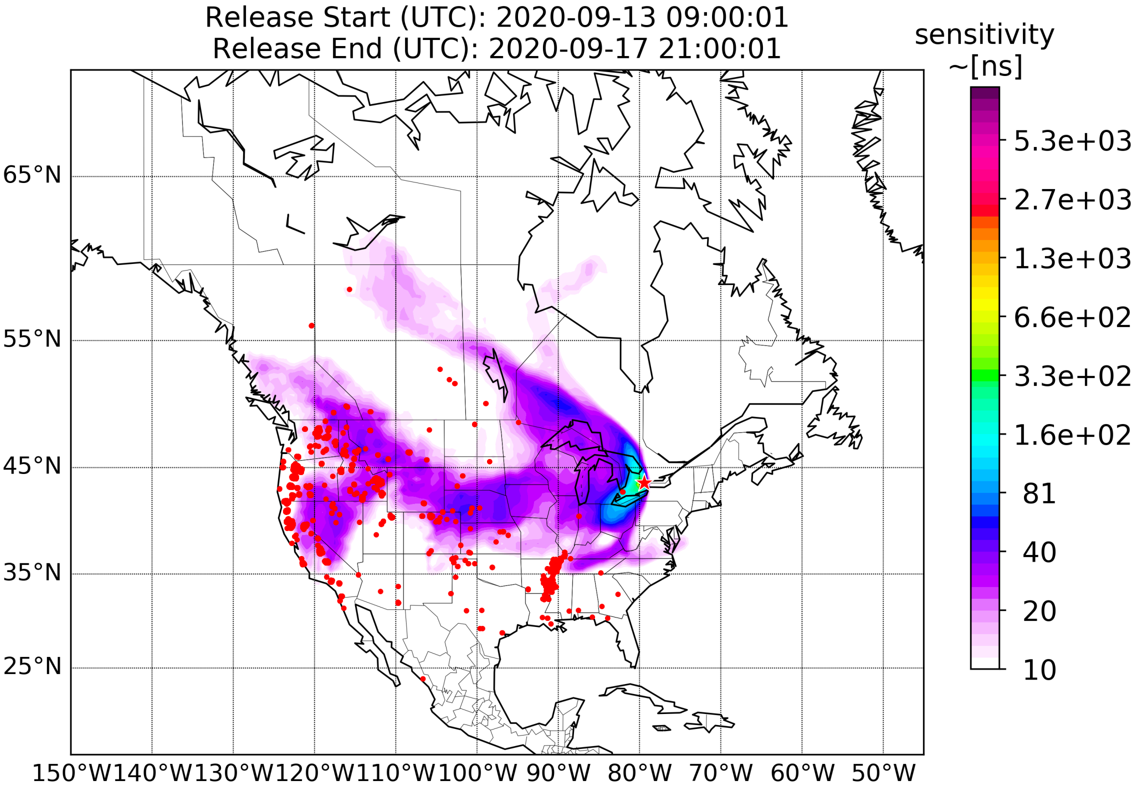

Figure 3.48: FLEXPART seven-day back-trajectory sensitivity plot for the CO enhancement event in September 2020. Particles were released between 13 and 17 September. The red points indicate fires from the Moderate Resolution Imaging Spectroradiometer (MODIS) Burned Area Data Product. Details of the model can be found in Section 4.1.1.

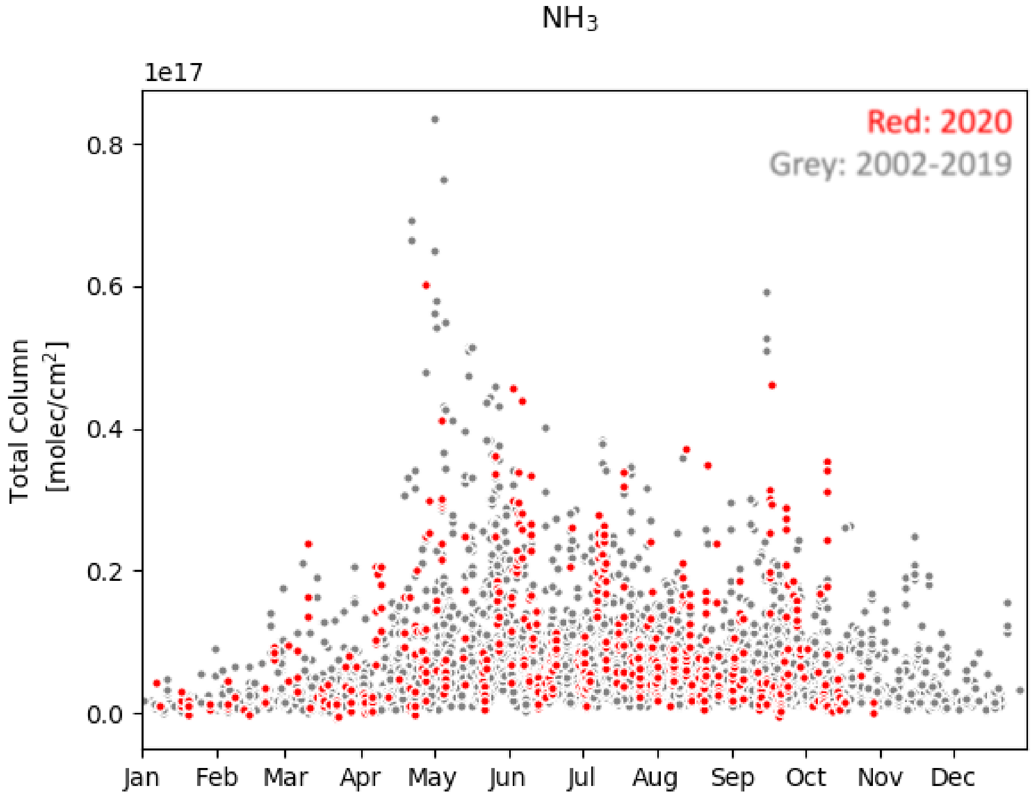

Figure 3.49: TAO NH_3 total columns from 2002 to 2020 October. Data from 2002 to 2019 are shown as grey points and 2020 are shown by red points.

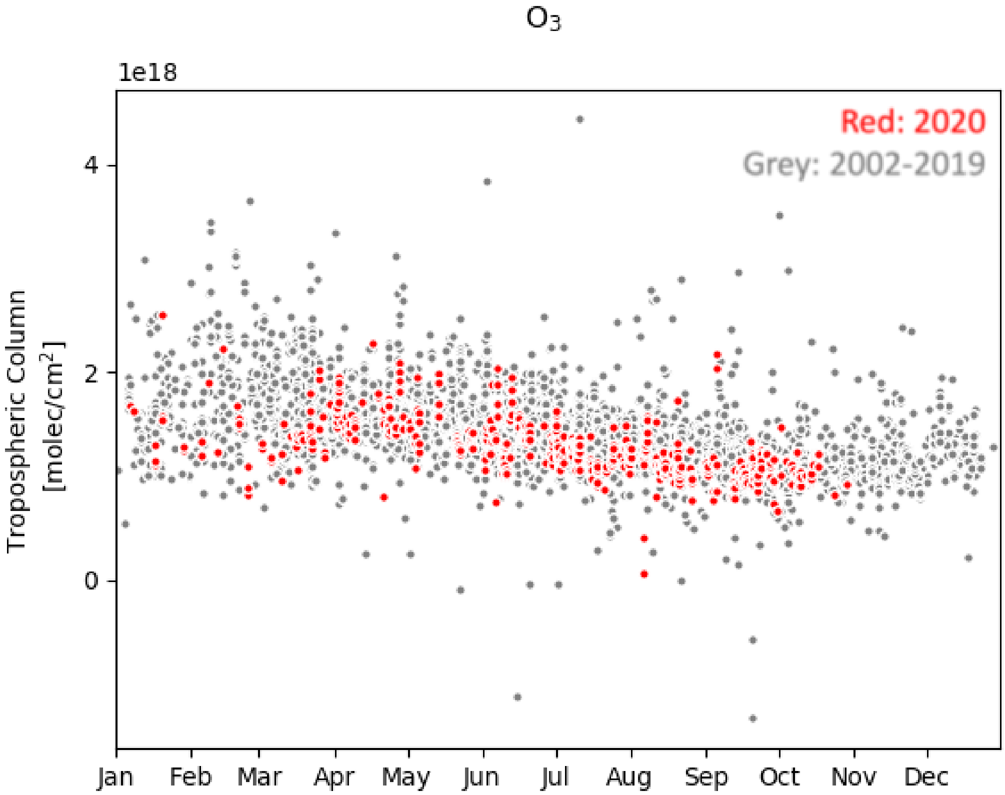

Figure 3.50: TAO O$_3$ tropospheric columns from 2002 to 2020 October. Data from 2002 to 2019 are shown as grey points and 2020 are shown by red points.

3.11 Conclusions

In this study, trends of a suite of trace gases were examined, using 18 years of TAO FTIR column data. All species that are archived to NDACC were analyzed.

TAO CH_4 was seen to have an upward trend of 0.41 ± 0.03 %/year and 0.38 ± 0.02 %/year after 2009, with and without enhancement events, compared to 0.26 ± 0.10 %/year (0.24 ± 0.07 %/year after removing enhancement events) for 2002 to 2008. The GEOS-Chem tagged CH_4 run shows the largest contributor to CH_4 over Toronto to be wetland emissions, with an average relative contribution of 31.7 ± 0.5 %. A similar analysis of C_2H_6 showed a negative trend from 2002 to 2008, at a rate of −0.74 ± 0.73 (−1.31 ± 0.61 %/year without enhancement events), followed by a positive trend of 1.19 ± 0.27 %/year (no enhancement data: 0.94 ± 0.20 %/year) from 2009 to 2019.

TAO CO was found to be decreasing at a rate of −0.90 ± 0.07 %/year. The GEOS-Chem tagged CO simulation showed that contributions from Asian fossil fuel sources increased, while that from North America decreased, at rates of 0.37 ± 0.08 and −2.64 ± 0.18 %/year, respectively. North American biomass burning contributions showed a positive trend of 1.56 ± 0.47 %/year.

N_2O over TAO also showed a robust trend, increasing at 0.28 ± 0.02 %/year (0.26 ± 0.02 %/year without enhancement events). Tropospheric O_3 columns (0-12 km) exhibited a trend of 0.28 ± 0.19 %/year (0.41 ± 0.15 %/year without enhancement events), while the stratospheric column (12-50 km) showed no statistically significant trend (−0.05 ± 0.07 %/year). Bootstrap reanalysis resulted in statistically robust trends for most species, with the exception of CH_3OH and H_2CO.

Chapter 4

Biomass Burning Enhancements at TAO

This chapter examines enhancements in total columns of several biomass burning species due to the transport of wildfire plumes over Toronto. The results and discussion in this chapter are based on a paper published in Journal of Geophysical Research: Atmospheres (Yamanouchi et al., 2020). Several biomass burning enhancement events were observed at TAO between 2002 and 2018, which are marked by simultaneous increases in the total columns of CO, HCN, and C_2H_6. Three enhancement episodes, observed in 2012, 2015, and 2017, were examined and the measured columns were used to derive emission ratios and emission factors. In all three events, simultaneous enhancements of CO, HCN, and C_2H_6 were observed, with total column measurements being at, or greater than, two standard deviations above the monthly mean. The 2015 and 2017 episodes also showed enhancements of HCOOH and CH_3OH, and the possibility of these enhancements being caused by biomass burning is discussed.

4.1 Biomass Burning Analysis Methodology

The TAO FTIR time series spanning 2002 to 2018 was analyzed for simultaneous enhancements of CO, HCN, and C_2H_6. Enhancement was defined as a total column more than 2σ above the monthly average (over all years). After an enhancement episode was found, the enhancement ratio (EnhR) was calculated for each of the gases excluding CO. The enhancement ratio can be used to quantify biomass burning emissions by comparing enhancements relative to CO in fire-affected observations, and is calculated as the slope of the linear fit between the total column of the species of interest and the CO total column. The unified least squares method described by York et al. (2004) was used to determine linear regressions in this study (following Lutsch et al., 2016). This method accounts for both the x-coordinate (abscissa) and y-coordinate (ordinal) errors (York et al., 2004). For this correlation, only measurements occurring within 3 h of a CO measurement were considered.

After obtaining the enhancement ratio, the emission ratio (ER) was calculated by applying a plume-aging correction to the enhancement ratio. This is necessary because measurements made at TAO are downwind of the fires and thus the observed smoke plumes have experienced aging, leading to some loss of each species. In this study, plume aging is estimated assuming a first-order exponential decay of each species (e.g., Viatte et al., 2015; Lutsch et al., 2016). The emission ratio is thus derived using:

$$\mathrm{ER_X} = \mathrm{EnhR_X} \cdot \frac{\exp\left(\frac{t}{\tau_\mathrm{X}}\right)}{\exp\left(\frac{t}{\tau_\mathrm{CO}}\right)}, \tag{4.1}$$

where τ_{X} and τ_{CO} are the lifetimes (e-folding time) of the species of interest and CO, respectively, and t is the estimated travel time (method for estimating travel time is discussed in Section 4.1.1). The lifetimes used in this study are listed in Table 4.1. The lifetimes of CO, HCN, C_2H_6, HCOOH, and CH_3OH were obtained from Müller and Brasseur (1995), Li et al. (2003), Xiao et al. (2008), Paulot et al. (2011) and Jacob et al. (2005), respectively. These values were used in similar biomass burning analyses by Viatte et al. (2013, 2014). Two additional CO and HCN lifetime estimates given by Viatte et al. (2015) and used by Lutsch et al. (2016) were also included in this study, to examine how shorter estimates on CO lifetime affect results. The emission factor (EF) is then calculated using the following:

$$\mathrm{EF}_{\mathrm{X}} = \mathrm{EF}_{\mathrm{CO}} \cdot \mathrm{ER}_{\mathrm{X}} \cdot \left(\frac{\mathrm{MW}_{\mathrm{X}}}{\mathrm{MW}_{\mathrm{CO}}} \right), \tag{4.2}$$

where MW_{X} and $\mathrm{MW}_{\mathrm{CO}}$ are the molecular weights of species X and CO respectively, and $\mathrm{EF}_{\mathrm{CO}}$ is the emission factor of CO, which is taken from the literature. In this study, $\mathrm{EF}_{\mathrm{CO}}$ was taken to be 127 ± 45 g/kg and 89 ± 32 g/kg for boreal and temperate forest, respectively (Akagi et al., 2011).

It should also be noted that this method of determining enhancement ratios (also sometimes referred to as normalized excess mixing ratios) has some limitations. Gases can be byproducts of reactions during transport, which this method does not account for. Additionally, in the case where the plume from the wildfire region encounters and mixes with ambient air that has different trace gas concentrations for whatever reason (e.g., different underlying ecosystem or anthropogenic emissions), this mixing will affect the enhancement ratio and may lead to erroneous results (Yokelson et al.,

Table 4.1: Lifetimes used in this study to calculate emission ratios.

Species	Lifetimes
CO	30 days[1], 61 days[2]
HCN	75 days[1], 150 days[3]
C_2H_6	45 days[4]
CH_3OH	7.5 days[5]
HCOOH	4 days[6]

[1] Viatte et al. (2015)
[2] Müller and Brasseur (1995)
[3] Li et al. (2003)
[4] Xiao et al. (2008)
[5] Jacob et al. (2005)
[6] Paulot et al. (2011)

2013). This mixing effect can potentially become problematic for plumes that have aged for one or more days (Yokelson et al., 2013), and may introduce uncertainty when comparing emission ratios derived from different plume-aged enhancement ratios (Andreae and Merlet, 2001; Akagi et al., 2011; Yokelson et al., 2013).

4.1.1 Models Used for Source Attribution

Three models were used in this study for source attribution and travel time estimation. The primary model used for source attribution was the FLEXPART Lagrangian dispersion model (v8.2) (Pisso et al., 2019). The model was set up to release an ensemble of 160,000 tracer particles in a 0.5° by 0.5° grid box centered around TAO from the surface to 12 km over 8 hours and was run backwards in time. Runs were performed for seven days using meteorological data from the NCEP Climate Forecast System (CFS v.2) 6-hour product (Saha et al., 2011). FLEXPART outputs the sensitivity of TAO measurements to various regions, which is calculated from the residence time of the tracer particles. This sensitivity plot was combined with the Moderate Resolution Imaging Spectroradiometer (MODIS) Burned Area Data Product (Giglio et al., 2015) to assess whether regions of sensitivity coincided with wildfire locations.

The age of the wildfire plume at the time of observation, i.e., the travel time in Equation 4.1, was calculated using the HYbrid Single-Particle Lagrangian Integrated Trajectory (HYSPLIT) back-trajectory model (Stein et al., 2015). For each enhancement event, HYSPLIT was run backwards in time for three trajectory altitudes ranging from 3 km to 10 km. Care was taken, by adjusting the release times and altitudes, to ensure that HYSPLIT back-trajectories led to the same area as indicated by FLEXPART and MODIS (following e.g., Viatte et al., 2013; Lutsch et al., 2016).

The GEOS-Chem (v.12.1.1) CTM tagged CO simulation was also used in this study, to interpret the FTIR data, and to analyze emission sources (Lutsch et al., 2020). This is the same tagged CO run as that used to interpret the trend of TAO CO time series, as discussed in Chapter 3.

4.2 Annual Cycles of Relevant Gases

CO exhibits an annual cycle with smaller total columns during summer and fall (see Figure 3.19), due to higher concentrations of OH, which reacts with CO. The primary sources of CO include fossil fuel combustion and oxidation of VOCs as well as CH_4. The primary sink is oxidation by OH (Jacob, 1999). Notably, there is a strong enhancement in August 2014, which was due to wildfire emissions as discussed in Lutsch et al. (2016). HCN also shows an annual cycle, with a peak in May (see Figure 3.22). Additionally, the HCN time series shows large standard deviations in July and August, most likely due to biomass burning enhancements that can skew the means. The main sink of HCN is reaction with OH and O(^{1}D) as well as ocean uptake, while its primary source is biomass burning, with minor sources from industrial activities and biofuel (Lobert et al., 1990; Li et al., 2009), and vegetation and fungal activity, which increase in spring (Cicerone and Zellner, 1983). C_2H_6 shows a strong annual cycle, with a minimum in the summer months due to higher OH concentrations (see Figure 3.16). C_2H_6 sources include natural gas production, and it has been suggested that C_2H_6 levels are on the rise due to the recent increase in oil and gas production activity in North America (Franco et al., 2016a; Helmig et al., 2016). The main sink of C_2H_6 is OH oxidation.

CH_3OH has a peak in July due to higher biogenic emissions in the spring and summer months (see Figure 3.18). This is consistent with CH_3OH observations and modeling results discussed by Wells et al. (2012). CH_3OH is a major source of CO and H_2CO, and is one of the most abundant organic gases found in the atmosphere, second only to CH_4 (Jacob et al., 2005). Major sources include emissions during plant growth, but it is also emitted from biomass burning. The principal sinks include OH oxidation, followed by dry deposition (Jacob et al., 2005). The CH_3OH total column at TAO, with a mean (over the entire time series) of 3.74×10^{16} molecules/cm^2, is much higher than CH_3OH columns obtained by FTIR measurements at Wollongong (Southern Hemisphere mid-latitudes), where the background CH_3OH was found to be 0.8×10^{16} molecules/cm^2 (Paton-Walsh et al., 2008), and Eureka (High Arctic), where the mean was 1.49 × 10^{16} molecules/cm^2 (Viatte et al., 2014). However, it should be noted that as the majority of measurements at TAO were made in the summer months, the mean is skewed to the higher values.

HCOOH also peaks in the summer, which is most likely due to increased biogenic emissions and increased photo-oxidation of VOCs and non-methane hydrocarbons (NMHCs), which are the primary sources of HCOOH (see Figure 3.23). It should be noted that, despite recent advancements made in atmospheric modeling and satellite measurements, large uncertainties remain regarding HCOOH sources and sinks (Stavrakou et al., 2012; Link et al., 2020). The mean HCOOH total column (over the entire time series) at TAO was 7.53 × 10^{15} molecules/cm^2, which is higher than other ground-based FTIR measurements (e.g., 1.94 × 10^{15} molecules/cm^2 at Eureka in Viatte et al. (2014)).

4.3 Biomass Burning Events

Simultaneous enhancements of two or all three of the three tracer species (CO, HCN, and C_2H_6) were identified on several occasions. The events analyzed in detail in this study were: 13-20 August 2012, 1-14 July 2015, and 4-18 September 2017. These enhancements can be seen in Figures 4.1, 4.2, and 4.3. The plots of the events in August, shown in Figure 4.1, do not include 2014 data, as the extreme enhancement event that occurred in August 2014 skewed the mean and standard deviation. This event was described by Lutsch et al. (2016). The total column monthly averages of CO, HCN, C_2H_6, HCOOH, and CH_3OH for July, August, and September over the entire time series are shown in Table 4.2.

Table 4.2: July, August, and September total column monthly averages (2002-2019) of CO, HCN, C_2H_6, CH_3OH, and HCOOH. Units are molecules/cm^2.

Species	July	August	September
CO	2.01×10^{18}	2.04×10^{18}	1.87×10^{18}
HCN	5.80×10^{15}	5.88×10^{15}	4.50×10^{15}
C_2H_6	1.72×10^{16}	1.55×10^{16}	1.70×10^{16}
CH_3OH	4.64×10^{16}	3.80×10^{16}	2.90×10^{16}
HCOOH	1.38×10^{16}	1.23×10^{16}	7.28×10^{15}

The enhancement ratios corresponding to each of the three episodes were calculated from the correlation plots shown in Figures 4.4, 4.5, and 4.6. For the 2015 and 2017 events, CH_3OH and HCOOH were enhanced simultaneously, and the possibility of the enhancements resulting from biomass burning were investigated. However, these species have other sources and can be chemically produced during transport, and thus will likely lead to large biases (see Section 4.5 for more discussion). The measurements during the fire-affected periods are indicated by colors representing dates. At least ten data points were required for each of the linear fits shown in these correlation plots. For the 2012 event, both HCN and C_2H_6 were enhanced with respect to CO, with the correlation coefficient (R) being 0.81 and 0.55 respectively. The lower correlation for C_2H_6 is likely due to it having more sources, including local sources given the urban location of TAO. Similar results were seen in a study by Lutsch et al. (2016), which examined 2014 biomass burning enhancements from FTIR observations at TAO as well as Eureka, which is a remote, high-latitude site (80.05°N, 86.42°W) with few local sources. Given this, enhancements of C_2H_6 were more evident in the Eureka time series than in that of TAO (Lutsch et al., 2016). The 2012 enhancement

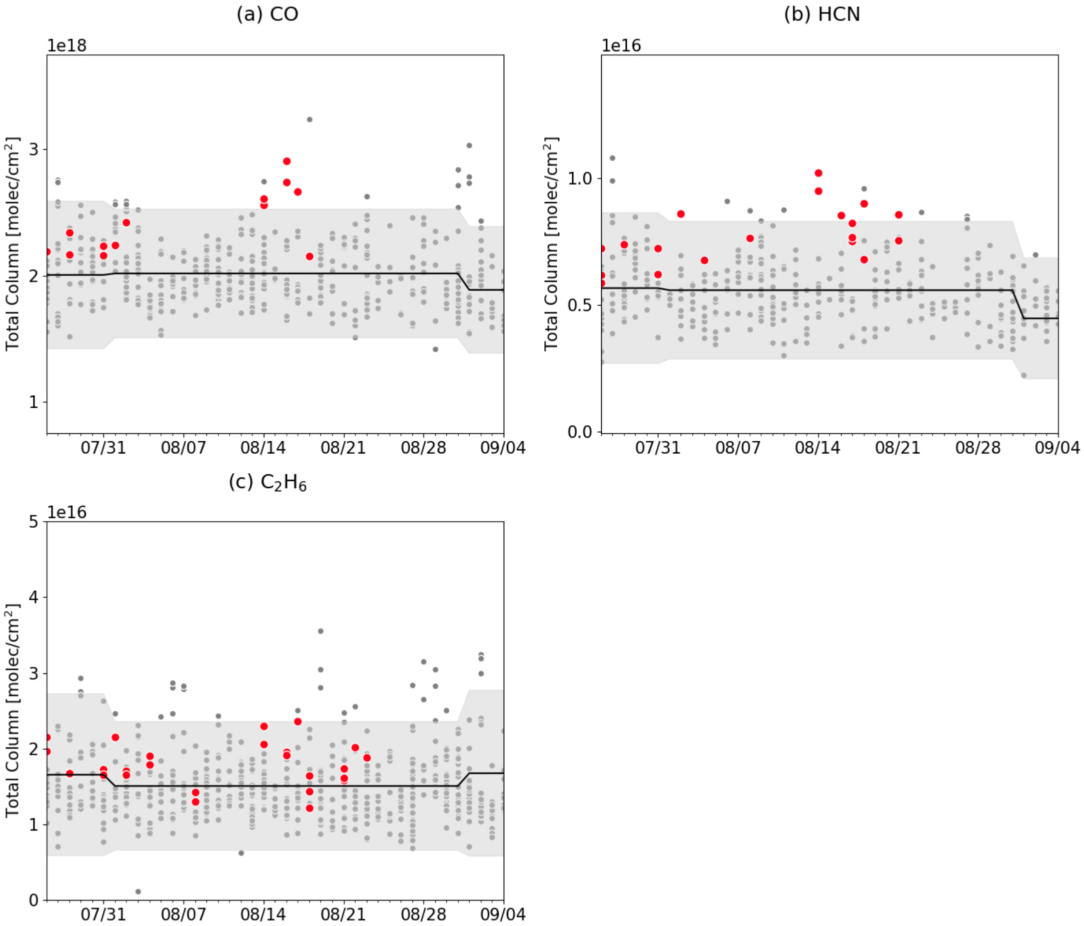

Figure 4.1: TAO total columns of (a) CO, (b) HCN, and (c) C_2H_6 for August 2002-2018, with 2012 data shown in red. The black line is the monthly mean, and the shading indicates ± 2σ (standard deviation).

ratio was calculated using data from 23 July to 6 September, which was necessary due to the sparse number of measurements.

The July 2015 event had correlation coefficients, R, of 0.85, 0.81, 0.77, and 0.95 for HCN, C_2H_6, CH_3OH, and HCOOH, respectively. The 2015 correlations were done using measurements from 1 to 23 July. The September 2017 event was analyzed with data from 4 to 18 September, resulting in correlation coefficients of 0.84, 0.70, 0.88, and 0.60 for HCN, C_2H_6, CH_3OH, and HCOOH, respectively.

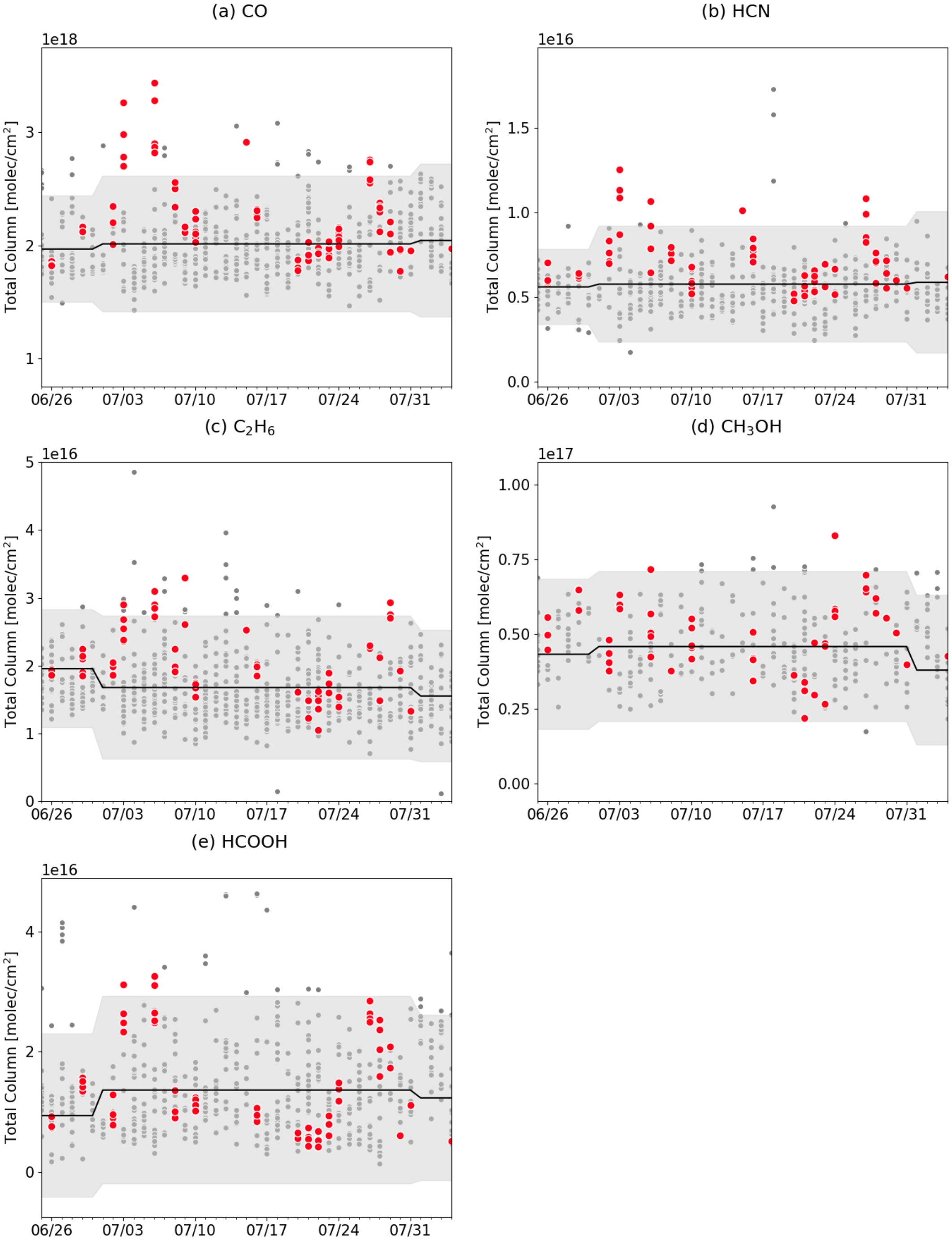

Figure 4.2: TAO total columns of (a) CO, (b) HCN (c) C_2H_6, (d) CH_3OH, and (e) HCOOH for July 2002-2018, with 2015 data shown in red. The black line is the monthly mean, and the shading indicates ± 2σ (standard deviation).

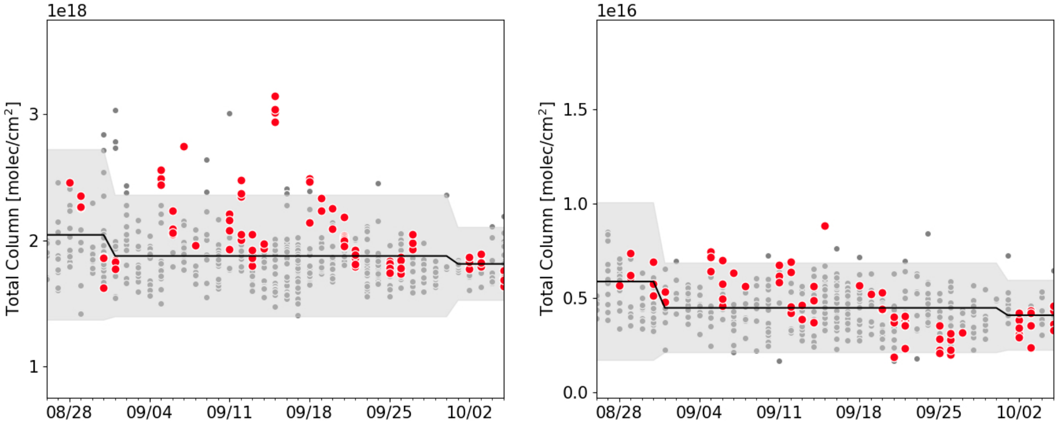

(a) CO

(b) HCN

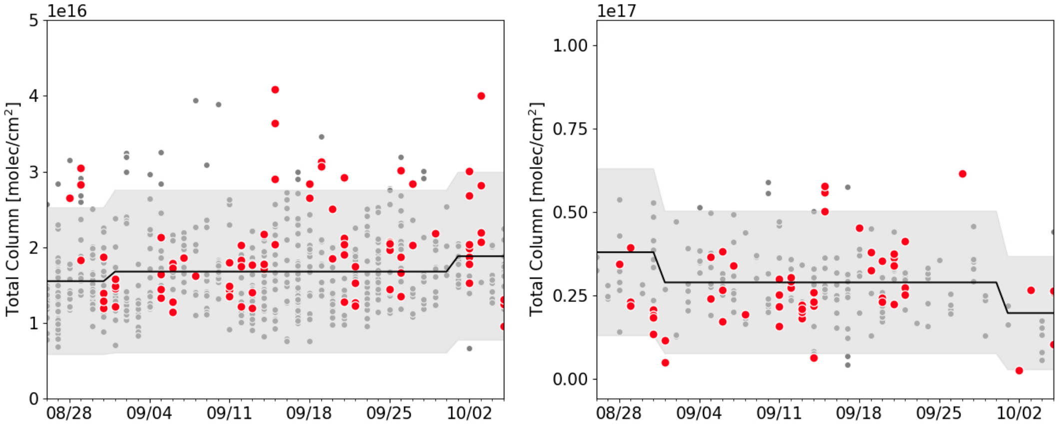

(c) C_2H_6

(d) CH_3OH

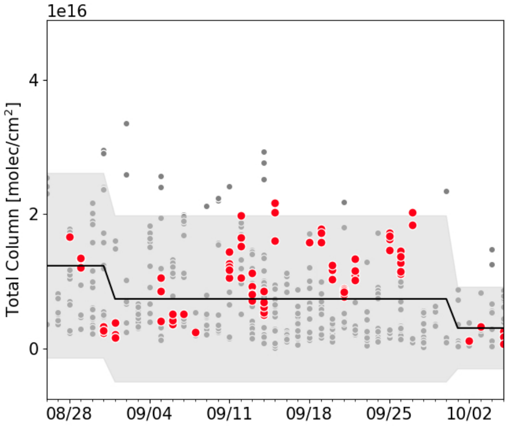

(e) HCOOH

Figure 4.3: TAO total columns of (a) CO, (b) HCN (c) C_2H_6, (d) CH_3OH, and (e) HCOOH for September 2002-2018, with 2017 data shown in red. The black line is the monthly mean, and the shading indicates ± 2σ (standard deviation).

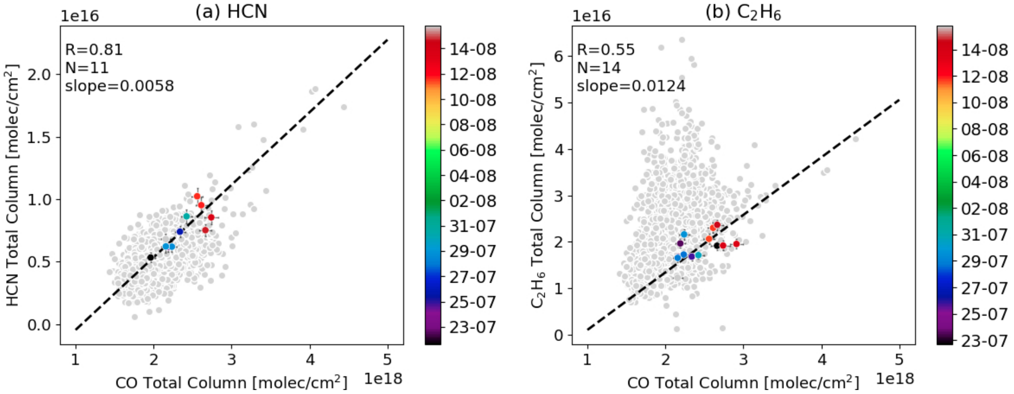

Figure 4.4: Correlation plots for (a) HCN and (b) C_2H_6 vs. CO, used to derive the enhancement ratios for the August 2012 episode. Data from 2002 to 2018 are in grey, and data used for calculating the enhancement ratios for the August 2012 episode are indicated by the colored legend. Error bars indicate FTIR total column errors. The statistics displayed were derived from the colored data points alone.

4.4 Source Attribution

FLEXPART and HYSPLIT were used to determine the source regions and travel times of each plume seen in Toronto as described in Section 3.2.1. FLEXPART sensitivity values for the 2012 enhancement episode are shown in Figures 4.7a and 4.7b. Panels (a) and (b) show the sensitivity of seven-day back-trajectories for particles released on 3 and 17 August, respectively, the days when TAO measurements were enhanced. The run on 3 August shows sensitivity to fires from North Dakota, Montana, and the Pacific Northwest, while the 17 August enhancement is likely due to a plume from a fire in the North Dakota and southern Manitoba region. For this event, the emission estimate was made using EF_{co} for both boreal and temperate forests. HYSPLIT back-trajectories were also calculated at various release altitudes between 3 km and 10 km (following e.g., Lutsch et al., 2016) and the average travel time for the 3 and 17 August 2012 episodes (treated as one event due to the lack of measurements to distinguish them) was taken to be 1.5 ± 0.5 days.

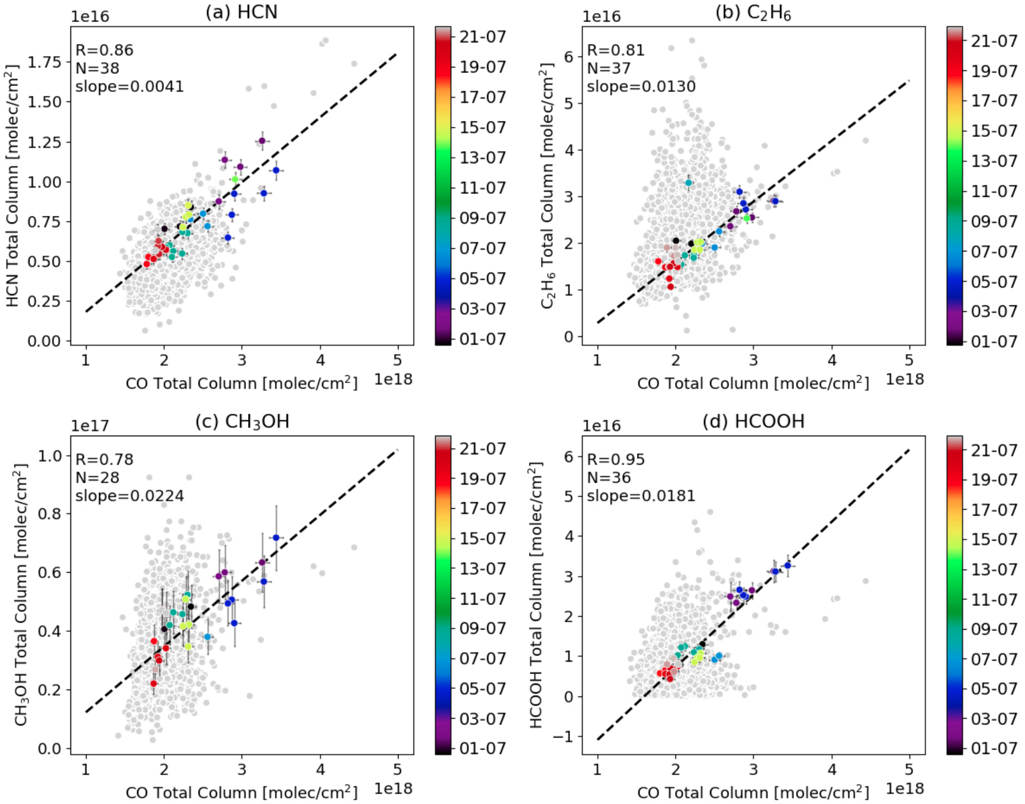

Figure 4.5: Correlation ratio plots for (a) HCN, (b) C_2H_6 (c) CH_3OH, and (d) HCOOH vs. CO, used to derive the enhancement ratios for the July 2015 episode. Data from 2002 to 2018 are in grey, and data used for calculating the enhancement ratios for the July 2015 episode are indicated by the colored legend. Error bars indicate FTIR total column errors. The statistics displayed were derived from the colored data points alone.

The enhancement episode in July 2015 is likely due to a boreal forest fire. Figure 4.7c shows the sensitivity of measurements in Toronto on 3 July. FLEXPART and GEOS-Chem total column CO (not shown) show plumes being transported from Alberta over Toronto. While FLEXPART shows sensitivity to the region south of Hudson Bay as well, MODIS Burned Area data are much sparser in comparison to Alberta and the rest of Western Canada. The travel time for this event was estimated to be 2.5 ± 1 days.

For the 2017 event, Figures 4.7d and 4.7e show back-trajectory plots for 5 and 15 September. The enhancement on 5 September is likely from a series of fires in

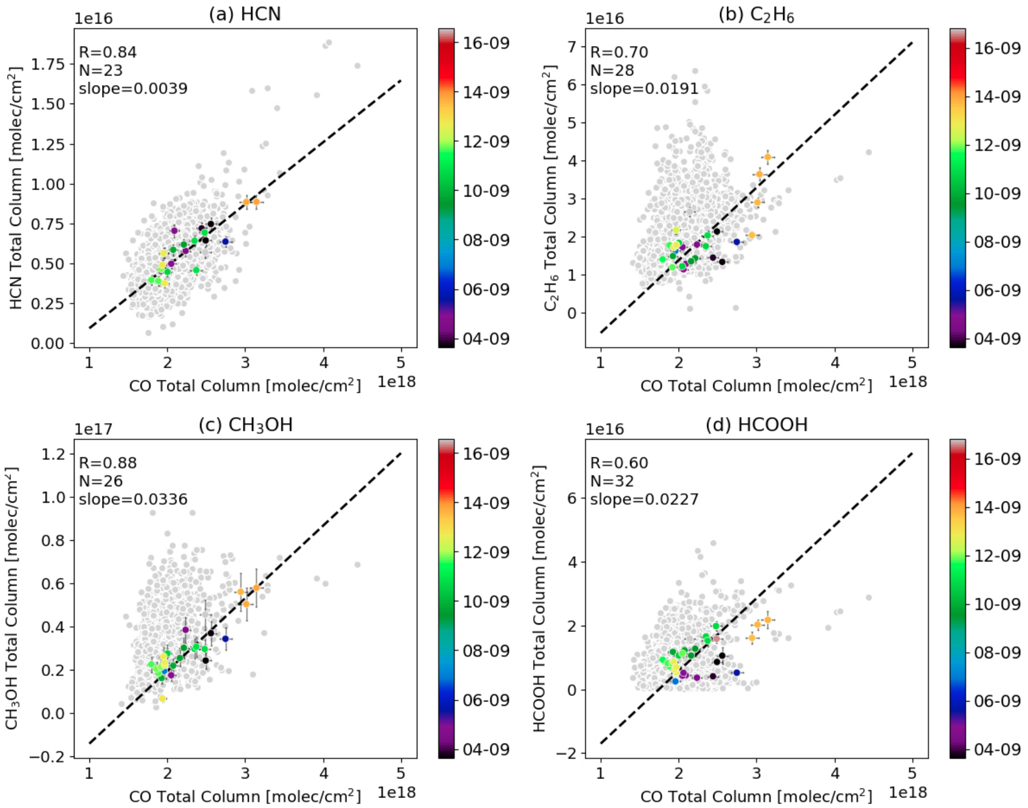

Figure 4.6: Correlation ratio plots for (a) HCN, (b) C_2H_6 (c) CH_3OH, and (d) HCOOH vs. CO, used to derive the enhancement ratios for the September 2017 episode. Data from 2002 to 2018 are in grey, and data used for calculating the enhancement ratios for the September 2017 episode are indicated by the colored legend. Error bars indicate FTIR total column errors. The statistics displayed were derived from the colored data points alone.

Manitoba, indicating a boreal fire, while that on 15 September is likely from a mix of fires in the United States, indicating temperate forest fires. Emission factors for this event were thus estimated using both temperate and boreal EF_{co} values. The travel time estimate for these events from HYSPLIT (treated as one event) was taken to be 2.5 ± 1 days (both events had travel time estimates within this range).

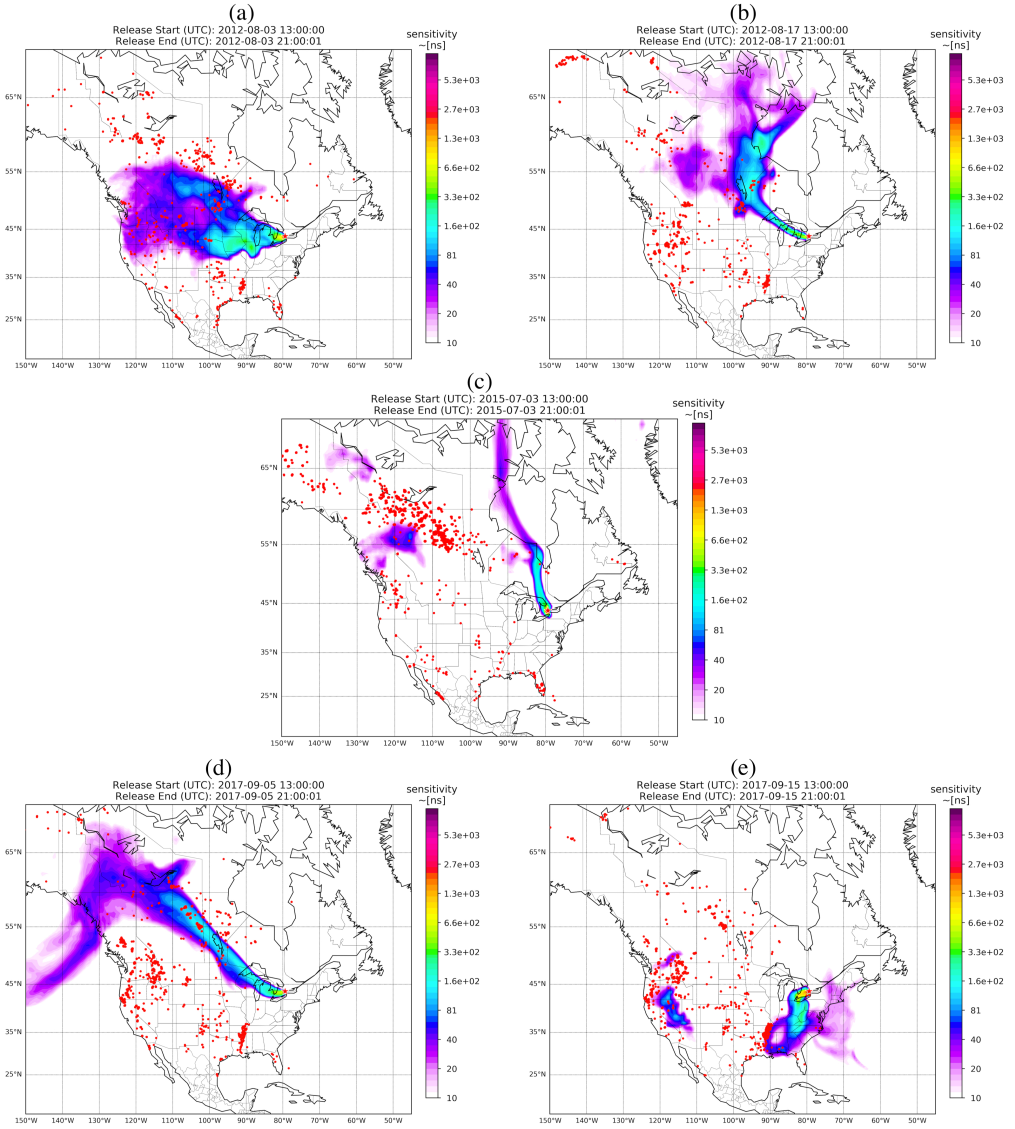

Figure 4.7: FLEXPART seven-day back-trajectory sensitivity plots for (a) 3 August 2012, (b) 17 August 2012, (c) 3 July 2015, (d) 5 September 2017, and (e) 15 September 2017. Red points are MODIS Burned Area data points.

4.5 Estimating Emissions

Emission ratios and emission factors derived for the three events are listed in Tables 4.3, 4.4, 4.5, and 4.6 for HCN, C_2H_6, CH_3OH, and HCOOH, respectively, along with values from other studies. The uncertainties were calculated by propagating travel time uncertainty, regression error (York et al., 2004), uncertainties on lifetime estimates of target species and CO, as well as the uncertainty on emission factors of CO. For longer-lived species like HCN and C_2H_6, the uncertainties on the linear regression were the largest sources of error, while for shorter-lived species, travel time uncertainties were the largest sources of error.

The emission ratios and emission factors for longer-lived species like HCN and C_2H_6 are in relatively good agreement with those from other ground-based FTIR studies. Emission factors for HCN from this study (Table 4.3) ranged from 0.32 ± 0.12 g/kg (temperate forest) to 0.70 ± 0.27 g/kg (boreal forest). This can be compared to EF_{HCN} estimates from ground-based FTIR measurements by Viatte et al. (2015) (0.36 ± 0.17 k/kg at Eureka) and Lutsch et al. (2016) (0.84 ± 0.30 g/kg at Toronto), as well as a compilation study by Andreae (2019), who estimated EF_{HCN} to be 0.53 ± 0.30 g/kg for boreal forest and 0.64 ± 0.39 g/kg for temperate forest. It should be noted that EF_{HCN} is highly dependent on fuel type (Akagi et al., 2013; Viatte et al., 2013). Pure wood (e.g., used for cooking) emits virtually no HCN when burned (below detection levels) (Christian et al., 2010), while some peat samples can have ER_{HCN} as high as 0.03 (Akagi et al., 2011).

C_2H_6 emission ratios and emission factors (Table 4.4), while in relatively good agreement with other FTIR and laboratory studies by Akagi et al. (2011), were found to be larger than those from aircraft observations. Emission factors for temperate forest fires (i.e., assuming EF_{CO} of 89 ± 32 g/kg, comparable to 88.8 g/kg used by Goode et al. (2000)) were found to be as large as 1.85 ± 0.67, compared to 0.66 found by Goode et al. (2000). This could be due to differences in sampling method, as suggested by Viatte et al. (2013). Additionally, it should be noted that the C_2H_6 ER and

EF values were found to be higher than those of Paton-Walsh et al. (2005), who examined emissions from Australian fires; the lowest EF value from this study was 0.85 ± 0.33 g/kg, while Paton-Walsh et al. (2005) estimated the EF to be 0.26 ± 0.11 g/kg. This is because of differences in fuel; Australian vegetation is predominantly Eucalyptus trees, which are known to have lower C_2H_6 emissions (Paton-Walsh et al., 2005). This is consistent with findings from Viatte et al. (2013). When compared to the compilation study by Andreae (2019), the values presented here are higher; while the estimate from the 2012 event (temperate forest) is comparable (EF of 1.17 ± 0.44 g/kg and 0.69 ± 0.56 g/kg for this study and Andreae (2019), respectively), the estimate from the 2017 event (boreal forest) is much higher than the compilation result, at 2.64 ± 0.95 g/kg for this study and 0.97 ± 0.37 g/kg for the compilation value. This may be due to contamination of the plume from emissions from oil and gas production, which is known to emit C_2H_6 that has been detected at TAO (Franco et al., 2016a); The 2017 back-trajectory plot (see Figure 4.7e) shows sensitivity to the Marcellus Shale region. The values presented here are in better agreement with the compilation study by Akagi et al. (2011), which estimates boreal forest $EF_{C_2H_6}$ to be 1.79 ± 1.14 g/kg. For longer-lived species like HCN and C_2H_6, lifetime did not affect the emission factors significantly.

Shorter-lived species like CH_3OH and HCOOH have large uncertainties due to travel time. Emission factor estimates of these two gases likely suffer from large biases due to the fact that the methodology used here does not account for other sources and production during transport. CH_3OH emission factors and ratios (Table 4.5) are within combined errors with findings from Viatte et al. (2015) who used

FTIR spectrometers stationed at Eureka and Thule (76.53°N, 68.74°W) and used a similar approach to estimating emission factors. 2015 and 2017 CH_3OH EF values are within their combined errors. The 2015 EF values of 4.35 ± 1.80 and 4.17 ± 1.68 (CO lifetimes of 61 and 30 days, respectively) are comparable with 3.44 ± 1.68 g/kg reported by Viatte et al. (2015), and are also within combined errors of the compilation study by Akagi et al. (2011) and Andreae (2019) (2.82 ± 1.62 and 2.33 ± 1.45 g/kg, respectively). Overall, CH_3OH ER and EF estimates from this study (2015 and 2017 events) were higher than other published values, including those of Viatte et al. (2015). This bias is likely due to photochemical production during transport, as well as local sources (Jacob et al., 2005) being detected given the urban location of TAO and time of measurements (July and September).

The ER and EF estimates for HCOOH (Table 4.6) from this study are higher than values from Eureka and Thule (Viatte et al., 2015), and compared to the compilation value given by Andreae and Merlet (2001) (EF value of 2.9 ± 2.2 g/kg) and Akagi et al. (2011) (0.57 ± 0.46 and 0.35 ± 0.33 g/kg for boreal and temperate forests, respectively). Similar to CH_3OH, this bias is likely due to HCOOH having other sources, especially given the urban location of TAO. 2015 EF values of 6.79 ± 3.81 and 7.25 ± 4.09 (CO lifetimes of 61 and 30 days, respectively) are within combined errors of published values by Viatte et al. (2015) of 3.14 ± 1.46 and 2.69 ± 1.14 (values from Thule and Eureka, respectively). It is possible that the high HCOOH total columns are the result of local biogenic emissions, as was suggested by Viatte et al. (2015). It should also be noted that CH_3OH and HCOOH can be byproducts of reactions during transport. This is especially true for HCOOH, which is formed from VOCs co-emitted from fires. The production of HCOOH from co-emitted VOCs may explain, at least partially, the relatively high correlation seen in the enhancement ratio plots. A study by R'Honi et al. (2013), who used IASI measurements to analyze biomass emissions from wildfires in Russia in 2010, also observed high correlation between HCOOH and CO, while acknowledging that the secondary production of HCOOH is likely responsible for their over-estimation of HCOOH emission ratios in comparison to laboratory studies. This was not accounted for in this study nor in previous FTIR studies (e.g., Viatte et al., 2015), and may explain why the EF and ER values are larger than those obtained from laboratory studies (e.g., Akagi et al., 2011; Andreae, 2019).

All of the species analyzed in this study have sources aside from wildfires, which may contribute to biases in the calculated values at Toronto compared to more remote sites (Viatte et al., 2015; Lutsch et al., 2016). This is evident in the FLEXPART sensitivity analyses. For 2012, the sensitivity to the Chicago/Detroit area is evident, especially in the 3 August run. For 2015, contributions from the wetlands region southwest of Hudson Bay as well as the Pittsburgh/Cleveland area can be seen, and the 2017 event, as discussed above, not only saw emissions from different forest types (see Section 4.4), but possibly other sources altogether, with measurements showing sensitivity to Detroit and areas around the Appalachian Mountains and Marcellus Shale. In addition, FTIR observations cannot distinguish plumes that have mixed emissions from different phases of combustion (e.g., flaming and smouldering), and this can lead to further uncertainties (Lutsch et al., 2019).

Table 4.3: Emission ratios and emission factors for HCN. EF_{CO} values of 89 ± 32 and 127 ± 45 represent temperate and boreal forest, respectively.

Source	Platform, Location	EF_{CO} (g/kg)	ER_{HCN}	EF_{HCN} (g/kg)
[a]2012 August	FTIR, Toronto	127 ± 45	0.0057 ± 0.0008	0.70 ± 0.27
[b]2012 August	FTIR, Toronto	127 ± 45	0.0056 ± 0.0008	0.69 ± 0.26
[a]2012 August	FTIR, Toronto	89 ± 32	0.0057 ± 0.0008	0.49 ± 0.19
[b]2012 August	FTIR, Toronto	89 ± 32	0.0056 ± 0.0008	0.48 ± 0.19
[a]2015 July	FTIR, Toronto	127 ± 45	0.0040 ± 0.0002	0.49 ± 0.18
[b]2015 July	FTIR, Toronto	127 ± 45	0.0039 ± 0.0002	0.48 ± 0.17
[a]2017 September	FTIR, Toronto	127 ± 45	0.0038 ± 0.0003	0.47 ± 0.17
[b]2017 September	FTIR, Toronto	127 ± 45	0.0037 ± 0.0003	0.45 ± 0.16
[a]2017 September	FTIR, Toronto	89 ± 32	0.0038 ± 0.0003	0.33 ± 0.12
[b]2017 September	FTIR, Toronto	89 ± 32	0.0037 ± 0.0003	0.32 ± 0.12
Lutsch et al. (2016)	FTIR, Toronto	127 ± 45	0.0068 ± 0.0003	0.84 ± 0.30
Viatte et al. (2015)	FTIR, Thule	127 ± 45	0.00429 ± 0.00245	0.44 ± 0.25
Viatte et al. (2015)	FTIR, Eureka	127 ± 45	0.00343 ± 0.00094	0.36 ± 0.17
Paton-Walsh et al. (2005)	FTIR, Wollongong	107 ± 37	0.0043 ± 0.0016	0.43 ± 0.22
Goode et al. (2000)	Aircraft, Alaska	88.8	0.0069	0.61
Akagi et al. (2011)	Compilation	127 ± 45	-	1.52 ± 0.82
Akagi et al. (2011)	Compilation	89 ± 32	-	0.73 ± 0.19
[c]Andreae and Merlet (2001)	Compilation/Extrapolation	107 ± 37	-	0.15
[d]Andreae (2019)	Compilation/Extrapolation	121 ± 47	-	0.53 ± 0.30
[e]Andreae (2019)	Compilation/Extrapolation	113 ± 50	-	0.64 ± 0.39

[a]This study, HCN and CO lifetimes 150 and 61 days respectively.
[b]This study, HCN and CO lifetimes 75 and 30 days respectively.
[c]Stated as “best guess” Andreae and Merlet (2001).
[d]Estimate for boreal forest.
[e]Estimate for temperate forest.

Table 4.4: Emission ratios and emission factors for C_2H_6. EF_{CO} values of 89 ± 32 and 127 ± 45 represent temperate and boreal forest, respectively.

Source	Platform, Location	EF_{CO} (g/kg)	$ER_{C_2H_6}$	$EF_{C_2H_6}$ (g/kg)
[a]2012 August	FTIR, Toronto	127 ± 45	0.0125 ± 0.0016	1.71 ± 0.64
[b]2012 August	FTIR, Toronto	127 ± 45	0.0122 ± 0.0015	1.66 ± 0.62
[a]2012 August	FTIR, Toronto	89 ± 32	0.0125 ± 0.0016	1.20 ± 0.45
[b]2012 August	FTIR, Toronto	89 ± 32	0.0122 ± 0.0015	1.17 ± 0.44
[a]2015 July	FTIR, Toronto	127 ± 45	0.013 ± 0.0006	1.79 ± 0.64
[b]2015 July	FTIR, Toronto	127 ± 45	0.013 ± 0.0006	1.72 ± 0.62
[a]2017 September	FTIR, Toronto	127 ± 45	0.019 ± 0.001	2.64 ± 0.95
[b]2017 September	FTIR, Toronto	127 ± 45	0.019 ± 0.001	2.53 ± 0.91
[a]2017 September	FTIR, Toronto	89 ± 32	0.019 ± 0.001	1.85 ± 0.67
[b]2017 September	FTIR, Toronto	89 ± 32	0.019 ± 0.001	1.77 ± 0.65
Lutsch et al. (2016)	FTIR, Toronto	127 ± 45	0.0101 ± 0.0005	1.38 ± 0.49
Viatte et al. (2015)	FTIR, Thule	127 ± 45	0.01211 ± 0.00476	1.39 ± 0.68
Viatte et al. (2015)	FTIR, Eureka	127 ± 45	0.00956 ± 0.00319	1.09 ± 0.74
Paton-Walsh et al. (2005)	FTIR, Wollongong	107 ± 37	0.0023 ± 0.0005	0.26 ± 0.11
Goode et al. (2000)	Aircraft, Alaska	88.8	0.0073	0.66
Akagi et al. (2011)	Compilation	127 ± 45	-	1.79 ± 1.14
Akagi et al. (2011)	Compilation	89 ± 32	-	1.12 ± 0.67
Andreae and Merlet (2001)	Compilation/Extrapolation	107 ± 37	-	0.60 ± 0.15
[c]Andreae (2019)	Compilation/Extrapolation	121 ± 47	-	0.97 ± 0.37
[d]Andreae (2019)	Compilation/Extrapolation	113 ± 50	-	0.69 ± 0.56

[a] This study, CO lifetime of 61 days.
[b] This study, CO lifetime of 30 days.
[c] Estimate for boreal forest.
[d] Estimate for temperate forest.

Table 4.5: Emission ratios and emission factors for CH_3OH. EF_{CO} values of 89 ± 32 and 127 ± 45 represent temperate and boreal forest, respectively.

Source	Platform, Location	EF_{CO} (g/kg)	ER_{CH_3OH}	EF_{CH_3OH} (g/kg)
[a]2015 July	FTIR, Toronto	127 ± 45	0.030 ± 0.006	4.35 ± 1.80
[b]2015 July	FTIR, Toronto	127 ± 45	0.029 ± 0.006	4.17 ± 1.68
[a]2017 September	FTIR, Toronto	127 ± 45	0.045 ± 0.008	6.54 ± 2.60
[b]2017 September	FTIR, Toronto	127 ± 45	0.043 ± 0.007	6.27 ± 2.43
[a]2017 September	FTIR, Toronto	89 ± 32	0.045 ± 0.008	4.58 ± 1.85
[b]2017 September	FTIR, Toronto	89 ± 32	0.043 ± 0.007	5.39 ± 1.72
Viatte et al. (2015)	FTIR, Eureka	127 ± 45	0.02813 ± 0.01252	3.44 ± 1.68
Goode et al. (2000)	Aircraft, Alaska	88.8	0.0135	1.41
Akagi et al. (2011)	Compilation	127 ± 45	-	2.82 ± 1.62
Akagi et al. (2011)	Compilation	89 ± 32	-	1.93 ± 1.38
Andreae and Merlet (2001)	Compilation/Extrapolation	107 ± 37	-	2.0 ± 1.4
[c]Andreae (2019)	Compilation/Extrapolation	121 ± 47	-	2.33 ± 1.45
[d]Andreae (2019)	Compilation/Extrapolation	113 ± 50	-	2.2 ± 0.9

[a] This study, CO lifetime of 61 days.
[b] This study, CO lifetime of 30 days.
[c] Estimate for boreal forest.
[d] Estimate for temperate forest.

Table 4.6: Emission ratios and emission factors for HCOOH. EF_{CO} values of 89 ± 32 and 127 ± 45 represent temperate and boreal forest, respectively.

Source	Platform, Location	EF_{CO} (g/kg)	ER_{HCOOH}	EF_{HCOOH} (g/kg)
[a]2015 July	FTIR, Toronto	127 ± 45	0.033 ± 0.014	6.79 ± 3.81
[b]2015 July	FTIR, Toronto	127 ± 45	0.035 ± 0.015	7.25 ± 4.09
[a]2017 September	FTIR, Toronto	127 ± 45	0.041 ± 0.018	8.51 ± 4.78
[b]2017 September	FTIR, Toronto	127 ± 45	0.039 ± 0.015	8.16 ± 4.30
[a]2017 September	FTIR, Toronto	89 ± 32	0.041 ± 0.018	5.96 ± 3.37
[b]2017 September	FTIR, Toronto	89 ± 32	0.039 ± 0.015	5.72 ± 3.04
Viatte et al. (2015)	FTIR, Thule	127 ± 45	0.01790 ±0.00937	3.14 ± 1.46
Viatte et al. (2015)	FTIR, Eureka	127 ± 45	0.01531 ± 0.00403	2.69 ± 1.14
Goode et al. (2000)	Aircraft, Alaska	88.8	0.0062	0.99
Akagi et al. (2011)	Compilation	127 ± 45	-	0.57 ± 0.46
Akagi et al. (2011)	Compilation	89 ± 32	-	0.35 ± 0.33
Andreae and Merlet (2001)	Compilation/Extrapolation	107 ± 37	-	2.9 ± 2.4
[c]Andreae (2019)	Compilation/Extrapolation	121 ± 47	-	1.04 ± 0.89
[d]Andreae (2019)	Compilation/Extrapolation	113 ± 50	-	0.91 ± 1.18

[a] This study, CO lifetime of 61 days.
[b] This study, CO lifetime of 30 days.
[c] Estimate for boreal forest.
[d] Estimate for temperate forest.

4.6 GEOS-Chem

To interpret the FTIR observations, a tagged-CO run of the GEOS-Chem (v.12.1.1) CTM was performed. The model was used in conjunction with FLEXPART sensitivity plots (Section 4.4) to identify the origins of the plumes detected in 2012, 2015, and 2017. It was also used to give an estimate of the number of days that saw enhanced relative CO contributions from biomass burning plumes. The regions of tagged biomass burning emissions are shown in Figure 4.8.

The GEOS-Chem time series from 2003 to 2018 for the grid cell containing Toronto is shown in Figure 4.9. The model was run with tagged CO emissions from several sources, including biomass burning emissions. MERRA-2 meteorological fields and the GFAS (Global Fire Assimilation System) biomass burning emissions database (Kaiser et al., 2012) were used (see Section 2.6 for details). The model output suggests that anthropogenic CO of North American origin accounts for 12.9 ± 3.86 % (1σ) of the CO in Toronto when averaged from 2003-2018 (the dark blue dashed line in Figure 4.9). The figures and the analysis here were done with daily averages. The time series also reveals a few biomass burning enhancements over Toronto that were not apparent from the FTIR measurements. There is a clear spike in the relative CO contribution from North American boreal forest fires (red line in Figure 4.9) in July/August 2010, which accounted for more CO than North American anthropogenic sources, although this was a short episode. There is also another minor episode in August/September 2013, which saw elevated relative CO contribution from North American boreal fires. Neither of these events were seen in the FTIR time series. However, these events are less pronounced than the August 2014 episode (Lutsch et al., 2016) or the 2015 and 2017 events discussed in this study. Overall, the model showed that the North American boreal forest fire contribution to CO columns at Toronto exceeded the mean North American anthropogenic contribution on 2.1 % of the days from 2003 to 2018.

GEOS-Chem captures the boreal fire event in 2015 (see Figure 4.10), with CO from North American boreal forest fires accounting for the largest percentage (peaking at 39.8 %) of CO seen over Toronto, followed by CO from North American anthropogenic sources (which were at the background levels of 12.9 ± 3.86 %).

The September 2017 event shows a similar pattern (Figure 4.11), with boreal forest fire emissions being a significant source of CO over Toronto with a maximum of 28.8 % relative contribution on 7 September. CO has some enhancements from temperate forests, but they are less pronounced, peaking at 13.9 %. GEOS-Chem was unable to capture the enhancement seen on 15 September. As with the 2015 plot, North American anthropogenic emissions are also a significant source of CO seen in Toronto in September 2017.

The 2012 enhancement differs from the 2015 and 2017 events in that it is largely dominated by a strong background CO from Eurasian biomass burning emissions. There is a small enhancement in fire emissions from North American temperate forests on 17 August. For this event, CO total columns from North American anthropogenic sources are consistently larger than those from temperate forest fire emissions, making the enhancement ratio estimates more uncertain than the 2015 and 2017 events. However, GEOS-Chem was unable to capture the enhanced CO total columns measured on 15 August 2012 (see Figure 4.12).

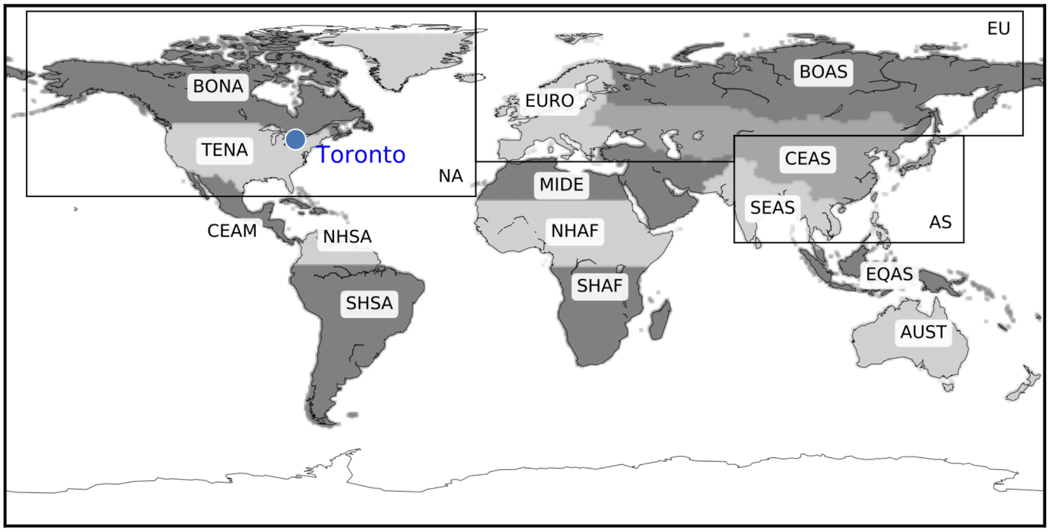

Figure 4.8: Map of GEOS-Chem tagged CO biomass burning emission source regions. North American boreal forest fire and North American temperate forest fire sources are shown as BONA and TENA, respectively. Other regions shown in the figure are Central America (CEAM), Boreal Eurasian (BOAS), Europe (EURO), Central Asia (CEAS), Middle East and Northern Africa (MIDE) and Mid-Africa (NHAF). The remaining regions shown in the figure, which are Southern Africa (SHAF), Southeast Asia (SEAS), Equatorial Asia (EQAS), and Oceania (AUST) were modeled in the simulation but not analyzed in this study, as their effects over Toronto were negligible.

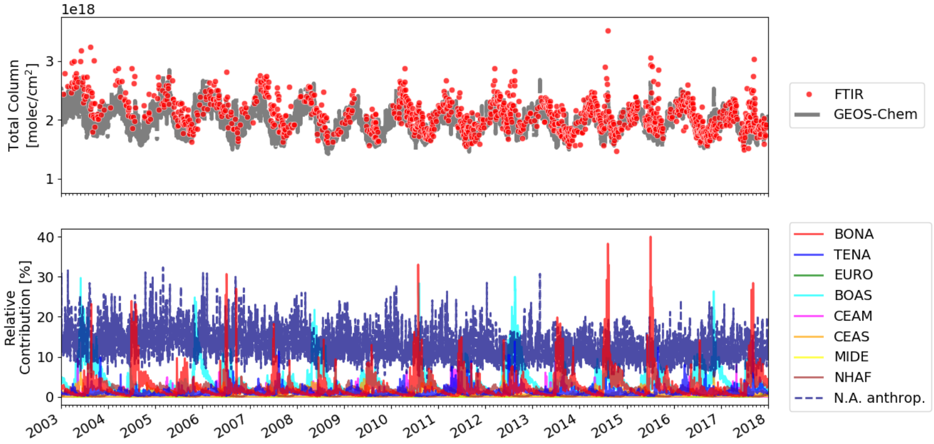

Figure 4.9: Time series of GEOS-Chem tagged CO output over Toronto. Top panel shows FTIR total column CO measurements and GEOS-Chem total column CO output. The lower panel shows the relative contributions of CO over Toronto from various sources in GEOS-Chem.

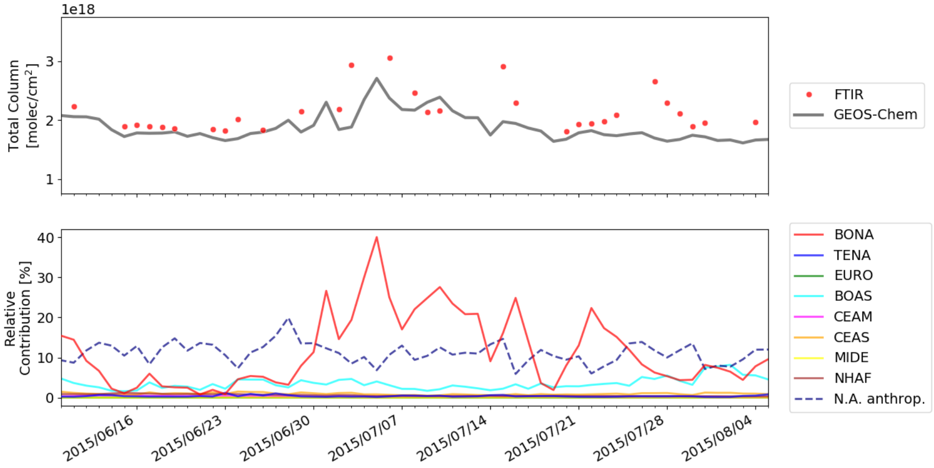

Figure 4.10: Time series of GEOS-Chem tagged CO output over Toronto for the July 2015 enhancement period. Top panel shows FTIR total column CO measurements and GEOS-Chem total column CO output. The lower panel shows the relative contributions of CO over Toronto from various sources.

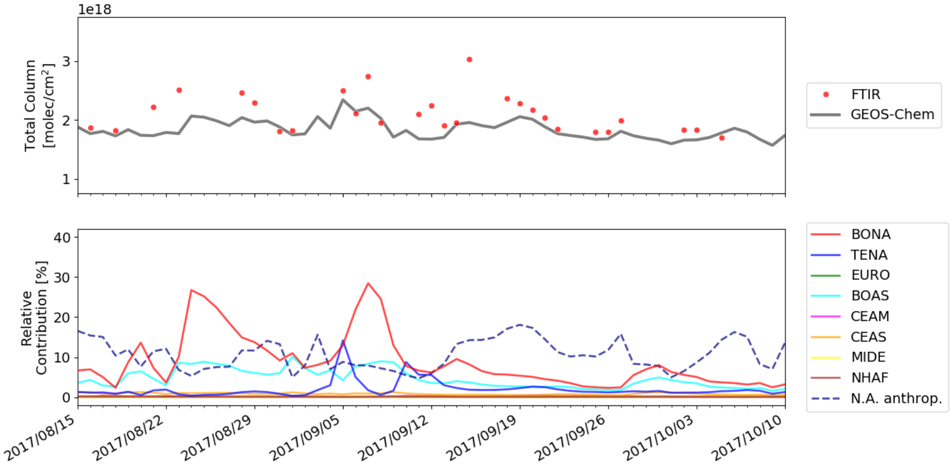

Figure 4.11: Time series of GEOS-Chem tagged CO output over Toronto for the September 2017 enhancement period. Top panel shows FTIR total column CO measurements and GEOS-Chem total column CO output. The lower panel shows the relative contributions of CO over Toronto from various sources.

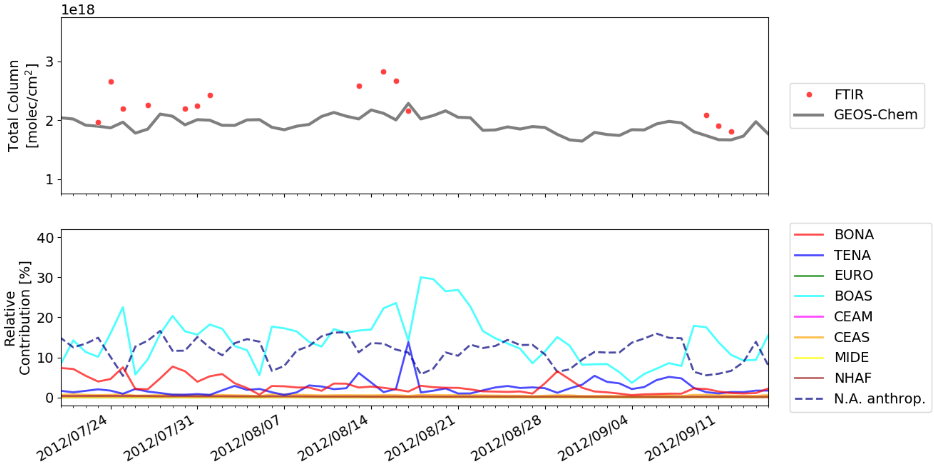

Figure 4.12: Time series of GEOS-Chem tagged CO output over Toronto for the August 2012 enhancement period. Top panel shows FTIR total column CO measurements and GEOS-Chem total column CO output. The lower panel shows the relative contributions of CO over Toronto from various sources.

4.7 Conclusions

TAO FTIR measurements of CO, HCN, C_2H_6, CH_3OH, and HCOOH total columns, were examined for biomass burning enhancements. Seasonal cycles, consistent with current understanding of sources and sinks, were visible in the time series of all five species. CO showed lower concentrations during the summer and fall due to increased OH that destroys CO. C_2H_6 also showed a strong annual cycle with a trough in the summer months, which is consistent with the fact that OH oxidation is a major sink of C_2H_6. HCN, while its main sink is also OH, had its maximum in the spring and summer, primarily due to biomass burning (Lobert et al., 1990; Li et al., 2009). CH_3OH and HCOOH both have maxima in the summer months as well, which is likely the result of increased biogenic emissions (Millet et al., 2008; Stavrakou et al., 2011; Millet et al., 2015). Overall, TAO columns for both CH_3OH and HCOOH were found to be higher than those from smaller urban sites like Wollongong (Paton-Walsh et al., 2008) and remote sites like Eureka (Viatte et al., 2014).

TAO FTIR total columns were used to identify enhancement episodes caused by biomass burning. The data showed simultaneous enhancements of CO, HCN, and C_2H_6 during events in 2012, 2015, and 2017. FLEXPART back-trajectories were used in conjunction with the MODIS Burned Area data product for source attribution, and emission ratios and emission factors for HCN and C_2H_6 (along with CH_3OH and HCOOH for the 2015 and 2017 events) were calculated. HCN emission ratios ranging from 0.0037 ± 0.0003 to 0.0057 ± 0.0008 were observed, while C_2H_6 emission ratios ranged from 0.00122 ± 0.0015 to 0.019 ± 0.001. For the 2015 and 2017 events, enhancements of CH_3OH and HCOOH were also observed. An attempt was made to estimate emission ratios for these species, but it should be noted that these species have other sources and have much shorter lifetimes than HCN and C_2H_6, potentially resulting in large biases. ER_{CH_3OH} varied from 0.029 ± 0.006 to 0.045 ± 0.008, while for HCOOH, the ratios were between 0.033 ± 0.014 and 0.041 ± 0.018. Emission factors of HCN ranged from 0.32 ± 0.13 to 0.70 ± 0.27 g/kg, and for C_2H_6, EF ranged from 1.17 ± 0.44 to 2.64 ± 0.95 g/kg. EF_{CH_3OH} varied from 4.17 ± 1.68 to 6.54 ± 2.60 g/kg g/kg, while for HCOOH, emission factors ranging from 5.72 ± 3.04 to 8.51 ± 4.78 g/kg were observed. These values are generally consistent with previous estimates obtained with other ground-based FTIR data, but are higher than values in compilation studies. As discussed in Section 4.5, this is likely due to the transported plumes being contaminated with emissions from other sources, as well as from chemical production during transport.

A GEOS-Chem tagged CO run was used to identify the sources of the observed enhancements and to quantify the relative contributions to the CO column of biomass burning from different regions. The model exhibited enhanced CO total columns over Toronto from forest fires for the events analyzed. Anthropogenic CO was the single largest source of background CO over Toronto, accounting for 14.0 ± 4.0 % of the total CO. However, during biomass burning enhancement events, the fires can contribute more CO to the total column over Toronto than anthropogenic sources, with contributions as large as 39.8 % from boreal North America for the 2017 event.

Chapter 5

NH_3 Observations Over Toronto

In this chapter, long-term measurements of NH_3 derived from multiscale datasets are examined. The TAO FTIR total columns of NH_3, as well as in-situ and satellite data, and model simulation data were examined. The results and discussion in this section are based on a paper published in Atmospheric Measurement Techniques (Yamanouchi et al., 2021b).

As discussed in Section 1.4.2, NH_3 is a major source of fine particulate matter. As such, there have been increasing efforts to measure the atmospheric abundance of NH_3 and its spatial and temporal variability. Toronto is the most populous city in Canada, and NH_3, along with other pollutants, is monitored by several instruments, including the FTIR at TAO. In downtown Toronto, local point sources of NH_3 (i.e., vehicle emissions), as well as nearby agricultural emissions, are major sources of NH_3 (Zbieranowski and Aherne, 2012; Hu et al., 2014; Wentworth et al., 2014). Toronto is also regularly affected by biomass burning plumes transported from the USA and other regions of Canada (Griffin et al., 2013; Whaley et al., 2015; Lutsch et al., 2016, 2020). As such, the time series of total column NH_3 measured at TAO exhibits long-term trends and pollution episodes. Toronto also has in-situ (surface) measurements of NH_3 (Hu et al., 2014), made by Environment and Climate Change Canada.

A study by Hu et al. (2014) investigating NH_3 in downtown Toronto has shown that greenery within the city, where chemical fertilizers are commonly used, is an important source of NH_3 when temperatures are above freezing, and that potential sources when temperatures are below freezing have yet to be investigated. Additionally, recent studies have shown the increased capacity for satellite-based instruments to measure spatial and temporal distributions of NH_3 total columns at global (Van Damme et al., 2014b; Warner et al., 2016; Shephard et al., 2020), regional (Van Damme et al., 2014a; Warner et al., 2017; Viatte et al., 2020), and point-source scales (Van Damme et al., 2018; Clarisse et al., 2019a; Dammers et al., 2019).

5.1 NH_3 Multiscale Observation Analysis Methodology

In addition to the TAO NH_3 total column, three years of surface in-situ measurements, and ten years of total column measurements from the Infrared Atmospheric Sounding Interferometer (IASI) were examined. The datasets were used to quantify NH_3 temporal variability over Toronto, Canada. The multiscale datasets were also compared to assess the representativeness of TAO NH_3 measurements, and the GEOS-Chem CTM was used to interpret observations. Trend analysis using the methodology discussed in Chapter 3 was applied to the additional datasets. An additional analysis to determine the number of years of measurements needed to give the derived trend statistical significance (2σ confidence) was conducted, following Weatherhead et al.

(1998). This analysis takes into account the need for longer time series to identify trends in data that are autocorrelated (as are atmospheric observations). It should be noted that a major limitation of this analysis is that it assumes that data are collected at regular intervals, while TAO measurements are made at irregular intervals (due to the need for sunny conditions). For this reason, the confidence intervals derived from bootstrap resampling is a more robust method of error analysis, in the case of TAO data. However, as pointed out by Weatherhead et al. (1998), failing to take into account autocorrelation of the noise can lead to underestimations of actual uncertainty, and for this reason, both bootstrap resampling and the Weatherhead method were used in this study. These techniques were combined to assess the intra- and inter-annual trends of NH_3 derived from TAO measurements, including a linear trend of the NH_3 total column along with its uncertainties and statistical significance.

5.1.1 Datasets

IASI is a nadir-viewing FTIR spectrometer on board the MetOp-A, MetOp-B and MetOp-C polar-orbiting satellites, operated by the European Organization for the Exploitation of Meteorological Satellites (EUMETSAT), which have been operational since 2006, 2012 and 2018, respectively. The MetOp A, B and C satellites are in the same polar orbit. For all three satellites, IASI makes measurements at 09:30 and 21:30 mean local solar time for the descending and ascending orbits, respectively. IASI records spectra in the 645-2760 cm^{-1} spectral range at a resolution of 0.5 cm^{-1}, with apodization. IASI can make off-nadir measurements up to 48.3° on either side of the track, leading to a swath of about 2200 km. At nadir, the field of view is a

2 × 2 matrix of circular pixels, each with a 12 km diameter (Clerbaux et al., 2009).

The IASI NH_3 total columns (IASI ANNI-NH3-v3) are retrieved using an artificial neural network retrieval algorithm, with ERA5 meteorological reanalysis input data (Van Damme et al., 2017; Franco et al., 2018). Due to this retrieval scheme, there are no averaging kernels nor vertical sensitivity information for the retrieved columns (Van Damme et al., 2014b). Details of the retrieval scheme and error analysis can be found in Whitburn et al. (2016) and Van Damme et al. (2017). IASI-A and IASI-B NH_3 were combined and used in this study, as this allows for a longer time series and more data points for robust analysis. The retrieved columns of NH_3 from both satellites have been shown to be consistent with each other (Clarisse et al., 2019b; Viatte et al., 2020).

To examine how TAO total columns compare with in-situ measurements, data obtained by Environment and Climate Change Canada (ECCC) as a part of the National Air Pollution Surveillance Program (NAPS) were used (`http://maps-cartes.ec.gc.ca/rnspa-naps/data.aspx`, last accessed: November, 2021). The data span December 2013 to April 2017, with a sampling frequency of one in three days. The sampling interval is 24 hours, from 00:00 to 24:00 local time, and samples were collected with a Met One SuperSASS-Plus Sequential Speciation Sampler. The detection limit is 0.6 ppb (Yao and Zhang, 2013). The integrated samples were brought back to the lab for analysis (Yao and Zhang, 2016). While errors are not reported in the dataset, the uncertainty is 10% when the NH_3 VMR is between 3 to 20 ppb (Hu et al., 2014). The instrument is situated less than 500 m away from the FTIR, at 43.66°N, 79.40°W, 63 masl.

To assess the representative spatial and temporal scale of TAO FTIR NH_3 columns, the NH_3 total column measurements around Toronto made by IASI were compared against TAO FTIR total columns and modeled NH_3 columns (see Section 5.4). As NH_3 shows high spatiotemporal variability, several definitions of coincident measurements were used in this study, with spatiotemporal criteria of varying strictness. As NH_3 concentrations can vary significantly during the day, the temporal coincidence criterion was chosen to be $\leq$ 90 minutes (Dammers et al., 2016). In addition, values of $\leq$ 60, 45, 30 and 20 minutes were also tested. For spatial coincidence criteria, $\leq$ 25 km (Dammers et al., 2016), 30 km, 50 km, and 100 km were tested. For each criterion, correlations (both R and slope) were calculated. This analysis was used to evaluate the spatial and temporal scales represented by the TAO FTIR NH_3 columns.

The in-situ NH_3 VMRs were compared against the TAO FTIR columns by standardizing both measurements, following Equation 5.1 (Viatte et al., 2020):

$$X^{i}_{\text{standardized}} = \frac{X_i - \mu_X}{\sigma_X} \tag{5.1}$$

where X is the dataset, indexed by i, μ is the mean, and σ is the standard deviation of the dataset. The standardized dataset is centered around zero, and normalized by the standard deviation of the measurements. As the standardized dataset is unitless, it allows for comparison between different measurements in different units. In this study, the TAO FTIR NH_3 total columns were used, because the DOFS for the retrieval was around 1 (mean DOFS of the entire time series was 1.10), meaning there is only about one piece of vertical information in these measurements.

The GEOS-Chem (v11-01) global CTM (in its standard mode) was also used in this study to interpret and compare against observational data. The model was spun up for one year, and output was saved from 2002 to 2018. The model was run in 2° × 2.5° resolution using MERRA-2 meteorological fields. Further details of the model and its configuration can be found in Section 2.6.

5.2 FTIR Measurements

The TAO FTIR total column time series of NH_3 is shown in Figure 3.42. The purple points indicate enhancements, and the trends (with and without outliers) are shown as red and cyan lines, respectively. As discussed in Section 3, the trend from 2002 to 2019 was found to be 3.56 ± 0.85 %/year and 2.36 ± 0.57 %/year (2σ confidence interval from bootstrap resampling), with and without outliers, respectively (see Table 5.2). The number of years of measurements needed for the trend to be statistically (2σ) significant was found to be 32.8 years and 29.3 years, with and without enhancement events, respectively. Due to the irregular FTIR measurement intervals, these numbers may not represent the true significance of the trends, and should be regarded as best estimates of the significance of the observed trend. The lower magnitude of the upward trend in the analysis without enhancement values indicates that the intra-annual variability of NH_3 is increasing. This is also evident when comparing the mean total column and standard deviations from, for example, the periods 2002-2005 and 2016-2019. In the former period, the mean NH_3 total column and standard deviation (1σ) were $5.94 \pm 5.14 \times 10^{15}$ molecules/cm^2, while in the latter time frame, they were $8.74 \pm 8.72 \times 10^{15}$ molecules/cm^2. The observed trend with the FTIR is comparable to a study by Warner et al. (2017), who observed an increasing NH_3

trend of 2.61 %/year over the United States from 2002 to 2016 using data from the Atmospheric Infrared Sounder (AIRS) satellite-based instrument.

Figure 3.27 shows the annual cycle of the FTIR NH_3 total columns, color coded by year, along with the monthly averages and $\pm 2\sigma$. FTIR NH_3 columns have a maximum in May with a monthly total column average of $13.74 \pm 12.34 \times 10^{15}$ molecules/cm^2, largely due to agricultural and soil emissions increasing in spring/summer (Hu et al., 2014; Dammers et al., 2016), and a minimum in January with a monthly total column average of $1.99 \pm 1.73 \times 10^{15}$ molecules/cm^2. The lower NH_3 columns during winter months may be due to lower temperatures favoring the formation of NH_4NO_3 (Li et al., 2014). The seasonal cycle observed with the FTIR is consistent with findings by Van Damme et al. (2015b), who observed maximum NH_3 columns over the central United States during March-April-May (MAM). The mean NH_3 total column across the entire FTIR time series was $7.71 \pm 7.50 \times 10^{15}$ molecules/cm^2. These values are higher than remote areas, such as Eureka (located at 80.05°N, 86.42°W), where the highest monthly average was 0.279×10^{15} molecules/cm^2, in July (Lutsch et al., 2016). However, the TAO FTIR NH_3 total columns are far below values observed by the FTIR in Bremen (located at 53.10°N, 8.85°E), which saw values in the range of $\sim 100 \times 10^{15}$ molecules/cm^2 (Dammers et al., 2016). Monthly mean NH_3 columns are listed in Table 5.1.

5.3 Comparison with NAPS In-Situ Data

The NAPS in-situ NH_3 time series is shown in Figure 5.1. The purple points indicate enhancements, and trendlines with and without these outliers are shown as

Table 5.1: Monthly mean (1σ in parenthesis) NH_3 total columns of the TAO FTIR (2002-2019).

Month	Mean Columns ($\times 10^{15}$ molecules/cm^2)
January	1.99 (1.73)
February	3.74 (3.61)
March	3.98 (3.95)
April	6.86 (8.65)
May	13.74 (12.34)
June	7.63 (5.80)
July	8.58 (6.30)
August	6.89 (4.89)
September	7.86 (6.82)
October	5.74 (4.36)
November	5.18 (5.16)
December	3.18 (3.15)
Overall Mean	7.53 (7.10)

the red and cyan lines, respectively. The trendline was found to have a slope of 8.88 ± 5.08 %/year and 6.40 ± 4.37 %/year (2σ confidence interval from bootstrap resampling), with and without outliers, respectively. The number of years needed for this trend to be 2σ significant was 8.4 years for both. Since NAPS data have very regular measurement intervals (once every three days), they are well suited for this trend significance analysis. Given that NAPS data only spans 3 years and 5 months, and 8.4 years of measurements are needed for 2σ confidence in the observed trend, it is uncertain if the increase in NH_3 levels is a definitive trend. For comparison, analysis of TAO FTIR NH_3 total columns during the same time period resulted in trends of 9.31 ± 5.73 %/year and 7.42 ± 4.48 %/year, with and without outliers, respectively.

The in-situ NH_3 VMRs were compared against the TAO FTIR columns by standardizing both measurements, following Equation 5.1. Standardized FTIR and NAPS NH_3 are plotted in Figure 5.2a. Monthly averages and monthly standard deviations

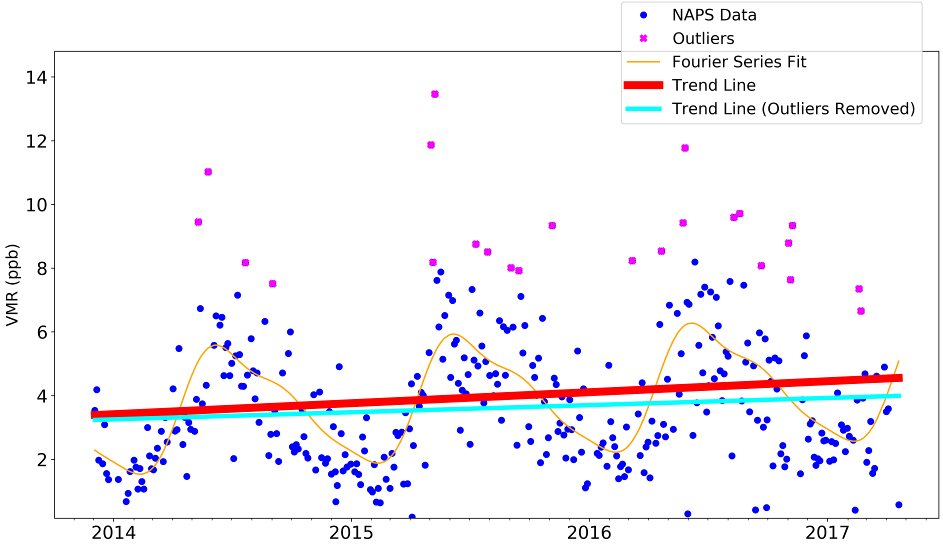

Figure 5.1: Time series of NAPS NH_3 surface VMR from 2013 to 2017 with third-order Fourier series fit and linear trends.

Table 5.2: Comparison of NH_3 trends and 2σ confidence intervals observed in Toronto. All trends are in %/year.

Dataset	Timeframe	Trends	Trends without outliers	TAO trends during the same timeframe as either the NAPS or IASI data (with outliers)
TAO	2002-2019	3.56 ± 0.85	2.36 ± 0.57	-
NAPS	2013-2017	8.88 ± 5.08	6.40 ± 4.37	9.31 ± 5.73
IASI	2008-2018	8.38 ± 1.54	-	4.02 ± 1.42

are shown in Figure 5.2b (in these plots, FTIR data from the years where NAPS data were also available are plotted). The two measurements show similar seasonal cycles, with a maximum in May, and a minimum in December and January. There is a smaller secondary peak in November for both measurements. This may be due to late-season fertilizer application and cover crop growth. The Ontario Ministry of Agriculture, Food and Rural Affairs recommends applying fertilizer in spring and fall (Munroe et al., 2018). Correlation between the two datasets can be seen in Figure 5.3a, where each NAPS measurement is plotted against the average of FTIR measurements on that day (if any measurements are available). This simple comparison does not show a strong correlation, with $R = 0.51$, and slope = 0.501. However, resampling the measurements by 15-day averages (Figure 5.3b), 18-day averages (Figure 5.3c), 24-day averages (Figure 5.3d) and by monthly averages (Figure 5.3e), show stronger correlations. Resampling to 15-day averages show better correlation with $R = 0.63$, and a larger slope = 0.707. Averaging to every 18 days and 24 days leads to $R = 0.68$ and 0.72, respectively. Monthly averages show the highest correlation with $R = 0.75$, and a slope = 0.758. This indicates that the FTIR and NAPS see similar low-frequency variabilities (period of 2 weeks or longer) in NH_3.

It should be noted that a bias would be expected to be observed between the FTIR and NAPS data, as the FTIR can only make measurements during sunny conditions, while NAPS data are 24-hour averages, made once every three days. This means that NAPS data include observations made during nighttime and rainy conditions. This is noteworthy, as surface NH_3 concentrations may be affected by diurnal variability in the planetary boundary layer height.

Temperature may also affect NH_3 enhancement events. When coincident datasets were analyzed for enhancements, three days showed simultaneous enhancements (25 May 2014, 23 May 2016, 26 May 2016). On all three days, the daily average temperature (measured by the TAO weather station) was higher than the corresponding monthly average: 19.3 ± 2.8 °C (uncertainties indicate 1 standard deviation) on 25 May, 2014 vs. May 2014 monthly mean of 13.8 °C, and 19.6 ± 3.4 and 21.2 ± 2.8 °C for 23 May and 26 May, 2016, respectively, vs. the May 2016 monthly mean of 14.1 °C. This is unsurprising, given that increased NH_3 is correlated with higher temperatures (e.g., Meng et al., 2011). Since the FTIR can only make measurements on sunny days, its measurements may be biased high compared to NAPS, which makes measurements regardless of weather.

5.4 Comparison with IASI Observations

The time series of IASI NH_3 total columns (2008 to 2018) within 50 km of TAO is shown in Figure 5.4. The trend of these IASI measurements is 8.38 ± 1.43 %/year, where the error indicates the 2σ confidence interval obtained by bootstrap resampling

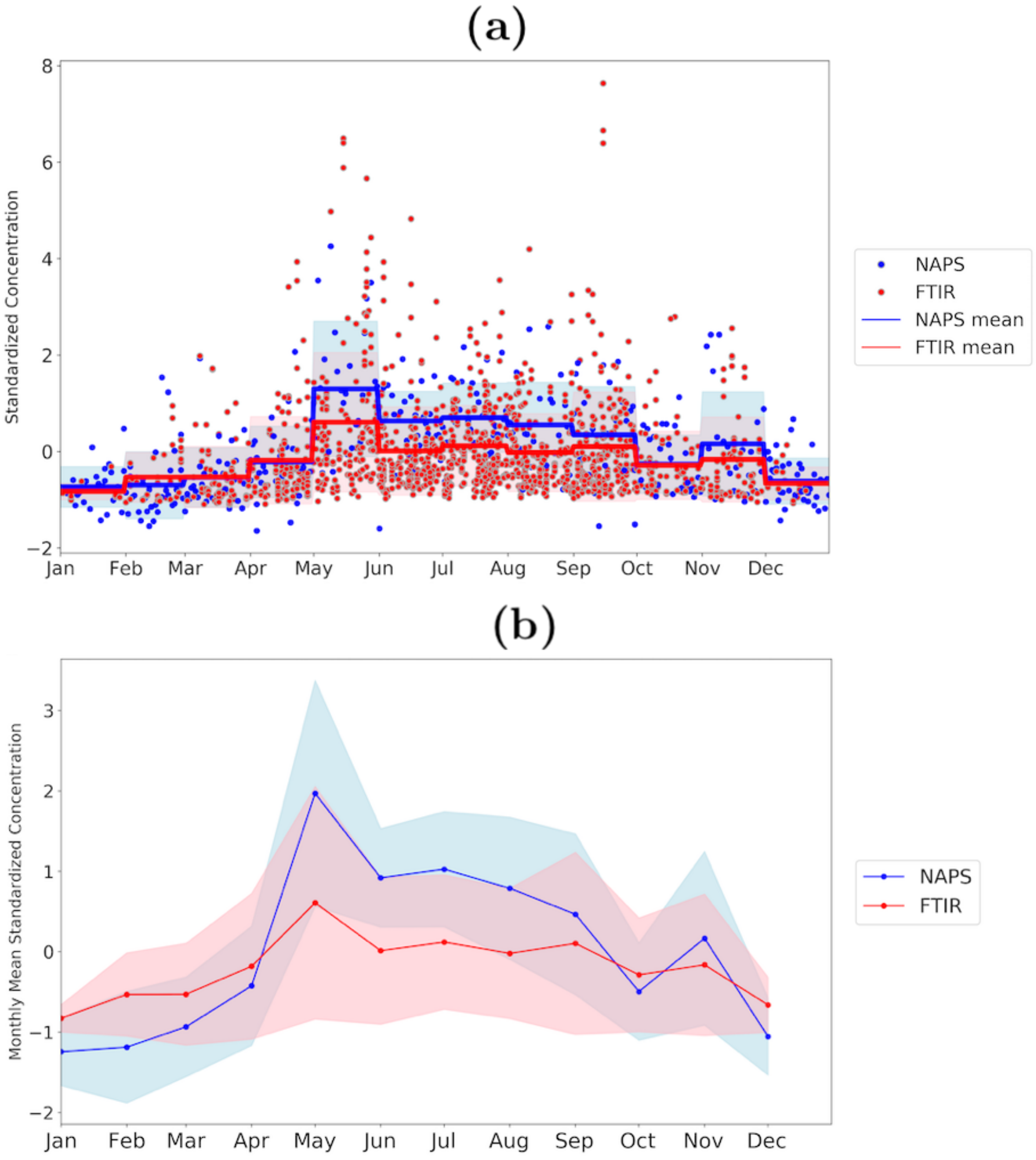

Figure 5.2: (a) Standardized FTIR total column and NAPS surface VMR of NH_3 plotted from January to December. Monthly averages and $\pm 1\sigma$ are indicated by the red and blue lines and shading for the FTIR and NAPS, respectively. (b) The standardized FTIR NH_3 total column (red) and NAPS surface NH_3 VMR (blue) monthly averages with their respective $\pm 1\sigma$ (shading). FTIR data from the years where NAPS data were also available (2013 to 2017) are plotted.

analysis. The Weatherhead et al. (1998) method for finding the statistical significance of this trend was not utilized here, as the analysis requires calculating the autocor-

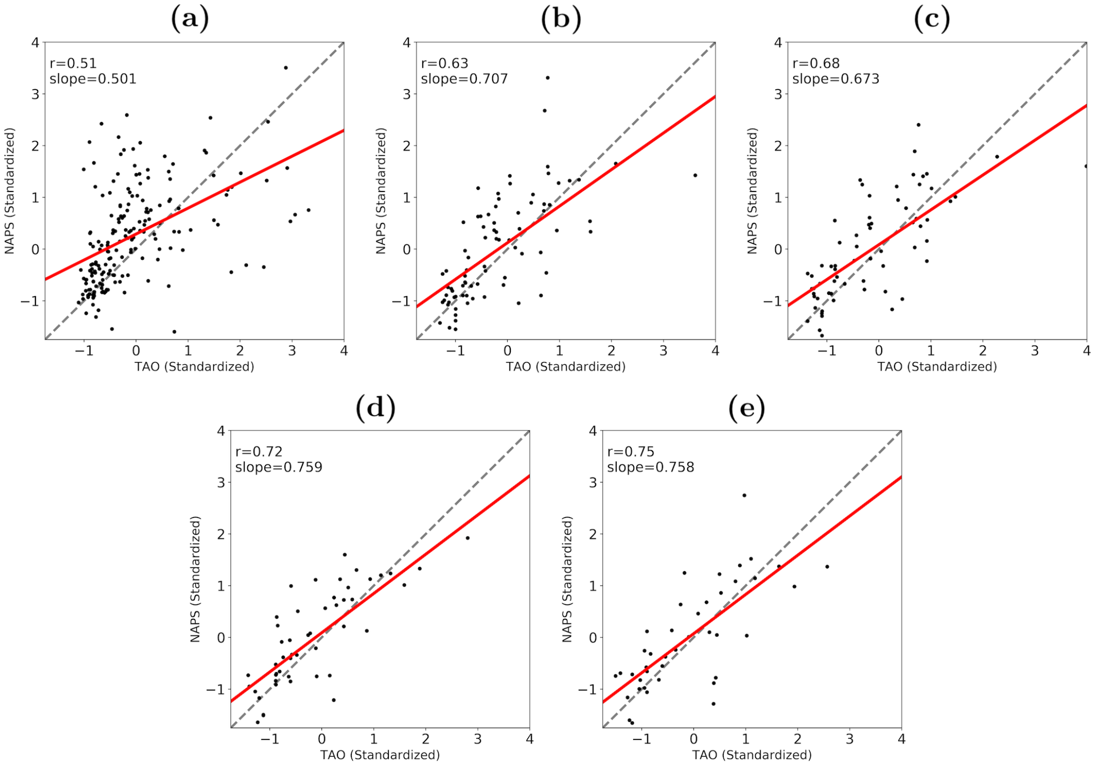

Figure 5.3: Standardized NAPS NH_3 surface VMR plotted against standardized FTIR NH_3 total column. (a) The raw comparison, where for each NAPS observation, the closest daily average FTIR measurement, if there are any within 72 hours, is plotted. FTIR and in-situ resampled to (b) 15-day, (c) 18-day, (d) 24-day and (e) monthly averages. The dashed lines indicate slope = 1, and the red lines indicate the fit to the data.

relation of data, which is not possible given the spatially scattered dataset. For comparison, the TAO FTIR trend over the same period is 4.02 ± 1.42 %/year.

The correlations between IASI and TAO FTIR NH_3 columns for the various coincidence criteria listed in Section 5.1.1 are shown in Table 5.3, along with the slopes, mean relative difference (MRD), and total number of data points. The MRD was calculated by subtracting the TAO FTIR column from the IASI column, then dividing by the TAO FTIR column (Dammers et al., 2016). To maximize the number of coincident data points, no significant data filtering (e.g., filtering by relative errors) was performed. The coincidence criteria used by Dammers et al. (2016) (90 minutes,

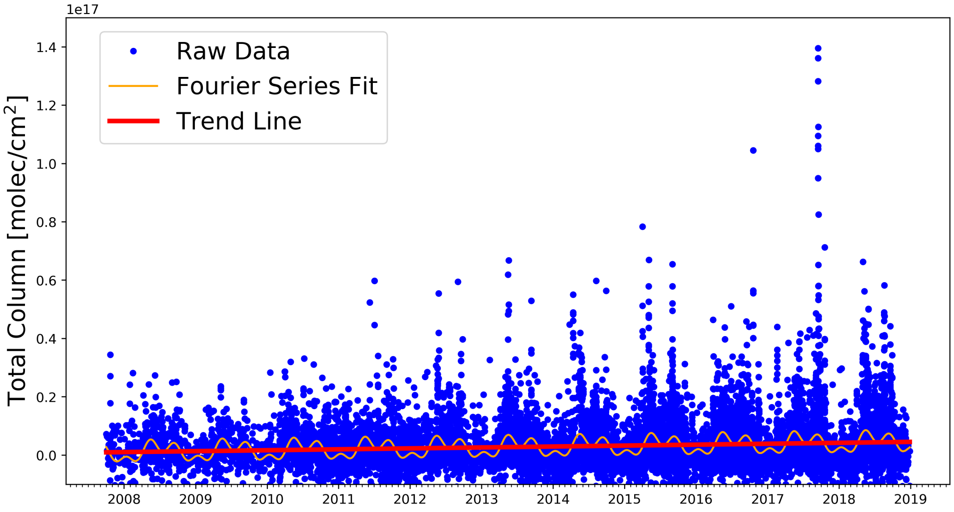

Figure 5.4: Time series of IASI NH_3 total columns measured within 50 km of TAO. The third-order Fourier series fit and the trend line are shown in orange and red, respectively.

25 km) result in a correlation with $R = 0.65$ and slope = 0.88 in this study, comparable to $R = 0.79$ and slope = 0.84 reported by Dammers et al. (2016). The MRD was -45.5 ± 207.2 % for this study, consistent with -46.0 ± 47.0 % calculated by Dammers et al. (2016) for TAO FTIR data. The larger standard deviation of the MRD in this work is most likely because the data used here were not filtered by relative errors.

The best correlation was achieved when using measurements made within 20 minutes and within 25 km of each other, which resulted in $R = 0.73$ and slope of 1.14. Coincidence criteria of 20 minutes and 50 km gave $R = 0.68$ and slope = 1.06. Criteria of 45 minutes and 50 km also show a correlation comparable to the 90 minutes, 25 km criteria, with $R = 0.64$ and slope = 0.92. This suggests that TAO FTIR measurements provide a good indicator of NH_3 concentrations on a city-wide scale ($\sim$ 50 km). This is also evident when looking at the correlation between TAO FTIR columns vs. daily averaged IASI measurements within 50 km, which had $R = 0.69$, although the slope was smaller, at 0.82. The better correlations seen with the stricter temporal criteria suggest that NH_3 near Toronto exhibits high-frequency variability. The values obtained in this study are also comparable to recent findings by Tournadre et al. (2020), who compared NH_3 columns from an FTIR stationed in Paris to IASI NH_3 columns. With 15 km and 30 minutes coincidence criteria, the FTIR in Paris showed a correlation of $R = 0.79$ and slope $= 0.73$. The same study also found that the FTIR in Paris is capable of providing information about NH_3 variability at a "regional" scale ($\sim$ 120 km) (Tournadre et al., 2020). Although not quantified in this study, the line-of-sight through the atmosphere (which changes throughout the day) may also affect the representative scale of ground-based solar-pointing FTIR observations. Additionally, the number of observations is relatively large for each criterion (e.g., $N = 923$ for 90 minutes, 25 km, while $N = 679$ for 45 minutes, 50 km), suggesting that the differences in correlation are not simply due to the differences in the number of data points.

The correlation plots for 20 min/25 km, 90 min/25 km, 20 min/50 km and 45 min/50 km are shown in Figures 5.5a, 5.5b, 5.5c and 5.5d, respectively. It should be noted that the slope was calculated through a simple linear least-squares regression. For comparison, an additional analysis was done propagating measurement uncertainty using the unified least squares procedure outlined by York et al. (2004) and yielded similar results, with a smaller slope for all cases due to the larger relative uncertainty on IASI measurements ($\sim$68 % for IASI compared to $\sim$19 % for TAO FTIR). Correlations for various coincidence criteria using the York method are listed in Table 5.4, and plots for 20 min/25 km, 90 min/25 km, 20 min/50 km and 45 min/50 km are shown in Figures 5.6a, 5.6b, 5.6c and 5.6d, respectively.

IASI column and NAPS surface NH_3 were also compared in this study by converting to standardized data (see Equation 5.1). Comparing the monthly means resulted in $R = 0.79$ and slope = 0.79 when looking at IASI measurements made within 50 km of NAPS, and $R = 0.74$ and slope = 0.74 for 30 km. Without temporal averaging, no significant correlation was found ($R \leq 0.27$) for any spatial coincidence criteria. This is in line with findings from Van Damme et al. (2015a), where significant correlation was found when comparing monthly averaged surface and IASI measurements. Van Damme et al. (2015a) report $R = 0.28$ when comparing IASI with an ensemble of surface observations over Europe, and R as high as 0.81 and 0.71 for measurements made at Fyodorovskoye, Russia and the Monte Bondone, Italy, respectively. It should be noted that the comparisons in Van Damme et al. (2015a) were done by converting IASI NH_3 columns to surface concentration by using the same model used in the retrieval process, as opposed to the standardized dataset approach used in this study.

5.5 GEOS-Chem Comparisons

The NH_3 total column from the GEOS-Chem CTM model grid cell containing Toronto (grid center at 44°N, 80°W) is shown in Figure 5.7a, along with TAO FTIR data. The correlation was obtained by comparing the hourly model data for each FTIR observation. Comparison with the FTIR data was done with and without smoothing the model data with the FTIR averaging kernel and a priori profile (Rodgers and Connor, 2003). As smoothing the model data only resulted in differ-

Table 5.3: IASI vs. TAO FTIR correlation coefficient, slope (regression standard error in parenthesis), MRD (1σ RMS in parenthesis) (in %), and number of data points, calculated for each TAO FTIR measurement, for varying spatial and temporal coincidence criteria.

Coincidence criteria	$\leq$ 25 km	$\leq$ 30 km	$\leq$ 50 km	$\leq$ 100 km
$\leq$ 20 minutes	R = 0.73 slope = 1.14 (0.06) MRD = -61.9 (161.6) % N = 314	R = 0.72 slope = 1.11 (0.06) MRD = -58.3 (156.7) % N = 337	R = 0.68 slope = 1.06 (0.06) MRD = -51.2 (166.1) % N = 384	R = 0.63 slope = 1.24 (0.08) MRD = -47.7 (190.9) % N = 421
$\leq$ 30 minutes	R = 0.71 slope = 1.06 (0.05) MRD = -48.1 (216.8) % N = 438	R = 0.70 slope = 1.04 (0.05) MRD = -43.1 (204.2) % N = 470	R = 0.65 slope = 0.98 (0.05) MRD = -42.0 (200.4) % N = 528	R = 0.59 slope = 1.07 (0.06) MRD = -40.9 (186.7) % N = 575
$\leq$ 45 minutes	R = 0.68 slope = 0.93 (0.04) MRD = -47.4 (198.2) % N = 588	R = 0.67 slope = 0.92 (0.04) MRD = -42.8 (190.6) % N = 623	R = 0.64 slope = 0.92 (0.04) MRD = -41.0 (185.5) % N = 679	R = 0.58 slope = 0.97 (0.05) MRD = -42.4 (177.9) % N = 732
$\leq$ 60 minutes	R = 0.66 slope = 0.89 (0.04) MRD = -46.4 (188.4) % N = 708	R = 0.65 slope = 0.90 (0.04) MRD = -42.8 (180.3) % N = 750	R = 0.62 slope = 0.89 (0.04) MRD = -38.2 (176.7) % N = 815	R = 0.56 slope = 0.93 (0.05) MRD = -40.7 (172.1) % N = 866
$\leq$ 90 minutes	R = 0.65 slope = 0.88 (0.03) MRD = -45.5 (207.2) % N = 923	R = 0.65 slope = 0.88 (0.03) MRD = -44.1 (192.4) % N = 967	R = 0.61 slope = 0.89 (0.04) MRD = -40.7 (193.5) % N = 1039	R = 0.56 slope = 0.93 (0.04) MRD = -36.9 (186.3) % N = 1093

Table 5.4: IASI vs. TAO FTIR correlation coefficient, error-weighted slopes using the York method (respective errors), MRD (1σ RMS in parenthesis) (in %), and number of data points, calculated for each TAO FTIR measurement, for varying spatial and temporal coincidence criteria.

Coincidence criteria	≤ 25 km	≤ 30 km	≤ 50 km	≤ 100 km
≤ 20 minutes	R = 0.70 slope = 0.81 (0.04) MRD = -61.9 (161.6) % N = 314	R = 0.68 slope = 0.78 (0.04) MRD = -58.3 (156.7) % N = 337	R = 0.65 slope = 0.79 (0.04) MRD = -51.2 (166.1) % N = 384	R = 0.57 slope = 0.72 (0.04) MRD = -47.7 (190.9) % N = 421
≤ 30 minutes	R = 0.68 slope = 0.79 (0.03) MRD = -48.1 (216.8) % N = 438	R = 0.67 slope = 0.76 (0.03) MRD = -43.1 (204.2) % N = 470	R = 0.63 slope = 0.78 (0.03) MRD = -42.0 (200.4) % N = 528	R = 0.55 slope = 0.72 (0.04) MRD = -40.9 (186.7) % N = 575
≤ 45 minutes	R = 0.66 slope = 0.80 (0.03) MRD = -47.4 (198.2) % N = 588	R = 0.65 slope = 0.76 (0.03) MRD = -42.8 (190.6) % N = 623	R = 0.62 slope = 0.75 (0.03) MRD = -41.0 (185.5) % N = 679	R = 0.55 slope = 0.71 (0.03) MRD = -42.4 (177.9) % N = 732
≤ 60 minutes	R = 0.64 slope = 0.76 (0.03) MRD = -46.4 (188.4) % N = 708	R = 0.63 slope = 0.74 (0.03) MRD = -42.8 (180.3) % N = 750	R = 0.60 slope = 0.73 (0.03) MRD = -38.2 (176.7) % N = 815	R = 0.53 slope = 0.68 (0.03) MRD = -40.7 (172.1) % N = 866
≤ 90 minutes	R = 0.64 slope = 0.78 (0.02) MRD = -45.5 (207.2) % N = 923	R = 0.64 slope = 0.76 (0.02) MRD = -44.1 (192.4) % N = 967	R = 0.59 slope = 0.73 (0.02) MRD = -40.7 (193.5) % N = 1039	R = 0.53 slope = 0.70 (0.02) MRD = -36.9 (186.3) % N = 1093

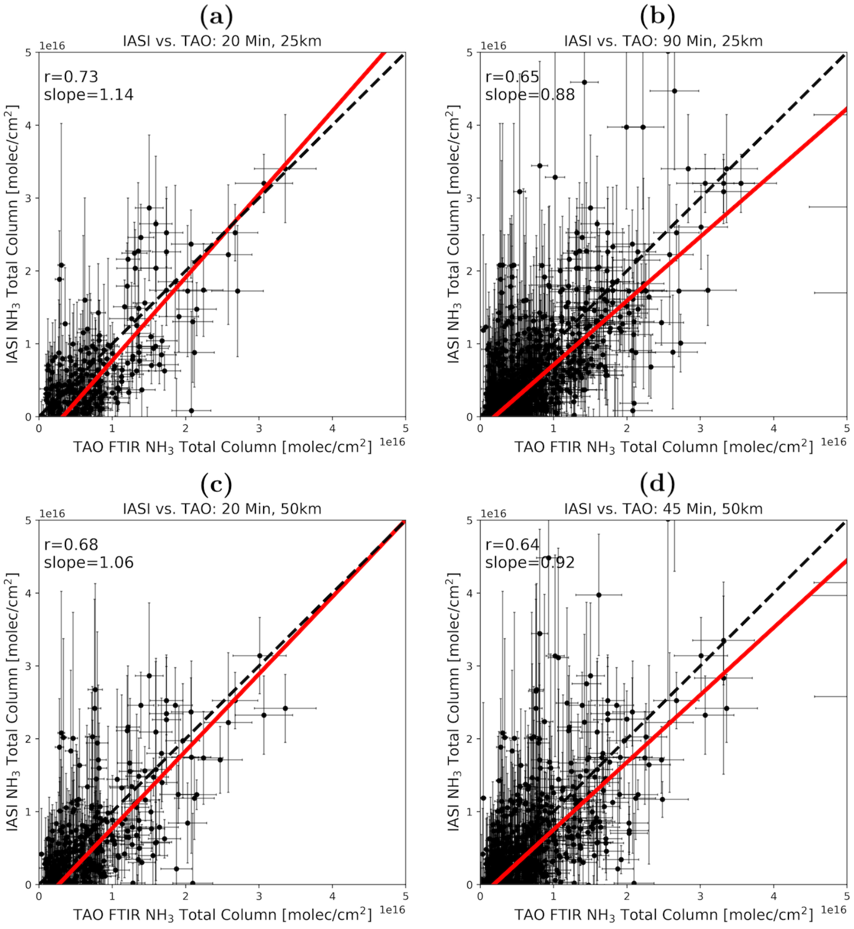

Figure 5.5: Correlation plots for IASI vs. TAO FTIR NH_3 total columns, with coincidence criteria of (a) 20 minutes and 25 km, (b) 90 minutes and 25 km, (c) 20 minutes and 50 km, and (d) 45 minutes and 50 km. Data from 2008 to 2018 are plotted. Dashed lines indicate slope = 1, while the red lines are the lines of best fit. Error bars are the reported observational uncertainties.

ences of less than 1 %, the discussion here will focus on the unsmoothed dataset to be consistent with the comparison with IASI. While GEOS-Chem is able to capture the seasonal cycle seen with the FTIR, the correlation is not strong, with $R =$ 0.51 and the coefficient of determination, R^2, at 0.26 (see Figure 5.8a). The calculated slope was 1.16. Both of these values are without smoothing the model data. Smoothing the data resulted in $R^2 = 0.28$, and slope = 1.01. It is likely that the model is too coarse (the 2° × 2.5° grid box corresponds to approximately 220 km × 200 km), and the

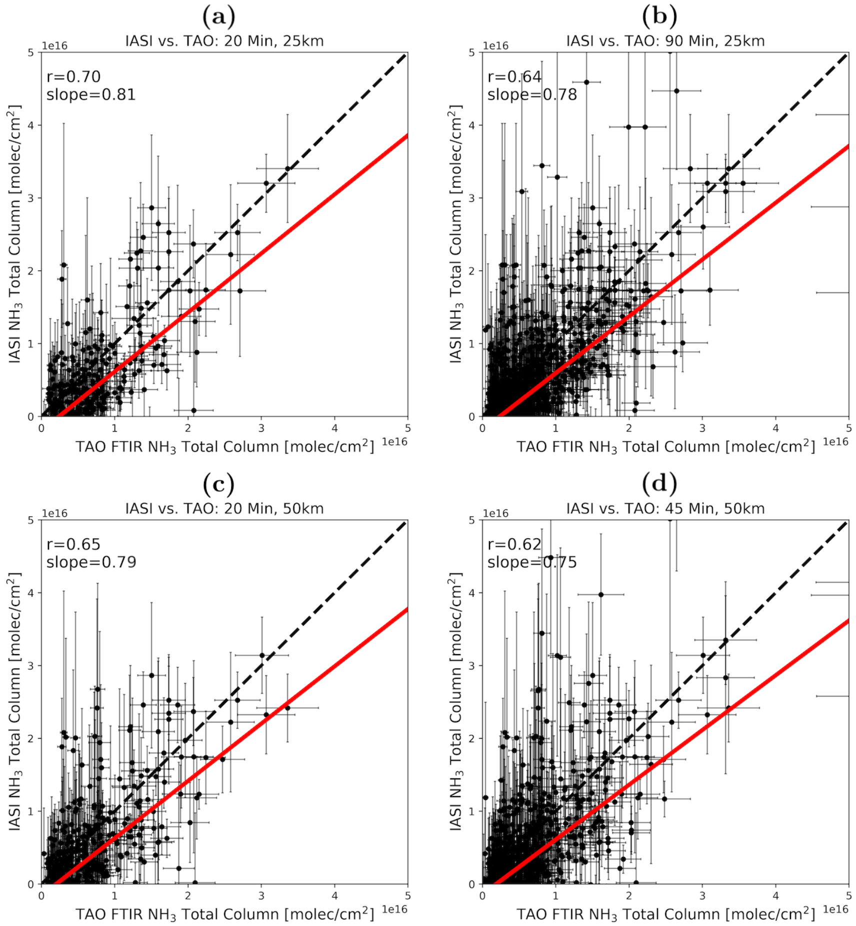

Figure 5.6: Error-weighted correlation plots for IASI vs. TAO FTIR NH_3 total columns using the York method, with coincidence criteria of (a) 20 minutes and 25 km, (b) 90 minutes and 25 km, (c) 20 minutes and 50 km, and (d) 45 minutes and 50 km. Data from 2008 to 2018 are plotted. Dashed lines indicate slope = 1, while the red lines are the lines of best fit. Error bars are the reported observational uncertainties.

FTIR, while able to capture larger-scale variability in NH_3 than in-situ observations, is not sensitive to observations at spatial scales of 100 km or larger. Given the short lifetime of NH_3, it is unsurprising to see large variability at these spatial scales.

For comparison with IASI, a larger domain was chosen to assess the correlation of the model and satellite observations at a larger regional scale. Model grids spanning 35°N to 53°N, and 93.75°W to 63.75°W were used for the analysis, as these grids capture Toronto, the Great Lakes, and the Atlantic Ocean coastline. The spatial

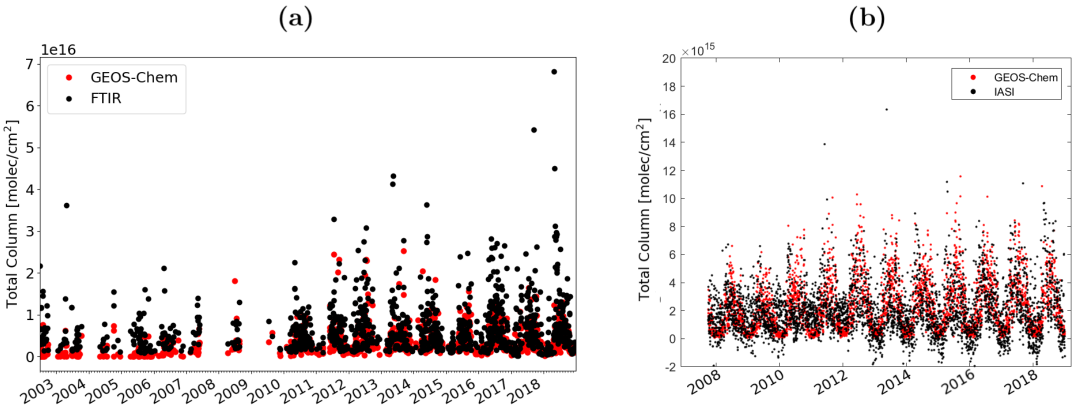

Figure 5.7: (a) GEOS-Chem and TAO FTIR NH$_3$ total columns from 2002 to 2018. GEOS-Chem data shown here were not smoothed with the FTIR averaging kernel and a priori profile. (b) GEOS-Chem and IASI NH$_3$ total columns (averaged over domain spanning from 35°N to 53°N, and 93.75°W to 63.75°W) from 2008 to 2018.

coincidence was calculated by binning the IASI data into the grids of GEOS-Chem, and temporal coincidence was determined by calculating the mean overpass time in the domain and averaging the model data between one hour before and one hour after the mean overpass time.

The time series (both GEOS-Chem and IASI were averaged over the domain) and correlation plots are shown in Figures 5.7b and 5.8b, respectively. Correlation of GEOS-Chem against IASI is higher than GEOS-Chem against TAO FTIR, with $R^2 = 0.33$ (see Figure 5.8b). Removing enhancement events from observational data led to poorer correlation with GEOS-Chem, with $R^2 = 0.22$ and $R^2 = 0.29$ for the FTIR and IASI, respectively (see Figures 5.8c and 5.8d). This can be contrasted to findings by Schiferl et al. (2016), who observed IASI and GEOS-Chem correlations (R) of 0.6-0.8 in the United States Great Plains and the Midwest during the summer.

In this study, the slope was 0.85, meaning NH$_3$ is overestimated in GEOS-Chem when compared to IASI at this scale. Comparing GEOS-Chem and IASI for one

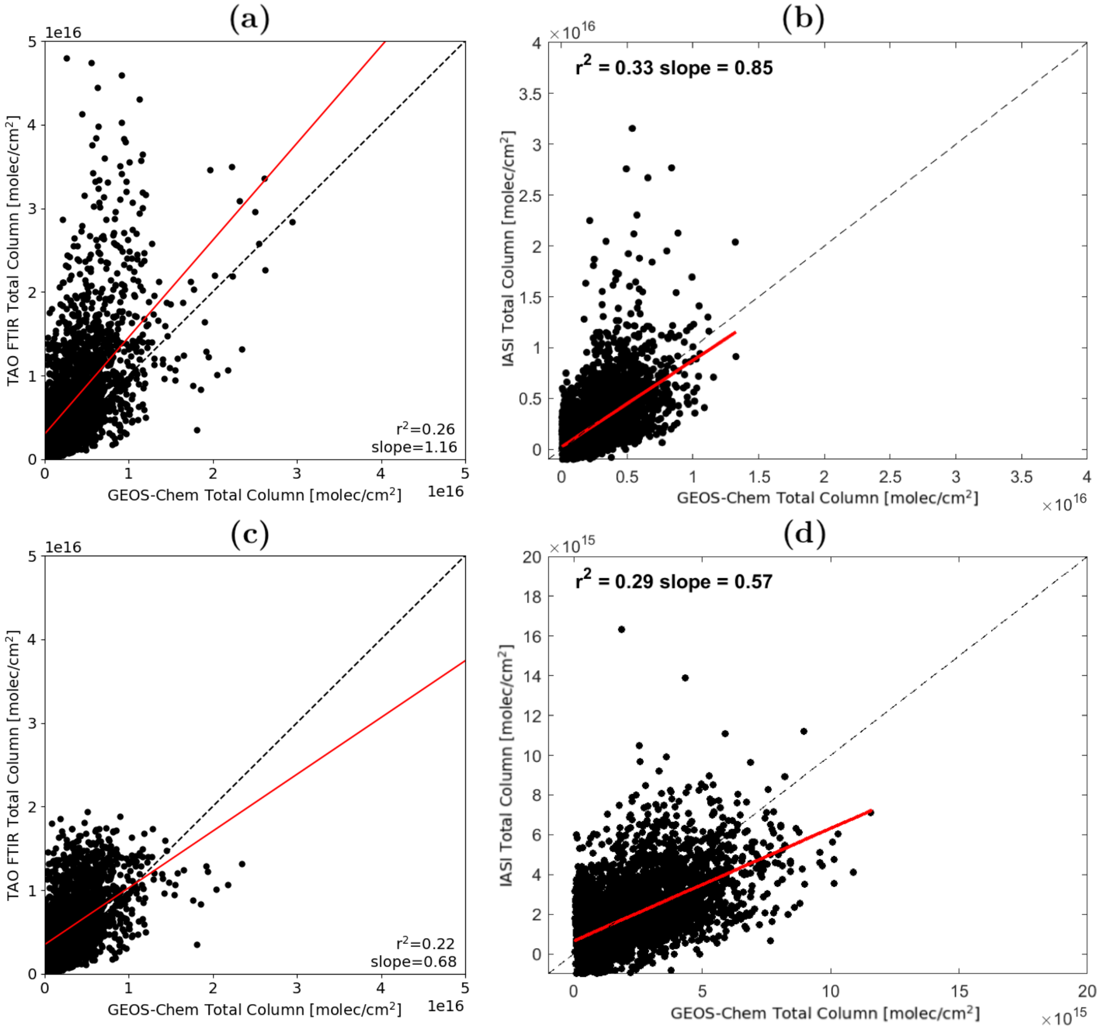

Figure 5.8: Correlation plots of (a) TAO FTIR vs. GEOS-Chem NH_3 total columns, (b) IASI vs. GEOS-Chem NH_3 total columns (c) TAO FTIR with enhancement events removed vs. GEOS-Chem NH_3 total columns, and (d) IASI with enhancement events removed vs. GEOS-Chem NH_3 total columns. Data from 2002 to 2018 are plotted for TAO and data from 2008 to 2018 are plotted for IASI.

grid cell over Toronto (same cell as the one used for comparison with TAO FTIR) resulted in a lower correlation, at $R^2 = 0.13$. These results suggest GEOS-Chem is able to model NH_3 on larger regional scales, but a finer resolution is needed for better comparison with smaller regions.

In addition, while the modeled NH_3 was overestimated in comparison with IASI over a larger regional domain, the comparison for the single grid box over Toronto resulted in slope = 2.44, meaning the model underestimated NH_3 in this smaller region, which may indicate underestimation of local NH_3 sources near Toronto in the model. This can be contrasted to recent findings by Van Damme et al. (2014a), who observed an overall underestimation of NH_3 in the LOTOS-EUROS model over Europe when compared against IASI. In a four-year period from 2008 to 2011 over the Netherlands, for example, IASI NH_3 columns are as high as 6.5 mg/m^2, while the modeled NH_3 go up to 5.2 mg/m^2 (Van Damme et al., 2014a).

5.6 Conclusions

TAO NH_3 total columns were examined in conjunction with other NH_3 observations (IASI column and NAPS in-situ surface VMR) and GEOS-Chem model data. Analysis of the FTIR NH_3 columns showed an upward annual trend of 3.56 ± 0.85 %/year and 2.36 ± 0.57 %/year over the period 2002-2019, with and without outliers, respectively. The larger trend with outliers included, along with a larger variance in the total column measurements in the later years, suggest that NH_3 enhancements are becoming more frequent and seasonal variability is increasing. These values are in agreement with trends observed by other studies. For example, Warner et al. (2017) observed a trend of 2.61 %/year from 2002 to 2016 over the USA using data from AIRS (at 918 hPa) aboard NASA's Aqua satellite, and Yu et al. (2018) derived surface NH_3 trends of ~5 %/year and ~5-12 %/year in the Western and Eastern United States from 2001 to 2016, respectively, using GEOS-Chem modeled NH_3.

Similar analysis of the NAPS in-situ time series (2013-2017) showed that NH_3 at the surface is also increasing, with an annual increase of 8.88 ± 5.08 %/year and 6.40 ± 4.37 %/year calculated with and without outliers, respectively. The FTIR total columns during the same period showed trends of 9.31 ± 5.73 %/year and 7.42 ± 4.48 %/year with and without outliers, respectively. The FTIR and NAPS comparisons showed that the FTIR columns are well correlated with surface NH_3 when resampled to monthly means to reduce high-frequency variability.

IASI NH_3 total columns measured within 50 km of TAO exhibited an annual trend of 8.38 ± 1.54 %/year from 2008 to 2018. For comparison, TAO FTIR NH_3 total columns over the same period showed a trend of 4.02 ± 1.42 %/year. The IASI columns were also compared against FTIR columns, with the largest correlations being obtained with distance criterion of ∼50 km, indicating that the TAO FTIR measurements are representative of NH_3 at a city-size scale. Comparing different coincidence criteria showed that, at least in Toronto, distance criteria can be larger than the 25 km used by Dammers et al. (2016), but temporal criteria may need to be stricter, at around ∼45 minutes (instead of 90 minutes). The highest correlation ($R = 0.73$) was seen with coincidence criteria of 25 km and 20 minutes.

TAO FTIR and IASI NH_3 columns were also compared with GEOS-Chem model data. The model did not show a very high correlation with the TAO FTIR for a single grid cell containing Toronto, with $R^2 = 0.26$, and $R^2 = 0.28$ when the model data were smoothed with the FTIR averaging kernels. The model comparison with IASI showed slightly better agreement on a domain spanning 35°N to 53°N, and 93.75°W to 63.75°W, with $R^2 = 0.33$. These results suggest that TAO FTIR mesasurements, representative of NH_3 at a city-size scale (∼50 km), require higher-resolution model runs for comparison. This is also evident when comparing GEOS-Chem against IASI within the single model grid cell that includes TAO; this comparison led to a poorer correlation with $R^2 = 0.13$. In addition, GEOS-Chem overestimated NH_3 in the larger domain when compared with IASI. However, in the single grid cell over TAO, the model underestimated NH_3 columns compared to both IASI and TAO FTIR.

This study showed a positive trend of NH_3 over Toronto derived from ground-based FTIR, satellite, and in-situ measurements. The NH_3 total columns using an FTIR situated in downtown Toronto are representative of a city-size scale, although this also highlights the need for models simulating NH_3 to be run at higher resolution than $2° \times 2.5°$ for comparisons with ground-based measurements.

Chapter 6

Conclusions and Future Work

6.1 Conclusions

Ground-based FTIR spectroscopy is a powerful technique for remote sounding of the atmosphere, and can be used to simultaneously measure the concentrations of multiple trace gases. The FTIR spectrometer situated at TAO in downtown Toronto, Ontario, Canada has been operational since mid-2002, making total column measurements of C_2H_2, C_2H_6, CH_4, CH_3OH, CO, H_2CO, HCl, HCN, HCOOH, HF, HNO_3, N_2O, NH_3 and O_3. In this thesis, the total column time series of these gases, along with supplementary observations and model simulations, were used to address the scientific objectives presented in Chapter 1, which were: (1) To quantify trends in the time series of trace gas concentrations over Toronto, and for CO, to examine if it is possible to identify what drives the trend. (2) To determine how emissions from biomass burning events affect air quality over Toronto, and whether observations in Toronto can be used to quantify wildfire emissions. (3) To examine the spatial representativeness and temporal variability of the FTIR NH_3 columns in Toronto. The datasets and model data were examined for trends, biomass burning enhancements, and to discern the representativeness of the FTIR NH_3 columns, as well as the temporal variability of NH_3 in Toronto.

To address the first scientific objective, time series data of the TAO FTIR total columns were analyzed to identify trends. Trends and enhancement events were determined by fitting trended Fourier series, and bootstrapping was used to identify the statistical significance. Bootstrap reanalysis resulted in statistically robust trends for most species retrieved at TAO, with the exception of CH_3OH and H_2CO. Trends from 2002 to 2019 (%/year, with 2σ uncertainties) were found for C_2H_2 (-1.12 ± 0.30), C_2H_6 (-0.74 ± 0.73 from 2002-2008 and 1.19 ± 0.27 from 2009-2019), CH_4 (0.26 ± 0.10 from 2002-2008 and 0.41 ± 0.03 from 2009-2019), CO (-0.90 ± 0.07), HCN (-0.51 ± 0.21), HCOOH (-2.15 ± 0.64), HF (0.59 ± 0.11), HNO_3 (0.36 ± 0.13), N_2O (0.28 ± 0.02) and NH_3 (3.56 ± 0.85).

The GEOS-Chem chemical transport model showed that the largest contributor to CH_4 near TAO was wetland emissions (average relative contribution of 31.7 %), and that CH_4 oxidation was a major source of CO (accounting for 30.9 %). The GEOS-Chem tagged CO simulation showed that contributions from Asian fossil fuel sources increased, while that from North America decreased, at rates of 0.37 ± 0.08 and -2.64 ± 0.18 %/year, respectively from 2003 to 2018. North American biomass burning contributions showed an increasing trend of 1.56 ± 0.47 %/year.

To address the second scientific objective, five species in particular, CO, HCN, C_2H_6, CH_3OH, and HCOOH, were examined for biomass burning enhancements. The data showed simultaneous enhancements of CO, HCN and C_2H_6 during events in 2012, 2015 and 2017. FLEXPART back-trajectories were used in conjunction with the MODIS Burned Area data product for source attribution, and emission ratios and emission factors for HCN and C_2H_6 (along with CH_3OH and HCOOH for the 2015 and 2017 events) were calculated. HCN emission ratios range between 0.0037 ± 0.0003 and 0.0057 ± 0.0008, while C_2H_6 emission ratios vary from 0.00122 ± 0.0015 to 0.019 ± 0.001.

Enhanced columns of CH_3OH and HCOOH were also observed during the 2015 and 2017 events, and an attempt was made to estimate emission ratios for these species, but it should be noted that these species have other sources and have much shorter lifetimes than HCN and C_2H_6, potentially resulting in large biases. Overall, TAO columns for both CH_3OH and HCOOH were found to be higher than those from smaller urban sites like Wollongong (Paton-Walsh et al., 2008) and remote sites like Eureka (Viatte et al., 2014). CH_3OH and HCOOH both have maxima in the summer months as well, which is likely the result of increased biogenic emissions (Millet et al., 2008; Stavrakou et al., 2011; Millet et al., 2015).

A GEOS-Chem tagged CO run showed that anthropogenic CO was the single largest source of background CO over Toronto, accounting for 14.0 ± 4.0 % of the total CO. However, during biomass burning enhancement events, the fires can contribute more CO to the total column over Toronto than anthropogenic sources, with contributions as large as 39.8 % from boreal North America for the 2017 event.

Lastly, to address the third scientific objective, TAO NH_3 total columns were examined in conjunction with, and compared against, IASI total column NH_3 and NAPS in-situ surface NH_3 VMR, as well as GEOS-Chem model data. All three measurement time series showed positive trends in NH_3 over Toronto. FTIR columns showed an increasing trend of 3.56 ± 0.85 %/year and 2.36 ± 0.57 % over the period 2002-2019, with and without outliers, respectively. The larger trend with outliers included, along with a larger variance in the total column measurements in the later years, suggest that NH_3 enhancements are becoming more frequent and seasonal variability is increasing. Surface in-situ measurements of NH_3 increased at 8.88 ± 5.08 %/year from 2013 to 2017, and IASI columns at 8.38 ± 1.54 %/year from 2008 to 2018.

To assess the representative scale of the FTIR NH_3 columns, correlations between the datasets were examined. The best correlation between FTIR and IASI was obtained with coincidence criteria of $\leq$ 25 km and $\leq$ 20 minutes, with $R = 0.73$ and a slope of 1.14 ± 0.06. Comparing different coincidence criteria showed that, at least in Toronto, distance criteria can be larger than the 25 km used by Dammers et al. (2016), but temporal criteria may need to be stricter, at around ∼45 minutes (instead of 90 minutes). Overall, good correlations were obtained with distance criterion of ∼50 km, indicating that the TAO FTIR measurements are representative of NH_3 at a city-size scale. Additionally, FTIR column and in-situ measurements were standardized and correlated. Comparison of 24-day averages and monthly averages resulted in correlation coefficients of $R = 0.72$ and $R = 0.75$, respectively, although correlation without averaging to reduce high-frequency variability led to a poorer correlation, with $R = 0.39$.

The GEOS-Chem full chemistry model NH_3 was compared against FTIR and IASI to assess model performance and investigate correlations of model output, with both local column measurements (FTIR) and measurements on a regional scale (IASI). Comparisons on a regional scale (a domain spanning 35°N to 53°N, and 93.75°W to 63.75°W) resulted in $R^2 = 0.33$, but comparing a single model grid point against the FTIR resulted in a poorer correlation, with $R^2 = 0.13$, indicating that a finer spatial resolution is needed for modeling NH_3.

Continued atmospheric monitoring is essential for determining atmospheric composition and understanding trace gas trends, as well as for evaluating emissions from wildfires and anthropogenic activities such as oil and gas production. TAO FTIR measurements over 18 years enabled the determination of trends of 14 species, including stratospheric gases, tropospheric pollutants, and greenhouse gases.

6.2 Future Work

Monitoring the atmosphere is a continuous effort, and the DA8 FTIR at TAO requires manual operations to start measurements, as well as routine maintenance for smooth operations. The tracker could be improved as a future project, as it is known to have several bugs that result in instrument downtime. Additionally, introducing some level of automation to the spectra quality control procedure that is usually done at the end of the day (after measurements) may improve the quality and consistency of overall retrievals, as the procedure is currently done by hand, and may be subject to different standards depending on the instrument operator for that day.

Aside from continuing ongoing measurements, there are several suggestions for future work. The first is to more thoroughly examine the column data from 2020 for the effects on air quality of the lockdown due to the COVID-19 pandemic. The lockdown has had large effects on the economy and industrial productivity, leading to reduced emissions of polluting species (e.g., Miyazaki et al., 2020). Further discussion of the lockdown, along with preliminary results examining TAO CO, tropospheric O_3 and NH_3 are presented in Section 3.10.

Another suggestion for future work is to restart measurements with the DA8 FTIR stationed at Environment and Climate Change Canada's Centre for Atmospheric Research Experiments (CARE) in Egbert, Ontario. The Egbert site is located at 44.23° N, 79.78° W, 251 masl, about 90 km northwest of TAO. The spectrometer at Egbert began making measurements in 1996, but has not been operational since 2010. In 2019, a new solar tracker was installed by our group, and an SFIT4 retrieval environment was set up in an effort to resume measurements at Egbert (previous retrievals were done with SFIT2, an older version of the retrieval algorithm). Efforts to resume regular measurements have been interrupted due to the COVID-19 pandemic, which has restricted access to CARE. While Egbert is relatively close to TAO, it is located in a rural area, and thus measurements at Egbert are thought to be subject to similar long-range transport, but with fewer local sources, other than possible additional agricultural sources (Whaley, 2014). Once regular measurements resume at Egbert, the dataset can complement the TAO time series.

There are several followup studies to the results presented in this thesis that may be undertaken as future projects. In Chapter 3, GEOS-Chem tagged CO and CH_4 runs were used to determine major sources of CO and CH_4 over Toronto. This can be expanded upon by performing simulations with more specific tags. For example, CO from North American anthropogenic sources can be divided up into Canada, and

Western, Central, and Eastern US. GEOS-Chem also offers a tagged O_3 simulation, which can be used to determine major sources of O_3 over Toronto. Additionally, a more in-depth analysis of TAO CH_4 and C_2H_6 can be done to identify sources of trends, and a study investigating the drivers of the negative trend of HCN seen at TAO can be performed. The method used in Chapter 4 to estimate biomass burning emissions can be used to analyze the biomass burning plume observed in September 2020 that was briefly discussed in Section 3.10. In Chapter 5, trend analysis was performed on NAPS NH_3; since the NAPS program measures numerous other species, a similar analysis can be applied to these measurements. Lastly, in the same chapter, it was found that the GEOS-Chem model at $2° \times 2.5°$ resolution was too coarse for comparisons with TAO FTIR NH_3. Since GEOS-Chem can be run in a higher-resolution "nested" mode, a natural next step is to do a similar comparison study with a higher resolution run (e.g., $0.25° \times 0.3125°$).

Bibliography

Akagi, S. K., Yokelson, R. J., Wiedinmyer, C., Alvarado, M. J., Reid, J. S., Karl, T., Crounse, J. D., and Wennberg, P. O.: Emission factors for open and domestic biomass burning for use in atmospheric models, Atmospheric Chemistry and Physics, 11, 4039–4072, https://doi.org/10.5194/acp-11-4039-2011, 2011.

Akagi, S. K., Yokelson, R. J., Burling, I. R., Meinardi, S., Simpson, I., Blake, D. R., McMeeking, G. R., Sullivan, A., Lee, T., Kreidenweis, S., Urbanski, S., Reardon, J., Griffith, D. W. T., Johnson, T. J., and Weise, D. R.: Measurements of reactive trace gases and variable O_3 formation rates in some South Carolina biomass burning plumes, Atmospheric Chemistry and Physics, 13, 1141–1165, https://doi.org/10.5194/acp-13-1141-2013, 2013.

Andreae, M. O.: Emission of trace gases and aerosols from biomass burning – an updated assessment, Atmospheric Chemistry and Physics, 19, 8523–8546, https://doi.org/10.5194/acp-19-8523-2019, 2019.

Andreae, M. O. and Merlet, P.: Emission of trace gases and aerosols from biomass burning, Global Biogeochemical Cycles, 15, 955–966, https://doi.org/10.1029/2000GB001382, 2001.

Angelbratt, J., Mellqvist, J., Blumenstock, T., Borsdorff, T., Brohede, S., Duchatelet, P., Forster, F., Hase, F., Mahieu, E., Murtagh, D., Petersen, A. K., Schneider, M., Sussmann, R., and Urban, J.: A new method to detect long term trends of methane (CH_4) and nitrous oxide (N_2O) total columns measured within the NDACC ground-based high resolution solar FTIR network, Atmospheric Chemistry and Physics, 11, 6167–6183, https://doi.org/10.5194/acp-11-6167-2011, 2011a.

Angelbratt, J., Mellqvist, J., Simpson, D., Jonson, J. E., Blumenstock, T., Borsdorff, T., Duchatelet, P., Forster, F., Hase, F., Mahieu, E., De Mazière, M., Notholt, J., Petersen, A. K., Raffalski, U., Servais, C., Sussmann, R., Warneke, T., and Vigouroux, C.: Carbon monoxide (CO) and ethane (C_2H_6) trends from ground-based solar FTIR measurements at six European stations, comparison and sensitivity analysis with the EMEP model, Atmospheric Chemistry and Physics, 11, 9253–9269, https://doi.org/10.5194/acp-11-9253-2011, 2011b.

Archer, D., Kheshgi, H., and Maier-Reimer, E.: Multiple timescales for neutralization of fossil fuel CO_2, Geophysical Research Letters, 24, 405–408, https://doi.org/10.1029/97GL00168, 1997.

Bader, W., Bovy, B., Conway, S., Strong, K., Smale, D., Turner, A. J., Blumenstock, T., Boone, C., Collaud Coen, M., Coulon, A., Garcia, O., Griffith, D. W. T., Hase, F., Hausmann, P., Jones, N., Krummel, P., Murata, I., Morino, I., Nakajima, H., O'Doherty, S., Paton-Walsh, C., Robinson, J., Sandrin, R., Schneider, M., Servais, C., Sussmann, R., and Mahieu, E.: The recent increase of atmospheric methane from 10 years of ground-based NDACC FTIR observations since 2005, Atmospheric

Chemistry and Physics, 17, 2255–2277, https://doi.org/10.5194/acp-17-2255-2017, 2017.

Baray, S., Darlington, A., Gordon, M., Hayden, K. L., Leithead, A., Li, S.-M., Liu, P. S. K., Mittermeier, R. L., Moussa, S. G., O'Brien, J., Staebler, R., Wolde, M., Worthy, D., and McLaren, R.: Quantification of methane sources in the Athabasca Oil Sands Region of Alberta by aircraft mass balance, Atmospheric Chemistry and Physics, 18, 7361–7378, https://doi.org/10.5194/acp-18-7361-2018, 2018.

Bauwens, M., Compernolle, S., Stavrakou, T., Müller, J.-F., van Gent, J., Eskes, H., Levelt, P. F., van der A, R., Veefkind, J. P., Vlietinck, J., Yu, H., and Zehner, C.: Impact of Coronavirus Outbreak on NO_2 Pollution Assessed Using TROPOMI and OMI Observations, Geophysical Research Letters, 47, e2020GL087 978, https://doi.org/10.1029/2020GL087978, 2020.

Bell, M., Dominici, F., and Samet, J.: A Meta-Analysis of Time-Series Studies of Ozone and Mortality With Comparison to the National Morbidity, Mortality, and Air Pollution Study, Epidemiology (Cambridge, Mass.), 16, 436–445, https://doi.org/10.1097/01.ede.0000165817.40152.85, 2005.

Bell, R.: Introductory Fourier Transform Spectroscopy, pp. 1–168, Academic Press, Cambridge, Massachusetts, United States, 1972.

Bernath, P.: Spectra of Atoms and Molecules, pp. 112–282, Oxford University Press, Oxford, United Kingdom, 2005.

Bernath, P., Steffen, J., Crouse, J., and Boone, C.: Sixteen-year trends in atmospheric trace gases from orbit, Journal of Quantitative Spectroscopy and Radiative Transfer, 253, 107 178, https://doi.org/10.1016/j.jqsrt.2020.107178, 2020.

Bobbink, R., Hicks, K., Galloway, J., Spranger, T., Alkemade, R., Ashmore, M., Bustamante, M., Cinderby, S., Davidson, E., Dentener, F., Emmett, B., Erisman, J.-W., Fenn, M., Gilliam, F., Nordin, A., Pardo, L., and De Vries, W.: Global assessment of nitrogen deposition effects on terrestrial plant diversity: a synthesis, Ecological Applications, 20, 30–59, https://doi.org/10.1890/08-1140.1, 2010.

Bouwman, A. F., Lee, D. S., Asman, W. A. H., Dentener, F. J., Van Der Hoek, K. W., and Olivier, J. G. J.: A global high-resolution emission inventory for ammonia, Global Biogeochemical Cycles, 11, 561–587, https://doi.org/10.1029/97GB02266, 1997.

Brewer, A.: Evidence for a World Circulation Provided by the Measurements of Helium and Water vapour Distribution in the Stratosphere, Quarterly Journal of the Royal Meteorological Society, 75, 351 363, https://doi.org/10.1002/qj.49707532603, 1949.

Bruhwiler, L. M., Basu, S., Bergamaschi, P., Bousquet, P., Dlugokencky, E., Houweling, S., Ishizawa, M., Kim, H.-S., Locatelli, R., Maksyutov, S., Montzka, S., Pandey, S., Patra, P. K., Petron, G., Saunois, M., Sweeney, C., Schwietzke, S., Tans, P., and Weatherhead, E. C.: U.S. CH_4 emissions from oil and gas production: Have recent large increases been detected?, Journal of Geophysical Research: Atmospheres, 122, 4070–4083, https://doi.org/10.1002/2016JD026157, 2017.

Buchholz, R. R., Deeter, M. N., Worden, H. M., Gille, J., Edwards, D. P., Hannigan,

J. W., Jones, N. B., Paton-Walsh, C., Griffith, D. W. T., Smale, D., Robinson, J., Strong, K., Conway, S., Sussmann, R., Hase, F., Blumenstock, T., Mahieu, E., and Langerock, B.: Validation of MOPITT carbon monoxide using ground-based Fourier transform infrared spectrometer data from NDACC, Atmospheric Measurement Techniques, 10, 1927–1956, https://doi.org/10.5194/amt-10-1927-2017, 2017.

Butchart, N.: The Brewer-Dobson circulation, Reviews of Geophysics, 52, 157–184, https://doi.org/10.1002/2013RG000448, 2014.

Canadell, J. G., Ciais, P., Dhakal, S., Dolman, H., Friedlingstein, P., Gurney, K. R., Held, A., Jackson, R. B., Quéré, C. L., Malone, E. L., Ojima, D. S., Patwardhan, A., Peters, G. P., and Raupach, M. R.: Interactions of the carbon cycle, human activity, and the climate system: a research portfolio, Current Opinion in Environmental Sustainability, 2, 301–311, https://doi.org/10.1016/j.cosust.2010.08.003, 2010.

Chameides, W. L. and Davis, D. D.: Aqueous-phase source of formic acid in clouds, Nature, 304, 427–429, https://doi.org/10.1038/304427a0, 1983.

Cheng, M.-D.: Atmospheric chemistry of hydrogen fluoride, Journal of Atmospheric Chemistry, 75, 1–16, https://doi.org/10.1007/s10874-017-9359-7, 2018.

Christian, T. J., Yokelson, R. J., Cárdenas, B., Molina, L. T., Engling, G., and Hsu, S.-C.: Trace gas and particle emissions from domestic and industrial biofuel use and garbage burning in central Mexico, Atmospheric Chemistry and Physics, 10, 565–584, https://doi.org/10.5194/acp-10-565-2010, 2010.

Cicerone, R. J. and Zellner, R.: The atmospheric chemistry of hydrogen cyanide (HCN), Journal of Geophysical Research: Oceans, 88, 10 689–10 696, https://doi.org/10.1029/JC088iC15p10689, 1983.

Clarisse, L., Van Damme, M., Clerbaux, C., and Coheur, P.-F.: Tracking down global NH_3 point sources with wind-adjusted superresolution, Atmospheric Measurement Techniques, 12, 5457–5473, https://doi.org/10.5194/amt-12-5457-2019, 2019a.

Clarisse, L., Van Damme, M., Gardner, W., Coheur, P.-F., Clerbaux, C., Whitburn, S., Hadji-Lazaro, J., and Hurtmans, D.: Atmospheric ammonia (NH_3) emanations from Lake Natron's saline mudflats, Scientific Reports, 9, 4441–4452, https://doi.org/10.1038/s41598-019-39935-3, 2019b.

Clerbaux, C., Boynard, A., Clarisse, L., George, M., Hadji-Lazaro, J., Herbin, H., Hurtmans, D., Pommier, M., Razavi, A., Turquety, S., Wespes, C., and Coheur, P.-F.: Monitoring of atmospheric composition using the thermal infrared IASI/MetOp sounder, Atmospheric Chemistry and Physics, 9, 6041–6054, https://doi.org/10.5194/acp-9-6041-2009, 2009.

Cohen, N. Y., Gerber, E. P., and Bühler, O.: What Drives the Brewer–Dobson Circulation?, Journal of the Atmospheric Sciences, 71, 3837–3855, https://doi.org/10.1175/JAS-D-14-0021.1, 2014.

Colarco, P. R., Schoeberl, M. R., Doddridge, B. G., Marufu, L. T., Torres, O., and Welton, E. J.: Transport of smoke from Canadian forest fires to the surface near Washington, D.C.: Injection height, entrainment, and optical properties, Journal of Geophysical Research: Atmospheres, 109, D06 203, https://doi.org/10.1029/2003JD004248, 2004.

Connecticut Department of Energy and Environmental Protection: May 2016 Ozone Exceptional Event Analysis Technical Support Document, Tech. rep., Connecticut Department of Energy and Environmental Protection, URL: `https://www.ct.gov/deep/cwp/view.asp?a=2684&Q=591378` (last accessed: November, 2020), 2017.

Connes, J. and Connes, P.: Near-Infrared Planetary Spectra by Fourier Spectroscopy. I. Instruments and Results, Journal of the Optical Society of America, 56, 896–910, https://doi.org/10.1364/JOSA.56.000896, 1966.

Coogan, S. C., Robinne, F.-N., Jain, P., and Flannigan, M. D.: Scientists' warning on wildfire - a Canadian perspective, Canadian Journal of Forest Research, 49, 1015–1023, https://doi.org/10.1139/cjfr-2019-0094, 2019.

Croft, B., Wentworth, G. R., Martin, R. V., Leaitch, W. R., Murphy, J. G., Murphy, B. N., Kodros, J. K., Abbatt, J. P. D., and Pierce, J. R.: Contribution of Arctic seabird-colony ammonia to atmospheric particles and cloud-albedo radiative effect, Nature Communications, 7, 13 444, https://doi.org/10.1038/ncomms13444, 2016.

Dammers, E., Vigouroux, C., Palm, M., Mahieu, E., Warneke, T., Smale, D., Langerock, B., Franco, B., Van Damme, M., Schaap, M., Notholt, J., and Erisman, J. W.: Retrieval of ammonia from ground-based FTIR solar spectra, Atmospheric Chemistry and Physics, 15, 12 789–12 803, https://doi.org/10.5194/acp-15-12789-2015, 2015.

Dammers, E., Palm, M., Van Damme, M., Vigouroux, C., Smale, D., Conway, S., Toon, G. C., Jones, N., Nussbaumer, E., Warneke, T., Petri, C., Clarisse, L., Clerbaux, C., Hermans, C., Lutsch, E., Strong, K., Hannigan, J. W., Nakajima, H., Morino, I., Herrera, B., Stremme, W., Grutter, M., Schaap, M., Wichink Kruit, R. J., Notholt, J., Coheur, P.-F., and Erisman, J. W.: An evaluation of IASI-NH_3 with ground-based Fourier transform infrared spectroscopy measurements, Atmospheric Chemistry and Physics, 16, 10 351–10 368, https://doi.org/10.5194/acp-16-10351-2016, 2016.

Dammers, E., McLinden, C. A., Griffin, D., Shephard, M. W., Van Der Graaf, S., Lutsch, E., Schaap, M., Gainairu-Matz, Y., Fioletov, V., Van Damme, M., Whitburn, S., Clarisse, L., Cady-Pereira, K., Clerbaux, C., Coheur, P. F., and Erisman, J. W.: NH_3 emissions from large point sources derived from CrIS and IASI satellite observations, Atmospheric Chemistry and Physics, 19, 12 261–12 293, https://doi.org/10.5194/acp-19-12261-2019, 2019.

Dobson, G. M. B.: Origin and Distribution of the Polyatomic Molecules in the Atmosphere, Proceedings of the Royal Society of London. Series A, Mathematical and Physical Sciences, 236, 187–193, https://doi.org/10.1098/rspa.1956.0127, 1956.

Duflot, V., Wespes, C., Clarisse, L., Hurtmans, D., Ngadi, Y., Jones, N., Paton-Walsh, C., Hadji-Lazaro, J., Vigouroux, C., De Mazière, M., Metzger, J.-M., Mahieu, E., Servais, C., Hase, F., Schneider, M., Clerbaux, C., and Coheur, P.-F.: Acetylene (C_2H_2) and hydrogen cyanide (HCN) from IASI satellite observations: global distributions, validation, and comparison with model, Atmospheric Chemistry and Physics, 15, 10 509–10 527, https://doi.org/10.5194/acp-15-10509-2015, 2015.

Enting, I., Wigley, T., and Heimann, M.: Future Emissions and Concentrations of

Carbon Dioxide: Key Ocean/atmosphere/land Analyses, pp. 108–129, Division of Atmospheric Research technical paper, CSIRO, Clayton, Victoria, Australia, 1994.

Erisman, J. W., Sutton, M. A., Galloway, J., Klimont, Z., and Winiwarter, W.: How a century of ammonia synthesis changed the world, Nature Geoscience, 1, 636–639, https://doi.org/10.1038/ngeo325, 2008.

Eyring, V., Waugh, D. W., Bodeker, G. E., Cordero, E., Akiyoshi, H., Austin, J., Beagley, S. R., Boville, B. A., Braesicke, P., Brühl, C., Butchart, N., Chipperfield, M. P., Dameris, M., Deckert, R., Deushi, M., Frith, S. M., Garcia, R. R., Gettelman, A., Giorgetta, M. A., Kinnison, D. E., Mancini, E., Manzini, E., Marsh, D. R., Matthes, S., Nagashima, T., Newman, P. A., Nielsen, J. E., Pawson, S., Pitari, G., Plummer, D. A., Rozanov, E., Schraner, M., Scinocca, J. F., Semeniuk, K., Shepherd, T. G., Shibata, K., Steil, B., Stolarski, R. S., Tian, W., and Yoshiki, M.: Multimodel projections of stratospheric ozone in the 21st century, Journal of Geophysical Research: Atmospheres, 112, D16 303, https://doi.org/10.1029/2006JD008332, 2007.

Fellget, P. B.: The multiplex advantage, Ph.D. thesis, University of Cambridge, Cambridge, United Kingdom, 1951.

Fisher, J. A., Murray, L. T., Jones, D. B. A., and Deutscher, N. M.: Improved method for linear carbon monoxide simulation and source attribution in atmospheric chemistry models illustrated using GEOS-Chem v9, Geoscientific Model Development, 10, 4129–4144, https://doi.org/10.5194/gmd-10-4129-2017, 2017.

Flannigan, M. and Cantin, A.: Climate change impacts on future boreal regimes, Forest Ecology and Management, 294, 35–44, https://doi.org/10.1016/j.foreco.2012.09.027, 2012.

Fortems-Cheiney, A., Dufour, G., Hamaoui-Laguel, L., Foret, G., Siour, G., Van Damme, M., Meleux, F., Coheur, P.-F., Clerbaux, C., Clarisse, L., Favez, O., Wallasch, M., and Beekmann, M.: Unaccounted variability in NH_3 agricultural sources detected by IASI contributing to European spring haze episode, Geophysical Research Letters, 43, 5475–5482, https://doi.org/10.1002/2016GL069361, 2016.

Fountoukis, C. and Nenes, A.: ISORROPIA II: a computationally efficient thermodynamic equilibrium model for K^+-Ca^{2+}-Mg^{2+}-$NH_4{}^+$-Na^+-$SO_4{}^{2-}$-$NO_3{}^-$-Cl^--H_2O aerosols, Atmospheric Chemistry and Physics, 7, 4639–4659, https://doi.org/10.5194/acp-7-4639-2007, 2007.

Franco, B., Mahieu, E., Emmons, L. K., Tzompa-Sosa, Z. A., Fischer, E. V., Sudo, K., Bovy, B., Conway, S., Griffin, D., Hannigan, J. W., Strong, K., and Walker, K. A.: Evaluating ethane and methane emissions associated with the development of oil and natural gas extraction in North America, Environmental Research Letters, 11, 044 010, https://doi.org/10.1088/1748-9326/11/4/044010, 2016a.

Franco, B., Marais, E. A., Bovy, B., Bader, W., Lejeune, B., Roland, G., Servais, C., and Mahieu, E.: Diurnal cycle and multi-decadal trend of formaldehyde in the remote atmosphere near 46°N, Atmospheric Chemistry and Physics, 16, 4171–4189, https://doi.org/10.5194/acp-16-4171-2016, 2016b.

Franco, B., Clarisse, L., Stavrakou, T., Müller, J.-F., Van Damme, M., Whitburn, S., Hadji-Lazaro, J., Hurtmans, D., Taraborrelli, D., Clerbaux, C., and Coheur, P.-F.: A General Framework for Global Retrievals of Trace Gases From IASI: Application to Methanol, Formic Acid, and PAN, Journal of Geophysical Research: Atmospheres, 123, 13 963–13 984, https://doi.org/10.1029/2018JD029633, 2018.

Franco, B., Clarisse, L., Stavrakou, T., Müller, J.-F., Taraborrelli, D., Hadji-Lazaro, J., Hannigan, J. W., Hase, F., Hurtmans, D., Jones, N., Lutsch, E., Mahieu, E., Ortega, I., Schneider, M., Strong, K., Vigouroux, C., Clerbaux, C., and Coheur, P.-F.: Spaceborne Measurements of Formic and Acetic Acids: A Global View of the Regional Sources, Geophysical Research Letters, 47, e2019GL086 239, https://doi.org/10.1029/2019GL086239, 2020.

Franklin, J.: Solar Absorption Spectroscopy at the Dalhousie Atmospheric Observatory, Ph.D. thesis, Dalhousie University, Halifax, Nova Scotia, Canada, permanent link: `https://dalspace.library.dal.ca//handle/10222/64642`, 2015.

Galloway, J. N., Aber, J. D., Erisman, J. W., Seitzinger, S. P., Howarth, R. W., Cowling, E. B., and Cosby, B. J.: The Nitrogen Cascade, BioScience, 53, 341–356, https://doi.org/10.1641/0006-3568(2003)053[0341:TNC]2.0.CO;2, 2003.

Gardiner, T., Forbes, A., de Mazière, M., Vigouroux, C., Mahieu, E., Demoulin, P., Velazco, V., Notholt, J., Blumenstock, T., Hase, F., Kramer, I., Sussmann, R., Stremme, W., Mellqvist, J., Strandberg, A., Ellingsen, K., and Gauss, M.: Trend analysis of greenhouse gases over Europe measured by a network of ground-based remote FTIR instruments, Atmospheric Chemistry and Physics, 8, 6719–6727, https://doi.org/10.5194/acp-8-6719-2008, 2008.

Gaubert, B., Arellano Jr., A. F., Barré, J., Worden, H. M., Emmons, L. K., Tilmes, S., Buchholz, R. R., Vitt, F., Raeder, K., Collins, N., Anderson, J. L., Wiedinmyer, C., Martinez Alonso, S., Edwards, D. P., Andreae, M. O., Hannigan, J. W., Petri, C., Strong, K., and Jones, N.: Toward a chemical reanalysis in a coupled chemistry-climate model: An evaluation of MOPITT CO assimilation and its impact on tropospheric composition, Journal of Geophysical Research: Atmospheres, 121, 7310–7343, https://doi.org/10.1002/2016JD024863, 2016.

Gaudel, A., Cooper, O., Ancellet, G., Barret, B., Boynard, A., Burrows, J., Clerbaux, C., Coheur, P.-F., Cuesta, J., Cuevas, E., Doniki, S., Dufour, G., Ebojie, F., Foret, G., Garcia, O., Granados Muños, M., Hannigan, J., Hase, F., Huang, G., Hassler, B., Hurtmans, D., Jaffe, D., Jones, N., Kalabokas, P., Kerridge, B., Kulawik, S., Latter, B., Leblanc, T., Le Flochmoën, E., Lin, W., Liu, J., Liu, X., Mahieu, E., McClure-Begley, A., Neu, J., Osman, M., Palm, M., Petetin, H., Petropavlovskikh, I., Querel, R., Rahpoe, N., Rozanov, A., Schultz, M., Schwab, J., Siddans, R., Smale, D., Steinbacher, M., Tanimoto, H., Tarasick, D., Thouret, V., Thompson, A., Trickl, T., Weatherhead, E., Wespes, C., Worden, H., Vigouroux, C., Xu, X., Zeng, G., and Ziemke, J.: Tropospheric Ozone Assessment Report: Present-day distribution and trends of tropospheric ozone relevant to climate and global atmospheric chemistry model evaluation, Elementa: Science of the Anthropocene, 6, 39, https://doi.org/10.1525/elementa.291, 2018.

Ghasemi, A. and Zahediasl, S.: Normality Tests for Statistical Analysis: A Guide for Non-Statisticians, International Journal of Endocrinology and Metabolism, 10, 486–489, https://doi.org/10.5812/ijem.3505, 2012.

Giannadaki, D., Pozzer, A., and Lelieveld, J.: Modeled global effects of airborne desert dust on air quality and premature mortality, Atmospheric Chemistry and Physics, 14, 957–968, https://doi.org/10.5194/acp-14-957-2014, 2014.

Giglio, L., Justice, C., Boschetti, L., and Roy, D.: MCD64A1 MODIS/Terra+Aqua Burned Area Monthly L3 Global 500m SIN Grid V006, Distributed by NASA EOSDIS Land Processes DAAC. https://doi.org/10.5067/MODIS/MCD64A1.006, 2015.

Goode, J. G., Yokelson, R. J., Ward, D. E., Susott, R. A., Babbitt, R. E., Davies, M. A., and Hao, W. M.: Measurements of excess O_3, CO_2, CO, CH_4, C_2H_4, C_2H_2, HCN, NO, NH_3, HCOOH, CH_3COOH, HCHO, and CH_3OH in 1997 Alaskan biomass burning plumes by airborne Fourier transform infrared spectroscopy (AFTIR), Journal of Geophysical Research: Atmospheres, 105, 22 147–22 166, https://doi.org/10.1029/2000JD900287, 2000.

Griffin, D., Walker, K. A., Franklin, J. E., Parrington, M., Whaley, C., Hopper, J., Drummond, J. R., Palmer, P. I., Strong, K., Duck, T. J., Abboud, I., Bernath, P. F., Clerbaux, C., Coheur, P.-F., Curry, K. R., Dan, L., Hyer, E., Kliever, J., Lesins, G., Maurice, M., Saha, A., Tereszchuk, K., and Weaver, D.: Investigation of CO, C_2H_6 and aerosols in a boreal fire plume over eastern Canada during BORTAS 2011 using ground- and satellite-based observations and model simulations, Atmospheric Chemistry and Physics, 13, 10 227–10 241, https://doi.org/10.5194/acp-13-10227-2013, 2013.

Griffiths, P., De Haseth, J., and Winefordner, J.: Fourier Transform Infrared Spectrometry, pp. 1–224, Chemical Analysis: A Series of Monographs on Analytical

Chemistry and Its Applications, John Wiley & Sons, Ltd, Hoboken, New Jersey, United States, 2007.

Hanke, M., Umann, B., Uecker, J., Arnold, F., and Bunz, H.: Atmospheric measurements of gas-phase HNO_3 and SO_2 using chemical ionization mass spectrometry during the MINATROC field campaign 2000 on Monte Cimone, Atmospheric Chemistry and Physics, 3, 417–436, https://doi.org/10.5194/acp-3-417-2003, 2003.

Hartmann, D. L.: Global Physical Climatology, Elsevier Science, Boston, Massachusetts, United States, 2nd edn., 2016.

Hase, F.: Improved instrumental line shape monitoring for the ground-based, high-resolution FTIR spectrometers of the Network for the Detection of Atmospheric Composition Change, Atmospheric Measurement Techniques, 5, 603–610, https://doi.org/10.5194/amt-5-603-2012, 2012.

Hay, W. W.: Experimenting on a Small Planet: A Scholarly Entertainment, Springer, Berlin, Heidelberg, 1st edn., https://doi.org/10.1007/978-3-642-28560-8, 2013.

Held, I. M. and Hou, A. Y.: Nonlinear Axially Symmetric Circulations in a Nearly Inviscid Atmosphere, Journal of Atmospheric Sciences, 37, 515 –533, https://doi.org/10.1175/1520-0469(1980)037⟨0515:NASCIA⟩2.0.CO;2, 1980.

Helmig, D., Rossabi, S., Hueber, J., Tans, P., Montzka, S. A., Masarie, K., Thoning, K., Plass-Duelmer, C., Claude, A., Carpenter, L., Lewis, A., Punjabi, S., Reimann, S., Vollmer, M. K., Steinbrecher, R., Hannigan, J., Emmons, L., Mahieu, E., Franco, B., and Pozzer, A.: Reversal of global atmospheric ethane and propane trends largely due to US oil and natural gas production, Nature Geoscience, 9, 490–495, https://doi.org/10.1038/NGEO2721, 2016.

Höpfner, M., Volkamer, R., Grabowski, U., Grutter, M., Orphal, J., Stiller, G., von Clarmann, T., and Wetzel, G.: First detection of ammonia (NH_3) in the Asian summer monsoon upper troposphere, Atmospheric Chemistry and Physics, 16, 14 357–14 369, https://doi.org/10.5194/acp-16-14357-2016, 2016.

Hu, Q., Zhang, L., Evans, G. J., and Yao, X.: Variability of atmospheric ammonia related to potential emission sources in downtown Toronto, Canada, Atmospheric Environment, 99, 365–373, https://doi.org/10.1016/j.atmosenv.2014.10.006, 2014.

Innocenti, F., Robinson, R., Gardiner, T., Finlayson, A., and Connor, A.: Differential Absorption Lidar (DIAL) Measurements of Landfill Methane Emissions, Remote Sensing, 9, 953, https://doi.org/10.3390/rs9090953, 2017.

IPCC: Climate Change 1995 - The Science of Climate Change, Cambridge University Press, Cambridge, United Kingdom, 1995.

IPCC: Changes in Atmospheric Constituents and in Radiative Forcing, pp. 129–144, Cambridge University Press, https://doi.org/10.1260/095830507781076194, 2007.

IPCC: Summary for Policymakers, pp. 1–30, Cambridge University Press, Cambridge, United Kingdom, https://doi.org/10.1017/CBO9781107415324.004, 2014.

Jacob, D. J.: Chemistry of OH in remote clouds and its role in the production of formic acid and peroxymonosulfate, Journal of Geophysical Research: Atmospheres, 91, 9807–9826, https://doi.org/10.1029/JD091iD09p09807, 1986.

Jacob, D. J.: Introduction to Atmospheric Chemistry, pp. 232–243, Princeton University Press, Princeton, New Jersey, United States, 1999.

Jacob, D. J.: Heterogeneous chemistry and tropospheric ozone, Atmospheric Environment, 34, 2131–2159, https://doi.org/10.1016/S1352-2310(99)00462-8, 2000.

Jacob, D. J., Field, B. D., Li, Q., Blake, D. R., de Gouw, J., Warneke, C., Hansel, A., Wisthaler, A., Singh, H. B., and Guenther, A.: Global budget of methanol: Constraints from atmospheric observations, Journal of Geophysical Research: Atmospheres, 110, D08 303, https://doi.org/10.1029/2004JD005172, 2005.

Jacobson, M. Z.: Effects of biomass burning on climate, accounting for heat and moisture fluxes, black and brown carbon, and cloud absorption effects, Journal of Geophysical Research: Atmospheres, 119, 8980–9002, https://doi.org/10.1002/2014JD021861, 2014.

Jacquinot, P., Dufour, C., and Rech, J.: Optical conditions in the use of photoelectric cells in spectrographs and interferometers, Centre national de la recherche scientifique, 6, 91, 1948.

Janssens-Maenhout, G., Crippa, M., Guizzardi, D., Muntean, M., Schaaf, E., Dentener, F., Bergamaschi, P., Pagliari, V., Olivier, J. G. J., Peters, J. A. H. W., van Aardenne, J. A., Monni, S., Doering, U., Petrescu, A. M. R., Solazzo, E., and Oreggioni, G. D.: EDGAR v4.3.2 Global Atlas of the three major greenhouse gas emissions for the period 1970-2012, Earth System Science Data, 11, 959–1002, https://doi.org/10.5194/essd-11-959-2019, 2019.

Jen, C. N., Hatch, L. E., Selimovic, V., Yokelson, R. J., Weber, R., Fernandez,

A. E., Kreisberg, N. M., Barsanti, K. C., and Goldstein, A. H.: Speciated and total emission factors of particulate organics from burning western US wildland fuels and their dependence on combustion efficiency, Atmospheric Chemistry and Physics, 19, 1013–1026, https://doi.org/10.5194/acp-19-1013-2019, 2019.

Johnson, T. J., Sams, R. L., Blake, T. A., Sharpe, S. W., and Chu, P. M.: Removing aperture-induced artifacts from fourier transform infrared intensity values, Applied Optics, 41, 2831–2839, https://doi.org/10.1364/AO.41.002831, 2002.

Jose, V. S., Sejian, V., Bagath, M., Ratnakaran, A. P., Lees, A. M., Al-Hosni, Y. A. S., Sullivan, M., Bhatta, R., and Gaughan, J. B.: Modeling of Greenhouse Gas Emission from Livestock, Frontiers in Environmental Science, 4, 27, https://doi.org/10.3389/fenvs.2016.00027, 2016.

Kaiser, J. W., Heil, A., Andreae, M. O., Benedetti, A., Chubarova, N., Jones, L., Morcrette, J.-J., Razinger, M., Schultz, M. G., Suttie, M., and van der Werf, G. R.: Biomass burning emissions estimated with a global fire assimilation system based on observed fire radiative power, Biogeosciences, 9, 527–554, https://doi.org/10.5194/bg-9-527-2012, 2012.

Kesik, T.: Best Practices Guide: Management of Inflow and Infiltration in New Urban Developments, Tech. rep., Institute for Catastrophic Loss Reduction, Toronto, Ontario, Canada, https://doi.org/10.13140/RG.2.1.4906.2240, 2015.

Kim, Y., Hatsushika, H., Muskett, R. R., and Yamazaki, K.: Possible effect of boreal wildfire soot on Arctic sea ice and Alaska glaciers, Atmospheric Environment, 39, 3513–3520, https://doi.org/10.1016/j.atmosenv.2005.02.050, 2005.

Kirchmeier-Young, M. C., Gillett, N. P., Zwiers, F. W., Cannon, A. J., and Anslow, F. S.: Attribution of the Influence of Human-Induced Climate Change on an Extreme Fire Season, Earth's Future, 7, 2–10, https://doi.org/10.1029/2018EF001050, 2019.

Kleeman, M. J., Hughes, L. S., Allen, J. O., and Cass, G. R.: Source Contributions to the Size and Composition Distribution of Atmospheric Particles: Southern California in September 1996, Environmental Science & Technology, 33, 4331–4341, https://doi.org/10.1021/es990632p, 1999.

Kohlhepp, R., Ruhnke, R., Chipperfield, M. P., De Mazière, M., Notholt, J., Barthlott, S., Batchelor, R. L., Blatherwick, R. D., Blumenstock, T., Coffey, M. T., Demoulin, P., Fast, H., Feng, W., Goldman, A., Griffith, D. W. T., Hamann, K., Hannigan, J. W., Hase, F., Jones, N. B., Kagawa, A., Kaiser, I., Kasai, Y., Kirner, O., Kouker, W., Lindenmaier, R., Mahieu, E., Mittermeier, R. L., Monge-Sanz, B., Morino, I., Murata, I., Nakajima, H., Palm, M., Paton-Walsh, C., Raffalski, U., Reddmann, T., Rettinger, M., Rinsland, C. P., Rozanov, E., Schneider, M., Senten, C., Servais, C., Sinnhuber, B.-M., Smale, D., Strong, K., Sussmann, R., Taylor, J. R., Vanhaelewyn, G., Warneke, T., Whaley, C., Wiehle, M., and Wood, S. W.: Observed and simulated time evolution of HCl, $ClONO_2$, and HF total column abundances, Atmospheric Chemistry and Physics, 12, 3527–3556, https://doi.org/10.5194/acp-12-3527-2012, 2012.

Krupa, S.: Atmosphere and agriculture in the new millennium, Environmental Pollution, 126, 293–300, https://doi.org/10.1016/S0269-7491(03)00242-2, 2003.

Lachatre, M., Fortems-Cheiney, A., Foret, G., Siour, G., Dufour, G., Clarisse, L., Clerbaux, C., Coheur, P.-F., Van Damme, M., and Beekmann, M.: The unintended consequence of SO_2 and NO_2 regulations over China: increase of ammonia levels and impact on $PM_{2.5}$ concentrations, Atmospheric Chemistry and Physics, 19, 6701–6716, https://doi.org/10.5194/acp-19-6701-2019, 2019.

Li, Q., Jacob, D. J., Yantosca, R. M., Heald, C. L., Singh, H. B., Koike, M., Zhao, Y., Sachse, G. W., and Streets, D. G.: A global three-dimensional model analysis of the atmospheric budgets of HCN and CH_3CN: Constraints from aircraft and ground measurements, Journal of Geophysical Research: Atmospheres, 108, D218 827, https://doi.org/10.1029/2002JD003075, 2003.

Li, Q., Palmer, P. I., Pumphrey, H. C., Bernath, P., and Mahieu, E.: What drives the observed variability of HCN in the troposphere and lower stratosphere?, Atmospheric Chemistry and Physics, 9, 8531–8543, https://doi.org/10.5194/acp-9-8531-2009, 2009.

Li, Y., Schwandner, F. M., Sewell, H. J., Zivkovich, A., Tigges, M., Raja, S., Holcomb, S., Molenar, J. V., Sherman, L., Archuleta, C., Lee, T., and Collett, J. L.: Observations of ammonia, nitric acid, and fine particles in a rural gas production region, Atmospheric Environment, 83, 80–89, https://doi.org/10.1016/j.atmosenv.2013.10.007, 2014.

Lieschke, K. J., Fisher, J. A., Paton-Walsh, C., Jones, N. B., Greenslade, J. W., Burden, S., and Griffith, D. W. T.: Decreasing Trend in Formaldehyde Detected

From 20-Year Record at Wollongong, Southeast Australia, Geophysical Research Letters, 46, 8464–8473, https://doi.org/10.1029/2019GL083757, 2019.

Link, M. F., Nguyen, T. B., Bates, K., Müller, J.-F., and Farmer, D. K.: Can Isoprene Oxidation Explain High Concentrations of Atmospheric Formic and Acetic Acid over Forests?, ACS Earth and Space Chemistry, 4, 730–740, https://doi.org/10.1021/acsearthspacechem.0c00010, 2020.

Liou, K.: An Introduction to Atmospheric Radiation, pp. 13–226, International Geophysics, Elsevier Science, Amsterdam, Netherlands, 2002.

Lisok, J., Rozwadowska, A., Pedersen, J. G., Markowicz, K. M., Ritter, C., Kaminski, J. W., Struzewska, J., Mazzola, M., Udisti, R., Becagli, S., and Gorecka, I.: Radiative impact of an extreme Arctic biomass-burning event, Atmospheric Chemistry and Physics, 18, 8829–8848, https://doi.org/10.5194/acp-18-8829-2018, 2018.

Liu, L., Zhang, X., Xu, W., Liu, X., Lu, X., Wang, S., Zhang, W., and Zhao, L.: Ground Ammonia Concentrations over China Derived from Satellite and Atmospheric Transport Modeling, Remote Sensing, 9, 247, https://doi.org/10.3390/rs9050467, 2017.

Liu, M., Huang, X., Song, Y., Tang, J., Cao, J., Zhang, X., Zhang, Q., Wang, S., Xu, T., Kang, L., Cai, X., Zhang, H., Yang, F., Wang, H., Yu, J. Z., Lau, A. K. H., He, L., Huang, X., Duan, L., Ding, A., Xue, L., Gao, J., Liu, B., and Zhu, T.: Ammonia emission control in China would mitigate haze pollution and nitrogen deposition, but worsen acid rain, Proceedings of the National Academy of Sciences, 116, 7760–7765, https://doi.org/10.1073/pnas.1814880116, 2019.

Lobert, J. M., Scharffe, D. H., Hao, W. M., and Crutzen, P. J.: Importance of biomass burning in the atmospheric budgets of nitrogen-containing gases, Nature, 346, 552–554, https://doi.org/10.1038/346552a0, 1990.

Luecken, D. J., Napelenok, S. L., Strum, M., Scheffe, R., and Phillips, S.: Sensitivity of Ambient Atmospheric Formaldehyde and Ozone to Precursor Species and Source Types Across the United States, American Chemical Society, 52, 4668–4675, https://doi.org/10.1021/acs.est.7b05509, 2018.

Luers, J. K. and Eskridge, R. E.: Temperature corrections for the VIZ and VAISALA radiosondes, Tech. rep., Department of Commerce, Asheville, NC, United States, https://doi.org/10.2172/548868, 1994.

Lutsch, E.: The Influence of Biomass Burning on the Arctic Atmosphere, Ph.D. thesis, University of Toronto, Toronto, Ontario, Canada, permanent link: http://hdl.handle.net/1807/97562, 2019.

Lutsch, E., Dammers, E., Conway, S., and Strong, K.: Long-range transport of NH_3, CO, HCN, and C_2H_6 from the 2014 Canadian Wildfires, Geophysical Research Letters, 43, 8286–8297, https://doi.org/10.1002/2016GL070114, 2016.

Lutsch, E., Strong, K., Jones, D. B. A., Ortega, I., Hannigan, J. W., Dammers, E., Shephard, M. W., Morris, E., Murphy, K., Evans, M. J., Parrington, M., Whitburn, S., Van Damme, M., Clarisse, L., Coheur, P.-F., Clerbaux, C., Croft, B., Martin, R. V., Pierce, J. R., and Fisher, J. A.: Unprecedented Atmospheric Ammonia Concentrations Detected in the High Arctic From the 2017 Canadian Wildfires, Journal of Geophysical Research: Atmospheres, 12, 8178–8202, https://doi.org/10.1029/2019JD030419, 2019.

Lutsch, E., Strong, K., Jones, D. B. A., Blumenstock, T., Conway, S., Fisher, J. A., Hannigan, J. W., Hase, F., Kasai, Y., Mahieu, E., Makarova, M., Morino, I., Nagahama, T., Notholt, J., Ortega, I., Palm, M., Poberovskii, A. V., Sussmann, R., and Warneke, T.: Detection and attribution of wildfire pollution in the Arctic and northern midlatitudes using a network of Fourier-transform infrared spectrometers and GEOS-Chem, Atmospheric Chemistry and Physics, 20, 12 813–12 851, https://doi.org/10.5194/acp-20-12813-2020, 2020.

Maasakkers, J. D., Jacob, D. J., Sulprizio, M. P., Turner, A. J., Weitz, M., Wirth, T., Hight, C., DeFigueiredo, M., Desai, M., Schmeltz, R., Hockstad, L., Bloom, A. A., Bowman, K. W., Jeong, S., and Fischer, M. L.: Gridded National Inventory of U.S. Methane Emissions, Environmental Science & Technology, 50, 13 123–13 133, https://doi.org/10.1021/acs.est.6b02878, 2016.

Mahieu, E., Chipperfield, M. P., Notholt, J., Reddmann, T., Anderson, J., Bernath, P. F., Blumenstock, T., Coffey, M. T., Dhomse, S. S., Feng, W., Franco, B., Froidevaux, L., Griffith, D. W. T., Hannigan, J. W., Hase, F., Hossaini, R., Jones, N. B., Morino, I., Murata, I., Nakajima, H., Palm, M., Paton-Walsh, C., III, J. M. R., Schneider, M., Servais, C., Smale, D., and Walker, K. A.: Recent Northern Hemisphere stratospheric HCl increase due to atmospheric circulation changes, Nature, 515, 104–107, https://doi.org/10.1038/nature13857, 2014.

Maier-Reimer, E. and Hasselmann, K.: Transport and storage of CO_2 in the ocean

- an inorganic ocean-circulation carbon cycle model, Climate Dynamics, 2, 63–90, https://doi.org/10.1007/BF01054491, 1987.

Manabe, S. and Strickler, R. F.: Thermal Equilibrium of the Atmosphere with a Convective Adjustment, Journal of Atmospheric Sciences, 21, 361–385, https://doi.org/10.1175/1520-0469(1964)021⟨0361:TEOTAW⟩2.0.CO;2, 1964.

Marsh, D. R., Mills, M. J., Kinnison, D. E., Lamarque, J.-F., Calvo, N., and Polvani, L. M.: Climate Change from 1850 to 2005 Simulated in CESM1(WACCM), Journal of Climate, 26, 7372–7391, https://doi.org/10.1175/JCLI-D-12-00558.1, 2013.

Matthews, H. D., Weaver, A. J., Meissner, K. J., Gillett, N. P., and Eby, M.: Natural and anthropogenic climate change: incorporating historical land cover change, vegetation dynamics and the global carbon cycle, Climate Dynamics, 22, 461–479, https://doi.org/10.1007/s00382-004-0392-2, 2004.

McNab, I. R.: Encyclopedia of Spectroscopy and Spectrometry, pp. 978–987, Academic Press, Cambridge, Massachusetts, United States, 3rd edn., 2017.

McQuarrie, D., Simon, J., Cox, H., and Choi, J.: Physical Chemistry: A Molecular Approach, G - Reference, Information and Interdisciplinary Subjects Series, University Science Books, 1997.

Meng, Z. Y., Lin, W. L., Jiang, X. M., Yan, P., Wang, Y., Zhang, Y. M., Jia, X. F., and Yu, X. L.: Characteristics of atmospheric ammonia over Beijing, China, Atmospheric Chemistry and Physics, 11, 6139–6151, https://doi.org/10.5194/acp-11-6139-2011, 2011.

Millet, D. B., Jacob, D. J., Custer, T. G., de Gouw, J. A., Goldstein, A. H., Karl, T., Singh, H. B., Sive, B. C., Talbot, R. W., Warneke, C., and Williams, J.: New constraints on terrestrial and oceanic sources of atmospheric methanol, Atmospheric Chemistry and Physics, 8, 6887–6905, https://doi.org/10.5194/acp-8-6887-2008, 2008.

Millet, D. B., Baasandorj, M., Farmer, D. K., Thornton, J. A., Baumann, K., Brophy, P., Chaliyakunnel, S., de Gouw, J. A., Graus, M., Hu, L., Koss, A., Lee, B. H., Lopez-Hilfiker, F. D., Neuman, J. A., Paulot, F., Peischl, J., Pollack, I. B., Ryerson, T. B., Warneke, C., Williams, B. J., and Xu, J.: A large and ubiquitous source of atmospheric formic acid, Atmospheric Chemistry and Physics, 15, 6283–6304, https://doi.org/10.5194/acp-15-6283-2015, 2015.

Ministry of the Environment and Climate Change: Air Quality in Ontario: 2016 Report, Distributed by the Ministry of the Environment, Conservation and Parks (current name), Toronto, Ontario, Canada, URL: http://www.airqualityontario.com/press/publications.php (last accessed: October, 2020), 2016.

Miyazaki, K., Bowman, K., Sekiya, T., Jiang, Z., Chen, X., Eskes, H., Ru, M., Zhang, Y., and Shindell, D.: Air Quality Response in China Linked to the 2019 Novel Coronavirus (COVID-19) Lockdown, Geophysical Research Letters, 47, e2020GL089 252, https://doi.org/10.1029/2020GL089252, 2020.

Molod, A., Takacs, L., Suarez, M., and Bacmeister, J.: Development of the GEOS-5 atmospheric general circulation model: evolution from MERRA to

MERRA2, Geoscientific Model Development, 8, 1339–1356, https://doi.org/10.5194/gmd-8-1339-2015, 2015.

Mostafavi Pak, N., Heerah, S., and Wunch, D.: Methane Emission Inventory for the Greater Toronto Area (GTA), Scholars Portal Dataverse. Draft version. https://doi.org/10.5683/SP2/HTNDSO, 2019.

Müller, J.-F. and Brasseur, G.: IMAGES: A three-dimensional chemical transport model of the global troposphere, Journal of Geophysical Research: Atmospheres, 100, 16 445–16 490, https://doi.org/10.1029/94JD03254, 1995.

Munroe, J., Brown, C., Kessel, C., Verhallen, A., Lauzon, J., O'Halloran, I., Bruulsema, T., and Cowan, D.: Soil Fertility Handbook Publication 611, Guelph, Ontario, Canada, URL: `http://www.omafra.gov.on.ca/english/crops/pub611/pub611.pdf` (last accessed: October, 2020), 2018.

NAS: The Future of Atmospheric Chemistry Research: Remembering Yesterday, Understanding Today, Anticipating Tomorrow, pp. 2–115, The National Academies Press, Washington, DC, https://doi.org/10.17226/23573, 2016.

Nicely, J. M., Canty, T. P., Manyin, M., Oman, L. D., Salawitch, R. J., Steenrod, S. D., Strahan, S. E., and Strode, S. A.: Changes in Global Tropospheric OH Expected as a Result of Climate Change Over the Last Several Decades, Journal of Geophysical Research: Atmospheres, 123, 10 774–10 795, https://doi.org/10.1029/2018JD028388, 2018.

Nowak, J. B., Neuman, J. A., Bahreini, R., Brock, C. A., Middlebrook, A. M., Wollny, A. G., Holloway, J. S., Peischl, J., Ryerson, T. B., and Fehsenfeld, F. C.:

Airborne observations of ammonia and ammonium nitrate formation over Houston, Texas, Journal of Geophysical Research: Atmospheres, 115, D22, https://doi.org/10.1029/2010JD014195, 2010.

Olivier, J., Bouwman, A., Van der Hoek, K., and Berdowski, J.: Global air emission inventories for anthropogenic sources of NO_x, NH_3 and N_2O in 1990, Environmental Pollution, 102, 135–148, https://doi.org/10.1016/S0269-7491(98)80026-2, 1998.

Olsen, K. S., Strong, K., Walker, K. A., Boone, C. D., Raspollini, P., Plieninger, J., Bader, W., Conway, S., Grutter, M., Hannigan, J. W., Hase, F., Jones, N., de Mazière, M., Notholt, J., Schneider, M., Smale, D., Sussmann, R., and Saitoh, N.: Comparison of the GOSAT TANSO-FTS TIR CH_4 volume mixing ratio vertical profiles with those measured by ACE-FTS, ESA MIPAS, IMK-IAA MIPAS, and 16 NDACC stations, Atmospheric Measurement Techniques, 10, 3697–3718, https://doi.org/10.5194/amt-10-3697-2017, 2017.

Park, R. J., Jacob, D. J., Field, B. D., Yantosca, R. M., and Chin, M.: Natural and transboundary pollution influences on sulfate-nitrate-ammonium aerosols in the United States: Implications for policy, Journal of Geophysical Research: Atmospheres, 109, D15 204, https://doi.org/10.1029/2003JD004473, 2004.

Paton-Walsh, C., Jones, N. B., Wilson, S. R., Haverd, V., Meier, A., Griffith, D. W. T., and Rinsland, C. P.: Measurements of trace gas emissions from Australian forest fires and correlations with coincident measurements of aerosol optical depth, Journal of Geophysical Research: Atmospheres, 110, D24 305, https://doi.org/10.1029/2005JD006202, 2005.

Paton-Walsh, C., Wilson, S. R., Jones, N. B., and Griffith, D. W. T.: Measurement of methanol emissions from Australian wildfires by ground-based solar Fourier transform spectroscopy, Geophysical Research Letters, 35, L08 810, https://doi.org/10.1029/2007GL032951, 2008.

Paulot, F., Wunch, D., Crounse, J. D., Toon, G. C., Millet, D. B., DeCarlo, P. F., Vigouroux, C., Deutscher, N. M., González Abad, G., Notholt, J., Warneke, T., Hannigan, J. W., Warneke, C., de Gouw, J. A., Dunlea, E. J., De Mazière, M., Griffith, D. W. T., Bernath, P., Jimenez, J. L., and Wennberg, P. O.: Importance of secondary sources in the atmospheric budgets of formic and acetic acids, Atmospheric Chemistry and Physics, 11, 1989–2013, https://doi.org/10.5194/acp-11-1989-2011, 2011.

Perkins, W. D.: Fourier transform-infrared spectroscopy: Part l. Instrumentation, Journal of Chemical Education, 63, A5, https://doi.org/10.1021/ed063pA5, 1986.

Perrin, F.: Whose absorption law?, Journal of the Optical Society of America, 38, 72, https://doi.org/10.1364/josa.38.000072, 1948.

Peterson, D., Campbell, J., Hyer, E., Fromm, M., Kablick, G., Cossuth, J., and Deland, M.: Wildfire-driven thunderstorms cause a volcano-like stratospheric injection of smoke, npj Climate and Atmospheric Science, 1, 30, https://doi.org/10.1038/s41612-018-0039-3, 2018.

Pisso, I., Sollum, E., Grythe, H., Kristiansen, N. I., Cassiani, M., Eckhardt, S., Arnold, D., Morton, D., Thompson, R. L., Groot Zwaaftink, C. D., Evangeliou, N., Sodemann, H., Haimberger, L., Henne, S., Brunner, D., Burkhart, J. F., Fouilloux, A., Brioude, J., Philipp, A., Seibert, P., and Stohl, A.: FLEXPART 10.4, Zenodo. https://doi.org10.5281/zenodo.3542277, 2019.

Pope, C. A., Ezzati, M., and Dockery, D. W.: Fine-Particulate Air Pollution and Life Expectancy in the United States, New England Journal of Medicine, 360, 376–386, https://doi.org/10.1056/NEJMsa0805646, 2009.

Pozzer, A., Tsimpidi, A. P., Karydis, V. A., de Meij, A., and Lelieveld, J.: Impact of agricultural emission reductions on fine-particulate matter and public health, Atmospheric Chemistry and Physics, 17, 12 813–12 826, https://doi.org/10.5194/acp-17-12813-2017, 2017.

Ramanathan, V. and Carmichael, G.: Global and regional climate changes due to black carbon, Nature Geoscience, 1, 221–227, https://doi.org/10.1038/ngeo156, 2008.

Randerson, J., van der Werf, G., Giglio, L., Collatz, G., and Kasibhatla, P.: Global Fire Emissions Database, Version 4.1 (GFEDv4), ORNL Distributed Active Archive Center, Oak Ridge, Tennessee. https://doi.org/10.3334/ORNLDAAC/1293, 2017.

Ravishankara, A. R., Portmann, R. W., and Daniel, J. S.: Nitrous oxide (N_2O): the dominant ozone-depleting substance emitted in the 21st century, Science, 326, 123–125, https://doi.org/10.1126/science.1176985, 2009.

R'Honi, Y., Clarisse, L., Clerbaux, C., Hurtmans, D., Duflot, V., Turquety, S., Ngadi, Y., and Coheur, P.-F.: Exceptional emissions of NH_3 and HCOOH in the 2010 Russian wildfires, Atmospheric Chemistry and Physics, 13, 4171–4181, https://doi.org/10.5194/acp-13-4171-2013, 2013.

Riehl, H.: The Jet Stream, pp. 23–37, American Meteorological Society, Boston, Massachusetts, United States, 1st edn., 1954.

Rinsland, C. P., Zander, R., and Demoulin, P.: Ground-based infrared measurements of HNO_3 total column abundances: Long-term trend and variability, Journal of Geophysical Research: Atmospheres, 96, 9379–9389, https://doi.org/10.1029/91JD00609, 1991.

Rinsland, C. P., Mahieu, E., Chiou, L., and Herbin, H.: First ground-based infrared solar absorption measurements of free tropospheric methanol (CH_3OH): Multidecade infrared time series from Kitt Peak (31.9°N 111.6°W): Trend, seasonal cycle, and comparison with previous measurements, Journal of Geophysical Research: Atmospheres, 114, D04 309, https://doi.org/10.1029/2008JD011003, 2009.

Rodgers, C. D.: Characterization and error analysis of profiles retrieved from remote sounding measurements, Journal of Geophysical Research: Atmospheres, 95, 5587–5595, https://doi.org/10.1029/JD095iD05p05587, 1990.

Rodgers, C. D.: Inverse Methods for Atmospheric Sounding, pp. 13–100, Atmospheric, Oceanic and Planetary Physics, World Scientific, Singapore, https://doi.org/10.1142/3171, 2000.

Rodgers, C. D. and Connor, B. J.: Intercomparison of remote sounding instruments, Journal of Geophysical Research: Atmospheres, 108, ACH 13, https://doi.org/10.1029/2002JD002299, 2003.

Rothman, L., Gordon, I., Barbe, A., Benner, D., Bernath, P., Birk, M., Boudon, V., Brown, L., Campargue, A., Champion, J.-P., Chance, K., Coudert, L., Dana, V., Devi, V., Fally, S., Flaud, J.-M., Gamache, R., Goldman, A., Jacquemart, D., Kleiner, I., Lacome, N., Lafferty, W., Mandin, J.-Y., Massie, S., Mikhailenko, S., Miller, C., Moazzen-Ahmadi, N., Naumenko, O., Nikitin, A., Orphal, J., Perevalov, V., Perrin, A., Predoi-Cross, A., Rinsland, C., Rotger, M., Šimečková, M., Smith, M., Sung, K., Tashkun, S., Tennyson, J., Toth, R., Vandaele, A., and Vander Auwera, J.: The HITRAN 2008 molecular spectroscopic database, Journal of Quantitative Spectroscopy and Radiative Transfer, 110, 533–572, https://doi.org/10.1016/j.jqsrt.2009.02.013, 2009.

Saha, S., Moorthi, S., Wu, X., Wang, J., Nadiga, S., Tripp, P., Behringer, D., Hou, Y.-T., Chuang, H.-y., Iredell, M., Ek, M., Meng, J., Yang, R., Mendez, M. P., van den Dool, H., Zhang, Q., Wang, W., Chen, M., and Becker, E.: NCEP Climate Forecast System Version 2 (CFSv2) 6-hourly Products, Research Data Archive at the National Center for Atmospheric Research, Computational and Information Systems Laboratory, Boulder CO. https://doi.org/10.5065/D61C1TXF, 2011.

Saunois, M., Stavert, A. R., Poulter, B., Bousquet, P., Canadell, J. G., Jackson, R. B., Raymond, P. A., Dlugokencky, E. J., Houweling, S., Patra, P. K., Ciais, P., Arora, V. K., Bastviken, D., Bergamaschi, P., Blake, D. R., Brailsford, G., Bruhwiler, L., Carlson, K. M., Carrol, M., Castaldi, S., Chandra, N., Crevoisier, C., Crill, P. M., Covey, K., Curry, C. L., Etiope, G., Frankenberg, C., Gedney, N., Hegglin, M. I., Höglund-Isaksson, L., Hugelius, G., Ishizawa, M., Ito, A., Janssens-Maenhout, G., Jensen, K. M., Joos, F., Kleinen, T., Krummel, P. B., Langenfelds, R. L., Laruelle, G. G., Liu, L., Machida, T., Maksyutov, S., McDonald, K. C., McNorton, J., Miller, P. A., Melton, J. R., Morino, I., Müller, J., Murguia-Flores, F., Naik, V., Niwa, Y., Noce, S., O'Doherty, S., Parker, R. J., Peng, C., Peng, S., Peters, G. P., Prigent, C., Prinn, R., Ramonet, M., Regnier, P., Riley, W. J., Rosentreter, J. A., Segers, A., Simpson, I. J., Shi, H., Smith, S. J., Steele, L. P., Thornton, B. F., Tian, H., Tohjima, Y., Tubiello, F. N., Tsuruta, A., Viovy, N., Voulgarakis, A., Weber, T. S., van Weele, M., van der Werf, G. R., Weiss, R. F., Worthy, D., Wunch, D., Yin, Y., Yoshida, Y., Zhang, W., Zhang, Z., Zhao, Y., Zheng, B., Zhu, Q., Zhu, Q., and Zhuang, Q.: The Global Methane Budget 2000–2017, Earth System Science Data, 12, 1561–1623, https://doi.org/10.5194/essd-12-1561-2020, 2020.

Schaap, M., van Loon, M., ten Brink, H. M., Dentener, F. J., and Builtjes, P. J. H.: Secondary inorganic aerosol simulations for Europe with special attention to nitrate, Atmospheric Chemistry and Physics, 4, 857–874, https://doi.org/10.5194/acp-4-857-2004, 2004.

Schiferl, L. D., Heald, C. L., Nowak, J. B., Holloway, J. S., Neuman, J. A., Bahreini, R., Pollack, I. B., Ryerson, T. B., Wiedinmyer, C., and Murphy, J. G.: An investigation of ammonia and inorganic particulate matter in California during the CalNex campaign, Journal of Geophysical Research: Atmospheres, 119, 1883–1902, https://doi.org/10.1002/2013JD020765, 2014.

Schiferl, L. D., Heald, C. L., Van Damme, M., Clarisse, L., Clerbaux, C., Coheur, P.-F., Nowak, J. B., Neuman, J. A., Herndon, S. C., Roscioli, J. R., and Eilerman, S. J.: Interannual variability of ammonia concentrations over the United States: sources and implications, Atmospheric Chemistry and Physics, 16, 12 305–12 328, https://doi.org/10.5194/acp-16-12305-2016, 2016.

Schoeberl, M. R., Lait, L. R., Newman, P. A., and Rosenfield, J. E.: The structure of the polar vortex, Journal of Geophysical Research: Atmospheres, 97, 7859–7882, https://doi.org/10.1029/91JD02168, 1992.

Schoennagel, T., Balch, J. K., Brenkert-Smith, H., Dennison, P. E., Harvey, B. J., Krawchuk, M. A., Mietkiewicz, N., Morgan, P., Moritz, M. A., Rasker, R., Turner, M. G., and Whitlock, C.: Adapt to more wildfire in western North American forests as climate changes, Proceedings of the National Academy of Sciences, 114, 4582–4590, https://doi.org/10.1073/pnas.1617464114, 2017.

Sheese, P. E., Walker, K. A., Boone, C. D., Bernath, P. F., and Funke, B.: Nitrous oxide in the atmosphere: First measurements of a lower thermospheric source, Geophysical Research Letters, 43, 2866–2872, https://doi.org/10.1002/2015GL067353, 2016.

Sheng, J.-X., Jacob, D. J., Maasakkers, J. D., Sulprizio, M. P., Zavala-Araiza, D., and Hamburg, S. P.: A high-resolution ($0.1^{\circ} \times 0.1^{\circ}$) inventory of methane emissions from Canadian and Mexican oil and gas systems, Atmospheric Environment, 158, 211–215, https://doi.org/10.1016/j.atmosenv.2017.02.036, 2017.

Shephard, M. W., Dammers, E., Cady-Pereira, K. E., Kharol, S. K., Thompson, J., Gainariu-Matz, Y., Zhang, J., McLinden, C. A., Kovachik, A., Moran, M., Bittman, S., Sioris, C. E., Griffin, D., Alvarado, M. J., Lonsdale, C., Savic-Jovcic, V., and Zheng, Q.: Ammonia measurements from space with the Cross-track Infrared Sounder: characteristics and applications, Atmospheric Chemistry and Physics, 20, 2277–2302, https://doi.org/10.5194/acp-20-2277-2020, 2020.

Shi, X. and Brasseur, G. P.: The Response in Air Quality to the Reduction of Chinese Economic Activities During the COVID-19 Outbreak, Geophysical Research Letters, 47, e2020GL088 070, https://doi.org/10.1029/2020GL088070, 2020.

Stavrakou, T., Guenther, A., Razavi, A., Clarisse, L., Clerbaux, C., Coheur, P.-F., Hurtmans, D., Karagulian, F., De Mazière, M., Vigouroux, C., Amelynck, C., Schoon, N., Laffineur, Q., Heinesch, B., Aubinet, M., Rinsland, C., and Müller, J.-F.: First space-based derivation of the global atmospheric methanol emission fluxes, Atmospheric Chemistry and Physics, 11, 4873–4898, https://doi.org/10.5194/acp-11-4873-2011, 2011.

Stavrakou, T., Müller, J.-F., Peeters, J., Razavi, A., Clarisse, L., Clerbaux, C., Coheur, P.-F., Hurtmans, D., De Mazière, M., Vigouroux, C., Deutscher, N. M., Griffith, D. W. T., Jones, N., and Paton-Walsh, C.: Satellite evidence for a large source of formic acid from boreal and tropical forests, Nature Geoscience, 5, 26–30, https://doi.org/10.1038/ngeo1354, 2012.

Stein, A. F., Draxler, R. R., Rolph, G. D., Stunder, B. J. B., Cohen, M. D., and Ngan, F.: NOAA's HYSPLIT Atmospheric Transport and Dispersion Modeling System, Bulletin of the American Meteorological Society, 96, 2059–2077, https://doi.org/10.1175/BAMS-D-14-00110.1, 2015.

Steinbrecht, W., Kubistin, D., Plass-Dülmer, C., Davies, J., Tarasick, D. W., Gathen, P. v. d., Deckelmann, H., Jepsen, N., Kivi, R., Lyall, N., Palm, M., Notholt, J., Kois, B., Oelsner, P., Allaart, M., Piters, A., Gill, M., Van Malderen, R., Delcloo, A. W., Sussmann, R., Mahieu, E., Servais, C., Romanens, G., Stübi, R., Ancellet, G., Godin-Beekmann, S., Yamanouchi, S., Strong, K., Johnson, B., Cullis, P., Petropavlovskikh, I., Hannigan, J. W., Hernandez, J.-L., Rodriguez, A. D., Nakano, T., Chouza, F., Leblanc, T., Torres, C., Garcia, O., Röhling, A. N., Schneider, M., Blumenstock, T., Tully, M., Paton-Walsh, C., Jones, N., Querel, R., Strahan, S., Stauffer, R. M., Thompson, A. M., Inness, A., Engelen, R., Chang, K.-L., and Cooper, O. R.: COVID-19 Crisis Reduces Free Tropospheric Ozone across the Northern Hemisphere, Geophysical Research Letters, 48, e2020GL091 987, https://doi.org/10.1029/2020GL091987, 2021.

Stephens, G. L., O'Brien, D., Webster, P. J., Pilewski, P., Kato, S., and Li, J.-l.: The albedo of Earth, Reviews of Geophysics, 53, 141–163, https://doi.org/10.1002/2014RG000449, 2015.

Stuart, B.: Kirk-Othmer Encyclopedia of Chemical Technology: Infrared Spectroscopy, pp. 1–20, American Cancer Society, Atlanta, Georgia, United States, https://doi.org/10.1002/0471238961.0914061810151405.a01.pub2, 2005.

Sun, Y., Liu, C., Zhang, L., Palm, M., Notholt, J., Yin, H., Vigouroux, C., Lutsch, E., Wang, W., Shan, C., Blumenstock, T., Nagahama, T., Morino, I., Mahieu, E., Strong, K., Langerock, B., De Mazière, M., Hu, Q., Zhang, H., Petri, C., and Liu, J.: Fourier transform infrared time series of tropospheric HCN in eastern China: seasonality, interannual variability, and source attribution, Atmospheric Chemistry and Physics, 20, 5437–5456, https://doi.org/10.5194/acp-20-5437-2020, 2020.

Sussmann, R., Forster, F., Rettinger, M., and Jones, N.: Strategy for high-accuracy-and-precision retrieval of atmospheric methane from the mid-infrared FTIR network, Atmospheric Measurement Techniques, 4, 1943–1964, https://doi.org/10.5194/amt-4-1943-2011, 2011.

Thompson, R. L., Lassaletta, L., Patra, P. K., Wilson, C., Wells, K. C., Gressent, A., Koffi, E. N., Chipperfield, M. P., Winiwarter, W., Davidson, E. A., Tian, H., and Canadell, J. G.: Acceleration of global N_2O emissions seen from two decades of atmospheric inversion, Nature Climate Change, 9, 993–998, https://doi.org/10.1038/s41558-019-0613-7, 2019.

Tikhonov, A. and Glasko, V.: Use of the regularization method in non-linear problems, USSR Computational Mathematics and Mathematical Physics, 5, 93–107, https://doi.org/10.1016/0041-5553(65)90150-3, 1965.

Tikhonov, A. N.: Solution of incorrectly formulated problems and the regularization method, Soviet Mathematics Doklady, 4, 1035–1038, URL: `https://ci.nii.ac.jp/naid/10004315593/en/` (last accessed: November, 2020), 1963.

Toon, G. C., Blavier, J.-F., Sen, B., Margitan, J. J., Webster, C. R., May, R. D., Fahey, D., Gao, R., Del Negro, L., Proffitt, M., Elkins, J., Romashkin, P. A., Hurst, D. F., Oltmans, S., Atlas, E., Schauffler, S., Flocke, F., Bui, T. P., Stimpfle, R. M., Bonne, G. P., Voss, P. B., and Cohen, R. C.: Comparison of MkIV balloon and ER-2 aircraft measurements of atmospheric trace gases, Journal of Geophysical Research: Atmospheres, 104, 26 779–26 790, https://doi.org/10.1029/1999JD900379, 1999.

Tournadre, B., Chelin, P., Ray, M., Cuesta, J., Kutzner, R. D., Landsheere, X., Fortems-Cheiney, A., Flaud, J.-M., Hase, F., Blumenstock, T., Orphal, J., Viatte, C., and Camy-Peyret, C.: Atmospheric ammonia (NH_3) over the Paris megacity: 9 years of total column observations from ground-based infrared remote sensing, Atmospheric Measurement Techniques, 13, 3923–3937, https://doi.org/10.5194/amt-13-3923-2020, 2020.

Turetsky, M. R., Kane, E. S., Harden, J. W., Ottmar, R. D., Manies, K. L., Hoy, E. E., and Kasischke, E. S.: Recent acceleration of biomass burning and carbon losses in Alaskan forests and peatlands, Nature Geoscience, 4, 27–31, https://doi.org/10.1038/ngeo1027, 2010.

Turner, A. J., Jacob, D. J., Benmergui, J., Wofsy, S. C., Maasakkers, J. D., Butz, A., Hasekamp, O., and Biraud, S. C.: A large increase in U.S. methane emissions over the past decade inferred from satellite data and surface observations, Geophysical Research Letters, 43, 2218–2224, https://doi.org/10.1002/2016GL067987, 2016.

Tzompa-Sosa, Z. A., Mahieu, E., Franco, B., Keller, C. A., Turner, A. J., Helmig, D., Fried, A., Richter, D., Weibring, P., Walega, J., Yacovitch, T. I., Herndon, S. C., Blake, D. R., Hase, F., Hannigan, J. W., Conway, S., Strong, K., Schneider, M., and Fischer, E. V.: Revisiting global fossil fuel and biofuel emissions of ethane, Journal of Geophysical Research: Atmospheres, 122, 2493–2512, https://doi.org/10.1002/2016JD025767, 2017.

Tzompa-Sosa, Z. A., Henderson, B. H., Keller, C. A., Travis, K., Mahieu, E., Franco, B., Estes, M., Helmig, D., Fried, A., Richter, D., Weibring, P., Walega, J., Blake, D. R., Hannigan, J. W., Ortega, I., Conway, S., Strong, K., and Fischer, E. V.: Atmospheric Implications of Large C_2-C_5 Alkane Emissions From the U.S. Oil and

Gas Industry, Journal of Geophysical Research: Atmospheres, 124, 1148–1169, https://doi.org/10.1029/2018JD028955, 2019.

Ueyama, R., Gerber, E. P., Wallace, J. M., and Frierson, D. M. W.: The Role of High-Latitude Waves in the Intraseasonal to Seasonal Variability of Tropical Upwelling in the Brewer–Dobson Circulation, Journal of the Atmospheric Sciences, 70, 1631–1648, https://doi.org/10.1175/JAS-D-12-0174.1, 2013.

Urbanski, S.: Wildland fire emissions, carbon, and climate: Emission factors, Forest Ecology and Management, 317, 51–60, https://doi.org/10.1016/j.foreco.2013.05.045, 2014.

Van Damme, M., Wichink Kruit, R., Schaap, M., Clarisse, L., Clerbaux, C., Coheur, P.-F., Dammers, E., Dolman, A., and Erisman, J.: Evaluating 4 years of atmospheric ammonia (NH_3) over Europe using IASI satellite observations and LOTOS-EUROS model results, Journal of Geophysical Research: Atmospheres, 119, 9549–9566, https://doi.org/10.1002/2014JD021911, 2014a.

Van Damme, M., Clarisse, L., Heald, C. L., Hurtmans, D., Ngadi, Y., Clerbaux, C., Dolman, A. J., Erisman, J. W., and Coheur, P. F.: Global distributions, time series and error characterization of atmospheric ammonia (NH_3) from IASI satellite observations, Atmospheric Chemistry and Physics, 14, 2905–2922, https://doi.org/10.5194/acp-14-2905-2014, 2014b.

Van Damme, M., Clarisse, L., Dammers, E., Liu, X., Nowak, J. B., Clerbaux, C., Flechard, C. R., Galy-Lacaux, C., Xu, W., Neuman, J. A., Tang, Y. S., Sutton, M. A., Erisman, J. W., and Coheur, P. F.: Towards validation of ammonia (NH_3)

measurements from the IASI satellite, Atmospheric Measurement Techniques, 8, 1575–1591, https://doi.org/10.5194/amt-8-1575-2015, 2015a.

Van Damme, M., Erisman, J. W., Clarisse, L., Dammers, E., Whitburn, S., Clerbaux, C., Dolman, A. J., and Coheur, P.-F.: Worldwide spatiotemporal atmospheric ammonia (NH_3) columns variability revealed by satellite, Geophysical Research Letters, 42, 8660–8668, https://doi.org/10.1002/2015GL065496, 2015b.

Van Damme, M., Whitburn, S., Clarisse, L., Clerbaux, C., Hurtmans, D., and Coheur, P.-F.: Version 2 of the IASI NH_3 neural network retrieval algorithm: near-real-time and reanalysed datasets, Atmospheric Measurement Techniques, 10, 4905–4914, https://doi.org/10.5194/amt-10-4905-2017, 2017.

Van Damme, M., Clarisse, L., Whitburn, S., Hadji-Lazaro, J., Hurtmans, D., Clerbaux, C., and Coheur, P.-F.: Industrial and agricultural ammonia point sources exposed, Atmospheric Chemistry and Physics, 564, 99–103, https://doi.org/10.1038/s41586-018-0747-1, 2018.

van der Werf, G. R., Randerson, J. T., Giglio, L., Collatz, G. J., Mu, M., Kasibhatla, P. S., Morton, D. C., DeFries, R. S., Jin, Y., and van Leeuwen, T. T.: Global fire emissions and the contribution of deforestation, savanna, forest, agricultural, and peat fires (1997-2009), Atmospheric Chemistry and Physics, 10, 11 707–11 735, https://doi.org/10.5194/acp-10-11707-2010, 2010.

van Doremalen, N., Bushmaker, T., Morris, D. H., Holbrook, M. G., Gamble, A., Williamson, B. N., Tamin, A., Harcourt, J. L., Thornburg, N. J., Gerber, S. I., Lloyd-Smith, J. O., de Wit, E., and Munster, V. J.: Aerosol and Surface Stability of SARS-CoV-2 as Compared with SARS-CoV-1, New England Journal of Medicine, 382, 1564–1567, https://doi.org/10.1056/NEJMc2004973, 2020.

van Vuuren, D. P., Edmonds, J., Kainuma, M., Riahi, K., Thomson, A., Hibbard, K., Hurtt, G. C., Kram, T., Krey, V., Lamarque, J.-F., Masui, T., Meinshausen, M., Nakicenovic, N., Smith, S. J., and Rose, S. K.: The representative concentration pathways: an overview, Climatic Change, 109, 5–31, https://doi.org/10.1007/s10584-011-0148-z, 2011.

Viatte, C., Strong, K., Paton-Walsh, C., Mendonca, J., O'Neill, N. T., and Drummond, J. R.: Measurements of CO, HCN, and C_2H_6 Total Columns in Smoke Plumes Transported from the 2010 Russian Boreal Forest Fires to the Canadian High Arctic, Atmosphere-Ocean, 51, 522–531, https://doi.org/10.1080/07055900.2013.823373, 2013.

Viatte, C., Strong, K., Walker, K. A., and Drummond, J. R.: Five years of CO, HCN, C_2H_6, C_2H_2, CH_3OH, HCOOH and H_2CO total columns measured in the Canadian high Arctic, Atmospheric Measurement Techniques, 7, 1547–1570, https://doi.org/10.5194/amt-7-1547-2014, 2014.

Viatte, C., Strong, K., Hannigan, J., Nussbaumer, E., Emmons, L. K., Conway, S., Paton-Walsh, C., Hartley, J., Benmergui, J., and Lin, J.: Identifying fire plumes in the Arctic with tropospheric FTIR measurements and transport models, Atmospheric Chemistry and Physics, 15, 2227–2246, https://doi.org/10.5194/acp-15-2227-2015, 2015.

Viatte, C., Wang, T., Van Damme, M., Dammers, E., Meleux, F., Clarisse, L., Shephard, M. W., Whitburn, S., Coheur, P. F., Cady-Pereira, K. E., and Clerbaux, C.: Atmospheric ammonia variability and link with particulate matter formation: a case study over the Paris area, Atmospheric Chemistry and Physics, 20, 577–596, https://doi.org/10.5194/acp-20-577-2020, 2020.

Viatte, C., Petit, J.-E., Yamanouchi, S., Van Damme, M., Doucerain, C., Germain-Piaulenne, E., Gros, V., Favez, O., Clarisse, L., Coheur, P.-F., Strong, K., and Clerbaux, C.: Ammonia and $PM_{2.5}$ Air Pollution in Paris during the 2020 COVID Lockdown, Atmosphere, 12, 160, https://doi.org/10.3390/atmos12020160, 2021.

Vigouroux, C., Hendrick, F., Stavrakou, T., Dils, B., De Smedt, I., Hermans, C., Merlaud, A., Scolas, F., Senten, C., Vanhaelewyn, G., Fally, S., Carleer, M., Metzger, J.-M., Müller, J.-F., Van Roozendael, M., and De Mazière, M.: Ground-based FTIR and MAX-DOAS observations of formaldehyde at Réunion Island and comparisons with satellite and model data, Atmospheric Chemistry and Physics, 9, 9523–9544, https://doi.org/10.5194/acp-9-9523-2009, 2009.

Vigouroux, C., Blumenstock, T., Coffey, M., Errera, Q., García, O., Jones, N. B., Hannigan, J. W., Hase, F., Liley, B., Mahieu, E., Mellqvist, J., Notholt, J., Palm, M., Persson, G., Schneider, M., Servais, C., Smale, D., Thölix, L., and De Mazière, M.: Trends of ozone total columns and vertical distribution from FTIR observations at eight NDACC stations around the globe, Atmospheric Chemistry and Physics, 15, 2915–2933, https://doi.org/10.5194/acp-15-2915-2015, 2015.

Vigouroux, C., Bauer Aquino, C. A., Bauwens, M., Becker, C., Blumenstock, T., De Mazière, M., García, O., Grutter, M., Guarin, C., Hannigan, J., Hase, F., Jones, N., Kivi, R., Koshelev, D., Langerock, B., Lutsch, E., Makarova, M., Metzger, J.-M., Müller, J.-F., Notholt, J., Ortega, I., Palm, M., Paton-Walsh, C., Poberovskii, A., Rettinger, M., Robinson, J., Smale, D., Stavrakou, T., Stremme, W., Strong, K., Sussmann, R., Té, Y., and Toon, G.: NDACC harmonized formaldehyde time series from 21 FTIR stations covering a wide range of column abundances, Atmospheric Measurement Techniques, 11, 5049–5073, https://doi.org/10.5194/amt-11-5049-2018, 2018.

Vigouroux, C., Langerock, B., Bauer Aquino, C. A., Blumenstock, T., Cheng, Z., De Mazière, M., De Smedt, I., Grutter, M., Hannigan, J. W., Jones, N., Kivi, R., Loyola, D., Lutsch, E., Mahieu, E., Makarova, M., Metzger, J.-M., Morino, I., Murata, I., Nagahama, T., Notholt, J., Ortega, I., Palm, M., Pinardi, G., Röhling, A., Smale, D., Stremme, W., Strong, K., Sussmann, R., Té, Y., van Roozendael, M., Wang, P., and Winkler, H.: TROPOMI–Sentinel-5 Precursor formaldehyde validation using an extensive network of ground-based Fourier-transform infrared stations, Atmospheric Measurement Techniques, 13, 3751–3767, https://doi.org/10.5194/amt-13-3751-2020, 2020.

Vitousek, P. M., Mooney, H. A., Lubchenco, J., and Melillo, J. M.: Human Domination of Earth's Ecosystems, Science, 277, 494–499, https://doi.org/10.1126/science.277.5325.494, 1997.

Vohra, K., Vodonos, A., Schwartz, J., Marais, E. A., Sulprizio, M. P., and Mickley, L. J.: Global mortality from outdoor fine particle pollution generated by fossil fuel combustion: Results from GEOS-Chem, Environmental Research, p. 110754, https://doi.org/10.1016/j.envres.2021.110754, 2021.

Wallace, J. M. and Hobbs, P. V.: Atmospheric Science, Academic Press, San Diego, California, United States, 2nd edn., 2006.

Warner, J. X., Wei, Z., Strow, L. L., Dickerson, R. R., and Nowak, J. B.: The global tropospheric ammonia distribution as seen in the 13-year AIRS measurement record, Atmospheric Chemistry and Physics, 16, 5467–5479, https://doi.org/10.5194/acp-16-5467-2016, 2016.

Warner, J. X., Dickerson, R. R., Wei, Z., Strow, L. L., Wang, Y., and Liang, Q.: Increased atmospheric ammonia over the world's major agricultural areas detected from space, Geophysical Research Letters, 44, 2875–2884, https://doi.org/10.1002/2016GL072305, 2017.

Weatherhead, E. C., Reinsel, G. C., Tiao, G. C., Meng, X.-L., Choi, D., Cheang, W.-K., Keller, T., DeLuisi, J., Wuebbles, D. J., Kerr, J. B., Miller, A. J., Oltmans, S. J., and Frederick, J. E.: Factors affecting the detection of trends: Statistical considerations and applications to environmental data, Journal of Geophysical Research: Atmospheres, 103, 17 149–17 161, https://doi.org/10.1029/98JD00995, 1998.

Wells, K. C., Millet, D. B., Hu, L., Cady-Pereira, K. E., Xiao, Y., Shephard, M. W., Clerbaux, C. L., Clarisse, L., Coheur, P.-F., Apel, E. C., de Gouw, J., Warneke, C., Singh, H. B., Goldstein, A. H., and Sive, B. C.: Tropospheric methanol observations from space: retrieval evaluation and constraints on the seasonality of biogenic emissions, Atmospheric Chemistry and Physics, 12, 5897–5912, https://doi.org/10.5194/acp-12-5897-2012, 2012.

Wentworth, G., Murphy, J., and Sills, D.: Impact of lake breezes on ozone and nitrogen oxides in the Greater Toronto Area, Atmospheric Environment, 109, 52–60, https://doi.org/10.1016/j.atmosenv.2015.03.002, 2015.

Wentworth, G. R., Murphy, J. G., Gregoire, P. K., Cheyne, C. A. L., Tevlin, A. G., and Hems, R.: Soil-atmosphere exchange of ammonia in a non-fertilized grassland: measured emission potentials and inferred fluxes, Biogeosciences, 11, 5675–5686, https://doi.org/10.5194/bg-11-5675-2014, 2014.

Whaley, C.: Improvements to our Understanding of Toronto-Area Atmospheric Composition, Ph.D. thesis, University of Toronto, Toronto, Ontario, Canada, permanent link: `http://hdl.handle.net/1807/68411`, 2014.

Whaley, C., Strong, K., Adams, C., Bourassa, A. E., Daffer, W. H., Degenstein, D. A., Fast, H., Fogal, P. F., Manney, G. L., Mittermeier, R. L., Pavlovic, B., and Wiacek, A.: Using FTIR measurements of stratospheric composition to identify midlatitude polar vortex intrusions over Toronto, Journal of Geophysical Research: Atmospheres, 118, 12 766–12 783, https://doi.org/10.1002/2013JD020577, 2013.

Whaley, C. H., Strong, K., Jones, D. B. A., Walker, T. W., Jiang, Z., Henze, D. K., Cooke, M. A., McLinden, C. A., Mittermeier, R. L., Pommier, M., and Fogal, P. F.: Toronto area ozone: Long-term measurements and modeled sources of poor air quality events, Journal of Geophysical Research: Atmospheres, 120, 11 368–11 390, https://doi.org/10.1002/2014JD022984, 2015.

Whitburn, S., Van Damme, M., Clarisse, L., Bauduin, S., Heald, C. L., Hadji-Lazaro, J., Hurtmans, D., Zondlo, M. A., Clerbaux, C., and Coheur, P.-F.: A flexible and robust neural network IASI-NH_3 retrieval algorithm, Journal of Geophysical

Research: Atmospheres, 121, 6581–6599, https://doi.org/10.1002/2016JD024828, 2016.

Wiacek, A.: First Trace Gas Measurements Using Fourier Transform Infrared Solar Absorption Spectroscopy at the University of Toronto Atmospheric Observatory, Ph.D. thesis, University of Toronto, Toronto, Ontario, Canada, permanent link: `https://librarysearch.library.utoronto.ca/permalink/01UTORONTO_INST/14bjeso/alma991106405283106196`, 2006.

Wiacek, A., Taylor, J. R., Strong, K., Saari, R., Kerzenmacher, T. E., Jones, N. B., and Griffith, D. W. T.: Ground-Based Solar Absorption FTIR Spectroscopy: Characterization of Retrievals and First Results from a Novel Optical Design Instrument at a New NDACC Complementary Station, Journal of Atmospheric and Oceanic Technology, 24, 432–448, https://doi.org/10.1175/JTECH1962.1, 2007.

Wielgosiński, G. and Czerwińska, J.: Smog Episodes in Poland, Atmosphere, 11, 277–290, https://doi.org/10.3390/atmos11030277, 2020.

WMO: Executive Summary: Scientific Assessment of Ozone Depletion: 2018, Tech. Rep. 58, World Meteorological Organization, Global Ozone Research and Monitoring Project, URL: `https://wedocs.unep.org/bitstream/handle/20.500.11822/26858/SAOD-2018.pdf` (last accessed: November, 2020), 2018.

Worden, H. M., Deeter, M. N., Frankenberg, C., George, M., Nichitiu, F., Worden, J., Aben, I., Bowman, K. W., Clerbaux, C., Coheur, P. F., de Laat, A. T. J., Detweiler, R., Drummond, J. R., Edwards, D. P., Gille, J. C., Hurtmans, D., Luo, M., Martínez-Alonso, S., Massie, S., Pfister, G., and Warner, J. X.: Decadal record of satellite carbon monoxide observations, Atmospheric Chemistry and Physics, 13, 837–850, https://doi.org/10.5194/acp-13-837-2013, 2013.

Worden, J., Bloom, A., Pandey, S., Jiang, Z., Worden, H., Walker, T., Houweling, S., and Röckmann, T.: Reduced biomass burning emissions reconcile conflicting estimates of the post-2006 atmospheric methane budget, Nature Communications, 8, 2227–2238, https://doi.org/10.1038/s41467-017-02246-0, 2017.

Wu, Y., Gu, B., Erisman, J. W., Reis, S., Fang, Y., Lu, X., and hang, X.: $PM_{2.5}$ pollution is substantially affected by ammonia emissions in China, Environmental pollution, 218, 86–94, https://doi.org/10.1016/j.envpol.2016.08.027, 2016.

Xiao, Y., Logan, J. A., Jacob, D. J., Hudman, R. C., Yantosca, R., and Blake, D. R.: Global budget of ethane and regional constraints on U.S. sources, Journal of Geophysical Research: Atmospheres, 113, D21 306, https://doi.org/10.1029/2007JD009415, 2008.

Xiong, X., Maddy, E. S., Barnet, C., Gambacorta, A., Patra, P. K., Sun, F., and Goldberg, M.: Retrieval of nitrous oxide from Atmospheric Infrared Sounder: Characterization and validation, Journal of Geophysical Research: Atmospheres, 119, 9107–9122, https://doi.org/10.1002/2013JD021406, 2014.

Yamanouchi, S., Strong, K., Lutsch, E., and Jones, D. B. A.: Detection of HCOOH, CH_3OH, CO, HCN, and C_2H_6 in Wildfire Plumes Transported Over Toronto Using Ground-Based FTIR Measurements From 2002–2018, Journal of Geophysical Research: Atmospheres, 125, e2019JD031 924, https://doi.org/10.1029/2019JD031924, 2020.

Yamanouchi, S., Strong, K., Colebatch, O., Conway, S., Jones, D. B. A., Lutsch, E., and Roche, S.: Atmospheric trace gas trends obtained from FTIR column measurements in Toronto, Canada from 2002-2019, Environmental Research Communications, https://doi.org/10.1088/2515-7620/abfa65, accepted for publication, 2021a.

Yamanouchi, S., Viatte, C., Strong, K., Lutsch, E., Jones, D. B. A., Clerbaux, C., Van Damme, M., Clarisse, L., and Coheur, P.-F.: Multiscale observations of NH_3 around Toronto, Canada, Atmospheric Measurement Techniques, 14, 905–921, https://doi.org/10.5194/amt-14-905-2021, 2021b.

Yao, X. and Zhang, L.: Analysis of passive-sampler monitored atmospheric ammonia at 74 sites across southern Ontario, Canada, Biogeosciences, 10, 7913–7925, https://doi.org/10.5194/bg-10-7913-2013, 2013.

Yao, X. and Zhang, L.: Trends in atmospheric ammonia at urban, rural, and remote sites across North America, Atmospheric Chemistry and Physics, 16, 11 465–11 475, https://doi.org/10.5194/acp-16-11465-2016, 2016.

Yokelson, R. J., Andreae, M. O., and Akagi, S. K.: Pitfalls with the use of enhancement ratios or normalized excess mixing ratios measured in plumes to characterize pollution sources and aging, Atmospheric Measurement Techniques, 6, 2155–2158, https://doi.org/10.5194/amt-6-2155-2013, 2013.

York, D., Evensen, N. M., Martinez, M. L., and De Basabe Delgado, J.: Unified equations for the slope, intercept, and standard errors of the best straight line, American Journal of Physics, 72, 367–375, https://doi.org/10.1119/1.1632486, 2004.

Yu, F., Nair, A. A., and Luo, G.: Long-Term Trend of Gaseous Ammonia Over the United States: Modeling and Comparison With Observations, Journal of Geophysical Research: Atmospheres, 123, 8315–8325, https://doi.org/10.1029/2018JD028412, 2018.

Zbieranowski, A. L. and Aherne, J.: Ambient concentrations of atmospheric ammonia, nitrogen dioxide and nitric acid across a rural–urban–agricultural transect in southern Ontario, Canada, Atmospheric Environment, 62, 481–491, https://doi.org/10.1016/j.atmosenv.2012.08.040, 2012.

Zellweger, C., Hüglin, C., Klausen, J., Steinbacher, M., Vollmer, M., and Buchmann, B.: Inter-comparison of four different carbon monoxide measurement techniques and evaluation of the long-term carbon monoxide time series of Jungfraujoch, Atmospheric Chemistry and Physics, 9, 3491–3503, https://doi.org/10.5194/acp-9-3491-2009, 2009.

Zeng, G., Wood, S. W., Morgenstern, O., Jones, N. B., Robinson, J., and Smale, D.: Trends and variations in CO, C_2H_6, and HCN in the Southern Hemisphere point to the declining anthropogenic emissions of CO and C_2H_6, Atmospheric Chemistry and Physics, 12, 7543–7555, https://doi.org/10.5194/acp-12-7543-2012, 2012.

Zhou, Y., Xing, X., Lang, J., Chen, D., Cheng, S., Wei, L., Wei, X., and Liu, C.: A comprehensive biomass burning emission inventory with high spatial and temporal resolution in China, Atmospheric Chemistry and Physics, 17, 2839–2864, https://doi.org/10.5194/acp-17-2839-2017, 2017.